NMR Kristallographie zur Strukturaufklärung von Metallorganischen Gerüstverbindungen und Charakterisierung von Wirts-Gast-Wechselwirkungen

Dissertation

zur Erlangung des Grades

Doktor der Naturwissenschaften (Dr. rer. nat.)

im Fach Chemie

an der Fakultät Biologie, Chemie und Geowissenschaften

der Universität Bayreuth

vorgelegt von

Julia Christine Margarete Wack

geboren in Schweinfurt

Bayreuth 2016

Die vorliegende Arbeit wurde in der Zeit von Mai 2009 bis Januar 2016 in Bayreuth am Lehrstuhl Anorganische Chemie III unter Betreuung von Herrn Professor Dr. Jürgen Senker angefertigt.

Vollständiger Abdruck der von der Fakultät Biologie, Chemie und Geowissenschaften der Universität Bayreuth genehmigten Dissertation zur Erlangung des akademischen Grades Doktor der Naturwissenschaften (Dr. rer. nat.).

Dissertation eingereicht am: 12.01.2016

Zulassung durch die Promotionskommission: 20.01.2016

Wissenschaftliches Kolloquium: 20.05.2016

Amtierender Dekan: Prof. Dr. Stefan Schuster

Prüfungsausschuss:

Prof. Dr. Jürgen Senker	(Erstgutachter)
Prof. Dr. Gerd Buntkowsky	(Zweitgutachter)
Prof. Dr. Georg Papastavrou	(Vorsitz)
Prof. Dr. Birgit Weber	

„Ein Problem sieht, wenn es einmal gelöst ist, immer einfach aus. Der große Sieg, der heute leicht errungen scheint, ist das Ergebnis einer Reihe kleiner, unbemerkter Siege. “

Paulo Coelho

Handbuch des Kriegers des Lichts

Inhaltsverzeichnis

Abkürzungsverzeichnis

Abkürzung	Bedeutung	Erläuterung in Abschnitt
*	Markierung von Rotationsseitenbanden in MAS Spektren	3.4, S. 16
1D	1-dimensional	3.4, S. 16
2D	2-dimensional	3.4, S. 16
δ_{aniso}	Anisotropie-Parameter	3.4, S. 16
η	Asymmetrie-Parameter	3.4, S. 16
δ_{iso}	isotrope chemische Verschiebung	3.4, S. 16
γ	gyromagnetisches Verhältnis	3.4, S. 16
$\mathbf{B_0}$	statisches Magnetfeld	3.4, S.16
bdc	Terephthalat (*Benzene-1,4-dicarboxylate*)	3.2, S. 8
BTB	4,4',4"-Benzol-1,3,5-triyl-tribenzoat	4.1, S. 36
CAU	Christian-Albrechts-Universität	3.2, S. 8
CT	*constant time*	3.4, S. 16
CP	Kreuzpolarisation (*cross polarization*)	3.4, S. 16
CRAMPS	*combined rotation and multiple-pulse spectroscopy*	3.4, S. 16
CSA	Anisotropie der chemischen Verschiebung (*chemical shift anisotropy*)	3.4, S. 16
DFT	Dichtefunktionaltherie (*density functional theory*)	4, S. 35
DMF	*N,N*-Dimethylformamid	3.2, S. 8
DUMBO	*decoupling using mind-boggling optimization*	3.4, S. 16
DQ	Doppelquanten (*double quantum*)	3.4, S. 16

Abkürzung	Bedeutung	Erläuterung in Abschnitt
f_1-Domäne	indirekte Frequenzdomäne in 2D-Spektren	3.4, S. 16
f_2-Domäne	direkte Frequenzdomäne in 2D-Spektren	3.4, S. 16
FK-NMR	Festkörper-NMR Spektroskopie	3.4 , S. 16
FID	*free induction decay*	3.4 , S. 16
HaIM	2-Phenylazoimidazol	4.1, S. 36
HIm	Imidazol	3.2, S. 8
IRMOF	isoretikulärer MOF	3.2, S. 8
MAS	Rotation um den magischen Winkel (*magic angle spinning*)	3.4 , S. 16
MIL	*(*Materials of Institut Lavoisier)	3.2, S. 8
MOF	Metallorganische Gerüstverbindung (*metal organic framework*)	3.2, S. 8
MQ	Multiquanten	3.4, S. 16
MQMAS	*multi quantum magic angle spectroscopy*	3.4, S. 16
NMR	Kernspin Resonanz (*nuclear magnetic resonance*)	3.4, S. 16
PBE	*Perdew-Burke-Ernzerhof Funktional*	4, S. 35
PSM	postsynthetische Modifizierung	3.2, S. 8
rf	Radiofrequenz (*radio frequency*)	3.4, S. 16
SQ	Einquanten (*single quantum*)	3.4, S. 16
IBU	anorganische Baueinheit (*inorganic building unit*)	3.2, S. 8
IRMOF	isoretikulärer MOF	3.2, S. 8
SOD	*sodalithe structure*	4, S. 35
UFF	Universal Kraftfeld (*universal force field*)	4.1 , S. 36
XRD	Röntgen-Pulverdiffraktometrie (*Xray powderdiffraction*)	4, S. 35
ZIF	*Zeolitic imidazolate frameworks*	3.2, S. 8

1 Summary

The scope of the present thesis was the investigation of host-guest interactions in functionalized Metal-Organic Frameworks. The investigations of these interactions required the characterization of new functionalized MOFs, as well as the determination of the accessibility of the functional groups in the pores of the framework and included a systematic study of the binding site and strength of different guest molecules in different functionalized frameworks.

Firstly, a concept for monitoring the synthesis and validation of the structure of two new frameworks, CAU-4 and ZIF-8, as well as a detailed strategy for the targeted functionalization of the pore wall and the IBU for the CAU-1-NH_2 framework, using NMR spectroscopy, is described. It could be shown that ^{27}Al-MQMAS is a powerful tool to determine the structure of the inorganic building unit for CAU-4, revealing that there are two different octaheadral Al^{3+} sites in the framework. 1D ^{13}C and ^{15}N CP MAS and direct MAS experiments gave information about the successful incorporation of the provided 2-phenylazoimidazolate linker molecules in a 1:1 ratio to the structure of ZIF-8. For CAU-1-NH_2 various modifications of the organic linker molecule, like methylation of the amino group triggerd by different synthesis conditions and acetylation of the amino group by post synthetic modification, as well as the modification of the inorganic building block, exchanging bridging methoxy groups with bridging hydroxy groups, could be monitored by liquid-state and solid-state NMR.

The orientation of the functional groups in the pores, provided by the linker molecules, was studied in order to determine their accessibility for guest molecules. Therefore, the formamido groups of MIL-53-NHCHO were fully ^{13}C labeled using the postsynthetic modification route of MIL-53-NH_2 with ^{13}C enriched formic acid. The arrangement of the NHCHO-groups with respect to the pores was than determined in detail by a combination

of ^{13}C-^{13}C DQ-build up solid-state NMR experiments, molecular modeling with DFT and SIMPSON simulations. The investigation revealed that the arrangement of the functional groups in MIL-53-NHCHO is not random but dominated from 70% up to 77 % by pairs of functional groups, which are only separated by the closest possible distance of 3.9± 0.1 Å. Furthermore, the torsion of the functional groups were determined to be 200° with respect to the aromatic core of the linker molecule. Additionally, it could be shown that the formamido groups occur in the naturally less abundant CIS configuration. Moreover, it has been demonstrated that this orientation effect of the functional groups is built during synthesis and is completely independent from the incorporated guest molecules.

Furthermore, a systematic study on host-guest interactions, were performed on a series of functionalized MOFs with MIL-53 topology. Beside MIL-53, also MIL-53-NH_2 and MIL-53-NHCHO, with functional groups providing different hydrogen bond donor acceptor possibilities, were investigated. Acetone, water and Ethanol were chosen as guest molecule because of their ability to act as hydrogen bond acceptor as well as hydrogen bond donor. For the study of the host-guest interactions high-resolution ^{1}H solid-state NMR techniques at high magnetic fields, taking advantage of DUMBO decoupling schemes to improve the ^{1}H resolution were used. All ^{1}H and ^{13}C signals of the MOF framework and guest molecules could be assigned unambiguously by high-resolution 2D HETCOR spectra (^{1}H-^{13}C, ^{1}H-^{27}Al and ^{1}H-^{14}N). The binding sites and strength of the guest molecules, with respect to the framework cavities were unraveled using ^{1}H-^{1}H-spindiffusion spectra and the evaluation of the chemical shift of the guest molecules. The results showed for all five combinations of hosts and guests that the guest molecules are confined in the pores. Moreover, are the chemical shifts and the dynamics of the water and ethanol molecules specific for non selectively bond molecules. In contrast, to the former was in the case of acetone in MIL-53-NH_2 and MIL-53-NHCHO a selective NH$\cdots$O=C bond, between the functional group of the linker molecules and the guest molecules, formed. Furthermore the carbonyl chemical shift of the acetone molecules indicated that the guest molecules are bound stronger in MIL-53-NHCHO than in MIL-53-NH_2. Based on ^{1}H-^{1}H-spindiffusion spectra a structure model for the bonding scenario with acetone could be proposed, which depicts that the methyl groups of the guest molecules are preferably aligned into the pores in close vicinity to the aromatic ring of the organic linker molecules.

2 Zusammenfassung

Der Schwerpunkt der vorliegenden Arbeit war die Untersuchung von Wirt-Gast-Wechselwirkungen in funktionalisierten Metallorganischen Gerüstverbindungen. Die Erforschung dieser Wechselwirkungen erfolgte auf Basis der Charakterisierung neuer funktionalisierter MOFs sowie der Bestimmung der Zugangsmöglichkeiten zu den funktionellen Gruppen in den Poren des Gerüstes und enthielt eine systematische Untersuchung der Bindungsstellen und Bindungsstärke von verschiedenen Gastmolekülen in unterschiedlichen funktionalisierten Netzwerken.

Zunächst wurde ein Konzept zur Überwachung der Synthese und der Validierung der Struktur zweier neuer funktionalisierter MOFs, CAU-4 und ZIF-8, sowie eine detaillierte Strategie für die gezielte Funktionalisierung der Porenwand und anorganischen Baueinheit für CAU-1-NH_2, mit Hilfe von NMR Spektroskopie, beschrieben. Es konnte gezeigt werden, dass ^{27}Al-MQMAS ein geeignetes Tool für die Bestimmung der Struktur der anorganischen Baueinheiten für CAU-4 ist und dass zwei verschiedene oktaedrische Al^{3+}-Sites in das Netzwerk eingebaut sind. Mit Hilfe von 1D ^{13}C und ^{15}N CP MAS und direkten MAS-Experimenten konnte gezeigt werden, dass 2-Phenylazoimidazolat Linkermoleküle in einem 1:1-Verhältnis in die Struktur von ZIF-8 erfolgreich eingebaut wurden. Für CAU-1-NH_2 konnten verschiedenste Modifikationen des organischen Linkermoleküls, wie Methylierung der Aminogruppe angesteuert von verschiedenen Synthesebedingungen und Acetylierung der Aminogruppe auf dem Weg der postsynthetischen Modifizierung, sowie der anorganischen Baueinheiten durch den Austausch von μ-Methoxygruppen mit μ-Hydroxygruppen, durch Flüssig- und Festkörper-NMR Spektroskopie überwacht werden.

Um zu zeigen, ob die funktionellen Gruppen, die durch die Linkermoleküle bereitgestellt werden, für Gastmoleküle zugänglich sind, wurde die Orientierung der funktionellen Gruppen in den Poren untersucht. Hierfür wurden die Formamido-Gruppen von MIL-53-NHCHO

vollständig über die postsynthetische Modifizierung von MIL-53-NH_2 mit ^{13}C-angereicherter Ameisensäure angereichert. Die Anordnung der NHCHO-Gruppen in Bezug auf die Poren konnte durch eine Kombination von ^{13}C-^{13}C DQ-Aufbau Festkörper-NMR-Experimenten mit Molekularer Modellierung mittels DFT und SIMPSON Simulationen detailliert beschrieben werden. Die Untersuchung ergab, dass die Anordnung der funktionellen Gruppen in MIL-53-NHCHO nicht zufällig ist, sondern zu 70 % bis 77 % durch Paare von funktionellen Gruppen dominiert wird, die mit dem kleinstmöglichen Abstand von 3,9±0,1 Å zueinander stehen. Des Weiteren wurde die Torsion der funktionellen Gruppen in Bezug auf den aromatischen Kern des Linkermoleküls auf 200° bestimmt. Darüber hinaus konnte gezeigt werden, dass die funktionellen Gruppen in der natürlich seltener vorkommenden CIS-Form vorliegen. Außerdem wurde nachgewiesen, dass diese Orientierung der funktionellen Gruppen während der Synthese aufgebaut wird und völlig unabhängig von den eingelagerten Gastmolekülen ist.

Zudem wurde eine systematische Untersuchung von verschiedenen Wirts-Gast-Wechselwirkungen an einer Reihe von funktionalisierten MOFs mit MIL-53-Topologie durchgeführt. Neben MIL-53 wurden auch MIL-53-NH_2 und MIL-53-NHCHO, die mit ihren funktionellen Gruppen unterschiedliche Wasserstoffbrücken-Donor-Akzeptor Möglichkeiten bereitstellen, untersucht. Aufgrund ihrer Fähigkeit sowohl als Wasserstoffbrücken-Akzeptor als auch -Donor wirken zu können, wurden Aceton, Wasser und Ethanol als Gastmolekül ausgewählt. Für die Studie der Wirt-Gast-Wechselwirkungen wurden hochauflösende ^{1}H Festkörper-NMR-Techniken bei hohen Magnetfeldern, unter Einsatz von homonuklearer Entkopplung nach DUMBO um die ^{1}H Auflösung zu verbessern, verwendet. Alle ^{1}H und ^{13}C Signale der MOFs und Gastmoleküle konnten durch hochauflösende 2D HETCOR Spektren (^{1}H -^{13}C, ^{1}H-^{27}Al und ^{1}H-^{14}N) eindeutig zugeordnet werden. Bindungsplätze und Stärke der Gastmoleküle bezogen auf die Poren konnten mit Hilfe von ^{1}H-^{1}H-Spindiffusionsspektren und der Auswertung der chemischen Verschiebung der Gastmoleküle charakterisiert werden. Die Ergebnisse zeigten, dass für alle fünf Wirts-Gast-Kombinationen die Gastmoleküle in den Poren eingeschlossen sind. Die chemische Verschiebung und die Dynamik der Wasser- und Ethanolmoleküle ist spezifisch für nicht selektiv gebundene Gastmoleküle. Im Gegensatz dazu wird im Falle von Aceton in MIL-53-NH_2 und MIL-53-NHCHO eine selektive NH$\cdots$O=C Bindung zwischen den funktionellen Gruppen der Linkermoleküle und den Gastmolekülen ausgebildet. Ferner zeigt die chemische Verschiebung der Carbonyl-Gruppen der

Aceton Moleküle an, dass die Gastmoleküle in MIL-53-NHCHO stärker gebunden sind als in MIL-53-NH_2. Auf der Basis von ^{1}H-^{1}H-Spindiffusionsspektren konnte ein Strukturmodell für die Bindungssituation vorgeschlagen werden, welches zeigt, dass die Methylgruppen der Gastmoleküle in den Porenraum ragen, sodass sie in großer Nähe zum aromatischen Kern der organischen Linkermoleküle sind.

3 Einführung

3.1 Zielsetzung der Arbeit

Metallorganische Gerüstverbindungen stellen eine vielseitige Klasse von porösen Verbindungen dar, deren Wechselwirkung mit Gastmolekülen durch Funktionalisierung der organischen Linkermoleküle aber auch der Koordinationsumgebung der Metallionen gesteuert werden kann. Das übergeordnete Ziel der vorliegenden Arbeit war das Verständnis und die Steuerung von Wirt-Gast-Wechselwirkungen in MOFs, die durch Funktionalisierung, sowohl der organischen Linkermoleküle, als auch der anorganischen Baueinheiten (IBUs) erreicht werden sollte.

Hierfür wurden zunächst geeignete FK-NMR-Methoden gesucht um den gezielten Einbau von spezifischen Funktionalitäten in das MOF Gitter nachzuverfolgen. So sollte für verschiedene Funktionalisierungs-Strategien, wie direkte Modifikation, gemischter Linkereinsatz und Postsynthetische Modifizierung gezeigt werden, ob und auch in welcher Quantität, die gewünschten Funktionalitäten ins Netzwerk eingebracht werden konnten.

Da bisher nur wenige Informationen zur lokalen Anordnung und damit zur Zugänglichkeit der funktionellen Gruppen eines Linkermoleküls für Gastmoleküle bereitgestellt wurden, hat sich ein weiterer Hauptaspekt dieser Arbeit mit der genaueren Untersuchung dieser beschäftigt. Da FK-NMR im Gegensatz zu Diffraktionsmethoden nicht auf periodische Randbedingung beschränkt ist, bietet es sich an, eine Strategie auf der Basis der NMR Kristallographie, einer Kombination aus NMR Experimenten, Erstellen von Strukturmodellen, Computer Simulation zu entwickeln. Im Rahmen dessen sollte auch überprüft werden, ob die Orientierung der funktionellen Gruppen von verschiedenen eingelagerten Gastmolekülen abhängig ist.

Ein weiteres Ziel der vorliegenden Arbeit war die Bestimmung der Position, Bindungsstärke und Dynamik von Gastmolekülen in funktionalisierten Systemen. Zentrale Frage, die es zu klären galt, war dabei ob eine selektive Wasserstoffbrückenbindung zwischen Gastmolekül und funktioneller Gruppe des Linkermoleküls getriggert werden kann. Hierzu wurde eine systematische Studie mit verschiedenen funktionalisierten MOFs, MIL-53, MIL-53-NH_2 und MIL-53-NHCHO, die verschiedene Möglichkeiten bieten um mit Gastmolekülen Wechselwirkungen einzugehen, durchgeführt. Als Gastmoleküle wurden H_2O, Ethanol und Aceton eingelagert um auch hier einen breiten Bereich an möglichen Wasserstoffbrückenbindungs–Donor und –Akzeptor Stärken zu erhalten. Herausforderung dabei war es, zum einen hochauflösende ^1H Festkörper NMR Spektren zu erhalten, die eine Diskriminierung der unterschiedlichen Signale im Netzwerk erlaubt. Zum anderen dann geeignete FK-NMR-Experimente durchzuführen, die erlauben, diese Signale zweifelsfrei den Gruppen, sowohl in den MOF-Netzwerken, als auch in den Gastmolekülen zuzuordnen. Ferner galt es geeignete Methoden zu finden, die unterschiedlichen Wirts-Gast-Wechselwirkungen in den Systemen zu beschreiben und hinsichtlich der Bindungsstärke zu untersuchen. Im Falle einer selektiven Bindung sollte dann ein Strukturmodell für den Bindungsplatz der Gastmoleküle hergeleitet werden.

Bei der vorliegenden Arbeit handelt es sich um eine kumulative Dissertation. Die Ergebnisse werden daher thematisch getrennt in den einzelnen Publikationen beschrieben.

3.2 Allgemeine Einführung in Metallorganische Gerüstverbindungen

Metallorganische Gerüstverbindungen (engl. *metal organic frameworks* MOF) stellen eine wichtige Substanzklasse im Bereich der porösen kristallinen Materialien dar.[1–3] Auf Grund ihrer hervorragenden Eigenschaften, wie hohe Oberflächen und permanenten Porosität, die zusätzlich noch die Möglichkeit zur Funktionalisierung der Porenwände bietet, eignen sie sich für vielfältige Anwendungen. Diese Anwendungen reichen vom Einsatz in der Gasspeicherung,[4–7] -aufreinigung und -trennung[8–11] über den Einsatz in der Katalyse[12,13] und zur gezielten und langsamen Freisetzung von Wirkstoffen[14–18] bis hin zum Einsatz in der Sensorik.[19–21] MOFs sind wie in Abbildung 3.1 dargestellt modular aufgebaut. Durch die

Verknüpfung von Knotenpunkten, die von anorganischen Baueinheiten, wie Metall-Oxid-Clustern (z.B. ZnO_4 in MOF-5[22]) oder Metall-Sauerstoff-Cluster-Ketten (z.B. AlO-Ketten in MIL-53[23]) gestellt werden, mit organischen Linkermolekülen (z.B. Terephthalsäure, Trimesinsäure) entstehen dreidimensionale Netzwerkstrukturen. Auf Grund dieses Aufbauprinzips werden Strukturen mit Poren gebildet, welche das Einlagern von Gastmolekülen in die Netzwerkstrukturen erlauben. Wegen ihres Aufbaus aus anorganischen Einheiten, die häufig auch als IBU (engl. *inorganic building unit*) bezeichnet werden, sowie aus organischen Einheiten, werden sie den anorganisch-organischen Hybridmaterialien zugeordnet. Metallorganische Gerüstverbindungen (engl. *metal organic frameworks* MOF) stellen eine wichtige Substanzklasse im Bereich der porösen kristallinen Materialien dar.[1–3] Auf Grund ihrer hervorragenden Eigenschaften, wie hohe Oberflächen und permanenten Porosität, die zusätzlich noch die Möglichkeit zur Funktionalisierung der Porenwände bietet, eignen sie sich für vielfältige Anwendungen. Diese Anwendungen reichen vom Einsatz in der Gasspeicherung,[4–7] -aufreinigung und -trennung[8–11] über den Einsatz in der Katalyse[12,13] und zur gezielten und langsamen Freisetzung von Wirkstoffen[14–18] bis hin zum Einsatz in der Sensorik.[19–21] MOFs sind wie in Abbildung 3.1 dargestellt modular aufgebaut. Durch die Verknüpfung von Knotenpunkten, die von anorganischen Baueinheiten, wie Metall-Oxid-Clustern (z.B. ZnO_4 in MOF-5[22]) oder Metall-Sauerstoff-Cluster-Ketten (z.B. AlO-Ketten in MIL-53[23]) gestellt werden, mit organischen Linkermolekülen (z.B. Terephthalsäure, Trimesinsäure) entstehen dreidimensionale Netzwerkstrukturen. Auf Grund dieses Aufbauprinzips werden Strukturen mit Poren gebildet, welche das Einlagern von Gastmolekülen in die Netzwerkstrukturen erlauben. Wegen ihres Aufbaus aus anorganischen Einheiten, die häufig auch als IBU (engl. *inorganic building unit*) bezeichnet werden, sowie aus organischen Einheiten, werden sie den anorganisch-organischen Hybridmaterialien zugeordnet.

Die Nomenklatur von MOFs ist bisher noch nicht offiziell geregelt,[24] sie orientiert sich allerdings an der für Zeolithe gebräuchlichen Benennung,[25] bei der zur Identifizierung der Netzwerke meist eine Kombination aus drei Buchstaben und einer fortlaufenden Nummer (z.B. MOF-n, MIL-n (Materials of Institut Lavoisier)) verwendet wird.

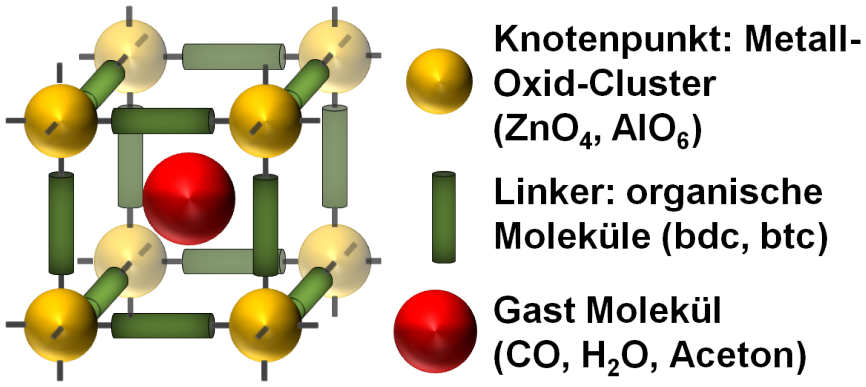

Abbildung 3.1: Schematische Darstellung von Metallorganischen Gerüstverbindungen.

3.2.1 Modifizierung der Porenoberfläche von MOFs

Der modulare Aufbau der MOFs erlaubt die Synthese neuer Netzwerkstrukturen, sowie deren Funktionalisierung, auf relativ einfach und vielfältigste Weise. Durch die Kombination verschiedener Salze und Linkermoleküle in unterschiedlichen Lösemitteln und dem Einsatz von vielseitigen Synthesestrategien, können Porengrößen, -zugänglichkeiten und -funktionalitäten gezielt für bestimmte Anwendungen eingestellt werden. So kann beispielsweise durch das Einbringen polarisierbarer Gruppen, wie Amino- oder Amidogruppen,[26,27] durch die gezielte Synthese von flexiblen Netzwerken,[28,29] oder auch durch das Einführen von ungesättigten Koordinationsstellen an den anorganischen Baueinheiten,[30–32] eine hohe Selektivität gegenüber der Adsorption von CO_2 erreicht werden. Während die Bindungsaffinität gegenüber H_2 im Hinblick auf erhöhte Wasserstoffspeicherungskapazität der porösen Materialien durch das Einbringen von Partialladungen auf der Oberfläche[33] oder durch die Synthese von interpenetrierten oder catenierten Netzwerken[34] deutlich verstärkt werden kann. Zur Modifizierung von MOFs gibt es zwei komplett verschiedene Ansätze die direkte Modifizierung und die postsynthetische Modifizierung (PSM).

Direkte Modifizierung

Die direkte Modifikation (vgl. Abbildung 3.2), beruht auf der Variation der MOFs vor dem Netzwerkaufbau. So bieten die MOFs durch ihren modularen Aufbau die Möglichkeit verschiedenste Salze, Linkermoleküle und Lösemittel zur Synthese einzusetzen und so unterschiedlich funktionalisierte Netzwerke zu erhalten.

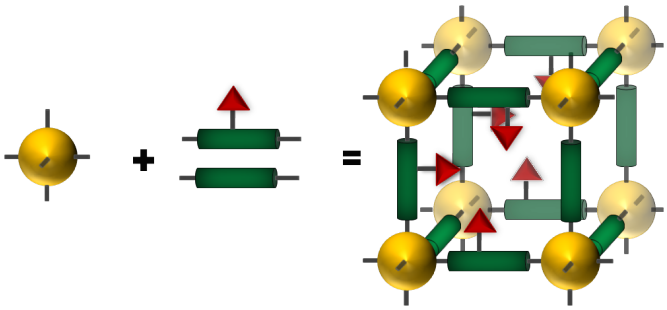

Abbildung 3.2: Schematische Darstellung einer direkten Modifizierung eines MOF am Beispiel des gemischten Linkeransatzes.

Die Modifikation der anorganischen Baueinheiten des MOFs kann z.B durch den Einsatz von verschieden Metallsalzen erreicht werden. So kann einer der bekanntesten MOFs, $Cu_3(btc)_2$ (HKUST-1),[35] mit verschiedensten Metallionen (M = Mo^{2+}, Fe^{2+}/Fe^{3+}, Cr^{2+} und Zn^{2+})[36–39] hergestellt werden. Die so erhaltenen Netzwerke sind dabei isostrukturell zum Ausgangs-MOF, d.h. sie haben alle die typischen Schaufelrad (engl. *paddle-wheel*) Einheiten die durch Trimesinsäureanionen zum gleichen 3D-Gerüst verknüpft sind.

Die Variation der organischen Baueinheit des MOFs, also der Linkermoleküle, wird als isoretikuläre Modifikation bezeichnet. Isoretikulär bedeutet, dass die Struktur des modifizierten Netzwerkes analog zu der Netzwerkstruktur des Ausgangs-MOFs ist, allerdings unterschiedliche Linkermoleküle eingebaut sind.[40] Diese Art der Modifikation erlaubt zum einen die Porengrößen von MOFs gezielt zu tunen, zum andern aber auch Funktionalität wie Polarisierbarkeit, Säure-Base Eigenschaften, Komplexierungsstellen oder Andockstellen für weitere chemische Umsetzung einzubauen. So konnten 2002 Yaghi et al. am Beispiel der IRMOF(isoretikulärer MOF)-Reihe zeigen, wie durch geeigneten Einsatz von verschiedenen Linkermolekülen der Porengrößenbereich von 3,8 Å (mikroporös), bis hin zu über 20 Å, in den mesoporösen Bereich abgedeckt werden kann.[41] Ausgehend von MOF-5, der als IBU ZnO_4-Cluster besitzt die durch bdc (engl. *benzene dicarboxylate*, Terephthalat) Moleküle verknüpft werden, werden IRMOFs mit stufenweise zunehmenden Porengrößen beschrieben. IRMOF-8 mit 2,6- Naphthalindicarboxylat als Linkermolekül, IRMOF-10 der Biphenyldicarboxylationen als Linker einbaut und IRMOF-16 bei dem die IBUs durch Terphenyldicarboxylate verknüpft sind. Dadurch werden die freien Volumina dieser MOFs von 55,8 % für MOF-5 bis 91,1 % für IRMOF-16 sukzessive erhöht.

Die Einführung von funktionellen Gruppen in das MOF-Gerüst kann durch den direkten Einsatz von funktionalisierten Linkermolekülen geschehen. So können die Eigenschaften der Porenoberfläche, von hydrophil bis hydrophob, oder gar Säure-Base Funktionalitäten, Polarität, aber auch die Stabilität des Netzwerkes eingestellt werden.[42] Auf diese Weise konnte UIO-66, welcher aus $Zr_6O_4(OH)_4$-Einheiten verknüpft mit Terephthalaten besteht, auf mannigfaltige Art funktionalisiert werden. Daraus resultieren UIO-66-X mit X = CH_3, $(CH_3)_2$, CF_3, $(CF_3)_2$, Br, $(Br)_2$, F, $(F)_2$, Cl, $(Cl)_2$, NH_2, $(NH_2)(Cl)$, $(NH_2)(Br)$, $(NH_2)(I)$, NO_2, OH, $(OH)_2$, SO_3H COOH, $(COOH)_2$.[42–52]

Das Maximum an Vielfältigkeit bietet der gemischte Linkeransatz (engl. *mixed linker approach*), dies bedeutet, wie in Abbildung 3.2 gezeigt, dass meist zwei verschiedene Linkermoleküle zum Aufbau des Netzwerkes verwendet werden.[53] Zum Beispiel kann der vorher genannte UIO-66 mit H_2bdcNH_2 und H_2bdcBr gleichzeitig synthetisiert werden und so ein bifunktionelles Netzwerk mit Amino und Bromo Funktionalität erhalten werden.[54] Allerdings konnte dieser Ansatz zur Modifikation bisher erst an wenigen Bespielen erfolgreich gezeigt werden.

Voraussetzungen für die direkte Modifikation von MOFs sind dabei, dass sich trotz Variation überhaupt noch ein Netzwerk ausbildet und die Funktionalisierungen die solvothermalen Synthesebedingungen überstehen.

Postsynthetische Modifizierung

Eine Möglichkeit um funktionelle Gruppen, die nicht hinreichend stabil sind um den Netzwerkaufbau zu überstehen in den MOF einzuführen, bietet die PSM. Hierbei wird das Netzwerk, wie in Abbildung 3.3 gezeigt, erst nach der Bildung auf heterogene Weise modifiziert. Die erste PSM eines MOFs wurde 2000 an dem enantiopuren MOF *D*-POST-1 ($[Zn_3(\mu_3\text{-}O)(Linker)_6]\cdot 2H_3O\cdot 12H_2O$, mit Linker = 2,2-Dimethyl-5-(Pyridin-4-Ylcarbamoyl)-1,3 -Dioxolane-4-Carboxylate), von Kim et al. beschrieben.[55] Sie konnten die Umwandlung der freien Pyridylgruppen in DMF mit einen Überschuss an Iodomethan zu N-methyl-Pyridinionen nachweisen. So konnte die Netzwerkladung von *D*-POST-1 durch PSM von negativ nach positiv verschoben werden.

Nach der ersten Publikation über PSM entwickelte sich ein florierendes Feld, das durch die Veröffentlichung von 2 Review-Artikeln unterstrichen wird, für die nachträgliche Modifika-

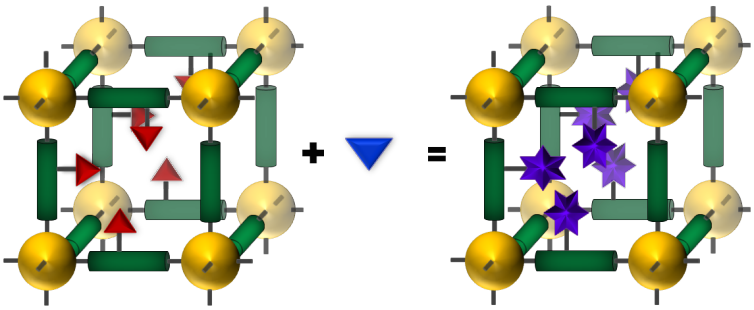

Abbildung 3.3: Schematische Darstellung einer postsynthetischen Modifizierung eines MOFs.

tion von Netzwerken.[56,57] So konnten verschiedenste Methoden zur PSM, sowohl von den IBUs, als auch von den Linkermolekülen gezeigt werden.

Bei der Modifikation der Koordinationsumgebung der IBU muss darauf geachtet werden, dass die Topologie des Netzwerkes unverändert bleibt. Dies kann durch die Einführung von zusätzlichen koordinierenden Liganden, wie Alkylaminen, Wassermolekülen, oder Pyridinen etc. an freie Koordinationsstellen in den Metallclustern des Netzwerkes stattfinden.[58,59] Zum Beispiel konnten Hupp et al. zeigen, dass der MOF, Zn_2-Clustern verknüpft mit 4,4',4",4"'-Benzol-1,2,4,5-Tetrayltetrabenzoat zu Schaufelradeinheiten, an der axialen Position der Zn_2-Cluster, die Lösemittelmoleküle DMF koordiniert. Diese konnten thermisch entfernt werden und durch verschiedene Pyridinderivate (Pyridin, 4-Methylpyridin, 4-Ethylpyridin, 4-Allylpyridin und 4-Tetrafluoromethanpyridin) ersetzt und damit die IBU Oberfläche des MOFs unterschiedlich funktionalisiert werden.[60]

Für die Modifikation der Linkermoleküle gibt es zwei verschiedene Ansätze. Zum einen die kovalente Modifikation und zum anderen die koordinative Modifikation. Bei der kovalenten Modifikation ist der Fokus auf der Suche nach geeigneten Reaktionen um aus direkt eingeführten funktionelle Gruppen noch komplexere und ausgedehntere Funktionalitäten zu synthetisieren. Die gängigste Ausgangsfunktionalität ist dabei die Amino-Gruppe, da sie einer Vielzahl an unterschiedlichen Reaktionen als Edukt dient. Die bekannteste und am häufigsten durchgeführte Reaktion von Amino-MOFs (z.B. UIO-66-NH_2) mit Anhydriden führt zur Ausbildung von Amido-MOFs.[46]

Des Weiteren konnten Morris et al. die Aminogruppen in UIO-66-NH_2 mit Acetaldehyd in Imingruppen umwandeln.[61] Eine weitere Möglichkeit ist die Umwandlung der freien Aminogruppen mit Hilfe von Isocyanaten um Harnstoffgruppen in den MOFs zu erhalten.

3.2.2 ZIFs

Eine spezielle Untergruppe der MOFs, die auch im Rahmen dieser Arbeit modifiziert wurde, sind die ZIFs (*Zeolitic imidazolate frameworks*).[62–64] Sie sind aufgebaut aus Metallzentren, welche die Koordinationszahl 4 besitzen (z.B. Zn^{2+} und Co^{2+}) und über vier Imidazolationen (Im) verknüpft sind. Jedes Imidazolat koordiniert mit seinen beiden Stickstoffatomen jeweils ein Metallion, bei dieser Koordinationsgeometrie ergibt sich ein Winkel (M-HIm-M) von 145 °, welches dem Si-O-Si Winkel in Zeolithen entspricht. Durch diese Koordinationsgeometrie ergeben sich für die ZIFs ähnliche 3D Netzwerke mit tetraedrischer Topologie, wie die der Zeolithkäfige. Mit dem Vorteil, dass die Netzwerke dann nicht nur auf die Elemente Sauerstoff, Aluminium und Silizium beschränkt sind und die Möglichkeit der Funktionalisierung der Imidazol-Linker besteht.

3.2.3 MIL-53

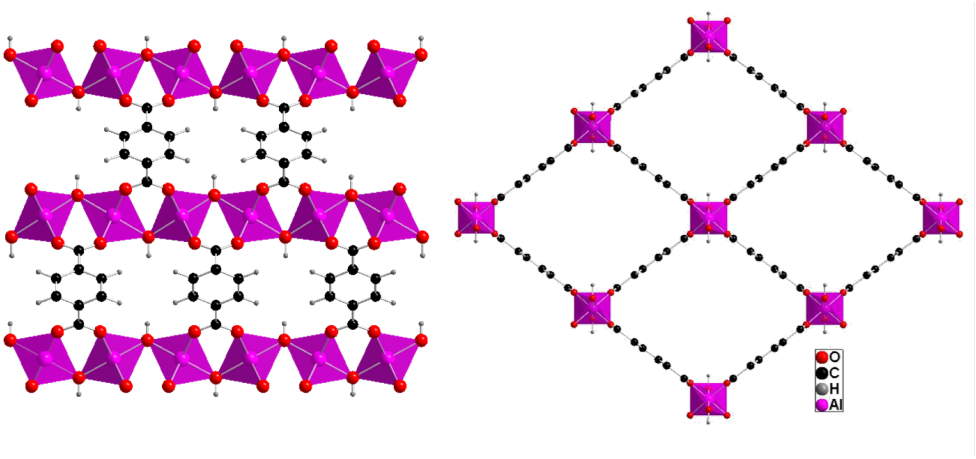

Abbildung 3.4: Struktur von MIL-53 entlang der b-Achse (links) und entlang der a-Achse (rechts).

Ein mittlerweile seit einem Jahrzehnt bekannter und sogar kommerziell als Basolite® A100 erhältlicher MOF, ist der in dieser Arbeit näher untersuchte MIL-53. Erstmals wurde MIL-53 2002 von Ferey et al. mit Cr^{3+} als Metall veröffentlicht.[65] Diesem folgten (Fe)MIL-53 und (Al)MIL-53.[23] Da sich diese Doktorarbeit nur mit (Al)MIL-53 beschäftigt, wird nur dieser hier näher beschrieben und wenn im Folgenden von MIL-53 die Rede ist, ist dies immer mit (Al)MIL-53 gleichzusetzen. Die Struktur von MIL-53 ist in Abbildung 3.4 gezeigt.

Abbildung 3.4 links zeigt MIL-53 entlang der b-Achse, in violett gezeigt ist die IBU des MOFs der aus Ketten von TRANS μ-hydroxy eckenverknüpften AlO_6-Oktaedern besteht. Diese Ketten sind über Terephthalate miteinander verknüpft, sodass ein dreidimensionales Netzwerk entsteht. Eine Ansicht auf das Netzwerk entlang der a-Achse ist in Abbildung 3.4 gezeigt, hier sind deutlich die rhomboedrische Poren zu sehen, die sich kanalförmig im MOF ausbreiten. Der Porendurchmesser beträgt bei MIL-53 ohne Gastmoleküle 8,5x8,5 Å. Die Porosität von MIL-53 wurde auf eine BET Oberfläche von 1140(39) m^2 g^{-1} bestimmt. MIL-53 ist ein MOF der dritten Generation,[66] d.h. er besitzt ein flexibles Netzwerk, dass auf externe Stimuli wie Druck- , Temperaturänderung, oder Gastmolekülaufnahme/abgabe, mit Vergrößerung oder Verkleinerung der Zellparameter reagiert. Dieser Effekt wird in der Literatur auch als Atmen (*breathing effect*) bezeichnet.[29] So ändern sich die Zellparameter und die Raumgruppe von MIL-53 von *Imma* mit den Parametern a = 6,6 Å, b = 16,7 Å, c = 12,8 Å, nach a = 19,5 Å, b = 7,6 Å, c = 6,6 Å, β =104.2 ° in der Raumgruppe *CC* je nach Temperatur, oder eingelagertem Gastmolekül. Bei hohen Temperaturen und ohne adsorbierte Moleküle in der Pore, liegt der MOF in der Raumgruppe *Imma* vor und wird als offenporig, oder MIL-53(ht) bezeichnet. Im Gegensatz dazu, kristallisiert bei tiefen Temperaturen oder bei der Adsorption von Wassermolekülen in der Pore der MOF in der Raumgruppe *CC*. Diese Form wird geschlossenporig oder MIL-53(lt) genannt.[66]

Auf Grund seiner hohen thermischen und chemischen Stabilität gibt es von MIL-53 zahlreiche isoretikuläre und funktionalisierte Varianten, wie MIL-53-NH_2, MIL-53-Cl, MIL-53-Br, MIL-53-CH_3, MIL-53-NO_2, MIL-53-(OH)(OH) und MIL-53-COOH.[67] Diese Vielzahl an unterschiedlichen Modifikationen macht ihn interessant für die systematische Untersuchung von Wirts-Gast-Systemen, die im Rahmen dieser Arbeit in Kapitel 10 durchgeführt wurden.

3.3 Wirts-Gast-Wechselwirkungen in MOFs

Um MOFs gezielt für Anwendungen zu tunen muss ein Verständnis der Wechselwirkungen mit den Gastmolekülen gegeben sein. Diese sogenannten Wirts-Gast-Wechselwirkungen sind in den Bereich der Supramolekularen Chemie anzusiedeln. Diese Wechselwirkungen können verschiedenster Natur sein und reichen von Dispersionswechselwirkungen über π-π-Wechselwirkungen hin zu H-Brückenbindungen. Die beliebteste Methode, um die Wechsel-

wirkung zwischen den Oberflächen der Poren in MOFs und Gastmolekülen zu charakterisieren, ist die Physisorption von Gasen.[48] So werden Argon- und Stickstoffsorptionsmessungen dazu verwendet, die Porengröße und Porengrößenverteilungen, sowie die spezifische Oberflächen von porösen Materialien zu bestimmen.[41] Zudem wird die Methode dazu verwendet, um die Selektivität der Adsorption eines Gases, z.B. CO_2, gegenüber eines anderen Gases, z.B. CH_4, zu bestimmen.[68,69] Oder generell zu eruieren wie viel CO_2 oder H_2 das Material aufnehmen kann.[58,70] Alle diese Studien haben gemein, dass die Wechselwirkung zwischen Gastmolekül und Netzwerk rein über Werte, wie den Vergleich der Aufnahmekapazität, bestimmt wird.[51]

Um eine Vorstellung zu bekommen, wo sich das Gastmolekül am wahrscheinlichsten in der Pore aufhält und welche Wechselwirkungen dabei adressiert werden, werden bisher häufig ausschließlich Simulationen[71] verwendet. Dies zeigt beispielsweise die Studie der Aufenthaltsplätze und Dynamik von Benzolmolekülen in IRMOF-1.[72]

Im Rahmen dieser Arbeit erfolgten zum ersten Mal Einblicke in Wirts-Gast Wechselwirkungen auf molekularer Ebene durch den Einsatz der FK-NMR-Spektroskopie. Des weiteren konnten spezifische Wechselwirkungen über Wasserstoffbrückenbindungen zwischen funktionalisierten MOFs und Gastmolekülen gezeigt werden. (Vgl. Kapitel 10).

3.4 Einführung in die NMR Kristallographie von MOFs

Um die Wechselwirkung zwischen den funktionalisierten MOFs und den eingelagerten Gastmolekülen gezielt steuern zu können, muss ein tiefer gehendes Verständnis nicht nur von den Wirts-Gast-Wechselwirkungen selber, sondern auch von den Strukturen des Netzwerkes erreicht werden. Obwohl die Bestimmung von MOF Strukturen allein durch Einkristallstrukturanalyse durchgeführt werden kann, ist für die allermeisten MOFs doch nur ein polykristallines Pulver erhältlich. Während es die Pulverdiffraktion erlaubt, die Topologie der Netzwerke zu bestimmen, bleiben hier Fragen nach der lokalen Struktur der Linkermoleküle und der funktionellen Gruppen gänzlich ungeklärt. An dieser Stelle erlaubt der Einsatz von FK-NMR-Spektroskopie das komplementäre Erforschen dieser Fragen, durch die Untersuchung von kurzen Abständen und Konnektivitäten, sowie der Umgebungen von Kernen, als auch der Kristallsymmetrie.[18,73–82]

3.4.1 FK-NMR-Spektroskopie zur Untersuchung der MOF Topologie

Die Linkermoleküle der MOFs bestehen größtenteils aus Kohlenstoff, Stickstoff, Sauerstoff und Wasserstoff. FK-NMR Untersuchungen an ^{13}C, ^{15}N und ^{1}H kann Informationen über die Anzahl an Linkermolekülen in der asymmetrischen Einheit liefern, oder die Modifizierung des Netzwerkes dokumentieren, sowie Einblick in die Linkerorientierung und -verteilung geben. Um diese Informationen aus den Spektren auch auslesen zu können, muss die Auflösung hinreichend gut sein. Diese ist im Festkörper allerdings durch die Orientierungsabhängigkeit, der Wechselwirkungen (Dipol-Dipol, Chemische Verschiebung, Quadrupol Wechselwirkung) limitiert, da durch die verschiedenen Kernorientierungen im Pulver verschiedene Resonanzfrequenzen erhalten werden, die nicht wie in der Flüssigkeit durch Brown'sche Molekurlarbewegung ausgemittelt werden, und so die Spektren sehr breit werden. Die standardmäßig angewandte Methode um die breiten Festkörperspektren aufzulösen ist die Rotation um den Magischen Winkel (*magic angle spinning* MAS).[83,84] Hierbei wird die Probe in einem Winkel von 54,736° zum B_0-Feld gekippt und dann um diesen Winkel rotiert. (Vgl. Abbildung 3.5)

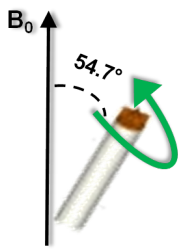

Abbildung 3.5: Skizze des experimentellen Aufbaus eines MAS Experimentes.

Unter der Voraussetzung, dass die Rotation schnell genug ist, erlaubt die resultierende Zeitabhängigkeit das Entfernen der Anisotropie der CSA und der dipolaren Kopplung, im speziellen also die Wechselwirkungen, die eine Orientierungsabhängigkeit von $P_2(\cos\theta) = 1/2(3\cos^2\theta - 1)$ besitzen. Sind die Wechselwirkungen allerdings sehr stark und die Rotation gleichzeitig nicht ausreichend schnell genug, wird die Wechselwirkung nicht vollständig ausgemittelt und es bleiben neben dem isotropen Signal zusätzlich sogenannte Rotationsseitenbanden zurück. Diese Rotationsseitenbanden sind jeweils $\pm n \cdot \nu_{rot}$ vom isotropen Signal entfernt und spiegeln in ihrer Intensitätsmodulation die Linienform eines statischen

Spektrums wider. (Vgl. Abbildung 3.6) Aus diesem Grund, können bei kleiner Rotationsfrequenz, aus dieser Linienform die Werte des CSA Tensors δ_{iso}, δ_{aniso}und η ermittelt werden.

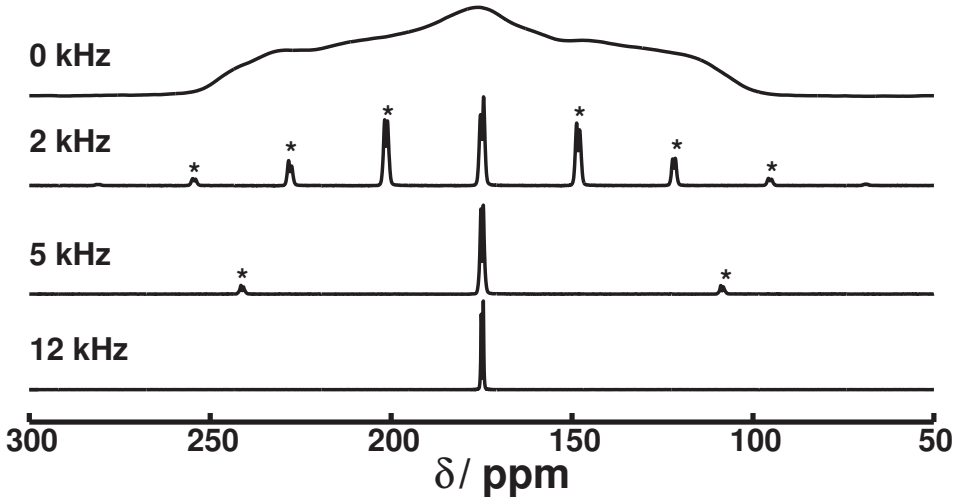

Abbildung 3.6: ^{13}C CP Spektren von Malonsäure bei unterschiedlichen Rotationsfrequenzen. Rotationsseitenbanden sind mit Sternchen gekennzeichnet.

Um neben der Auflösung ein gutes Signal/Rausch-Verhältnis und annehmbare Messzeiten für die Kerne mit geringer natürlicher Häufigkeit (^{13}C = 1,07 %, ^{15}N = 0,364 %) zu erhalten, wird das Prinzip der Kreuzpolarisation (CP, englisch *cross polarization*) ausgenutzt. Hierbei werden die Protonen angeregt und dann die Polarisation über das Protonenbad durch sogenanntes Hartmann-Hahn Matching (Einstellen des Energieniveauunterschieds mit Hilfe von richtig gewählten eingestrahlten rf-Pulsen (rf = Radiofrequenz) auf beiden Kernen gleichzeitig) auf die Kerne mit geringer natürlicher Häufigkeit übertragen.[85,86]

Mit Hilfe von 1D ^{13}C und ^{15}N CPMAS Spektren konnten, wie auch in dieser Arbeit, in der Literatur Strukturen validiert, der Einbau von Linkermolekülen überprüft, sowie die Modifizierung und der Grad der Modifizierung nachgewiesen werden.[87] Um bei ^{1}H NMR eine hinreichende Auflösung zu erhalten, reicht MAS häufig nicht aus, da dort die Dipol-Dipol Wechselwirkung durch das dichte Spinsystem und das große gyromagnetische Verhältnis ($\gamma(^1H)$ = 2,793) wesentlich stärker ist. Deshalb wird für ^{1}H NMR Spektren zusätzlich eine homonukleare Entkopplung mit CRAMPS (*combined rotation and multiple-pulse spectroscopy*) angewendet. Hier wird das Ausmitteln des Raumanteils der Dipolaren Wechselwirkung ($1/2\,(3cos^2\theta - 1)$) durch MAS, kombiniert mit der Ausmittelung des Spinanteils

$(\left(3\hat{I}_{1z}\hat{I}_{2z} - \mathbf{I_1I_2}\right))$ durch multiple Pulssequenzen. Dies führt zum vollständigen Aufheben der dipolaren Wechselwirkung. (Vgl. Gleichung 3.1)[88–90]

$$\hat{H}_{Dip} = D \cdot 1/2\left(3cos^2\theta - 1\right) \cdot \left(3\hat{I}_{1z}\hat{I}_{2z} - \mathbf{I_1I_2}\right) \tag{3.1}$$

Die Abbildung 3.7 a) zeigt das Standard-Einpuls Experiment. Die technische Umsetzung der homonuklearen Entkopplung und das daraus resultierende hochauflösende Spektrum ist am Beispiel von Glycin in Abbildung 3.7 b) dargestellt. Diese zeigt, dass die CRAMPS Pulszüge während der Aufnahme des FIDs (free induction decay) eingestrahlt werden. Da es allerdings technisch nicht möglich ist, gleichzeitig zu pulsen und aufzunehmen, muss die homonukleare Entkopplungssequenz in geschickter Länge und Abstand zwischen die Aufnahme der FID-Punkte gelegt werden. Die Herausforderung dabei ist, dass die Multipuls-Blöcke deutlich länger sein müssen als eine MAS Rotationsperiode und zusätzlich nicht der Bedingung $\tau_c/\tau_r = 0.25, 0.5$ gehorchten dürfen, trotzdem aber noch genügend Punkte für das Sampling des FIDs gegeben sein müssen. Für die hochauflösenden Experimente in dieser Arbeit wurde das DUMBO (*decoupling using mind-boggling optimization*) Schema verwendet, welches auf einer Phasenmodulation auf der Basis der Fourierserie in Gleichung 3.2 besteht.

$$\phi(t) = \sum_{n=0}^{+\infty} a_n \cos\left(n\omega_c t\right) + b_n \sin\left(n\omega_c t\right) \tag{3.2}$$

Die rechte Seite der Abbildung 3.7 b) zeigt den Auflösungsgewinn, gegenüber dem Standard-Experiment (vgl. Abbildung 3.7 a)), im 1D ^{1}H Spektrum für Glycin, der durch Anwendung von DUMBO während der Akquisition erreicht werden konnte. Im entkoppelten ^{1}H Spektrum können so das NH_2 Signal und die Dublettaufspaltung der CH_2-Gruppe aufgelöst werden. Darüber hinaus kann man in Abbildung 3.7 sehen, dass die DUMBO-Sequenz das Spektrum skaliert, dies bedeutet, man muss vor jeder Messung mit homonuklearer Entkopplung diesen Skalierungsfaktor, der für die Frequenzachse gilt, mit einer Modellsubstanz, wie z.B. hier gezeigt mit Glycin, bestimmen. Die Anwendung von homonuklearer Entkopplung ist dabei nicht auf 1D Spektren limitiert, sondern kann auch für 2D Spektren verwendet werden.[91]

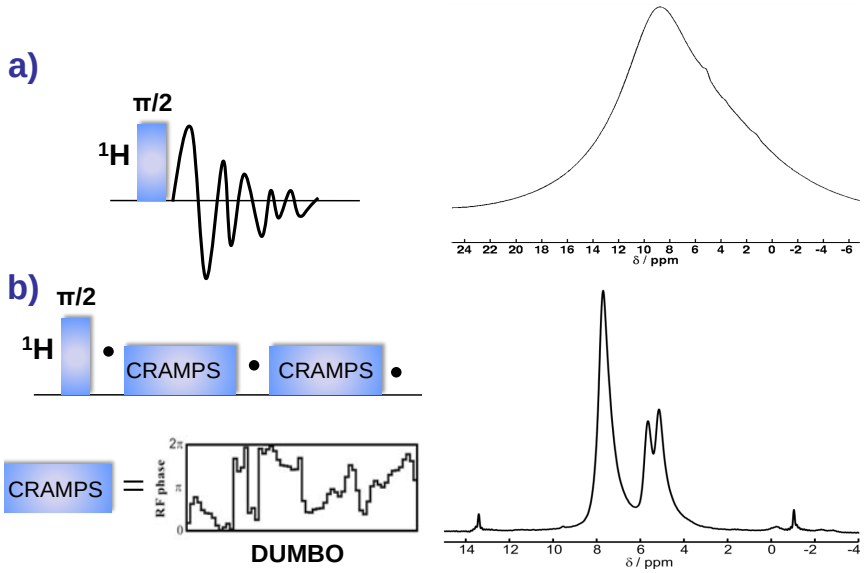

Abbildung 3.7: a) Klassische Einpuls-Sequenz (links). Resultierendes 1D ^{1}H NMR Spektrum von Glycin bei Messung mit Einpuls-Sequenz (rechts). b) Messsequenz mit CRAMPS-Einschub (links). Unskaliertes 1D ^{1}H NMR Spektrum von Glycin bei Anwendung von homonuklearer Entkopplung (rechts).

2D Spektren eignen sich für vielseitige Anwendungen, wie z.B. Zuordnung der Signale in den Spektren, Bestimmung von Konnektivitäten, oder Festlegung von Abständen,s sowohl intra- als auch intermolekular. In Abbildung 3.8 ist die grundlegende Wirkungsweise und der Aufbau von 2D Spektren gezeigt. Der erste Block nennt sich Präparations-Sequenz und ist dafür zuständig, einen Nicht-Equilibrium Spinzustand zu erzeugen. Gefolgt wird dieser Block von einer Zeit t_1, in der sich die gewünschten Kohärenzen entwickeln können. Diese Kohärenzen werden durch geeignete Phasenzyklisierung ausgewählt. Am Ende der t_1-Zeit befindet sich der sogenannte Mischblock, der die ausgewählten Kohärenzen in messbare -1-Kohärenz transferiert. Durch Wiederholung des Experiments bei t_1+x mit sukzessiv inkrementierten x erhält man so einen 2D Datensatz. Durch Fourier-Transformation wird ein 2-dimensionales Frequenzspektrum erzeugt, mit den klassischen -1-Kohärenzen in der f2-Domäne und den ausgewählten Kohärenzen als sogenannte Kreuzsignale in der f1-Domäne. Im Rahmen dieser Arbeit wurden verschiedene 2D Sequenzen auf der Basis von symmetriebasierten Wiedereinkopplungssequenzen verwendet.[92–98]

Um einen genauen Einblick in die Topologie der Netzwerke zu erhalten, ist es essentiell die

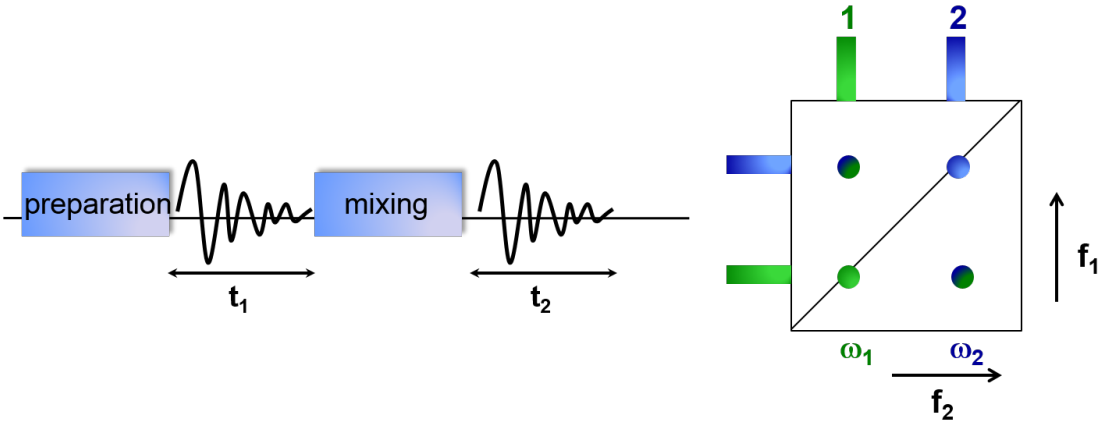

Abbildung 3.8: Schematische Darstellung zur Aufnahme von 2D Spektren in der NMR Spektroskopie.

Koordinationszahl, –umgebung und die Anzahl der verschiedenen Metallsites in der IBU zu kennen. Diese Informationen können durch FK-NMR-Messungen der Metallzentren direkt erhalten werden. Eine Grundvoraussetzung für die Messungen der Metalle ist, dass sie nicht paramagnetisch sind, also keine ungepaarten Elektronen besitzen, die im NMR Magneten Gegenfelder induzieren. Die große Herausforderung bei den messbaren diamagnetischen Metallionen ist, dass sie häufig ein elektrisches Quadrupolmoment besitzen, d.h. ihr Kernspin $I \neq 1/2$. Dieses Quadrupolmoment wechselwirkt mit dem Elektrischen Feldgradienten (EFG) am Kern und resultierende Spektren werden sehr breit. Um trotzdem eine hinreichende Auflösung in der f1-Domäne zu erhalten eignet sich die in dieser Arbeit verwendete MQMAS-Sequenz (multi quantum magic angle spectroscopy).[99,100]

Literaturverzeichnis

[1] Kitagawa, S.; Kitaura, R.; Noro, S. Functional porous coordination polymers. *Angewandte Chemie-international Edition* **2004**, *43*, 2334–2375.

[2] Ferey, G. Hybrid porous solids: past, present, future. *Chem. Soc. Rev.* **2008**, *37*, 191–214.

[3] Cook, T. R.; Zheng, Y. R.; Stang, P. J. Metal-Organic Frameworks and Self-Assembled Supramolecular Coordination Complexes: Comparing and Contrasting the Design, Synthesis, and Functionality of Metal-Organic Materials. *Chem. Rev.* **2013**, *113*, 734–777.

[4] Sumida, K.; Rogow, D. L.; Mason, J. A.; McDonald, T. M.; Bloch, E. D.; Herm, Z. R.; Bae, T. H.; Long, J. R. Carbon Dioxide Capture in Metal-Organic Frameworks. *Chem. Rev.* **2012**, *112*, 724–781.

[5] Dinca, M.; Long, J. R. Hydrogen storage in microporous metal-organic frameworks with exposed metal sites RID C-1345-2008. *Angewandte Chemie-International Edition* **2008**, *47*, 6766–6779.

[6] Rowsell, J. L. C.; Yaghi, O. M. Strategies for hydrogen storage in metal-organic frameworks. *Angewandte Chemie-International Edition* **2005**, *44*, 4670–4679.

[7] Murray, L. J.; Dinca, M.; Long, J. R. Hydrogen storage in metal-organic frameworks. *Chem. Soc. Rev.* **2009**, *38*, 1294–1314.

[8] Li, J. R.; Kuppler, R. J.; Zhou, H. C. Selective gas adsorption and separation in metal-organic frameworks RID G-2781-2010 RID A-3009-2011. *Chem. Soc. Rev.* **2009**, *38*, 1477–1504.

[9] Liu, X.; Oh, M.; Lah, M. S. Adsorbate Selectivity of Isoreticular Microporous Metal-Organic Frameworks with Similar Static Pore Dimensions. *Crystal Growth & Design* **2011**, *11*, 5064–5071.

[10] Xie, S. M.; Zhang, Z. J.; Wang, Z. Y.; Yuan, L. M. Chiral Metal-Organic Frameworks for High-Resolution Gas Chromatographic Separations. *J. Am. Chem. Soc.* **2011**, *133*, 11892–11895.

[11] Serra-Crespo, P.; Berger, R.; Yang, W.; Gascon, J.; Kapteijn, F. Separation of CO2/CH4 mixtures over NH2-MIL-53-An experimental and modelling study. *Chemical Engineering Science* **2015**, *124*, 96 –108, Metal-Organic Frameworks for Emerging Chemical Technologies.

[12] Lee, J.; Farha, O. K.; Roberts, J.; Scheidt, K. A.; Nguyen, S. T.; Hupp, J. T. Metal-organic framework materials as catalysts. *Chem. Soc. Rev.* **2009**, *38*, 1450–1459.

[13] Carson, F.; Agrawal, S.; Gustafsson, M.; Bartoszewicz, A.; Moraga, F.; Zou, X. D.; Martin-Matute, B. Ruthenium Complexation in an Aluminium Metal-Organic Framework and Its Application in Alcohol Oxidation Catalysis. *Chemistry-a European Journal* **2012**, *18*, 15337–15344.

[14] Miller, S. R.; Heurtaux, D.; Baati, T.; Horcajada, P.; Greneche, J. M.; Serre, C. Biodegradable therapeutic MOFs for the delivery of bioactive molecules. *Chem. Commun.* **2010**, *46*, 4526–4528.

[15] Horcajada, P. et al. Porous metal-organic-framework nanoscale carriers as a potential platform for drug delivery and imaging RID G-4844-2011 RID F-1487-2011. *Nat. Mater.* **2010**, *9*, 172–178.

[16] Chalati, T.; Horcajada, P.; Couvreur, P.; Serre, C.; Ben Yahia, M.; Maurin, G.; Gref, R. Porous metal organic framework nanoparticles to address the challenges related to busulfan encapsulation. *Nanomedicine (London, England)* **2011**, *6*, 1683–95.

[17] Della Rocca, J.; Liu, D. M.; Lin, W. B. Nanoscale Metal-Organic Frameworks for Biomedical Imaging and Drug Delivery. *Acc. Chem. Res.* **2011**, *44*, 957–968.

[18] Gordon, J.; Kazemian, H.; Rohani, S. MIL-53(Fe), MIL-101, and SBA-15 porous materials: Potential platforms for drug delivery. *Materials Science and Engineering: C* **2015**, *47*, 172–179.

[19] Xie, Z. G.; Ma, L. Q.; deKrafft, K. E.; Jin, A.; Lin, W. B. Porous Phosphorescent Coordination Polymers for Oxygen Sensing RID B-4330-2010 RID B-4151-2010. *J. Am. Chem. Soc.* **2010**, *132*, 922–923.

[20] Chen, B. L.; Xiang, S. C.; Qian, G. D. Metal-Organic Frameworks with Functional Pores for Recognition of Small Molecules. *Acc. Chem. Res.* **2010**, *43*, 1115–1124.

[21] Lu, G.; Farha, O. K.; Kreno, L. E.; Schoenecker, P. M.; Walton, K. S.; Van Duyne, R. P.; Hupp, J. T. Fabrication of Metal-Organic Framework-Containing Silica-Colloidal Crystals for Vapor Sensing. *Advanced Materials* **2011**, *23*, 4449–4452.

[22] Li, H.; Eddaoudi, M.; O'Keeffe, M.; Yaghi, O. M. Design and synthesis of an exceptionally stable and highly porous metal-organic framework. *Nature* **1999**, *402*, 276–279.

[23] Loiseau, T.; Serre, C.; Huguenard, C.; Fink, G.; Taulelle, F.; Henry, M.; Bataille, T.; Ferey, G. A rationale for the large breathing of the porous aluminum terephthalate (MIL-53) upon hydration. *Chemistry-A European Journal* **2004**, *10*, 1373–1382.

[24] Batten, S. R.; Champness, N. R.; Chen, X.-M.; Garcia-Martinez, J.; Kitagawa, S.; Ohrstrom, L.; O'Keeffe, M.; Suh, M. P.; Reedijk, J. Coordination polymers, metal-organic frameworks and the need for terminology guidelines. *CrystEngComm* **2012**, *14*, 3001–3004.

[25] McCusker, L. B.; Liebau, F.; Engelhardt, G. Nomenclature of structural and compositional characteristics of ordered microporous and mesoporous materials with inorganic hosts - (IUPAC recommendations 2001). *Pure Appl. Chem.* **2001**, *73*, 381–394.

[26] Xiong, S. S.; He, Y. B.; Krishna, R.; Chen, B. L.; Wang, Z. Y. Metal-Organic Framework with Functional Amide Groups for Highly Selective Gas Separation. *Cryst. Growth Des.* **2013**, *13*, 2670–2674.

[27] Devic, T.; Salles, F.; Bourrelly, S.; Moulin, B.; Maurin, G.; Horcajada, P.; Serre, C.; Vimont, A.; Lavalley, J. C.; Leclerc, H.; Clet, G.; Daturi, M.; Llewellyn, P. L.; Filinchuk, Y.; Ferey, G. Effect of the organic functionalization of flexible MOFs on the adsorption of CO2. *J. Mater. Chem.* **2012**, *22*, 10266–10273.

[28] Horike, S.; Shimomura, S.; Kitagawa, S. Soft porous crystals. *Nat. Chem.* **2009**, *1*, 695–704.

[29] Ferey, G.; Serre, C. Large breathing effects in three-dimensional porous hybrid matter: facts, analyses, rules and consequences. *Chem. Soc. Rev.* **2009**, *38*, 1380–1399.

[30] Llewellyn, P. L.; Maurin, G.; Devic, T.; Loera-Serna, S.; Rosenbach, N.; Serre, C.; Bourrelly, S.; Horcajada, P.; Filinchuk, Y.; Ferey, G. Prediction of the conditions for breathing of metal organic framework materials using a combination of X-ray powder diffraction, microcalorimetry, and molecular simulation. *J. Am. Chem. Soc.* **2008**, *130*, 12808–12814.

[31] Caskey, S. R.; Wong-Foy, A. G.; Matzger, A. J. Dramatic tuning of carbon dioxide uptake via metal substitution in a coordination polymer with cylindrical pores. *J. Am. Chem. Soc.* **2008**, *130*, 10870–10871.

[32] Bloch, E. D.; Britt, D.; Lee, C.; Doonan, C. J.; Uribe-Romo, F. J.; Furukawa, H.; Long, J. R.; Yaghi, O. M. Metal Insertion in a Microporous Metal-Organic Framework Lined with 2,2 '-Bipyridine. *J. Am. Chem. Soc.* **2010**, *132*, 14382–14384.

[33] Lochan, R. C.; Khaliullin, R. Z.; Head-Gordon, M. Interaction of molecular hydrogen with open transition metal centers for enhanced binding in metal-organic frameworks: A computational study. *Inorg. Chem.* **2008**, *47*, 4032–4044.

[34] Jiang, H. L.; Makal, T. A.; Zhou, H. C. Interpenetration control in metal-organic frameworks for functional applications. *Coord. Chem. Rev.* **2013**, *257*, 2232–2249.

[35] Chui, S. S.-Y.; Lo, S. M.-F.; Charmant, J. P. H.; Orpen, A. G.; Williams, I. D. A Chemically Functionalizable Nanoporous Material [Cu3(TMA)2(H2O)3]n. *Science* **1999**, *283*, 1148–1150.

[36] Kramer, M.; Ulrich, S. B.; Kaskel, S. Synthesis and properties of the metal-organic framework Mo-3(BTC)(2) (TUDMOF-1). *J. Mater. Chem.* **2006**, *16*, 2245–2248.

[37] Xie, L.; Liu, S.; Gao, C.; Cao, R.; Cao, J.; Sun, C.; Su, Z. Mixed-Valence Iron(II, III) Trimesates with Open Frameworks Modulated by Solvents. *Inorg. Chem.* **2007**, *46*, 7782–7788.

[38] Murray, L. J.; Dinca, M.; Yano, J.; Chavan, S.; Bordiga, S.; Brown, C. M.; Long, J. R. Highly-Selective and Reversible O-2 Binding in Cr-3(1,3,5-benzenetricarboxylate)(2). *J. Am. Chem. Soc.* **2010**, *132*, 7856–7857.

[39] Feldblyum, J. I.; Liu, M.; Gidley, D. W.; Matzger, A. J. Reconciling the Discrepancies between Crystallographic Porosity and Guest Access As Exemplified by Zn-HKUST-1. *J. Am. Chem. Soc.* **2011**, *133*, 18257–18263.

[40] Schneemann, A.; Bon, V.; Schwedler, I.; Senkovska, I.; Kaskel, S.; Fischer, R. A. Flexible metal-organic frameworks. *Chem. Soc. Rev.* **2014**, *43*, 6062–6096.

[41] Eddaoudi, M.; Kim, J.; Rosi, N.; Vodak, D.; Wachter, J.; O'Keeffe, M.; Yaghi, O. M. Systematic design of pore size and functionality in isoreticular MOFs and their application in methane storage. *Science* **2002**, *295*, 469–472.

[42] Huang, Y.; Qin, W.; Li, Z.; Li, Y. Enhanced stability and CO2 affinity of a UiO-66 type metal-organic framework decorated with dimethyl groups. *Dalton Trans.* **2012**, *41*, 9283–9285.

[43] Jasuja, H.; Zang, J.; Sholl, D. S.; Walton, K. S. Rational Tuning of Water Vapor and CO2 Adsorption in Highly Stable Zr-Based MOFs. *J. Phys. Chem. C* **2012**, *116*, 23526–23532.

[44] Biswas, S.; Van der Voort, P. A General Strategy for the Synthesis of Functionalised UiO-66 Frameworks: Characterisation, Stability and CO2 Adsorption Properties. *Eur. J. Inorg. Chem.* **2013**, 2154–2160.

[45] Zlotea, C.; Phanon, D.; Mazaj, M.; Heurtaux, D.; Guillerm, V.; Serre, C.; Horcajada, P.; Devic, T.; Magnier, E.; Cuevas, F.; Ferey, G.; Llewellyn, P. L.; Latroche, M. Effect of NH2 and CF3 functionalization on the hydrogen sorption properties of MOFs. *Dalton Trans.* **2011**, *40*, 4879–4881.

[46] Garibay, S. J.; Cohen, S. M. Isoreticular synthesis and modification of frameworks with the UiO-66 topology. *Chem. Commun.* **2010**, *46*, 7700–7702.

[47] Vermoortele, F.; Vandichel, M.; Van de Voorde, B.; Ameloot, R.; Waroquier, M.; Van Speybroeck, V.; De Vos, D. E. Electronic Effects of Linker Substitution on Lewis Acid Catalysis with Metal-Organic Frameworks. *Angewandte Chemie-international Edition* **2012**, *51*, 4887–4890.

[48] Duerinck, T.; Bueno-Perez, R.; Vermoortele, F.; De Vos, D. E.; Calero, S.; Baron, G. V.; Denayer, J. F. M. Understanding Hydrocarbon Adsorption in the UiO-66 Metal-Organic Framework: Separation of (Un)saturated Linear, Branched, Cyclic Adsorbates, Including Stereoisomers. *The Journal of Physical Chemistry C* **2013**, *117*, 12567–12578.

[49] Kim, M.; Boissonnault, J. A.; Dau, P. V.; Cohen, S. M. Metal-Organic Framework Regioisomers Based on Bifunctional Ligands. *Angewandte Chemie-international Edition* **2011**, *50*, 12193–12196.

[50] Yang, Q. Y.; Wiersum, A. D.; Llewellyn, P. L.; Guillerm, V.; Serred, C.; Maurin, G. Functionalizing porous zirconium terephthalate UiO-66(Zr) for natural gas upgrading: a computational exploration. *Chem. Commun.* **2011**, *47*, 9603–9605.

[51] Biswas, S.; Zhang, J.; Li, Z. B.; Liu, Y. Y.; Grzywa, M.; Sun, L. X.; Volkmer, D.; Van der Voort, P. Enhanced selectivity of CO2 over CH4 in sulphonate-, carboxylate- and iodo-functionalized UiO-66 frameworks. *Dalton Trans.* **2013**, *42*, 4730–4737.

[52] Foo, M. L.; Horike, S.; Fukushima, T.; Hijikata, Y.; Kubota, Y.; Takata, M.; Kitagawa, S. Ligand-based solid solution approach to stabilisation of sulphonic acid groups in porous coordination polymer Zr6O4(OH)(4)(BDC)(6) (UiO-66). *Dalton Trans.* **2012**, *41*, 13791–13794.

[53] Bunck, D. N.; Dichtel, W. R. Mixed Linker Strategies for Organic Framework Functionalization. *Chem. Eur. J.* **2013**, *19*, 818–827.

[54] Kim, M.; Cahill, J. F.; Prather, K. A.; Cohen, S. M. Postsynthetic modification at orthogonal reactive sites on mixed, bifunctional metal-organic frameworks. *Chem. Commun.* **2011**, *47*, 7629–7631.

[55] Seo, J. S.; Whang, D.; Lee, H.; Jun, S. I.; Oh, J.; Jeon, Y. J.; Kim, K. A homochiral metal-organic porous material for enantioselective separation and catalysis. *Nature* **2000**, *404*, 982–986.

[56] Wang, Z. Q.; Cohen, S. M. Modulating Metal-Organic Frameworks To Breathe: A Postsynthetic Covalent Modification Approach. *J. Am. Chem. Soc.* **2009**, *131*, 16675–16676.

[57] Tanabe, K. K.; Cohen, S. M. Postsynthetic modification of metal-organic frameworks-a progress report. *Chem. Soc. Rev.* **2011**, *40*, 498–519.

[58] Demessence, A.; D'Alessandro, D. M.; Foo, M. L.; Long, J. R. Strong CO2 Binding in a Water-Stable, Triazolate-Bridged Metal-Organic Framework Functionalized with Ethylenediamine. *J. Am. Chem. Soc.* **2009**, *131*, 8784–8785.

[59] Hwang, Y. K.; Hong, D. Y.; Chang, J. S.; Jhung, S. H.; Seo, Y. K.; Kim, J.; Vimont, A.; Daturi, M.; Serre, C.; Ferey, G. Amine grafting on coordinatively unsaturated metal centers of MOFs: Consequences for catalysis and metal encapsulation. *Angewandte Chemie-international Edition* **2008**, *47*, 4144–4148.

[60] Farha, O. K.; Mulfort, K. L.; Hupp, J. T. An Example of Node-Based Postassembly Elaboration of a Hydrogen-Sorbing, Metal-Organic Framework Material. *Inorg. Chem.* **2008**, *47*, 10223–10225.

[61] Morris, W.; Taylor, R. E.; Dybowski, C.; Yaghi, O. M.; Garcia-Garibay, M. A. Framework mobility in the metal-organic framework crystal IRMOF-3: Evidence for aromatic ring and amine rotation. *J. Mol. Struct.* **2011**, *1004*, 94–101.

[62] Phan, A.; Doonan, C. J.; Uribe-Romo, F. J.; Knobler, C. B.; O'Keeffe, M.; Yaghi, O. M. Synthesis, Structure, and Carbon Dioxide Capture Properties of Zeolitic Imidazolate Frameworks. *Acc. Chem. Res.* **2010**, *43*, 58–67.

[63] Gustafsson, M.; Zou, X. D. Crystal formation and size control of zeolitic imidazolate frameworks with mixed imidazolate linkers. *J. Porous Mater.* **2013**, *20*, 55–63.

[64] Park, K. S.; Ni, Z.; Cote, A. P.; Choi, J. Y.; Huang, R. D.; Uribe-Romo, F. J.; Chae, H. K.; O'Keeffe, M.; Yaghi, O. M. Exceptional chemical and thermal stability of zeolitic imidazolate frameworks. *Proc. Natl. Acad. Sci. U.S.A.* **2006**, *103*, 10186–10191.

[65] Millange, F.; Serre, C.; Ferey, G. Synthesis, structure determination and properties of MIL-53as and MIL-53ht: the first Cr-III hybrid inorganic-organic microporous solids: Cr-III(OH)center dotO2C-C6H4-CO2center dotHO2C-C6H4-CO2H(x). *Chem. Commun.* **2002**, 822–823.

[66] Ferey, G. Hybrid porous solids: past, present, future. *Chem. Soc. Rev.* **2008**, *37*, 191–214.

[67] Biswas, S.; Ahnfeldt, T.; Stock, N. New Functionalized Flexible Al-MIL-53-X (X = -Cl, -Br, -CH3, -NO2, -(OH)(2)) Solids: Syntheses, Characterization, Sorption, and Breathing Behavior. *Inorg. Chem.* **2011**, *50*, 9518–9526.

[68] Couck, S.; Denayer, J. F. M.; Baron, G. V.; Remy, T.; Gascon, J.; Kapteijn, F. An Amine-Functionalized MIL-53 Metal-Organic Framework with Large Separation Power for CO2 and CH4. *J. Am. Chem. Soc.* **2009**, *131*, 6326–6327.

[69] Hamon, L.; Llewellyn, P. L.; Devic, T.; Ghoufi, A.; Clet, G.; Guillerm, V.; Pirngruber, G. D.; Maurin, G.; Serre, C.; Driver, G.; van Beek, W.; Jolimaitre, E.; Vimont, A.; Daturi, M.; Ferey, G. Co-adsorption and Separation of CO2-CH4 Mixtures in the Highly Flexible MIL-53(Cr) MOF. *J. Am. Chem. Soc.* **2009**, *131*, 17490–17499.

[70] Gassensmith, J. J.; Furukawa, H.; Smaldone, R. A.; Forgan, R. S.; Botros, Y. Y.; Yaghi, O. M.; Stoddart, J. F. Strong and Reversible Binding of Carbon Dioxide in a Green Metal-Organic Framework. *J. Am. Chem. Soc.* **2011**, *133*, 15312–15315.

[71] Greathouse, J. A.; Allendorf, M. D. The interaction of water with MOF-5 simulated by molecular dynamics (vol 128, pg 10678, 2006). *J. Am. Chem. Soc.* **2006**, *128*, 13312–13312.

[72] Takakura, K.; Ueda, T.; Miyakubo, K.; Eguchi, T. Local structure and dynamics of benzene confined in the IRMOF-1 nanocavity as studied by molecular dynamics simulation. *Phys. Chem. Chem. Phys.* **2013**, *15*, 279–290.

[73] Hoffmann, H. C.; Debowski, M.; Muller, P.; Paasch, S.; Senkovska, I.; Kaskel, S.; Brunner, E. Solid-State NMR Spectroscopy of Metal-Organic Framework Compounds (MOFs). *Materials* **2012**, *5*, 2537–2572.

[74] Sutrisno, A.; Huang, Y. N. Solid-state NMR: A powerful tool for characterization of metal-organic frameworks. *Solid State Nucl. Magn. Reson.* **2013**, *49-50*, 1–11.

[75] Borisov, A. S.; Hazendonk, P.; Hayes, P. G. Solid-State Nuclear Magnetic Resonance Spectroscopy: A Review of Modern Techniques and Applications for Inorganic Polymers. *J. Inorg. Organomet. Polym. Mater.* **2010**, *20*, 183–212.

[76] Bradley, J. P.; Velaga, S. P.; Antzutkin, O. N.; Brown, S. P. Probing Intermolecular Crystal Packing in gamma-Indomethacin by High-Resolution (1)H Solid-State NMR Spectroscopy. *Crystal Growth & Design* **2011**, *11*, 3463–3471.

[77] Brown, S. P. Applications of high-resolution H-1 solid-state NMR. *Solid State Nucl. Magn. Reson.* **2012**, *41*, 1–27.

[78] Brunner, E. Solid-state Nmr - A Powerful Tool For the Investigation of Surface Hydroxyl-groups In Zeolites and Their Interactions With Adsorbed Probe Molecules. *J. Mol. Struct.* **1995**, *355*, 61–85.

[79] Brus, J.; Kobera, L.; Urbanova, M.; Kolousek, D.; Kotek, J. Insights into the Structural Transformations of Aluminosilicate Inorganic Polymers: A Comprehensive Solid-State NMR Study. *J. Phys. Chem. C* **2012**, *116*, 14627–14637.

[80] Davies, E.; Duer, M. J.; Ashbrook, S. E.; Griffin, J. M. Applications of NMR Crystallography to Problems in Biomineralization: Refinement of the Crystal Structure and 31P Solid-State NMR Spectral Assignment of Octacalcium Phosphate. *J. Am. Chem. Soc.* **2012**, *134*, 12508–12515.

[81] Martineau, C. {NMR} crystallography: Applications to inorganic materials. *Solid State Nuclear Magnetic Resonance* **2014**, *63–64*, 1 –12.

[82] Martineau, C.; Senker, J.; Taulelle, F. In *Chapter One - {NMR} Crystallography*; Webb, G. A., Ed.; Annual Reports on {NMR} Spectroscopy; Academic Press, 2014; Vol. 82; pp 1 –57.

[83] Andrew, E. R.; Bradbury, A.; Eades, R. G. Nuclear Magnetic Resonance Spectra From A Crystal Rotated At High Speed. *Nature* **1958**, *182*, 1659–1659.

[84] Lowe, I. J. Free Induction Decays of Rotating Solids. *Phys. Rev. Lett.* **1959**, *2*, 285–287.

[85] Pines, A.; Gibby, M. G.; Waugh, J. S. Proton-enhanced Nmr of Dilute Spins In Solids. *J. Chem. Phys.* **1973**, *59*, 569–590.

[86] Brinkmann, A.; Levitt, M. H. Symmetry principles in the nuclear magnetic resonance of spinning solids: Heteronuclear recoupling by generalized Hartmann-Hahn sequences. *J. Chem. Phys.* **2001**, *115*, 357–384.

[87] Klein, N.; Hoffmann, H. C.; Cadiau, A.; Getzschmann, J.; Lohe, M. R.; Paasch, S.; Heydenreich, T.; Adil, K.; Senkovska, I.; Brunner, E.; Kaskel, S. Structural flexibility and intrinsic dynamics in the M2(2,6-ndc)2(dabco) (M = Ni, Cu, Co, Zn) metal-organic frameworks. *J. Mater. Chem.* **2012**, *22*, 10303–10312.

[88] Bronnimann, C. E.; Hawkins, B. L.; Zhang, M.; Maciel, G. E. Combined Rotation And Multiple Pulse Spectroscopy As An Analytical Proton Nuclear Magnetic-Resonance Technique For Solids. *Anal. Chem.* **1988**, *60*, 1743–1750.

[89] Amoureux, J. P.; Hu, B.; Trebosc, J. Enhanced resolution in proton solid-state NMR with very-fast MAS experiments RID G-8930-2011. *J. Magn. Reson.* **2008**, *193*, 305–307.

[90] Bosman, L.; Madhu, P. K.; Vega, S.; Vinogradov, E. Improvement of homonuclear dipolar decoupling sequences in solid-state nuclear magnetic resonance utilising radiofrequency imperfections. *J. Magn. Reson.* **2004**, *169*, 39–48.

[91] Siegel, R.; Mafra, L.; Rocha, J. Improving the (1)H indirect dimension resolution of 2D CRAMPS NMR spectra: A simulation and experimental investigation. *Solid State Nucl. Magn. Reson.* **2011**, *39*, 81–87.

[92] Bayro, M. J.; Ramachandran, R.; Caporini, M. A.; Eddy, M. T.; Griffin, R. G. Radio frequency-driven recoupling at high magic-angle spinning frequencies: Homonuclear recoupling sans heteronuclear decoupling. *J. Chem. Phys.* **2008**, *128*, 052321.

[93] Carravetta, M.; Eden, M.; Zhao, X.; Brinkmann, A.; Levitt, M. H. Symmetry principles for the design of radiofrequency pulse sequences in the nuclear magnetic resonance of rotating solids. *Chem. Phys. Lett.* **2000**, *321*, 205–215.

[94] Bennett, A. E.; Weliky, D. P.; Tycko, R. Quantitative conformational measurements in solid state NMR by constant-time homonuclear dipolar recoupling. *J. Am. Chem. Soc.* **1998**, *120*, 4897–4898.

[95] Boender, G. J.; Vega, S. Phase sensitive detection of 2D homonuclear correlation spectra in MAS NMR. *J. Magn. Reson.* **1998**, *133*, 281–285.

[96] Cavadini, S. Indirect detection of nitrogen-14 in solid-state NMR spectroscopy. *Prog. Nucl. Magn. Reson. Spectrosc.* **2010**, *56*, 46–77.

[97] Cavadini, S.; Abraham, A.; Bodenhausen, G. Coherence transfer between spy nuclei and nitrogen-14 in solids. *J. Magn. Reson.* **2008**, *190*, 160–164.

[98] Cavadini, S.; Antonijevic, S.; Lupulescu, A.; Bodenhausen, G. Indirect detection of nitrogen-14 in solids via protons by nuclear magnetic resonance spectroscopy. *J. Magn. Reson.* **2006**, *182*, 168–172.

[99] Amoureux, J. P.; Fernandez, C.; Steuernagel, S. Z filtering in MQMAS NMR. *J. Magn. Reson., Ser A* **1996**, *123*, 116–118.

[100] Hajjar, R.; Millot, Y.; Man, P. P. Phase cycling in MQMAS sequences for half-integer quadrupole spins. *Prog. Nucl. Magn. Reson. Spectrosc.* **2010**, *57*, 306–342.

[101] Ahnfeldt, T.; Guillou, N.; Gunzelmann, D.; Margiolaki, I.; Loiseau, T.; Ferey, G.; Senker, J.; Stock, N. [Al-4(OH)(2)(OCH3)(4)(H2N-bdc)(3)]center dot xH(2)O: A 12-Connected Porous Metal-Organic Framework with an Unprecedented Aluminum-Containing Brick. *Angewandte Chemie-International Edition* **2009**, *48*, 5163–5166.

4 Synopsis

Die vorliegende Arbeit enthält fünf Publikationen und Manuskripte. In Abbildung 4.1 ist schematisch dargestellt, welche Gesichtspunkte von modifizierten MOFs und Wirts-Gast Wechselwirkungen untersucht wurden.

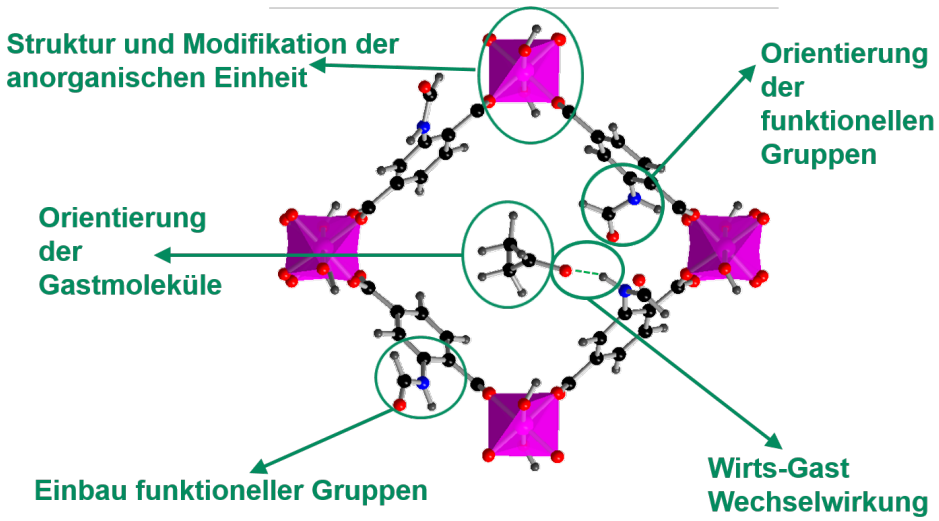

Abbildung 4.1: Schematische Darstellung der in dieser Dissertation bearbeiteten Themen.

So konnte mit FK-NMR-Spektroskopie die Struktur eines neuen MOFs charakterisiert werden (vgl. Kapitel 6). Des Weiteren konnte gezeigt werden, wie bereits bekannte ZIFs und MOFs nicht nur an den Linkermolekülen, sondern auch an den anorganischen IBUs, modifiziert werden und so Anknüpfungspunkte für selektive Wirts-Gast-Wechselwirkungen bereit gestellt werden (vgl. Kapitel 7 and 8). Zudem konnte in Kapitel 9 gezeigt werden, dass die Orientierung der funktionellen Gruppen in MIL-53-NHCHO nicht statistisch vorliegt, sondern sich Ordnung unabhängig von den verwendeten Gastmolekülen ausbildet. Ferner wurde die Wechselwirkung von funktionalisiertem MIL-53-X (X = H, NH_2, NHCHO, NO_2)

mit Gastmolekülen (Ethanol, Aceton und Wasser) systematisch, auch im Hinblick auf die Orientierung der Gastmoleküle in den Poren, untersucht (vgl. Kapitel 10).

4.1 Charakterisierung von neuen MOF Strukturen und Modifizierungen mit Hilfe von Festkörper NMR Spektroskopie

Basis für die Untersuchungen von selektiven Wirts-Gast Wechselwirkungen sind stabile MOFs, die die Möglichkeit bieten, funktionelle Gruppen einzubauen, große Porenoberflächen besitzen und trotzdem unter Normalbedingen stabil sind. Kapitel 6 beschreibt den ersten MOF, CAU-4, bestehend aus Al^{3+}-Ionen in Kombination mit dem Linker BTB (= 4,4',4"-Benzol-1,3,5-triyl-tribenzoat). Durch das verhältnismäßig große Linkermolekül, entsteht ein MOF mit einem sehr hohen organischen Anteil, im Vergleich zum anorganischen Anteil, wodurch sich vielseitige Möglichkeiten für Funktionalisierungen bieten. CAU-4 besitzt eine BET-Oberfläche von 1520 m^2/g und ein Mikroprorenvolumen von 0,61 cm^3/g. Um die Struktur von CAU-4 zu lösen wurde eine Kombination von Struktursimulation mit Kraftfeldmethoden, Röntgenpulverdiffraktometrie und FK-NMR-Spektroskopie angewendet. Ausgehend von der bereits bekannten Struktur von MIL-103, wurde die Struktur mit Hilfe des Kraftfeldes UFF (Universal force field) in P1 optimiert.

Tabelle 4.1: Gitterparameter der energieminimierten Struktur von CAU-4 im Vergleich zu den experimentell bestimmten Werten und im Vergleich zu MIL-103

Gitterparameter	MIL-103	opt. CAU-4	exp. CAU-4
Raumgruppe	R32	P312	P312
a=b [Å]	28,5344(8)	15,9822	16,273(1)
c [Å]	12,2148(5)	3,7721	12,956(6)

Die Gitterparameter der resultierenden Struktur mit der niedrigsten Energie, zeigen gute Übereinstimmung mit den experimentell bestimmten Werten (vgl. Tabelle 4.1).

Die Struktur von CAU-4 besteht aus AlO_6-Oktaedern, die durch die Carboxylategruppen der BTB-Linker verknüpft sind. Durch dieses Verknüpfungsmuster bilden sich Ketten

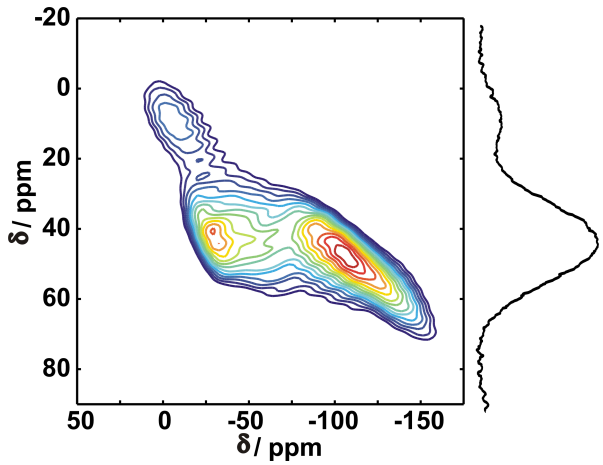

Abbildung 4.2: ^{27}Al-MQMAS Spektrum von CAU-4. Rechts neben dem 2D Spektrum ist die Summe über die F1-Domäne gezeigt.

aus Aluminiumoktaedern, die durch die BTB Linker ein honigwabenförmiges Netzwerk mit 1-dimensionalen Kanälen bilden. Genauere Information über die Struktur von CAU-4 konnten mit Hilfe von FK-NMR erhalten werden. So zeigt das ^{13}C CP NMR Spektrum von CAU-4, 5 große Signale bei 120 ppm – 150 ppm, die den Aromaten des BTB Linkermoleküls zugeordnet werden können. Bei 173 ppm ist ein Singulett zu sehen, dass sich den Carboxylgruppen des organischen Linkermoleküls zuordnen lässt. Dies zeigt, dass alle Linkermoleküle im Netzwerk auf gleiche Weise mit den Al^{3+}-Ionen verknüpft sind. Um die Aluminiumumgebung genauer zu beleuchten, wurde ein ^{27}Al-MQMAS Spektrum aufgenommen (siehe Abbildung 4.2). Dies veranschaulicht, dass alle Al^{3+}-Ionen im MOF Netzwerk eine typische chemische Verschiebung (45 ppm und 55 ppm) für eine sechsfach Koordination aufweisen. Weiterhin konnte gezeigt werden, dass es zwei verschiedene Al^{3+}-Sites im MOF gibt. Ferner konnte eine kleine Verunreinigung bei 10 ppm identifiziert werden. Zusammenfassend zeigte sich, dass FK-NMR Spektroskopie erfolgreich die Charakterisierung und Validierung von neuen MOFs unterstützen kann.

Der nächste Schritt war nun, verschiedene Modifizierungsmöglichkeiten von MOFs zu verfolgen. Die Veröffentlichung im Kapitel 7 zeigt die Synthese und Charakterisierung einer neuen, zu ZIF-8 isoretikulären Verbindung, nach dem gemischten Linkeransatz. Für die Synthese wurden dem Zink-Ion sowohl Imidazol (HIm), als auch 2-Phenylazoimidazol (HaIM) im Verhältnis 1:1 als Linkermolekül angeboten. Das HaIM wurde vorher, ausgehend von Anilin, durch Diazotization und anschließende Kupplung mit Imidazol synthetisiert.

Die Reaktion zum [Zn(Im)(aIm)] wurde durch eine High-throughput Methode untersucht und ergab, dass sich das Netzwerk nur im Lösemittel DMF als orangefarbene, luftstabile Einkristalle bildet. Mit Hilfe von ^{15}N und ^{13}C CP-MAS Spektren, konnte gezeigt werden, dass das dargebotene HaIM auch im neuen ZIF zu finden ist. Um zu bestimmen, in welcher Menge das funktionalisierte Molekül eingebaut wurde, wurde ein direktes ^{13}C-MAS Spektrum aufgenommen.

In Abbildung 4.3 ist dieses Spektrum der neuen ZIF-8 Verbindung gezeigt, sowie die eindeutige Zuordnung der Signale zu den Linkermolekülen und die Entfaltung in Einzelsignale zur Integration. Durch die Integration des Spektrums konnte der Einbau der Linkermoleküle im Verhältnis 1:1 nachgewiesen werden.

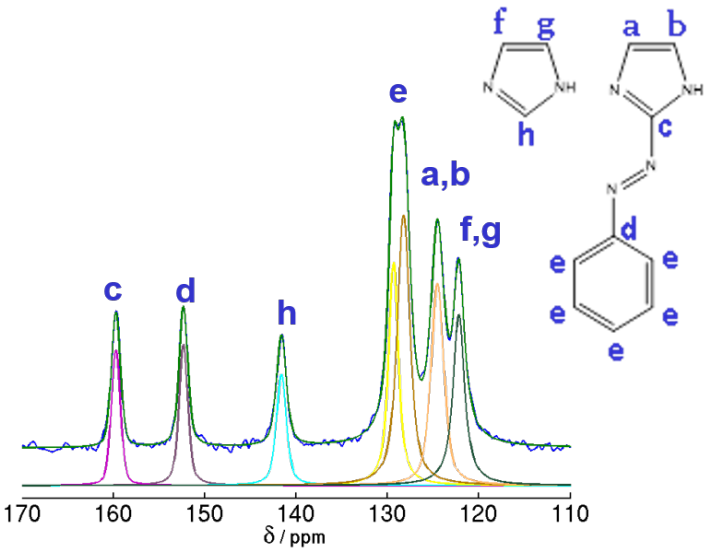

Abbildung 4.3: Direktes ^{13}C-MAS Spektrum von der neuen ZIF-8 Verbindung mit der Zuordnung zu den Linkermolekülen und der Entfaltung in Einzelsignale zur Integration.

Zur Untersuchung mit Röntgenpulverdiffraktometrie und Einkristalldiffraktometrie wurde das Produkt bei 200 °C unter HV aktiviert. Die Indizierung der XRD Daten ergab, dass [Zn(Im)(aIm)] in der Raumgruppe $I23$ (a = 17.009(6) Å, im Vergleich zur Einkristalllösung: a = 17.023(2) Å) kristallisiert. Die Struktur entspricht dem Sodalith (SOD)-Typ, der auch typisch ist für ZIF-8. Dies lässt den Schluss zu, dass das neue Netzwerk [Zn(Im)(aIm)] isoretikulär zu ZIF-8 ist.

Durch den Einbau dieses Linkermoleküls mit einer Azogruppe, besteht die Möglichkeit, das Netzwerk durch eine Photoisomerisierungs-Reaktion zu schalten (vgl. Abbildung 4.4). Diese Eigenschaft wurde mit UV/Vis Spektroskopie untersucht. Im Allgemeinen ist das trans-Isomer die thermodynamisch stabile Form. Das Schalten von der trans- nach der cis-Konfiguration wurde durch die Bestrahlung mit UV Licht der Wellenlänge $\lambda = 355$ nm für eine Stunde erreicht. Allerdings schaltet das Linkermolekül thermisch von cis auf trans zurück. Weiterhin ist es teilweise möglich, diesen Schaltprozess zu wiederholen. Die Tatsache, dass dieser Prozess nur teilweise reversibel ist, könnte von *Photobleaching* oder durch sterische Hinderung durch das Netzwerk herrühren.

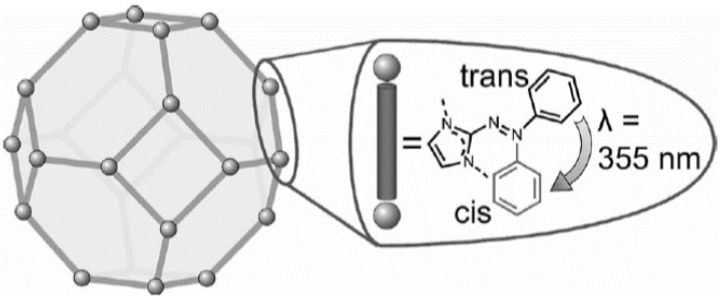

Abbildung 4.4: Schematische Darstellung der Schaltung des HaIm Linkers von cis nach trans und umgekehrt im Netzwerk von ZIF-8.

Die dritte Publikation im Rahmen der Charakterisierung der Strukturen von funktionalisierten Netzwerken, behandelt die Untersuchung der Modifikation sowohl der organischen als auch der anorganischen Einheit von CAU-1-NH_2 in Kapitel 8. In der vorhergehenden Veröffentlichung, der Erstsynthese von CAU-1-NH_2 von Ahnfeldt et al.,[101] wurde im ^{13}C CP-MAS Spektrum ein nicht näher identifiziertes Signal bei ca. 27 ppm gefunden. Dieses Signal konnte in der aktuellen Veröffentlichung unter Zuhilfenahme von ^{1}H-^{13}C-MAS-J-HMQC, ^{1}H-^{1}H HOMCOR und ^{15}N CPPI Spektren einer Methylierung der Aminogruppe zugeordnet werden. Des Weiteren wurde systematisch untersucht, wie sich in Abhängigkeit der Reaktionsbedingungen (Temperatur, Reaktionsdauer, Verwendung von konventionellem Ofen und Mikrowelle) und der Reaktionsgefäße (Teflon-, Glasautoklaven) der Methylierungsgrad einstellen lässt.

Der Methylierungsgrad wurde mit Hilfe von ^{1}H Flüssig-NMR-Spektroskopie der Linkermoleküle abgebildet, indem das aktivierte Netzwerk zuvor in 20% NaOD/H_2O aufgelöst

wurde. Grundsätzlich lässt sich sagen, dass je länger die Reaktionsdauer und je höher die Reaktionstemperatur ist, umso größer ist der Methylierungsgrad der Aminogruppe.

Zusätzlich wurde die Abhängigkeit des Methylierungsgrades des Materials vom Reaktionsgefäßes bei Verwendung eines konventionellen Ofens untersucht. So finden sich im Produkt, bei der Verwendung von Teflonautoklaven, nur wenige -$NHCH_3$-Gruppen, während bei der Synthese im Glasautoklaven, der MOF sehr viele -$NHCH_3$-Gruppen und sogar -$N(CH_3)_2$-Gruppen aufweist. Durch die Verwendung eines Mikrowellengerätes, lässt sich der Methylierungsgrad durch geschickte Wahl der Reaktionszeit und -temperatur sogar gezielt einstellen. Während bei 135 °C und 638 min ein Methylierungsgrad von 95 % erreicht wird, erzielen 140 °C und 2 min den geringsten Methylierungsgrad von nur 2 %. Allerdings wurde hier auch beobachtet, dass kurze Reaktionsdauern zu deutlich geringeren Ausbeuten führen. ($<$ 10 % in Bezug auf die eingesetzte Aminoterephthalsäure) Durch die nun frei zugänglichen Aminogruppen bei Produkten mit sehr geringen Methylierungsgrad, ist es nun möglich CAU-1-NH_2 postsynthetisch zu modifizieren. Hierzu wurde mit Hilfe von Essigsäureanhydrid die Verbindung CAU-1-$NHCHOCH_3$ synthetisiert. Der Fortschritt dieser PSM wurde mit FK-NMR untersucht. In Abbildung 4.5 sind die ^{13}C CP-MAS Spektren von CAU-1-NH_2 und CAU-1-$NHCHOCH_3$ mit den Zuordnungen der Signale zu den Linkermolekülen dargestellt. Es ist zu sehen, dass im schwarzen Spektrum von CAU-1-NH_2 kein Signal bei 27 ppm zu sehen ist und somit keine Methylierung der Aminogruppe vorhanden ist. Nach der PSM können die zwei neuen Signale bei 24 ppm und 178 ppm im Spektrum dem Methyl- und Carbonylsignal der eingebrachten funktionellen Gruppe zugeordnet werden. Auch die ^{15}N CP-MAS Spektren bestätigen die vollständige Umwandlung der -NH_2 in -$NHCHOCH_3$-Gruppen.

Durch den Einbau der funktionellen Gruppen wurden die Sorptionseigenschaften der Verbindungen sehr stark beeinflusst. So kann CAU1-$NHCH_3$ wesentlich mehr CO_2 aufnehmen, als CAU-1-NH_2 und CAU-1-$NHCHOCH_3$. Während CAU-1-$NHCHOCH_3$ bei kleinen $\frac{p}{p_0}$-Werten deutlich mehr Wasser aufnehmen kann als CAU1-$NHCH_3$ und CAU-1-NH_2. Dies weist auf die Ausbildung von stärkeren Wasserstoffbrückenbindung hin.

Neben der Funktionalisierung der Linkermoleküle wurde auch die Zusammensetzung der IBU variiert. Durch Erhitzen bei einer Temperatur von 190 °C von CAU-1-NH_2 an Luft konnten die OCH_3-Gruppen der $Al_8(OH)_4(OCH_3)_8{}^{12+}$-Cluster innerhalb von 24 h vollständig durch OH-Gruppen ausgetauscht werden. Dadurch entsteht, unter Erhalt der Kristal-

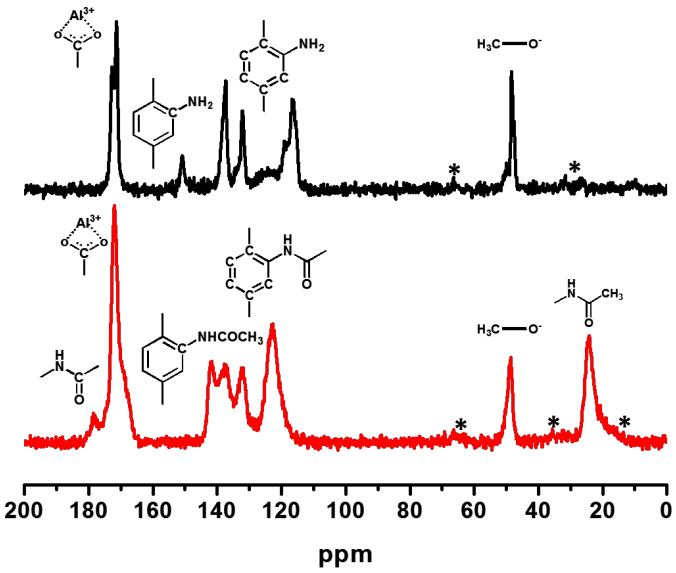

Abbildung 4.5: ^{13}C CP-MAS Spektrum von CAU-1-NH_2 und nach der PSM von CAU-1-$NHCHOCH_3$.

linität, CAU-1-NH_2(OH) mit der Zusammensetzung $[Al_4(OH)_6(BDC-NH_2)_3]\cdot xH_2O$. Dagegen bleiben bei der Aktivierung im Vakuum, die Methylengruppen im anorganischen Bauteil erhalten.

Diese Kapitel haben gezeigt wie neue MOFs synthetisiert werden konnten, und wie mit Hilfe von NMR Spektroskopie die Synthesen verfolgt werden konnten. Durch ein tieferes Verständnis der Strukturen im Falle von CAU-1-NH_2 wurden gezieltere Modifikationen ermöglicht. Im Anschluss stellt sich nun die Frage, mit welcher Orientierung funktionelle Gruppen in die Netzwerke eingebaut sind.

4.2 Untersuchung der Orientierung der funktionellen Gruppen in MIL-53-NHCHO mit Festkörper NMR Spektroskopie

In Kapitel 9 wurde die Orientierung der funktionellen Gruppen (-NHCHO), in Abhängigkeit von verschiedenen Gastmolekülen, innerhalb des Netzwerkes von MIL-53-NHCHO

mit Hilfe eines konzertierten Ansatzes aus Simulationen und FK-NMR bestimmt. Für die Studie wurde die Formamido-Gruppe, durch Einsatz von ^{13}C-Ameisensäure in der post-synthetischen Modifikation, ^{13}C angereichert. Aus einem statischen ^{13}C-CP 1D Spektrum konnte durch Simulation der Linienform mit SIMPSON der vollständige CSA Tensor extrahiert werden (δ_{aniso}= 86 ppm, η = 0,65). Um die Orientierung der einzelnen Formamido-Gruppen zu bestimmen, wurden DFT Rechnungen zur Bestimmung der CSA Parameter durchgeführt. Als Strukturmodell diente eine MOF Elementarzelle, in der der Torsionswinkel zwischen aromatischem Ring und funktioneller Gruppe der Linkermoleküle, in 40° Schritten, sowohl für die cis- als auch für die trans-Form, variiert wurden. Mit Hilfe von Molekularen Modellierungen mit der ebenen Wellen Methode (CASTEP), konnte eine gute Übereinstimmung zwischen experimentellen und simulierten CSA Werten erzielt werden. Mit CSA Werten von δ_{aniso}= 87,8 ppm und einem η= 0,69 (Abweichung vom experimentellen Wert δ_{aniso}= 2,1 % und η = 6,1 %) wurde eine Orientierung für die funktionellen Gruppen in cis-Konfiguration mit einer Torsion von 200° zum aromatischen Kern gefunden. Neben der Bestimmung der Struktur einer einzelnen funktionellen Gruppe, wurde auch die Beziehung dieser Ankergruppen zueinander, auch in Abhängigkeit zum eingelagerten Gastmolekül, ermittelt. Hierzu wurden ^{13}C-^{13}C DQ Aufbaukurven verwendet. Die richtigen Einstellungen für die Methoden wurden jeweils vorher, anhand der bekannten Struktur von Malonsäure, ermittelt.

Da im ^{13}C CP-Spektrum von MIL-53-NH^{13}CHO zwei verschiedene Signale identifiziert werden konnten, wurde eine Reihe von 2D ^{13}C-^{13}C DQ-SQ Spektren in Abhängigkeit der DQ-Anregungszeit (τ_{exc}) gemessen. Durch 2D Entfaltung der Spektren, konnte das Aufbauverhalten von drei DQ-Korrelationen, zwei Selbst- und eine Kreuz-Korrelation, bestimmt werden. Da alle drei Kurven das gleiche Aufbauverhalten zeigen, konnte die Auswertung der Abstände zwischen den ^{13}C-Kernen aus CT 1D DQ Aufbaukurven erfolgen. Durch die Simulation mit SIMPSON konnte gezeigt werden, dass die Kurven durch Spinpärchen dominiert werden (vgl. Abbildung 4.6 links). Während für MIL-53-NH^{13}CHO mit Wassermolekülen in der Pore der Abstand zwischen den ^{13}C-Kernen der funktionellen Gruppen 3,9 Å beträgt (vgl. Abbildung 4.6 links), konnte der Abstand für MIL-53-NH^{13}CHO mit Aceton Molekülen in der Pore auf 3,84 Å festgelegt werden. Zusätzlich konnte mit Hilfe von symmetrischen ^{13}DQ Aufbaukurven die Prozentzahl an Spinpärchen bestimmt werden. Der Anteil an Pärchen mit Abstand 3,9/3,8 ± 0,1 Å in MIL-53-NH^{13}CHO/H_2O beträgt

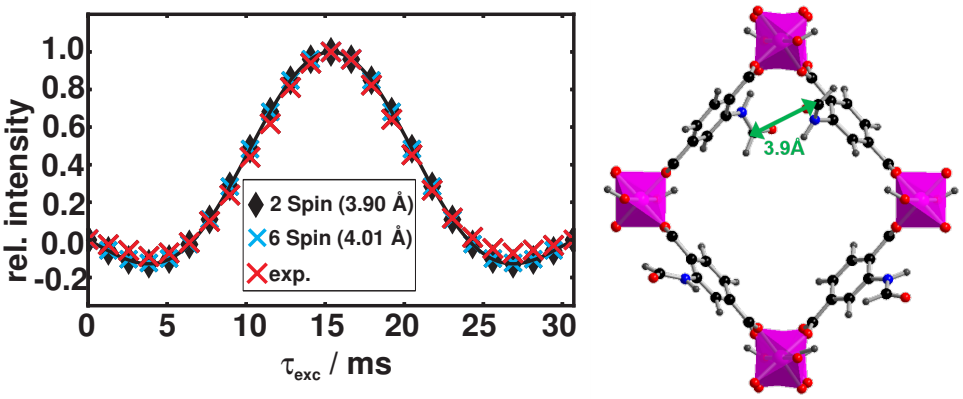

Abbildung 4.6: Links: 1D ^{13}C CT DQ ($SR26_4^{11}$) Aufbaukurve von MIL-53-NH^{13}CHO mit Wasser Molekülen in der Pore. Mit roten Kreuzen sind die experimentell bestimmten Punkte dargestellt, während die SIMPSON Simulation mit 2-Spinsystem in schwarzen Rauten und die Simulation eines 6-Spinsystems in blauen Kreuzen abgebildet ist. Rechts: Schematische Darstellung daraus entwickelten Strukturmodells mit funktionellen Gruppen die 3.9 Å voneinander entfernt sind, eine Torsionswinkel von 200° zum aromatischen Ring besitzen und als cis-Isomere im Netzwerk vorkommen.

70 % und in MIL-53-NH^{13}CHO/Aceton 77 %. Es konnte also gezeigt werden, dass die funktionellen Gruppen in MIL-53-NH^{13}CHO nicht statistisch verteilt, sondern spezifisch angeordnet sind (vgl. Abbildung 4.6). Diese Ordnung ist nicht abhängig vom eingelagerten Gastmolekül und bleibt auch beim Ausheizen unter Vakuum erhalten.

Zusammenfassend lässt sich festhalten, dass die funktionelle Gruppen in MIL-53-NHCHO nicht zufällig angeordnet sind, sondern zu einem Großteil sehr geordnet in Pärchen vorliegt. Dies ist unabhängig davon ob Wasser oder Aceton, die beide die Möglichkeit mitbringen um Wasserstoffbrückenbindungen mit der Funktionalisierung auszubilden, in den Poren eingelagert ist. Deshalb stellt sich nun die Frage, inwiefern diese Gastmoleküle mit den MOF Netzwerken wechselwirken.

4.3 Untersuchung von Wirts-Gast-Wechselwirkungen in verschieden funktionalisierten MIL-53 MOFs mit Festkörper NMR Spektroskopie

Die Wechselwirkung von verschiedenen Gastmolekülen - Aceton, Wasser und Ethanol - mit den funktionellen Gruppen an den Linkermolekülen, wird im letzten Kapitel (10) anhand von MIL-53, MIL-53-NH_2 und MIL-53-NHCHO systematisch, im Hinblick auf selektive Wasserstoffbrückenbindungen, Bindungsstärke und Bindungsplätze, untersucht. Hierfür wurden sowohl die chemischen Verschiebungen der MOF Netzwerke und der Gäste betrachtet, als auch Korrelationen zwischen Wirt und Gast mit Hilfe von ^{1}H-^{1}H Spindiffusionsspektren abgleitet. Um eine ausreichend hohe Auflösung der FK-NMR-Spektren zu erreichen, wurden die Messungen mit homonuklearer Entkopplung (DUMBO) und an sehr hohem Feld (B_0 = 18.8 T) durchgeführt. Für diese Untersuchung war es notwendig, dass eine eineindeutige Zuordnung der Resonanzen zu den jeweiligen Kernen der Netzwerke und Gastmoleküle erreicht wird. Durch die unterschiedlichen Umgebungen der ^{1}H Kerne, ist dies anspruchsvoll und nur durch teils aufwendige 2D Spektren zu bewerkstelligen. So wurden in dieser Arbeit ^{1}H-^{13}C PRESTO, ^{1}H-^{27}Al D-HMQC und ^{1}H-^{14}N D-HMQC Spektren verwendet um die ^{1}H und ^{13}C Signale von allen Wirts-Gast-Kombinationen vollständig zuzuordnen. Über die ^{1}H-^{13}C PRESTO Spektren konnten die aromatischen Linkermolekülanteile zugeordnet werden. Mit Hilfe der ^{1}H-^{27}Al D-HMQC wurde bestimmt, welche Kerne zur anorganischen IBU zugehörig sind. Das außergewöhnlichste 2D Spektrum der Reihe, ist das ^{1}H-^{14}N D-HMQC. Da ^{14}N die Spinquantenzahl I=1 und ein sehr große Quadrupolmoment hat. In Abbildung 4.7 ist das ^{1}H-^{14}N D-HMQC von MIL-53-NHCHO mit Aceton Molekülen in der Pore zu sehen. Das Spektrum zeigt zwei verschiedene Korrelationen bei 9,6 und 10,1 ppm an. Dies lässt erkennen, dass es wie auch im ^{1}H-^{13}C PRESTO zwei verschiedene Umgebungen für die -NHCHO-Gruppe gibt.

Anhand der zugeordneten chemischen Verschiebungen, konnten nun Aussagen über die Wirts-Gast Wechselwirkungen der unterschiedlichen Systeme getroffen werden. So zeigt die Einlagerung der verschiedenen Gastmoleküle keinen Einfluss auf die chemische Verschiebung der μ-OH Gruppe. Dies spricht dafür, dass keine Bindung an die anorganische Einheit erfolgt. Die ^{13}C Verschiebung der Aceton Carbonylgruppe kann als Indikator für

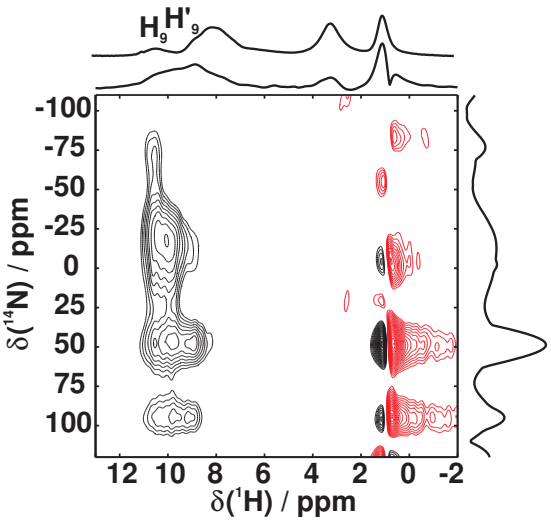

Abbildung 4.7: ^{1}H-^{14}N HMQC von MIL-53-NHCHO mit Aceton in den Poren. Auf der rechten Seite des 2D Spektrums ist die F1 Projektion gezeigt, während oberhalb des 2D Spektrums die F2 Projektion und über dieser Projektion das 1D ^{1}H Spektrum mit homonuklearer Entkopplung abgebildet ist. Positive Intensität ist in schwarz und Negative in rot dargestellt.

die Stärke der Wasserstoffbrückenbindung, an der das Aceton Molekül beteiligt ist, genommen werden. So hat diese Studie gezeigt, dass die chemische Verschiebung von Aceton, eingelagert in MIL-53-NCHO, mit δ_{iso}(CO) = 209,45 ppm am größten von allen untersuchten Systemen, ist. Daraus folgt, dass die H-Brückenbindung zwischen -NHCHO und der Carbonyl Gruppe des Aceton Molekül, am stärksten ist. Bei Aceton in MIL-53-NH_2 ist die H-Brücke schwächer (vgl. δ_{iso}(CO) = 208,3 ppm), während in MIL-53 keine H-Brückenbindungsbildung zwischen Wirt und Gast beobachtet werden kann (vgl. δ_{iso}(CO) = 206,4 ppm). Des Weiteren wurde im Rahmen der Veröffentlichung von Kapitel 10, mit Hilfe von ^{1}H-^{1}H Spindiffusionsspektren, die Orientierung der Aceton Moleküle in der Pore erarbeitet (vgl. Abbildung 4.8 für MIL-53-NHCHO mit Aceton). Es wurden die 2D Spektren mit einer Mischzeit von 2 ms gewählt, um die ersten Korrelationspeaks zwischen Netzwerk und Gastmolekül abzubilden. Aus diesen Spindiffusionsspektren konnte die Orientierung, die in Abbildung 4.8 gezeigt ist, abgeleitet werden.

Dies zeigt, dass trotz der im vorhergehenden Kapitel beschriebenen Pärchenbildung der funktionellen Gruppen in MIL-53-NHCHO die stärkste und vor allem eine selektive Wech-

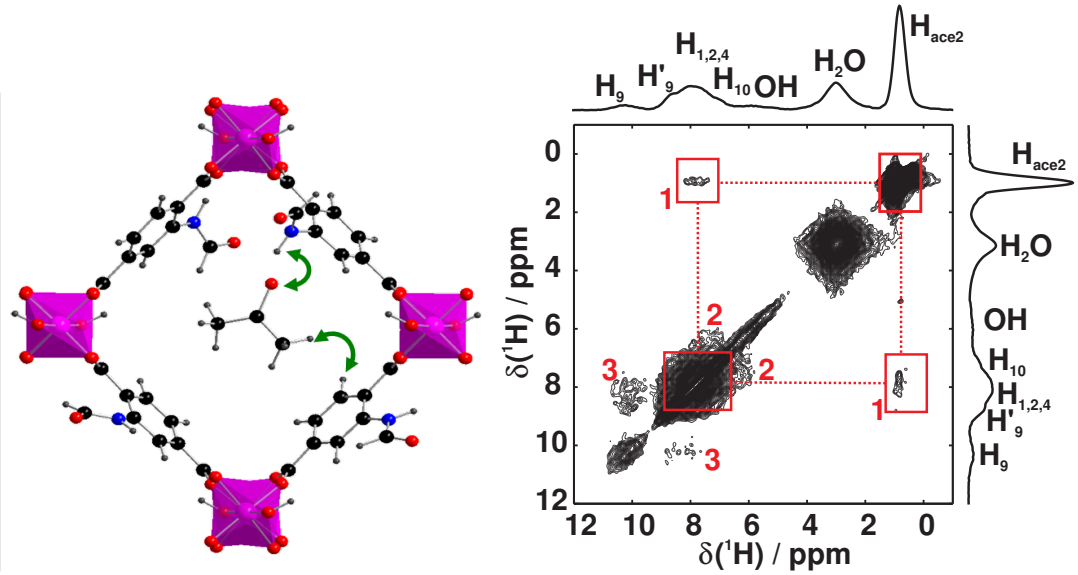

Abbildung 4.8: ^{1}H-^{1}H Spindiffusionsspektrum von MIL-53-NHCHO (rechts) mit Aceton Molekülen in der Pore. Die Mischzeit betrug 2 ms um die ersten Korrelationspeaks zwischen Netzwerk und Gastmolekül zu sehen. Rechts neben und über dem 2D Spektrum ist jeweils die F2 und F1 Projektion abgebildet. An den Projektionen sind jeweils die vorangegangen Zuordnungen der Signale gezeigt.

selwirkung zwischen der Carbonylgruppe der Aceton Moleküle und der Formamido Gruppe des Wirtssystems erzielt werden kann.

5 Darstellung des Eigenanteils

Die Ergebnisse der vorliegenden Arbeit wurden in Kollaboration mit anderen gewonnen und sind veröffentlicht oder werden wie unten angegeben noch eingereicht. Im Folgenden wird der Beitrag aller Co-Autoren zu den verschiedenen Publikationen angegeben. Der korrespondierende Autor wurde jeweils mit einem Sternchen gekennzeichnet.

Kapitel 6

Die Publikation wurde unter dem Titel: *A new aluminium-based microporous metal-organic framework: Al(BTB) (BTB = 1,3,5-benzenetrisbenzoate)* in Microporous Mesoporous Mater. **157**, 50 – 55 (2012) veröffentlicht.

Autoren: Helge Reinsch, Martin Krüger, Julia Wack, Jürgen Senker, Fabrice Salles, Guillaume Maurin, Norbert Stock*

Eigenanteil:

- Präparation der Proben für die FK-NMR Messungen
- Messungen des 1D ^{13}C CP FK-NMR Spektrums
- Messungen des 2D ^{27} Al FK-MQMAS Spektrums
- Zuordnung der Resonanzen in den NMR Spektren und deren Diskussion
- Co-Autorenschaft des Artikels
- Diskussion des hier gezeigten Themas

Anteil der Koautoren:

- Synthese der neuen Verbindung (Helge Reinsch)

- Mithilfe bei der Synthese als Hiwi (Martin Krüger)
- Co-Autorenschaft des Artikels (Helge Reinsch)
- Diskussion des hier gezeigten Themas (alle Autoren)
- Supervision und Korrekturen (Jürgen Senker, Norbert Stock, Guillaume Maurin)

Damit beläuft sich der Eigenanteil an dieser Publikation auf 30 %.

Kapitel 7

Die Publikation wurde unter dem Titel: *[Zn($C_3H_3N_2$($C_3H_2N_2$-N=N-C_6H_5)], a Mixed-Linker ZIF Containing a Photoswitchable Phenylazo Group* in Eur. J. Inorg. Chem., 5378–5383 (2011) veröffentlicht.

Autoren: Stephan Bernt, Mark Feyand, Antje Modrow, Julia Wack, Jürgen Senker, Norbert Stock*

Eigenanteil:

- Präparation der Proben für die FK-NMR Messungen
- Messungen der 1D ^{13}C und ^{15}N CP FK-NMR Spektren
- Messung und Entfaltung des direkten 1D ^{13}C FK-NMR Spektrums
- Zuordnung der Resonanzen in den NMR Spektren und deren Diskussion
- Co-Autorenschaft des Artikels
- Diskussion des hier gezeigten Themas

Anteil der Koautoren

- Synthese der neuen Verbindung (Stephan Bernt)
- Strukturlösung und Pulverdiffraktion (Mark Feyand)
- Messung der N_2-Adsorption (Antje Modrow)
- Co-Autorenschaft des Artikels (Stephan Bernt, Mark Feyand)

- Diskussion des hier gezeigten Themas (alle Autoren)
- Supervision und Korrekturen (Jürgen Senker, Norbert Stock)

Damit beläuft sich der Eigenanteil an dieser Publikation auf 25 %.

Kapitel 8

Die Publikation wurde unter dem Titel: *Controlled modification of the inorganic and organic bricks in an Al-based MOF by direct and post-synthetic synthesis routes* in CrystEngComm **14**, 4126–4136 (2012) veröffentlicht.

Autoren: Tim Ahnfeldt, Daniel Gunzelmann, Julia Wack, Jürgen Senker*, Norbert Stock*

Eigenanteil:

- Mikrowellensynthese des nicht methylierten CAU-1
- Postsynthetische Modifizierung von CAU-1 mit Acetanhydrid
- Präparation der Proben für die 1D FK-NMR Messungen
- Messungen der 1D ^{13}C und ^{15}N CP FK-NMR Spektren
- Zuordnung der Resonanzen in den FK-NMR Spektren und deren Diskussion
- Auswertung der Flüssig NMR Spektren
- Co-Autorenschaft des Artikels
- Diskussion des hier gezeigten Themas

Anteil der Koautoren

- Synthese der Verbindungen (Tim Ahnfeldt)
- Messung und Auswertung der Temperaturabhängigen XRDs (Tim Ahnfeldt)
- Sorptionsstudie von CAU-1 (Tim Ahnfeldt)
- Messung der 2D FK-NMR Spektren (Daniel Gunzelmann)
- Co-Autorenschaft des Artikels (alle)

- Diskussion des hier gezeigten Themas (alle)
- Supervision und Korrekturen (Jürgen Senker, Norbert Stock)

Damit beläuft sich der Eigenanteil an dieser Publikation auf 30 %.

Kapitel 9

Die Arbeit ist vorbereitet zur Einreichung in J. Am. Chem. Soc. unter dem Titel: *Preferred orientation of the formamido hydrogen bond anchor in MIL-53-NHCHO.*

Autoren: Julia Wack, Tim Ahnfeldt, Carsten B. L. Tschense, Norbert Stock, Jürgen Senker*

Eigenanteil:

- Präparation der Proben für die FK-NMR Messungen
- Messungen des 1D ^{13}C CP FK-NMR Spektrums
- Messungen der DQ ^{13}C NMR Spektren (CT und symmetrisch)
- Simulation der DQ Aufbaukurven mit Simpson
- Erstellen der Strukturmodelle für die DFT Rechnungen
- DFT Rechnungen der verschiedenen MOF Strukturen
- Autorenschaft des Artikels
- Diskussion des hier gezeigten Themas

Anteil der Koautoren

- PSM von MIL-53-NH_2 mit ^{13}C-angereicherter Ameisensäure (Tim Ahnfeldt)
- Hilfe bei der Durchführung der Messungen und Simulationen als Hiwi (Carsten Tschense)
- Diskussion des hier gezeigten Themas (alle)
- Supervision und Korrekturen (Jürgen Senker)

Damit beläuft sich der Eigenanteil an dieser Publikation auf 85 %.

Kapitel 10

Die Publikation wurde unter dem Titel: *Identifying Selective Host-guest Interactions Based on Hydrogen Bond Donor Acceptor Pattern in Functionalized Al-MIL-53 Metal-Organic Frameworks* in J. Phys. Chem. C **117**, 19991–20001 (2013) veröffentlicht.

Autoren: Julia Wack, Renée Siegel, Tim Ahnfeldt, Norbert Stock, Luís Mafra, Jürgen Senker *

Eigenanteil:

- Synthese von MIL-53 und MIL-53-NH_2
- Beladung alle MOFs mit den Gastmolekülen (Aceton, Ethanol und Wasser)
- Präparation der Proben für die FK-NMR Messungen
- Messungen aller NMR Spektren
- Zuordnung der ^{1}H und^{13}C-Resonanzen aller Proben
- Identifizierung der Bindungsstelle und Dynamik der Gastmoleküle
- Autorenschaft des Artikels
- Diskussion des hier gezeigten Themas

Anteil der Koautoren

- PSM von MIL-53-NH_2 mit Ameisensäure (Tim Ahnfeldt)
- Hilfestellung bei den *D*-HMQC Experimenten (Renée Siegel)
- Diskussion des hier gezeigten Themas (alle)
- Co-Autorenschaft des Artikels (alle)
- Supervision und Korrekturen (Jürgen Senker, Luís Mafra)

Damit beläuft sich der Eigenanteil an dieser Publikation auf 85 %.

6 A new aluminium-based microporous metal-organic framework: Al(BTB) (BTB = 1,3,5-benzenetrisbenzoate)

Erschienen in:
Microporous and Mesoporous Materials **157**, 50 – 55 (2012)

Microporous and Mesoporous Materials 157 (2012) 50–55

Contents lists available at ScienceDirect

Microporous and Mesoporous Materials

journal homepage: www.elsevier.com/locate/micromeso

A new aluminium-based microporous metal–organic framework: Al(BTB) (BTB = 1,3,5-benzenetrisbenzoate)

Helge Reinsch [a], Martin Krüger [a], Julia Wack [b], Jürgen Senker [b], Fabrice Salles [c], Guillaume Maurin [c], Norbert Stock [a,*]

[a] Institut für Anorganische Chemie, Christian-Albrechts-Universität, Max-Eyth Straße 2, D-24118 Kiel, Germany
[b] Anorganische Chemie I, Universität Bayreuth, Universitätsstr. 30, D-95447 Bayreuth, Germany
[c] Institut Charles Gerhardt – UMR CNRS 5253, UM2, ENSCM, Université de Montpellier II, Place Eugène Bataillon CC 003, F-34095 Montpellier cedex 5, France

ARTICLE INFO

Article history:
Received 23 December 2010
Received in revised form 12 May 2011
Accepted 13 May 2011
Available online 16 June 2011

Keywords:
Metal organic framework
High-throughput methods
Solvothermal synthesis
Metal carboxylate
Aluminium

ABSTRACT

The system Al^{3+}/H_3BTB/DMF/additive was systematically investigated using high-throughput methods and the new, microporous MOF [Al(BTB)] (BTB = 1,3,5-benzenetrisbenzoate), named CAU-4 (CAU = Christian-Albrechts-University), was discovered. The synthesis was optimized changing chemical and process parameters and the final synthesis procedure was scaled up to the gram scale. CAU-4 is thermally stable up to 400 °C in air and exhibits a BET-surface area of 1520 m^2/g and a micropore volume of 0.61 cm^3/g. A structure model was developed using a computationally assisted structure determination that was further validated by a good agreement with the experimental X-ray diffraction patterns and the geometrical features. The framework structure consists of isolated [AlO_6]-octahedra which are bridged by carboxylate groups of the BTB-linker to form chains. These chains are connected by the tritopic aromatic building blocks, to form one-dimensional hexagonal channels with a diameter of ca. 9.6 Å.

1. Introduction

In the last decade, the research on metal–organic frameworks (MOFs) has produced an amazing number of new porous framework materials [1]. These compounds are built up from organic linker molecules, typically containing carboxylate or phosphonate groups, and inorganic building blocks (bricks) like metal cations or metal-oxo-clusters [2]. Once the synthesis conditions of the inorganic building blocks are established, isoreticular synthesis can be employed to adjust the pore size and pore functionality [3–8]. Through post-synthetic modification the properties of the MOFs can be fine-tuned. The so-obtained compounds are investigated for their use in gas sorption or separation, in drug delivery or as catalysts [9,10].

MOFs which are based on trivalent cations have shown to be materials with highly desirable properties. Thus, many chromium- and aluminium-based MOFs show a very high thermal and chemical stability such as Al-MIL-53 [11], MIL-100 [12–14], and Cr-MIL-101 [15]. These MOFs are based on terephthalic acid (H_2BDC) or trimesic acid (H_3BTC). Extension of the organic linker has led to isoreticular compounds exhibiting larger pores and cavities. The use of the ditopic ligands napthyldicarboxylic acid and biphenyldicarboxylic acid resulted in the formation of the porous analogues of the Al-MIL-53 (DUT-4 and DUT-5) [16]. The tritopic ligand H_3BTC has been observed in the Al-based MOFs Al-MIL-96 [17], Al-MIL-100 [12], and MIL-110 [18] which exhibit large specific BET-surfaces and micropore volumes. The extension of H_3BTC by insertion of phenyl rings leads to 1,3,5-benzenetrisbenzoic acid (H_3BTB). Although there is a large number of MOFs containing this linker molecule that are based on beryllium [19], magnesium [20], copper [21], zinc [22–25] nickel [26], terbium [27] or iron [28], there is no example in the chemistry of aluminium.

In the course of our systematic investigation of Al-containing MOFs, we selected the tritopic linker H_3BTB for the exploration of the system Al^{3+}/H_3BTB/DMF/additive. Here, we present the synthesis and detailed characterization of the first Al- and BTB-containing MOF [Al(BTB)].

2. Experimental section

2.1. General

All chemicals used for the synthesis of CAU-4 are commercially available and were used without further purification. For the discovery and synthesis optimization high-throughput methods comprising our 24-high-throughput reactor system were employed [29,30]. The high-throughput XRPD measurements were performed using a STOE HT diffractometer equipped with a *xy*-stage and an IPDS system (Cu $K_{\alpha 1}$ radiation) in transmission geometry.

* Corresponding author. Tel.: +49 (0) 431 880 1675; fax: +49 (0) 431 880 1775.
E-mail address: stock@ac.uni-kiel.de (N. Stock).

1387-1811/$ - see front matter © 2011 Elsevier Inc. All rights reserved.
doi:10.1016/j.micromeso.2011.05.029

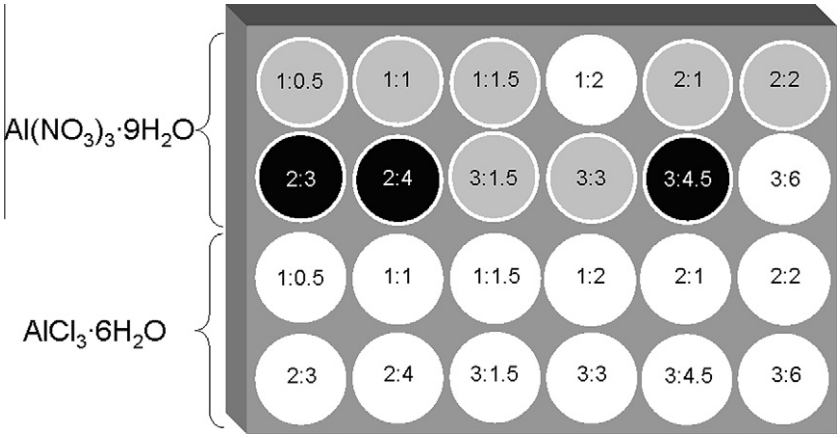

Fig. 1. Results of the high-throughput investigation of the system $Al^{3+}/H_3BTB/DMF$ at a reaction temperature of 190 °C. Grey (CAU-4), black (mixture of CAU-4 and the crystalline byproduct), white (X-ray amorphous product). The numbers represent the molar ratios $H_3BTB:Al^{3+}$.

High-precision powder diffraction data was measured on a STOE Stadi-P powder diffractometer equipped with a linear position sensitive detector system (Cu–$K_{\alpha1}$ radiation). MIR spectra were recorded on an ATI Matheson Genesis spectrometer in the spectral range of 400–4000 cm^{-1} using the KBr disk method. FT-Raman spectra were recorded on a Bruker IFS 66 FRA 106 in the range of 0–3500 cm^{-1} using a Nd/YAG-Laser (1064 nm). The thermogravimetric analyses were performed using a NETSCH STA 409 CD analyzer. The samples were heated in Al_2O_3 crucibles at a rate of 4 K min^{-1} under a flow of air (75 ml min^{-1}). The TG data were corrected for buoyancy and current effects. Sorption experiments were carried out using a Belsorp-max instrument (BEL JAPAN INC.) Before the sorption experiments, the samples were activated at 200 °C under vacuum (10^{-2} kPa) over night. ^{27}Al and ^{13}C solid-state NMR studies were performed on a commercial BRUKER Avance II 300 spectrometer operating at 7.05 T. The relative reference for ^{13}C shifts was TMS and for ^{27}Al shifts a hydrochloric solution of $AlCl_3$. The measurements were taken in a 4 mm triple-resonance probe from BRUKER. All experiments were measured under magic angle spinning (MAS) with spinning frequencies of 12.5 kHz for the ^{13}C- and 14430 Hz for the ^{27}Al-MQMAS spectrum. A ramped cross-polarization sequence with a contact time of 5 ms was used for the excitation of the ^{13}C nuclei, where the power of the ^{1}H radiation was linearly varied from 100% to 50%. During the acquisition a broadband proton decoupling with a nutation frequency of 70 kHz and SPINAL64 was applied. The ^{27}Al-MQMAS spectrum was recorded with a three-pulse sequence [31] with nutation frequencies of 108 kHz, 300 kHz and 11 kHz for the excitation, conversion and selective 90° pulses, respectively. The coherence pathway 0 ± 30−1 was selected via a cog-wheel phase cycle [32] COG60{11,1,0;30}.

2.2. Preparation

The optimized synthesis of CAU-4 in the HT reactor system (V_{max} = 2.0 ml per Teflon insert) is as follows: $Al(NO_3)_3{\cdot}9H_2O$ (45.7 μmol, 17.1 mg, Merck), benzoic acid (81.9 μmol, 10.0 mg, Merck) and 1,3,5-benzenetrisbenzoic acid (91.3 μmol, 40.0 mg, BASF) were dissolved in *N*,*N*-dimethylformamide (6.50 mmol, 0.50 mL, BASF). The reactor was heated for 24 h at 180 °C.

The reaction can be scaled up to the fourfold amount, using Pyrex glass tubes, or to the tenfold amount, using larger steel autoclaves with Teflon inserts (V = 30 mL). The same molar ratios Al^{3+}: H_3BTB: benzoic acid: DMF = 7:14:10:142 as well as the same temperature program were used. A yield of 47% (based on H_3BTB) was obtained from the reaction in the 30 ml reactor. Elemental analysis of the scaled-up synthesis product: $[Al(BTB)]{\cdot}1.6(DMF){\cdot}4.7(H_2O)$ calc (%): C 57.5, H 5.4, N 3.4, found (%): C 58.4 H 4.2, N 3.8. These values correspond well to the results of the TG measurements but may change upon long term exposure to air.

2.3. Molecular simulations

2.3.1. Computational assisted structure determination

The structure model for the CAU-4 was derived from an energy minimization procedure in the space group *P*1 using the classical universal force field (UFF) [33] and imposing the unit cell

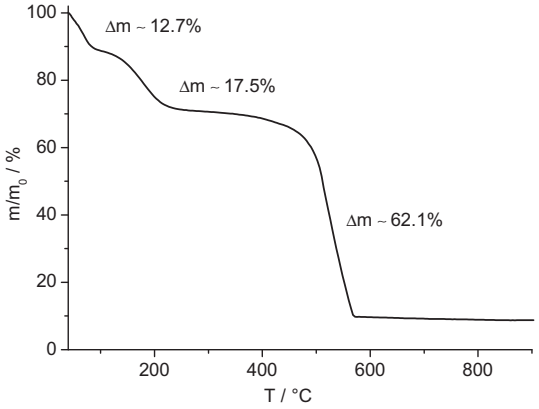

Fig. 2. TG analysis of [Al(BTB)] 1,6 DMF 4,7 H_2O (CAU-4-as).

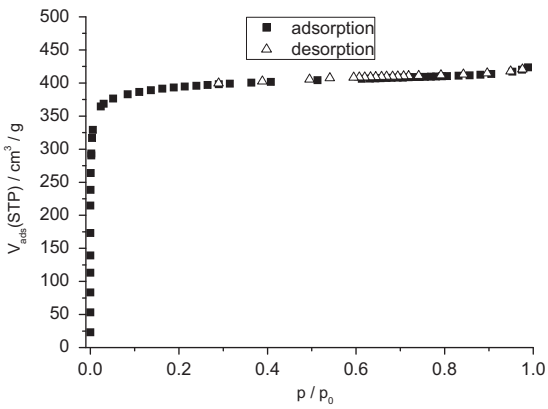

Fig. 3. Sorption isotherm of CAU-4 measured with N_2 at −196 °C.

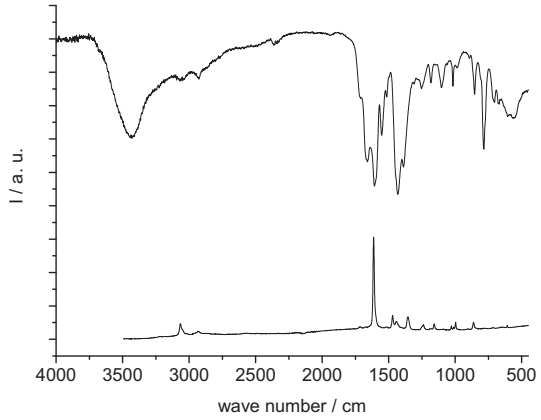

Fig. 4. IR- and Raman spectra of as synthesized CAU-4.

parameters determined experimentally. Such calculations were performed using the Forcite software implemented in Materials Studio (version 5.0) [34]. The UFF force field has been selected for its ability to reproduce successfully the structures of many metal–organic frameworks [5,35,36]. Since the UFF force field describes only aluminium with a tetrahedral coordination environment, the parameters for the octahedrally coordinated Al^{3+} present in CAU-4 were defined starting with those available for Fe^{2+} defined in an octahedral environment. This adjustment consisted of rescaling the σ-parameter taking into account the difference of ionic radii for the two elements [37]. Such a procedure was validated on the Al-MIL-53 structure with simulated Al–O distances and O–Al–O angles very similar to those experimentally determined [11]. The powder XRPD pattern for the resulting structure was further calculated using the Reflex software within Materials Studio.

2.3.2. Calculations of the geometrical features

The accessible surface area of the simulated structure model for CAU-4 was estimated using the strategy previously reported by Düren et al. [38]. The surface area was calculated from the center of a nitrogen probe molecule rolling across the surface. While the diameter of the nitrogen probe molecule was considered to be 3.681 Å, the diameters of each atom constituting the CAU-4 structure were taken from the forcefield described above. Using the same parametrization for the framework, the methodology of Gelb and Gubbins [39] was further used to calculate the pore size distribution (PSD). Finally, the solvent accessible volume was also determined from the crystal structure model using the standard setting in PLATON, which uses a random probe molecule with a diameter of 2.6 Å [40].

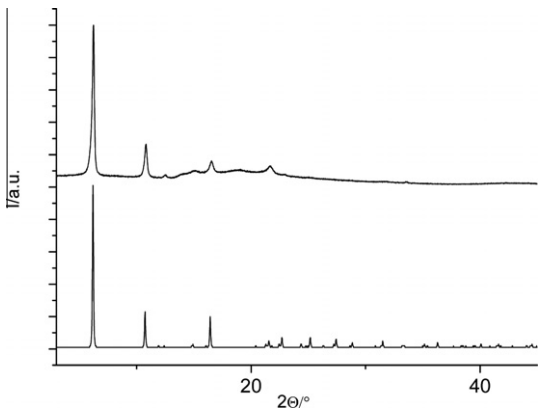

Fig. 5. Comparison of the diffractograms of MIL-103 (calculated, bottom) and CAU-4 (top).

3. Results and discussion

3.1. Synthesis

High-throughput methods have shown to be a valuable tool for the exploration of new chemical systems. Thus, the discovery of new compounds and the optimization of synthesis procedures can be rapidly achieved while using only small amounts of starting materials [30]. Due to the large number of experiments reaction trends can be extracted and fields of formation are easily established [41–43].

CAU-4 was discovered during a high-throughput investigation of the system Al^{3+}/H_3BTB/solvent using $Al(NO_3)_3{\cdot}9H_2O$ or $AlCl_3{\cdot}6H_2O$ respectively as the metal-source. Use of DMF as the solvent (190 °C/24 h) led to the formation of two new compounds depending on the molar ratios employed (Fig. 1).

Using $AlCl_3{\cdot}6H_2O$ as the aluminium source, only X-ray amorphous solids were obtained. Employing $Al(NO_3)_3{\cdot}9H_2O$, the formation of pure phase CAU-4 is observed at molar ratios H_3BTB:$Al^{3+} \geqslant 1$. Especially at higher concentrations (Fig. 1, 2nd row), mixtures of CAU-4 and a crystalline byproduct are formed, when $Al(NO_3)_3{\cdot}9H_2O$ is used in excess.

After the discovery of the new phase focused libraries were set up to determine the field of formation of CAU-4. First the overall concentration as well as molar ratio Al^{3+}/H_3BTB were optimized. Employing the molar ratio Al^{3+}:H_3BTB:DMF = 7:14:142 crystalline products were obtained. To further increase the crystallinity different additives such as water, NaOH, HNO_3, ethylenediamine or monodentate carboxylic acids were tested. Only the latter additives led to an improvement of the crystallinity. Small amounts of formic acid as well as benzoic acid had a slightly positive influence on the product formation (Fig. S1). In addition, the use of benzoic acid as the additive improves the reproducibility of synthesis procedure for CAU-4 which strongly depends on the purity of the DMF (Fig. S2). The molar ratio Al^{3+}:H_3BTB:benzoic acid:DMF = 7:14:10:142 was finally used for the scale-up synthesis of CAU-4.

Once the chemical parameters were established we focused on the optimization of the process parameters. The reaction temperature and the reaction time were found to be optimal at 180 °C for 24 h. Higher temperatures led to less crystalline products, while longer reaction times did not improve the product quality (Fig. S3). For the synthesis scale-up, the time-dependent formation of CAU-4 under stirring was also investigated. CAU-4 is obtained after 3 h and the crystallinity of the product improves with time (Fig. S4).

3.2. Thermal analysis and stability

The thermogravimetric experiment (Fig. 2) was performed under air with a heating rate of 4 K/min. The first weight loss between 40 and 100 °C corresponds to the removal of adsorbed water molecules (calc. 12.8%; obs. 12.7%), while the second step (120–200 °C) can be attributed to the removal of DMF molecules (calc. 17.6%; obs. 17.5%). The framework is stable up to 400 °C and decomposes under formation of X-ray amorphous Al_2O_3 (calc. 61.9%; obs. 62.1%). The observed weight losses are in very good agreement with the results of the elemental analysis. Thus the as synthesized compound has the composition [Al(BTB)]·1,6 DMF·4,7 H_2O.

The XRD pattern of a sample activated at 200 °C under vacuum for 12 h shows that the framework structure is stable in air after the removal of the guest molecules (Fig. S5). Thus, CAU-4 is

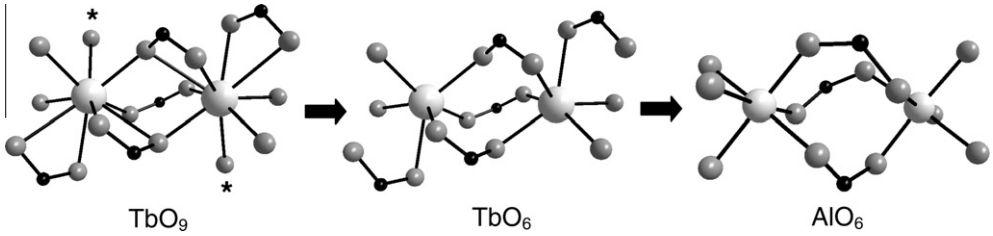

Fig. 6. Conversion of the ninefold coordination of edge-sharing [TbO_9]-polyhedra observed in MIL-103 into isolated [AlO_6]-octahedra connected by the carboxylate groups. The asterisk marks the water molecules coordinated to the Tb^{3+} ions. Grey:oxygen, black:carbon, white:metal.

Table 1
Cell parameters of MIL-103 (starting model), the structural model of CAU-4 (from force field calculations) and the final structural model, taking the experimental reflection positions into account.

Structure	MIL-103	CAU-4: structure of minimal energy	CAU-4: experimental lattice parameters
Space group	*R*32	*P*312	*P*312
a = *b*	28.5344(8) Å	15.9822 Å	16.273(1) Å
c	12.2148(5) Å	3.7721 Å	12.956(6) Å

another example of the high stability of Al-containing MOFs. Its stability is comparable to the one observed for other Al-containing MOFs such as of DUT-4 and DUT-5 exhibiting also unfunctionalized linker molecules, similar micropore volumes and easily accessible channels [16]. A similar functionalized porous Al-MOF such as CAU-1 decomposes around 310 °C [44].

3.3. Adsorption

The structural integrity of the activated compound was also demonstrated by sorption measurements. The N_2-isotherm was recorded at −196 °C (Fig. 3). Prior to the measurement, the sample was activated over night at 200 °C and 10^{-2} kPa. A type I isotherm is observed which is typical for microporous materials. The specific surface was calculated using the BET-equation according to the procedure proposed recently [45]. CAU-4 exhibits an apparent specific surface area of 1520 m^2/g and a micropore volume of 0.61 cm^3/g (calculated from the amount adsorbed at $p/p_0 = 0.5$). This corresponds well to the solvent accessible volume calculated from the crystal structure model using PLATON (0.67 cm^3/g) [40].

The pore size was determined from the N_2-isotherm by means of NLDFT/GCMC-methods using the BELSORP evaluation software [46]. Assuming a cylindrical pore shape and an oxidic surface, the pore radius was determined to be 4.1 Å, which is quite close to the expected value of 4.8 Å. The PSD as well as the simulated fit can be found in the supporting information (Figs. S6 and S7).

3.4. Spectroscopy

The IR- and Raman spectra (Fig. 4) of the as synthesized CAU-4 show the presence of water (3443 cm^{-1}) and residual DMF (2926, 1709 cm^{-1}) molecules in the pores. The presence of the coordinating carboxylate groups is demonstrated by the stretching vibrations ν_{as} and ν_s at 1628 cm^{-1} and 1431 cm^{-1}, respectively. The absorption at 787 cm^{-1} can be attributed to the C–H deformation vibration of the 1,3,5-substituted aromatic ring. In the Raman-spectrum, the C–H stretching vibrations of the aromatic protons are observed at 3065 cm^{-1} and the C–C ring stretching vibration at 1613 cm^{-1}.

4. Structure

Since no single crystals could be obtained, and due to the limited number of well resolved reflections in the XRPD pattern

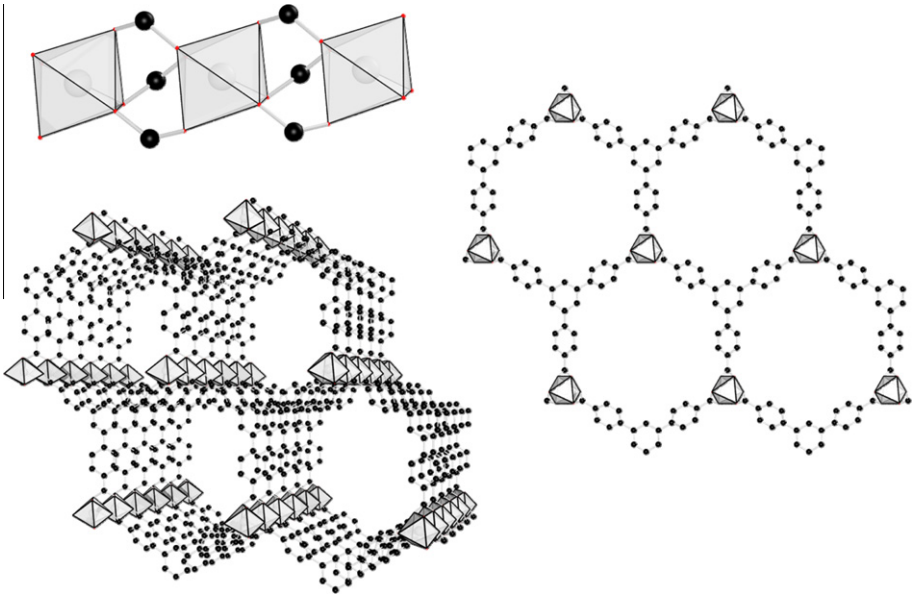

Fig. 7. Upper left: isolated [AlO_6]-octahedra connected by the carboxylate groups of the BTB-linker. Right: connection of the chains by the BTB ions result in the formation of a honeycomb-like framework. Lower left: representation of the hexagonal channels.

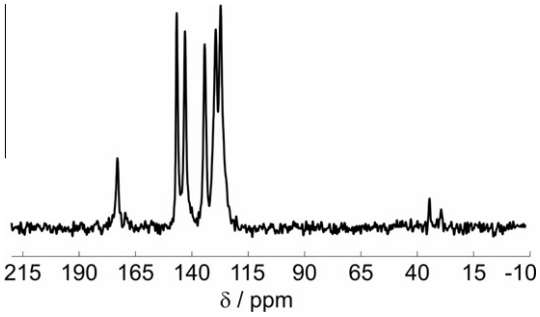

Fig. 8. ^{13}C CP-MAS spectrum of CAU-4.

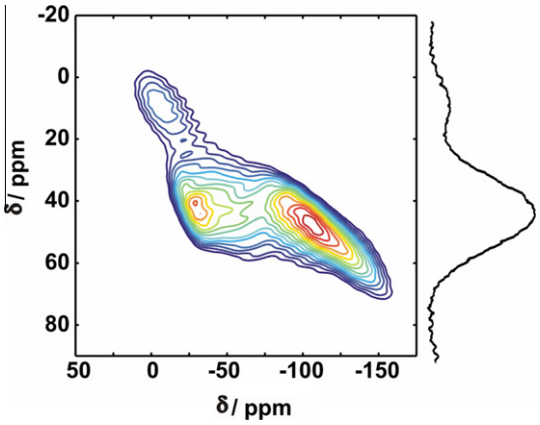

Fig. 9. ^{27}Al MQMAS Spectrum of CAU-4.

(Fig. 5), the crystal structure could not be determined using conventional methods. Comparison of the XRPD pattern of CAU-4 with calculated patterns of other BTB-containing MOFs led to the assumption that the structure of CAU-4 is related to the one of MIL-103 (Fig. 5) [27]. This MOF is built up from chains of edge-sharing [TbO_9]-polyhedra, which are formed by the coordination of carboxylate moieties and water molecules. The most common coordination numbers for aluminium are CN = 4 and 6 and in carboxylate-based Al-MOFs exclusively AlO_6 polyhedra have been observed [47]. Therefore, the structure of MIL-103 was used as a starting model and the coordination was adjusted to allow a sixfold coordination of the metal center. To adjust the coordination around the metal ion in CAU-4, the water molecules were deleted from the structure and the bridging (μ_2-) oxygen atoms of the carboxylate groups in MIL-103 were connected to only one M^{3+} ion (Fig. 6).

The computational assisted structure determination was performed in *P*1 symmetry. The so-obtained optimized structure adapts the space group *P*312 and was further transformed to the maximal isomorphic subgroup of lowest index using Powdercell [48] which results in a tripling of the *c*-axis parameter. This model was further adapted to the experimentally obtained cell parameters (Table 1). The final atomic positions are given in Table. S1.

Employing this structure model, all reflections observed in the experimental XRPD pattern are well reproduced, leading to the Pawley-Fit shown in Fig. S8.

Further validation of the proposed structure model was also obtained by a good agreement between the simulated geometrical features and those experimentally observed. Indeed, the simulated pore diameter (9.6 Å, Fig. S9, [39]), accessible surface area (1670 m^2/g, [38]) and solvent accessible volume (0.67 cm^3/g, PLATON [40]) compare well with the experimental data of 8.2 Å, 1520 m^2/g and 0.61 cm^3/g, respectively.

The resulting framework is based on single AlO_6-octahedra, which are connected via bridging carboxylate groups in a twisted face-to-face fashion (Fig. 7). A similar bridging mode was already observed in a scandium based MOF, based on terephtalate anions [49,50]. Thus, an infinite chain of bridged octahedra is formed. Like in MIL-103, the tritopic BTB-ligands connect these units to form a honeycomb framework with one-dimensional channels. These channels exhibit a diameter of ~9.6 Å, taking the van-der-Waals radii of the framework atoms into account.

Solid state ^{13}C and ^{27}Al NMR spectra of the activated compound were recorded (Figs. 8 and 9). As expected the ^{13}C spectrum (Fig. 8) is mainly dominated by the signals in aromatic region (120–150 ppm). Only one signal for the carboxylate group is observed (173 ppm) confirming that all $-COO^-$ groups are connected to the Al^{3+} ions in a similar way. The small signals at 29.5 and 35 ppm are due to traces of solvent molecules in the pores. The ^{27}Al-MQMAS spectrum (Fig. 9) is typical for sixfold coordinated Al^{3+} ions in a strongly distorted octahedral environment. At least two independent Al atoms are present.

5. Conclusion

We have discovered and characterized a new Al-based MOF named CAU-4. The framework is built up from isolated AlO_6-octahedra, which are bridged by the carboxylate groups of the incorporated BTB-anion. The synthesized sample exhibits a BET-surface area and a micropore volume of 1520 m^2/g and 0.61 cm^3/g, respectively. The low crystallinity of CAU-4 poses a challenge for the structure determination by common methods. Nevertheless a structure model could be set up that agrees well with all the analytical results.

Acknowledgements

The work has been supported by the DFG (SPP 1362). The research leading to these results has received funding from the European Community's Seventh Framework Program (FP7/2007-20013) under grant agreement n° 228862.

Appendix A. Supplementary data

Supplementary data associated with this article can be found, in the online version, at doi:10.1016/j.micromeso.2011.05.029.

References

[1] C. Janiak, J.K. Vieth, New J. Chem. 34 (2010) 2366.
[2] M. Eddaoudi, J. Kim, N. Rosi, D. Vodak, J. Wachter, M. O'Keeffe, O.M. Yaghi, Science 295 (2002) 469.
[3] M. Kandiah, S. Usseglio, S. Svelle, U. Olsbye, K.P. Lillerud, M. Tilset, J. Mater. Chem. 20 (2010) 9848.
[4] S. Surble, C. Serre, C. Mellot-Draznieks, F. Millange, G. Ferey, Chem. Commun. (2006) 284.
[5] T. Devic, P. Horcajada, C. Serre, F. Salles, G. Maurin, B. Moulin, D. Heurtaux, G. Clet, A. Vimont, J.-M. Greneche, B. Le Ouay, F. Moreau, E. Magnier, Y. Filinchuk, J. Marrot, J.-C. Lavalley, M. Daturi, G. Ferey, J. Am. Chem. Soc. 132 (2010) 1127.
[6] H. Chun, D.N. Dybtsev, H. Kim, K. Kim, Chem. Eur. J. 11 (2005) 3521.
[7] M.T. Wharmby, J.P.S. Mowat, S.P. Thompson, P.A. Wright, J. Am. Chem. Soc. 133 (2011) 1266.
[8] T. Ahnfeldt, J. Moellmer, V. Guillerm, R. Staudt, C. Serre, N. Stock, Chem. Eur. J. 17 (2011) 6462.
[9] A. Czaja, N. Trukhan, U. Müller, Chem. Soc. Rev. 38 (2009) 1284.
[10] P. Horcajada, T. Chalati, C. Serre, B. Gillet, C. Sebrie, T. Baati, J.F. Eubank, D. Heurtaux, P. Clayette, C. Kreuz, J.-S. Chang, Y.-K. Hwang, V. Marsaud, P.-N. Bories, L. Cynober, S. Gil, G. Ferey, P. Couvreur, R. Gref, Nature Mater 9 (2010) 172.
[11] T. Loiseau, C. Serre, C. Huguenard, G. Fink, F. Taulelle, M. Henry, T. Bataille, G. Férey, Chem. Eur. J. 10 (2004) 1373.

[12] C. Volkringer, D. Popov, T. Loiseau, G. Férey, M. Burghammer, C. Riekel, M. Haouas, F. Taulelle, Chem. Mater. 21 (2009) 5695.
[13] P. Horcajada, S. Surble, C. Serre, D. Hong, Y. Seo, J. Chang, J.-M. Greneche, I. Margiolaki, G. Ferey, Chem. Commun. (2007) 2820.
[14] G. Férey, C. Serre, C. Mellot-Draznieks, F. Millange, S. Surblé, J. Dutour, I. Margiolaki, Angew. Chem. Int. Edt. 433 (2004) 6296.
[15] G. Férey, C. Mellot-Draznieks, C. Serre, F. Millange, J. Dutour, S. Surblé, I. Margiolaki, Science 309 (2005) 2040.
[16] I. Senkovska, F. Hoffmann, M. Fröba, J. Getzschmann, W. Böhlmann, S. Kaskel, Micropor. Mesopor. Mater. 122 (2009) 93.
[17] T. Loiseau, L. Lecroq, C. Volkringer, J. Marrot, G. Férey, M. Haouas, F. Taulelle, S. Bourrelly, P.L. Llewellyn, M. Latroche, J. Am. Chem. Soc. 128 (2006) 10223.
[18] C. Volkringer, D. Popov, T. Loiseau, N. Guillou, G. Ferey, M. Haouas, F. Taulelle, C. Mellot-Draznieks, M. Burghammer, C. Riekel, Nat. Mater. 6 (2007) 760.
[19] K. Sumida, M.R. Hill, S. Horike, A. Dailly, J.R. Long, J. Am. Chem. Soc. 131 (2009) 15120.
[20] C. Volkringer, T. Loiseau, J. Marrot, G. Ferey, Cryst. Eng. Comm. 11 (2009) 58.
[21] B. Chen, M. Eddaoudi, S.T. Hyde, M. O'Keeffe, M. Yaghi, Science 291 (2001) 1021.
[22] H.K. Chae, D.Y. Siberio-Perez, J. Kim, Y.-B. Go, M. Eddaoudi, A.J. Matzger, M. O'Keeffe, O.M. Yaghi, Nature 427 (2004) 523.
[23] J. Kim, B. Chen, T.M. Reineke, H. Li, M. Eddaoudi, D.B. Moler, M. O'Keeffe, O.M. Yaghi, J. Am. Chem. Soc. 123 (2001) 8239.
[24] S.R. Caskey, A.G. Wong-Foy, A.J. Matzger, Inorg. Chem. 47 (2008) 7751.
[25] L. Hou, J. Zhang, X. Chen, S. Weng, Chem. Commun. (2008) 4019.
[26] K. Gedrich, I. Senkovska, N. Klein, U. Stoeck, A. Henschel, M.R. Lohe, I.A. Baburin, U. Mueller, S. Kaskel, Angew. Chem. Int. Ed. 49 (2010) 8489.
[27] T. Devic, C. Serre, N. Audebrand, J. Marrot, G. Férey, J. Am. Chem. Soc. 127 (2005) 12788.
[28] S. Choi, M. Seo, M. Cho, Y. Kim, M. Jin, D. Jung, J. Choi, W. Ahn, J. Rowsell, J. Kim, Cryst. Growth Des. 7 (2007) 2290.
[29] S. Bauer, C. Serre, T. Devic, P. Horcajada, J. Marrot, G. Ferey, N. Stock, Inorg. Chem. 47 (2008) 7568.
[30] N. Stock, Micropor. Mesopor. Mater. 129 (2010) 287.
[31] J.P. Amoureux, C. Fernandez, S. Steuernagel, J. Magn. Reson. A 123 (1996) 116.
[32] A. Jerschow, R. Kumar, J. Magn. Reson. 160 (2003) 59.
[33] K. Rappé, C.J. Casewit, K.S. Colwell, W.A. Goddard III, W.M. Skiff, J. Am. Chem. Soc. 114 (1992) 10024.
[34] Materials Studio Version 5.0, Accelrys Inc., San Diego, CA, 2009.
[35] A. Sonnauer, F. Hoffmann, M. Froba, L. Kienle, V. Duppel, M. Thommes, C. Serre, G. Férey, N. Stock, Angew. Chem. Int. Ed 48 (2009) 3849.
[36] F. Salles, G. Maurin, C. Serre, P.L. Llewellyn, C. Knöfel, H.J. Choi, J.R. Long, Y. Filinchuk, G. Férey, J. Am. Chem. Soc. 132 (2010) 13782.
[37] R.D. Shannon, C.T. Prewitt, Acta Cryst. B 25 (1969) 925.
[38] T. Düren, F. Millange, G. Férey, K.S. Walton, R.Q. Snurr, J. Phys. Chem. C 111 (2007) 15350.
[39] L.D. Gelb, K.E. Gubbins, Langmuir 15 (1999) 305.
[40] A.L. Spek, PLATON, A Multipurpose Crystallographic Tool, Utrecht University, Utrecht, The Netherlands, 2010.
[41] A. Sonnauer, N. Stock, Eur. J. Inorg. Chem. (2008) 5038.
[42] N. Stock, T. Bein, Solid State Sci. 5 (2009) 1207.
[43] C. Volkringer, T. Loiseau, N. Guillou, G. Ferey, M. Haouas, F. Taulelle, E. Elkaim, N. Stock, Inorg. Chem. 49 (2010) 9852.
[44] T. Ahnfeldt, N. Guillou, D. Gunzelmann, I. Margiolaki, T. Loiseau, G. Férey, J. Senker, N. Stock, Angew. Chem. Int. Ed. 21 (2009) 5265.
[45] J. Moellmera, E.B. Celerc, R. Luebkeb, A.J. Cairnsb, R. Staudta, M. Eddaoudib, M. Thommes, Micorpor. and Mesopor. Mater. 129 (2010) 345.
[46] Evaluation Software BEL Japan, INC. (2008).
[47] Cambridge Crystallographic Data Centre, CCDC Version 5.31 (2009).
[48] W. Kraus, G. Nolze, PowderCell 2.4, (2000).
[49] S.R. Miller, P.A. Wright, C. Serre, T. Loiseau, J. Marrot, G. Férey, Chem. Commun. (2005) 3850.
[50] J. Perles, M. Iglesias, M. Martín-Luengo, M. Ángeles Monge, C. Ruiz-Valero, N. Snejko, Chem. Mater. 23 (2005) 5837.

Supporting Information

A new aluminium-based microporous metal-organic framework: Al(BTB) (BTB = 1,3,5-benzenetrisbenzoate)*

Helge Reinsch,[a] Martin Krüger,[a] Julia Wack [b], Jürgen Senker [b], Fabrice Salles,[c] Guillaume Maurin,[c] Norbert Stock[a,]*

[a] Institut für Anorganische Chemie, Christian-Albrechts-Universität, Max-Eyth Straße 2, D-24118 Kiel, Germany
[b] Anorganische Chemie I, Universität Bayreuth, Universitätsstr. 30, D-95447 Bayreuth, Germany
[c] Institut Charles Gerhardt – UMR CNRS 5253, UM2, ENSCM
Université de Montpellier II
Place Eugène Bataillon CC 003,
F-34095 Montpellier cedex 5, France

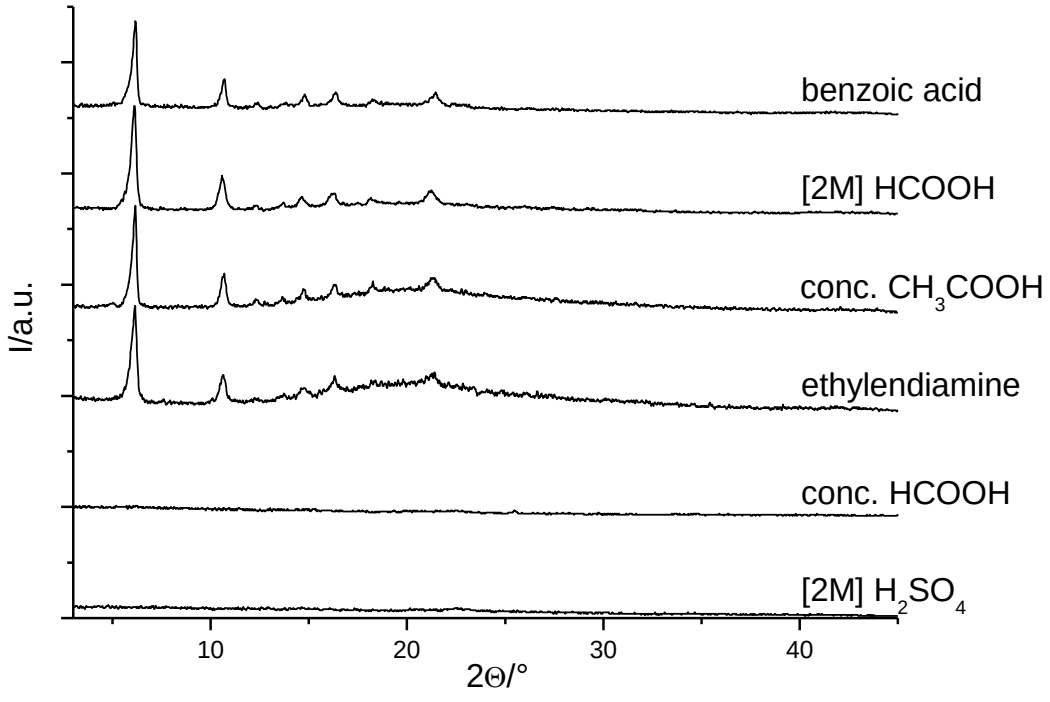

Figure S1: Comparison of the influence of additives on the formation of CAU-4.

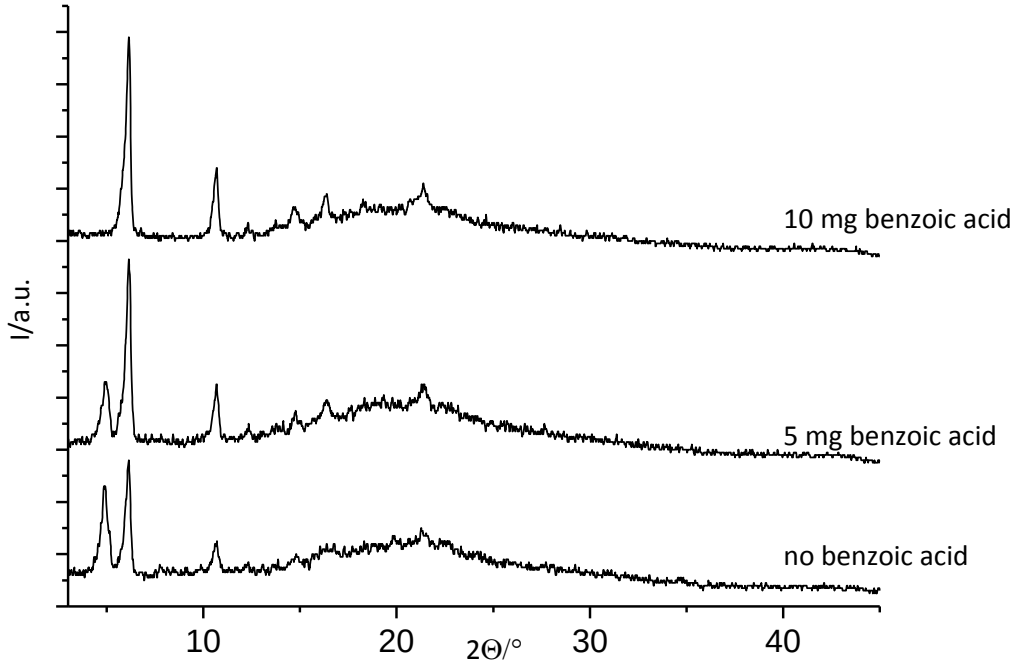

Figure S2: Influence of the addition of benzoic acid on the formation of the byproduct using technical DMF as the solvent.

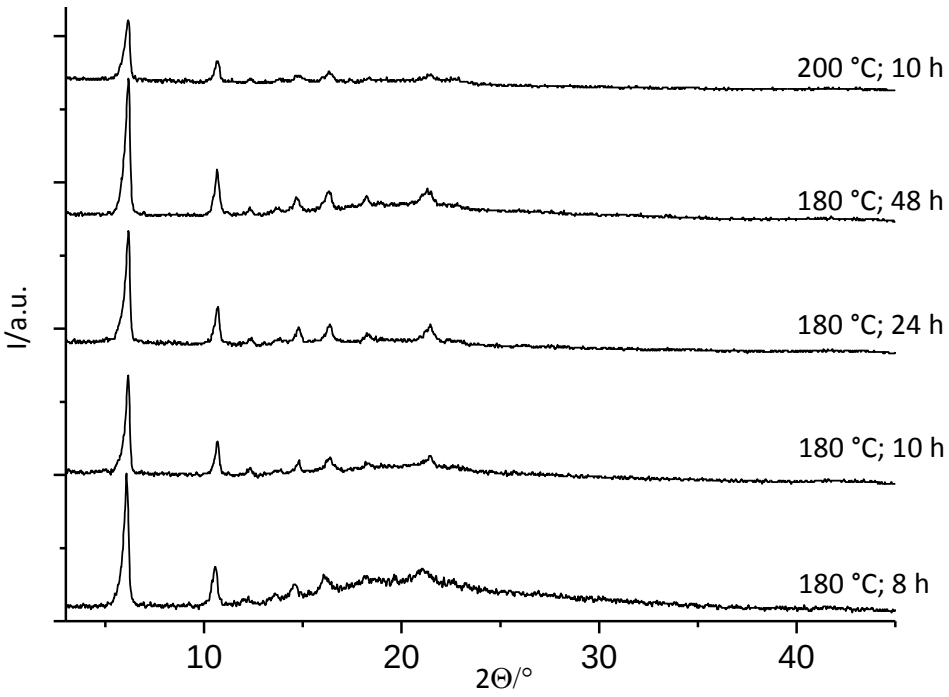

Figure S3: Time and temperature dependence of the crystallinity of CAU-4. The molar ratio Al^{3+} : H_3BTB : benzoic acid : DMF = 7 : 14: 10 : 142 was used.

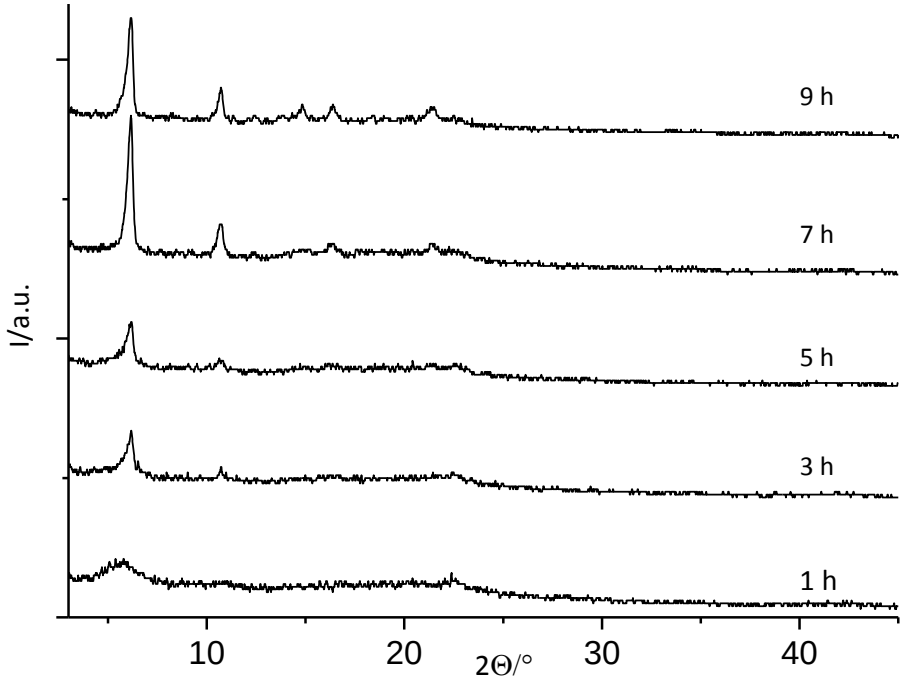

Figure S4: Ex-situ investigation of the formation of CAU-4 under stirring in pyrex glass tubes. The molar ratio Al^{3+} : H_3BTB : benzoic acid : DMF = 7 : 14: 10 : 142 was used

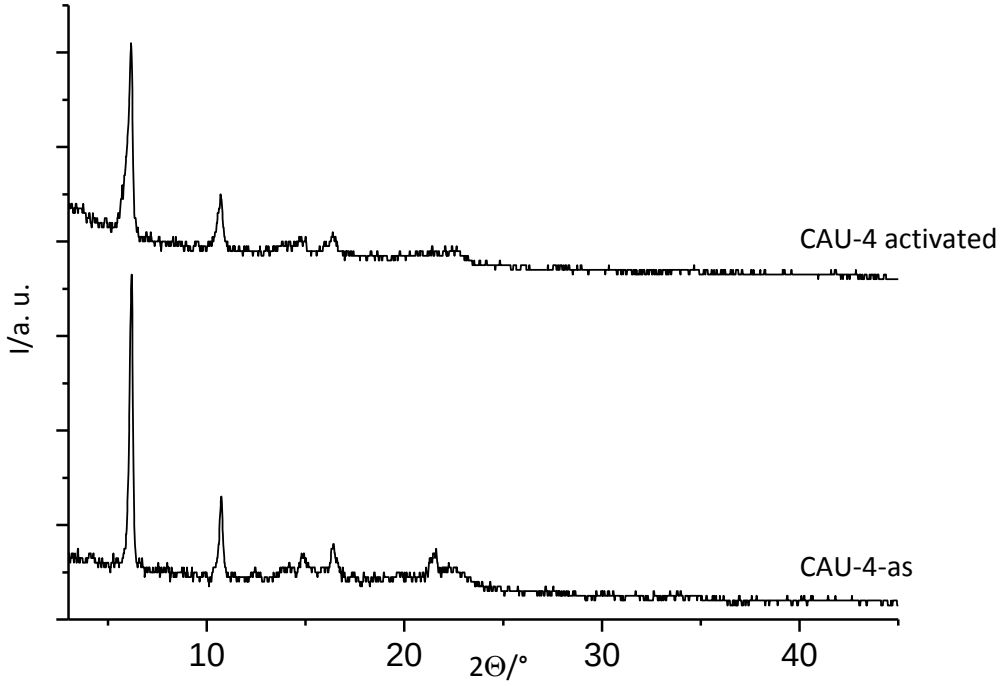

Figure S5: XRPD patterns of CAU-4-as and activated CAU-4.

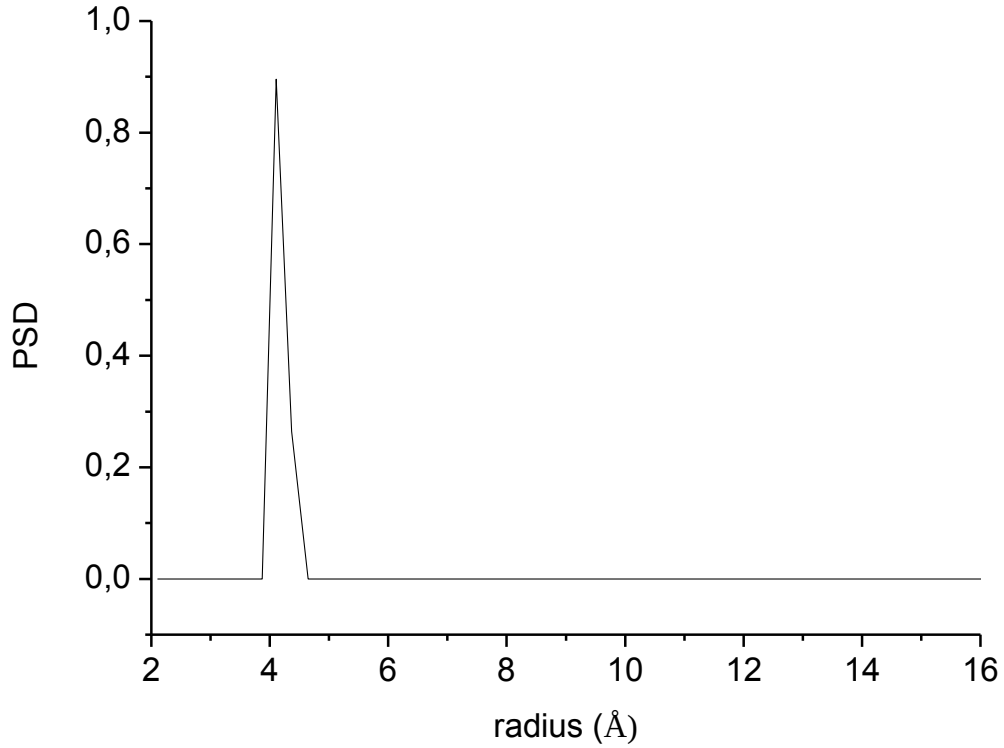

Figure S6: Pore Size Distribution determined by NLDFT/GCMC methods.

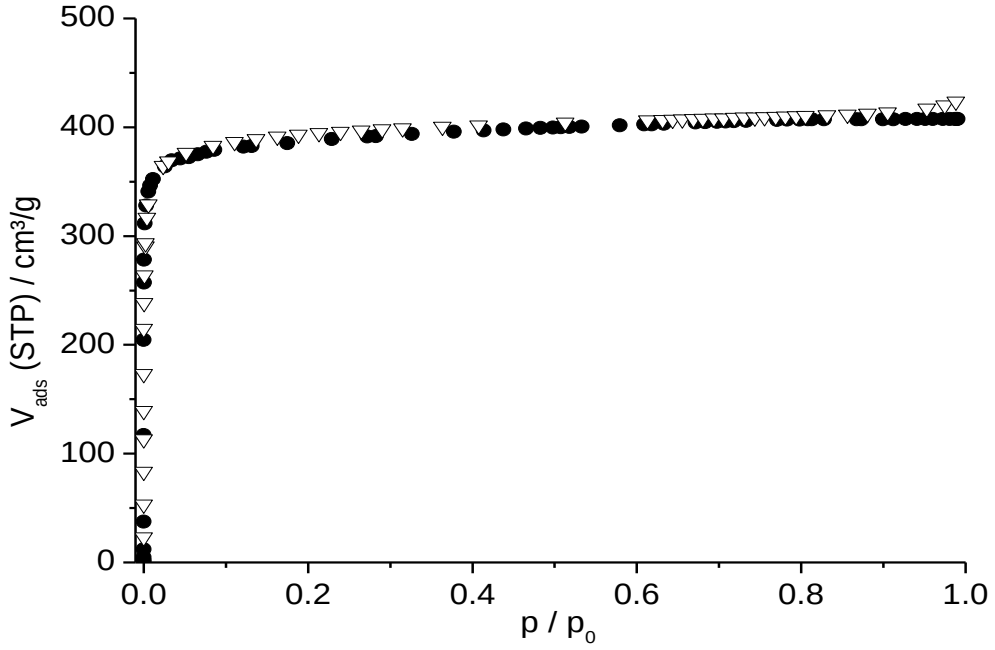

Figure S7: NLDFT/GCMC-fit in comparison with the experimental data (filled circles: simulation, empty triangles: experimental data).

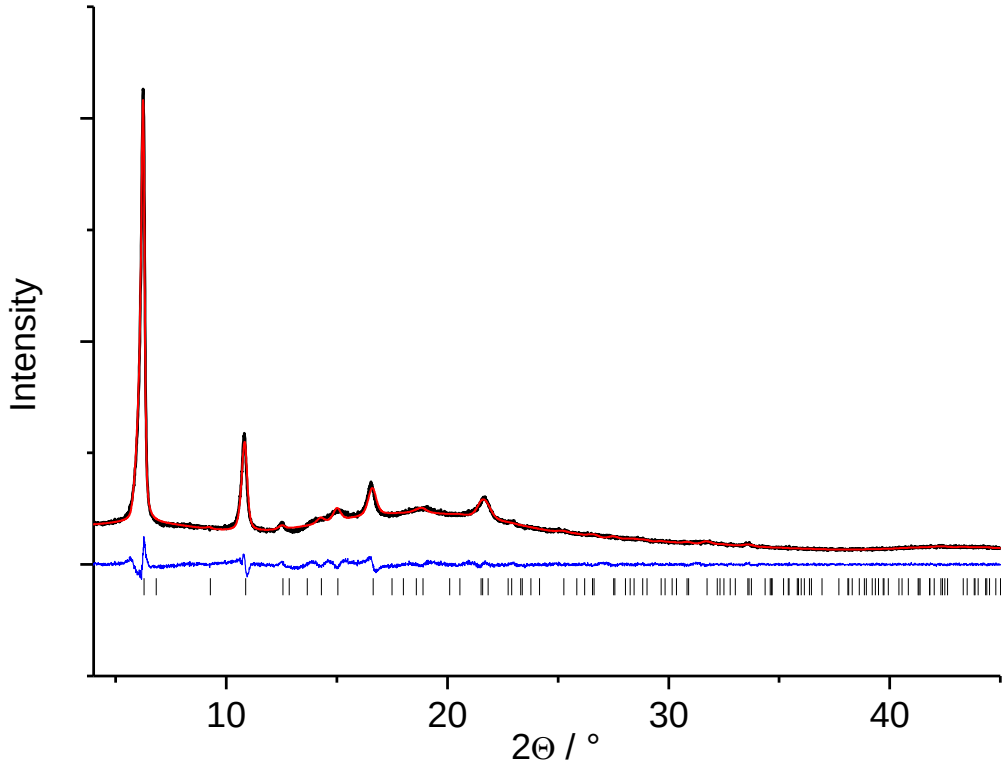

Figure S8: Pawley fit for CAU-4. The observed intensities are shown in black, the calculated intensities are shown in red. The difference curve is shown below in blue, vertical bars mark the Bragg positions.

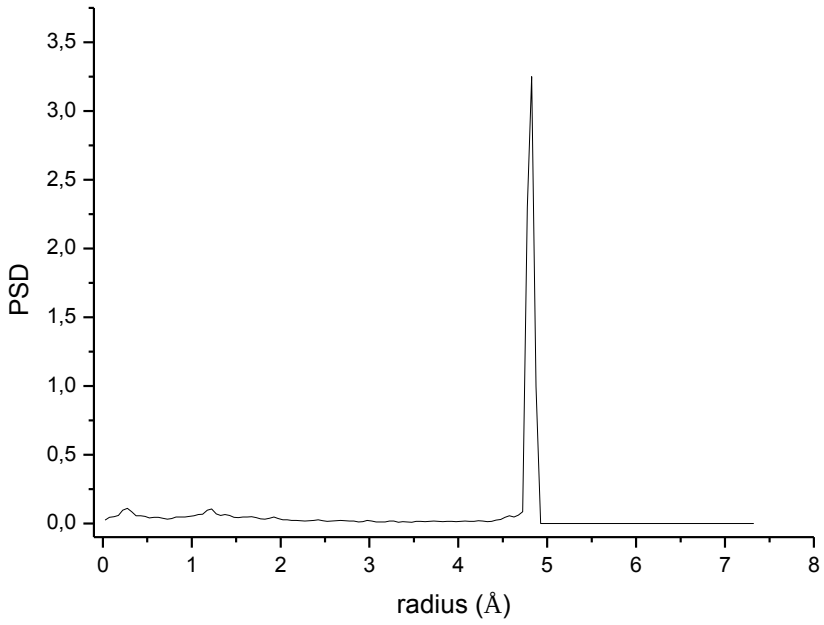

Figure S9: Simulated pore size distribution for the structural model of CAU-4.[39]

Tab S1: Atomic parameters of the structural model of CAU-4 obtained using Materials Studio software.

Atom	x/a	y/b	z/c	occ
O1	0.34341	0.57577	0.09223	1.00
O2	0.34341	0.57577	0.75890	1.00
O3	0.34341	0.57577	0.42556	1.00
C4	0.42787	0.45670	0.10846	1.00
C5	0.42787	0.45670	0.77513	1.00
C6	0.42787	0.45670	0.44179	1.00
H7	0.36414	0.42967	0.06221	1.00
H8	0.36414	0.42967	0.72887	1.00
H9	0.36414	0.42967	0.39554	1.00
C10	0.47770	0.40623	0.10896	1.00
C11	0.47770	0.40623	0.77563	1.00
C12	0.47770	0.40623	0.44230	1.00
H13	0.45107	0.34294	0.06204	1.00
H14	0.45107	0.34294	0.72871	1.00
H15	0.45107	0.34294	0.39538	1.00
C16	0.56700	0.28350	0.16667	1.00
H17	0.49021	0.24510	0.16667	1.00
C18	0.61586	0.23172	0.16667	1.00
C19	0.56188	0.12377	0.16667	1.00
C20	0.45947	0.91894	0.16667	1.00
C21	0.40566	0.81132	0.16667	1.00
C22	0.71650	0.28350	0.50000	1.00
H23	0.75490	0.24510	0.50000	1.00
C24	0.61586	0.38414	0.50000	1.00
C25	0.56188	0.43812	0.50000	1.00
C26	0.45947	0.54053	0.50000	1.00
C27	0.40566	0.59434	0.50000	1.00
Al28	0.33333	0.66667	0.00000	1.00
Al29	0.33333	0.66667	0.33333	1.00

7 ZIF-8 a Mixed-Linker ZIF Containing a Photoswitchable Phenylazo Group

Erschienen in:
Eur. J. Inorg. Chem., 5378–5383 (2011)

DOI: 10.1002/ejic.201100789

$[Zn(C_3H_3N_2)(C_3H_2N_2–N=N–C_6H_5)]$, a Mixed-Linker ZIF Containing a Photoswitchable Phenylazo Group

Stephan Bernt,[a] Mark Feyand,[a] Antje Modrow,[a] Julia Wack,[b] Jürgen Senker,[b] and Norbert Stock*[a]

Keywords: Metal-organic frameworks / Microporous materials / Structure elucidation / Optical switching / High-throughput methods

We report the synthesis and characterization of the new switchable Zn-based zeolitic imidazolate framework (ZIF) [Zn(Im)(aIm)] (**1**). The high-throughput investigation of the mixed linker system Zn^{2+}/imidazole (HIm)/2-phenylazoimidazole (HaIm)/DMF at 85 °C led to **1**, which is isostructural to ZIF-8 and crystallizes in a sodalite (SOD)-type structure. The preparation was also studied with microwave-assisted heating and ultrasound-assisted synthesis. The crystal structure was determined from single-crystal X-ray diffraction data. Although Im^- and aIm^- ions are present in a 1:1 molar ratio, no ordering of the 2-phenylazo group was observed. Incorporation of the Im^- and aIm^- linkers as an integral part of the framework structure was confirmed by elemental analysis, ^{13}C and ^{15}N MAS NMR, IR and Raman spectroscopy. In addition, the permanent porosity of **1** was demonstrated by N_2 sorption experiments and a specific surface area of S_{BET} = 580 $m^2 g^{-1}$ is observed. The photoswitching properties were investigated by UV/Vis spectroscopy as the *cis* and *trans* isomers exhibit different UV absorption spectra. Switching can be achieved by irradiation with UV light (λ = 355 nm), and back-switching using visible light (λ = 525 nm). Although changes in the UV/Vis spectra are detected, the switching process is only partially reversible.

Introduction

Metal-organic frameworks (MOFs) have gained increased attention in recent years due to their specific chemical and physical properties, such as pore size distribution, surface properties and chemical functionality.[1–4] They constitute a class of porous compounds that bridge the gap between microporous zeolites and ordered mesoporous silica-based materials.[5] MOFs are constructed from inorganic building units that are connected by organic linkers.[6] The choice of the linker molecule can vary the pore size, chemical functionality and physical properties such as sorption.[7,8] Functionality can be introduced directly by using functionalized linkers such as aminoterephthalic acid,[9,10] by coordination of guest molecules to unsaturated metal sites[11] or by postsynthetic covalent modification.[12,13]

Tian et al. have reported a new class of MOFs[14,15] called zeolitic imidazolate frameworks (ZIFs).[16] These compounds contain Zn^{2+} or Co^{2+} ions that are tetrahedrally surrounded by imidazolate linkers, which each bridge two Zn^{2+} or Co^{2+} ions. By employing imidazolate derivatives or mixtures thereof, various zeolitic topologies with numerous functional groups have been obtained.[17,18,19]

One goal in our current studies on MOFs is the introduction of functionality that can be modified by external stimuli. For example, sorption properties can be changed by ion exchange,[20] porosity can be switched by guest exchange[21] and the opening of pores can be triggered by gas adsorption.[22] In addition, guest-induced colour change[23] and temperature-induced cooperative spin-crossover behaviour in a 3D coordination polymer have been observed.[24] We are interested in the use of photoswitchable organic linker molecules for the synthesis of MOFs and have recently demonstrated the reversible switching of the mixed-linker MOF CAU-5, which contains azophenyl-4,4′-bipyridine and 2,6-naphthalenedicarboxylate ions.[25]

Aromatic molecules that contain azo groups, such as azobenzene or arylazoimidazole derivatives, are textbook examples for photoisomerization reactions.[26,27] In general the *trans* isomer of azobenzene is the thermodynamically more stable form[28,29] and exhibits two distinct absorption maxima. One with a lower intensity at λ_{max} = 444 nm ($n \rightarrow \pi^*$ transition) and another at λ_{max} = 316 nm ($\pi \rightarrow \pi^*$ transition). The *cis* isomer exhibits an absorption maximum at λ_{max} = 437 nm ($n \rightarrow \pi^*$ transition) and the $\pi \rightarrow \pi^*$ transition is shifted to λ_{max} = 270 nm. The *trans* isomer can be switched to the *cis* isomer by irradiation with UV light (ca. 365 nm). The switching process is schematically shown in

[a] Institut für Anorganische Chemie, Christian-Albrechts-Universität zu Kiel,
Max-Eyth-Straße 2, 24118 Kiel, Germany
Fax: +49-431-8801774
E-mail: stock@ac.uni-kiel.de
[b] Anorganische Chemie III, Universität Bayreuth,
Universitätsstr. 30, 95447 Bayreuth, Germany
Supporting information for this article is available on the WWW under http://dx.doi.org/10.1002/ejic.201100789.

Figure 1. This is clearly visible in the UV/Vis spectra as the intensity of the band at λ_{max} = 316 nm decreases and the intensity of the band at λ_{max} = 444 nm increases. Therefore, both isomers have distinct UV/Vis spectra and can easily be distinguished. The reversible back-switching can be achieved by heating or irradiation (ca. 440 nm).

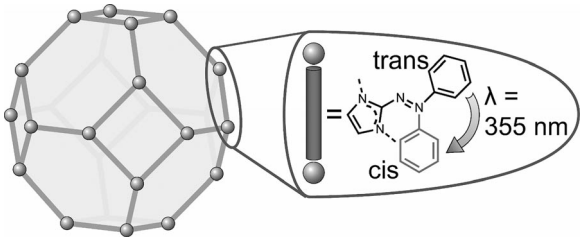

Figure 1. Schematic representation of the switching process.

MOFs containing azo groups are known in the literature.[25,30,31,32] In most of these structures the azo groups are an integral part of the linker molecules. Thus, switching is strongly hindered and has not been demonstrated to date. In contrast, reversible switching should be feasible for linker molecules with azo groups that protrude into the pores. The structure of a 1,1′-bis[(2-phenylazo)imidazol-1-yl]methane-based MOF that contains two phenylazo groups was recently published but no switching properties were shown.[33]

Here, we present the synthesis and detailed characterization of a switchable mixed-linker ZIF, [Zn(Im)(aIm)] (**1**), which contains imidazolate (Im^-) and 2-phenylazoimidazolate (aIm^-) ions.

Results and Discussion

The HaIm linker was synthesized from aniline and HIm[34] and purified by column chromatography (Figure 2). It was subsequently employed in the high-throughput investigation of the $Zn(NO_3)_2{\cdot}6H_2O$/HIm/HaIm/*N*,*N*-dimethylformamide (DMF) system. High-throughput (HT) methods allow the simultaneous investigation of different reaction parameters in solvothermal syntheses (Figure S1, Supporting Information) and are useful in the discovery of new phases and the subsequent synthesis optimization.[35] The discovery library was set up varying the solvent (DMF and methanol) and employing the molar ratios Zn^{2+}/HaIm/HIm = 1–3:1–4:0–3 (Figure 3 and Table S2). The reaction products were characterized by X-ray powder diffraction (XRPD) measurements and the results are shown in Figure 3.

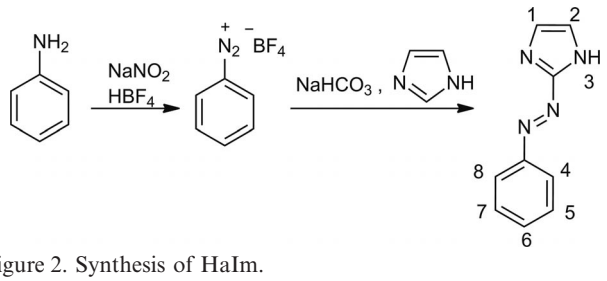

Figure 2. Synthesis of HaIm.

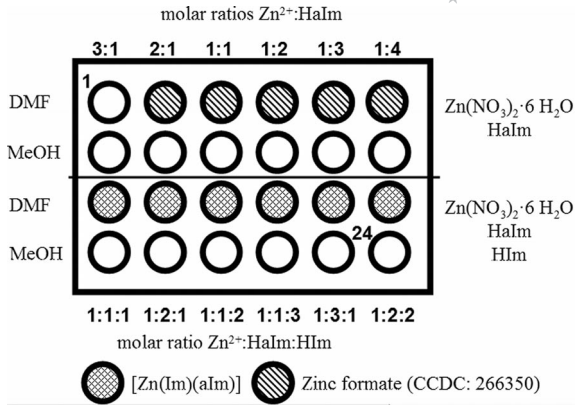

Figure 3. Discovery library of the high-throughput investigation. Empty circles denote clear solutions. The amounts used in each reactor are given in Table S2.

When HaIm was solely employed as the organic linker, reactions in methanol led exclusively to clear solutions, whereas reactions in DMF yielded zinc formate (CCDC-266350),[36] which is due to the partial hydrolysis of DMF. The mixed-linker system **1** was obtained with DMF and orange, air-stable single crystals (Figure S3) suitable for crystal structure determination were isolated from the mixture containing $Zn(NO_3)_2{\cdot}6H_2O$/HIm/HaIm/DMF in the molar ratio 1:3:1:97.

Compound **1** was also obtained using conventional heating (CH), microwave-assisted (MW) heating or ultrasound (US). The last two methods led to a substantially reduced reaction time (5 min). The three different synthetic methods resulted in phase-pure products. The CH synthesis led to large single crystals, whereas MW and US reactions yielded microcrystalline powders.

The orange, air stable compound was activated at 200 °C in vacuo for characterization by XRPD, thermogravimetric analysis (TGA), elemental analysis and IR, Raman, UV/Vis and solid-state NMR spectroscopy.

Compound **1** is isostructural to ZIF-8, which crystallizes in a sodalite (SOD)-type framework. The SOD structure has been observed in compounds that contain Zn^{2+} or Co^{2+} with 2-methyl-, 2-nitroimidazole, imidazole-2-carbaldehyde or benzimidazole (ZIF-7, -8, -9, -65, -67, -90, -91, -92).[19,37,38] Two linkers are incorporated in **1**: Im^- and aIm^-. Based on the single crystal data, no ordering of the phenylazo groups takes place. **1** is isostructural to ZIF-8 and crystallizes in the space group *I*23. Thus, we were able to establish the SOD framework as well as the position of the azo group during structure refinement (see experimental section for crystallographic data, Figures 4 and S4).

Indexing the XRPD pattern (Figures 5 and S5) unequivocally demonstrated the presence of only one crystalline phase. The lattice parameter [a = 17.009(6) Å] compares well with results from the single-crystal X-ray diffraction experiment [a = 17.023(2) Å].

The composition of activated **1** was established by elemental analysis and TGA. The observed and calculated C, H and N values compare well, and the TGA curve shows a

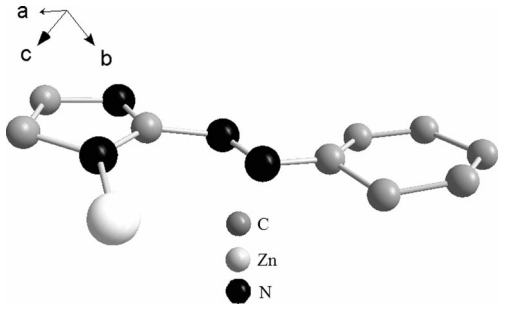

Figure 4. Asymmetric unit of **1**.

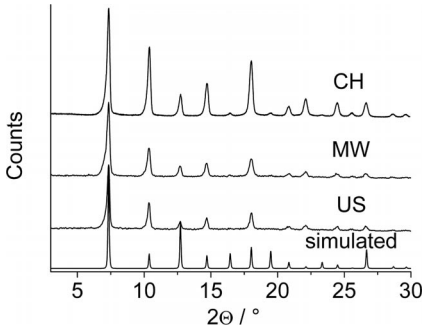

Figure 5. XRPD patterns of **1** compared to the simulated pattern, which is based on single crystal data.

weight loss of 73.14% for the CH and MW products and 66% for the US product between 340 and 700 °C (calcd. 73.54%) with ZnO as the final decomposition product (Figure S6). The incorporation of the aIm linker as part of the framework was confirmed by solid-state NMR and Raman spectroscopy (Figures 6, 7 and 8). The characteristic –N=N– asymmetric vibration band is located at 1441 cm^{-1} in the Raman spectrum, and characteristic aromatic =C–H stretching vibrations are observed between 3142 and 3047 cm^{-1}.

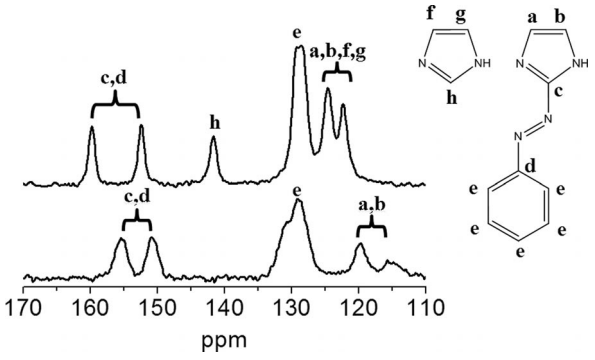

Figure 6. ^{13}C MAS NMR spectrum of **1** (top) and ^{13}C CP MAS NMR spectrum of pure HaIm (bottom).

The ^{13}C cross polarization (CP) magic angle spinning (MAS) NMR spectrum of the HaIm linker (Figure 6, bottom) shows five signals that can be clearly assigned. The signals of **1** can be assigned to both imidazolate linkers (Figures 6, top, and S8). Due to the deprotonation of HaIm and HIm, only two signals for a, b, f and g are observed,

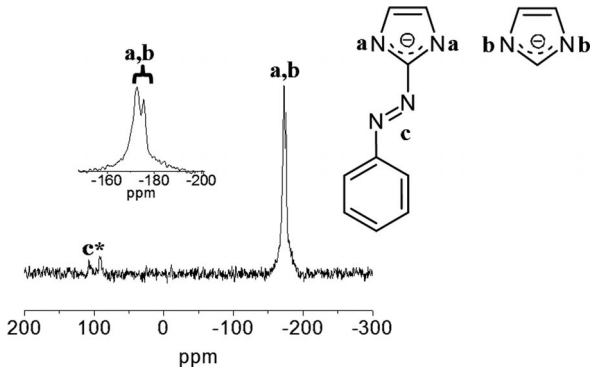

Figure 7. ^{15}N CP MAS NMR spectrum of **1**. The spinning sideband is marked with an asterisk.

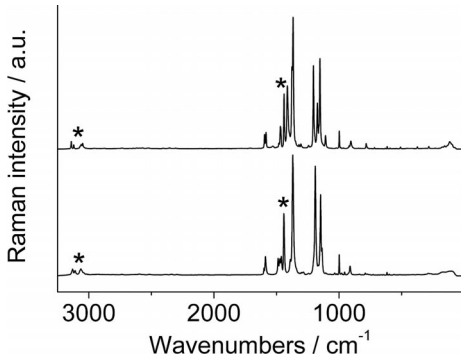

Figure 8. Raman spectra of **1** (bottom) and HaIm (top). The *trans* –N=N– vibration of **1** (1441 cm^{-1}) and the aromatic =C–H stretching vibrations (3142–3047 cm^{-1}) of the phenyl ring and the imidazolate ions are marked with asterisks.

which are shifted downfield. Two new signals (h and f, g) for Im^- are present.

The ^{15}N CP MAS NMR spectrum shows three signals that can be assigned to aIm and Im. The signal at 107 ppm is due to the nitrogen atoms of the azo group, and those at –172 and –175 ppm can be assigned to the nitrogen atoms of the imidazolate ions (Figure 7). A ^{15}N MAS NMR spectrum of the pure HaIm molecule cannot be recorded due to its very slow spin relaxation.

Although the aIm linker protrudes into the SOD cages, permanent porosity was demonstrated by N_2 sorption experiments at 77 K (Figure 9). The N_2 sorption isotherm of the activated sample (CH, 200 °C, 12 h, vacuum) shows a rapid increase at low p/p_0 values followed by a plateau, which is typical of type I isotherms. Evaluating the data with the Brunauer–Emmett–Teller (BET) equation resulted in a specific surface area (S_{BET}) of 580 $m^2 g^{-1}$ with a micropore volume (V_p) of 0.26 $cm^3 g^{-1}$. The N_2 sorption isotherms of the MW and US samples show similar behaviour but with slightly lower specific surface areas (US: S_{BET} = 544 $m^2 g^{-1}$, V_p = 0.25 $cm^3 g^{-1}$; MW: S_{BET} = 507 $m^2 g^{-1}$, V_p = 0.26 $cm^3 g^{-1}$). The specific surface area of **1** is significantly lower than ZIF-8 [S_{BET} = 1030 $m^2 g^{-1}$, V_p = 0.49 $cm^3 g^{-1}$ (calculated with PLATON as 0.54 $cm^3 g^{-1}$)], in which a methyl group protrudes into the SOD cages.[12,32]

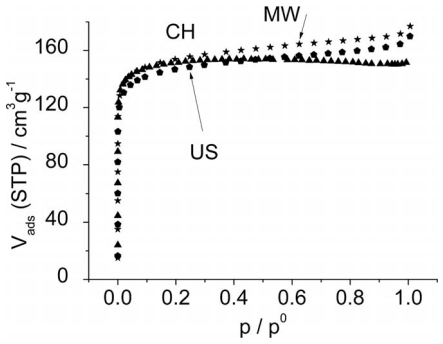

Figure 9. N_2 sorption isotherms of **1** (triangles: CH product, pentagons: US product, stars: MW product).

The switching properties of **1** were investigated using UV/Vis spectroscopy (Figures 10 and S9). Switching the azo groups from *trans* to *cis* configuration was accomplished by UV irradiation (355 nm, 150 W xenon lamp, 1 h). Back-switching was achieved by irradiation with visible light (525 nm, 150 W xenon lamp, 1 h) but not thermally (100 °C in air for 14 h). The switching of HaIm is hard to observe as fast thermal back-switching (*cis* to *trans*) takes place. In contrast, *N*-alkyl-substituted imidazolate derivatives exhibit much lower rate constants.[24,25]

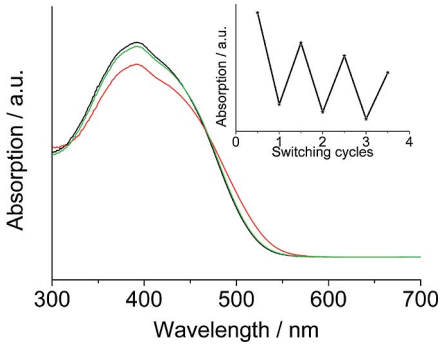

Figure 10. UV/Vis spectra of **1** before irradiation (black line), after irradiation at 355 nm for 1 h (red line) and after irradiation at 525 nm for 1 h (green line). Only one cycle is presented for clarity and more cycles are shown in Figure S9. The reversibility of the switching process (based on the π→π* absorption band at 392 nm) is shown in the inset. Every whole number represents a cycle of switching to the *cis* product and back-switching to the *trans* product.

Based on results reported for HaIm,[28,29] the bands can be assigned to the π→π* (392 nm) and *n*→π* transitions (450 nm). Upon irradiation with UV light, changes in the intensities of these bands are observed; the intensity of the π→π* band decreases, which is accompanied by an increase in the intensity of the *n*→π* band. Back-switching with visible light leads to an increase in the intensity of the π→π* band and a decrease in the intensity of the *n*→π* band. Although back-switching is not fully reversible, repeated switching and back-switching led to the corresponding changes in the UV/Vis spectra.

The partial reversibility could be due to a photobleaching effect or the steric hinderance of the switching process (confinement effect). Repeating this procedure led to the observation of the same behaviour. After three switching cycles the initial curve cannot be reached.

Conclusions

We have synthesized the porous, air-stable ZIF [Zn(Im)(aIm)] (**1**), which contains photoswitchable azophenyl groups. This compound was formed in a solvothermal reaction using a mixed-linker system. X-ray diffraction experiments demonstrated its structural relationship with ZIF-8, and the incorporation of aIm^- was proven by Raman and solid-state NMR spectroscopy. Although the large phenylazo group protrudes into the cage, **1** shows permanent prosity. UV/Vis switching experiments demonstrated the *cis–trans* isomerization and showed partial reversibility of the switching process.

Experimental Section

General: Synthetic procedures for HaIm and **1** and selected spectroscopic data are described in this section. All chemicals were used as obtained, unless stated otherwise.

2-Phenylazoimidazole (HaIm):[34] A mixture of aniline (10.6 mL, 116 mmol) and tetrafluoroboric acid (57.5 mL, 50%) was cooled to 0 °C. A solution of sodium nitrite in deionized water (18 mL) was slowly added. The precipitate was separated and washed with ethanol and diethyl ether to obtain benzenediazonium tetrafluoroborate (26.7 g).

Imidazole (6.8 g, 100 mmol) was added to a solution of sodium hydrogen carbonate (4.5 g, 53.6 mmol) in deionized water (45 mL). After homogenization of the solution, benzenediazonium tetrafluoroborate (19.2 g, 100 mmol) in deionized water (100 mL) was added. A brown precipitate formed immediately and the mixture was stirred for 30 min and allowed to stand for another 30 min. The precipitate was separated and washed with deionized water. The product was purified by column chromatography on basic aluminium oxide with ethyl acetate (+1% triethylamine) to give HaIm (9.8 g, 57%) as orange needles. $C_9H_8N_4$ (172.07): calcd. C 62.78, H 4.68, N 32.54; found C 62.54, H 4.64, N 32.61. ^{1}H NMR (200 MHz, [D$_6$]DMSO, 300 K, numbering according to Figure 2): δ = 7.38 [s, 2 H, 1,2-H], 7.6 [m, 3 H, 5,6,7-H], 7.85 [m, 2 H, 4,8-H], 13.2 [br. s, 1 H, 3-H] ppm. MS-EI: *m*/*z* (%) = 172.0 $[M]^+$ (77%), 144 (100), 117 (57), 105 (10); (CI) 173 $[M + H]^+$ (65%), 144 (100), 117 (48), 105 (11).

[Zn(Im)(aIm)] (1): Single crystals of **1** were formed from a solvothermal reaction in 2 mL Teflon® autoclaves in a high-throughput reactor (see Supporting Information). Solutions of $Zn(NO_3)_2{\cdot}6H_2O$ (193 μL, 0.3 M), HaIm (193 μL, 0.3 M) and imidazole (580 μL, 0.3 M) in DMF were mixed and additional DMF (433 μL) was added. The reaction mixture was heated at 85 °C in an isothermal oven for 96 h. The crystalline orange product was collected by filtration and washed with DMF (2 mL) and acetone (5 mL). The product was dried at room temperature in air for five days followed by 12 h at 200 °C in vacuo. $C_{12}H_{10}N_6Zn$ (302.03): calcd. C 47.46, H 3.32, N 27.68; found C 46.85, H 3.64, N 27.04.

Microwave-Assisted Synthesis of 1: In a typical reaction, solutions of $Zn(NO_3)_2{\cdot}6H_2O$ (193 μL, 0.3 M), HaIm (193 μL, 0.3 M) and imidazole (580 μL, 0.3 M) in DMF with additional DMF (433 μL)

were mixed in a 2 mL glass vial sealed with a Teflon®-coated cap. The reaction mixture was stirred and exposed to microwave irradiation for 5 min at 100 °C (Biotage Initiator Eight EXP). The orange solid was collected by centrifugation and redispersed in DMF (2 mL). The redispersing and centrifugation steps were repeated twice more with acetone. The product was dried at room temperature in air for five days followed by 12 h at 200 °C in vacuo. $C_{12}H_{10}N_6Zn$ (302.03): calcd. C 47.46, H 3.32, N 27.68; found C 46.86, H 3.32, N 27.42.

Ultrasound-Assisted Synthesis of 1: In a typical reaction, solutions of $Zn(NO_3)_2{\cdot}6H_2O$ (193 μL, 0.3 M), HaIm (193 μL, 0.3 M) and imidazole (580 μL, 0.3 M) in DMF with additional DMF (433 μL) were mixed in a 2 mL glass vial. The reaction mixture was sonicated using an ultrasonic generator with sonotrode (UP200S, Hielscher-Ultrasound Technology, 200 W, 24 kHz) for 10 min. The orange solid was collected by centrifugation and redispersed in DMF (2 mL). The redispersing and centrifugation steps were repeated twice more with acetone. The product was dried at room temperature in air for five days followed by 12 h at 200 °C in vacuo. $C_{12}H_{10}N_6Zn$ (302.03): calcd. C 47.46, H 3.32, N 27.68; found C 46.94, H 3.46, N 26.63.

Single-Crystal Structure Analysis: The crystal structure determination was performed with an imaging plate diffraction system (IPDS-1) with Mo-K_α radiation from STOE & CIE. The structure solution was carried out with direct methods using SHELXS-97 and structure refinements were performed against $|F|2$ using SHELXL-97. The structure solution in the space group $I43m$ (as found for ZIF-8) did not lead to a reasonable structure model. Choosing the subgroup $I23$ allowed the azophenyl rings to be assigned by a split model. The azophenyl rings were isotropically refined and the Zn and imidazolate ions were refined anisotropically. A numerical absorption correction was applied using X-Red (version 1.31) and X-Shape (version 2.11) of the program package X-Area. All non-hydrogen atoms were refined with anisotropic displacement parameters. Refinement of the structure led to a Flack parameter of 0.50(1). The model was therefore refined as a racemic twin using the TWIN and BASF command implemented in ShelXL. All aromatic C–H hydrogen atoms were positioned with idealized geometries and were refined with fixed isotropic displacement parameters [$U_{eq}(H) = -1.2{\cdot}U_{eq}(C)$] using a riding model with d_{C-H} = 0.93 Å. Details of the structure determination are given in Table 1.

Table 1. Selected crystal data and details of the structure determination of **1**.

Formula	$Zn_2C_{16}H_5N_{10}$
M [g mol^{-1}]	468.08
Crystal system	cubic
Space group	$I23$
a [Å]	17.023(2)
V [Å^3]	4933(1)
T [K]	293
Z	6
$D_{calcd.}$ [g cm^3]	0.945
μ [mm^{-1}]	1.472
Θ_{max} [°]	25.3
Measured reflections	19788
Unique reflections	1496
Reflections [$I_0 > 4\sigma(I_0)$]	1320
R_{int}	0.100
R_1 [all data]	0.1192
R_1 [$I_0 > 4\sigma(I_0)$]	0.1109
wR_2 [all data]	0.2717
wR_2 [$I_0 > 4\sigma(I_0)$]	0.2706
Gof	1.25
$\Delta\rho_{max}$, $\Delta\rho_{min}$ [e Å^{-3}]	0.51, –0.41

CCDC-836865 contains the supplementary crystallographic data for this paper. These data can be obtained free of charge from the Cambridge Crystallographic Data Centre via http://www.ccdc.cam.ac.uk/.

X-ray Powder Diffraction (XRPD): XRPD experiments were performed using an X′Pert Pro PANalytical Reflection Powder Diffraction System, with Cu-K_α radiation (λ = 154.0598 pm), equipped with a PIXcel semiconductor detector from PANalytical. Products of the HT investigations were characterized using a STOE HT X-ray powder diffractometer (Cu-K_α radiation) equipped with an image plate detector.

Supporting Information (see footnote on the first page of this article): Crystallographic data, HT methodology, the experimental data for the HT system where **1** was found and spectroscopic data.

Acknowledgments

We acknowledge funding from the Deutsche Forschungsgemeinschaft (DFG) (SFB 667, *Function by Switching*). We also thank Ursula Cornelissen for undertaking the Raman and UV/Vis measurements, Inke Jeß for the single crystal measurements, Adam Wutkowksi and Jan Boeckmann for the DTA/TG measurements and Dr. Frank Sönnichsen for recording solution ^{1}H NMR spectra.

[1] P. Horcajada, C. Serre, M. Vallet-Regí, M. Sebban, F. Taulelle, G. Férey, *Angew. Chem. Int. Ed.* **2006**, *45*, 5974–5978.
[2] M. Latroche, S. Surblé, C. Serre, C. Mellot-Daznieks, P. Llewellyn, J. Lee, J. Chang, S. Jhung, G. Férey, *Angew. Chem.* **2006**, *118*, 8407; *Angew. Chem. Int. Ed.* **2006**, *45*, 8227–8231.
[3] Z. Gu, X. Yan, *Angew. Chem.* **2010**, *122*, 1519–1522; *Angew. Chem. Int. Ed.* **2011**, *49*, 1477–1480.
[4] K. Tanabe, S. Cohen, *Angew. Chem.* **2009**, *121*, 7560; *Angew. Chem. Int. Ed.* **2009**, *48*, 7424–7427.
[5] G. Férey, *Chem. Soc. Rev.* **2008**, *37*, 191–214.
[6] S. James, *Chem. Soc. Rev.* **2003**, *32*, 276–288.
[7] Z. Wang, K. Tanabe, S. Cohen, *Chem. Eur. J.* **2010**, *16*, 212–217.
[8] A. Sonnauer, F. Hoffmann, M. Fröba, K. Kienle, V. Duppel, M. Thommes, C. Serre, G. Férey, N. Stock, *Angew. Chem.* **2009**, *121*, 3849; *Angew. Chem. Int. Ed.* **2009**, *48*, 3791–3794.
[9] S. Bauer, C. Serre, T. Devic, P. Horcajada, J. Marrot, G. Férey, N. Stock, *Inorg. Chem.* **2008**, *47*, 7568–7576.
[10] T. Ahnfeldt, D. Gunzelmann, T. Loiseau, D. Hirsemann, J. Senker, G. Férey, N. Stock, *Inorg. Chem.* **2009**, *48*, 3057.
[11] D.-Y. Hong, Y. K. Hwang, C. Serre, G. Férey, J.-S. Chang, *Adv. Funct. Mater.* **2009**, *19*, 1537–1552.
[12] K. K. Tanabe, S. M. Cohen, *Chem. Soc. Rev.* **2011**, *40*, 498–519.
[13] S. Bernt, V. Guillerm, C. Serre, N. Stock, *Chem. Commun.* **2011**, *47*, 2838–2840.
[14] Y.-Q. Tian, C.-X. Cai, Y. Ji, X.-Z. You, S.-M. Peng, G.-H. Lee, *Angew. Chem.* **2002**, *114*, 1442; *Angew. Chem. Int. Ed.* **2002**, *41*, 1384–1386.
[15] X.-C. Huang, Y.-Y. Lin, J.-P. Zhang, X.-M. Chen, *Angew. Chem.* **2006**, *118*, 1587; *Angew. Chem. Int. Ed.* **2006**, *45*, 1557–1559.
[16] A. Phan, C. Doonan, F. Uribe-Romo, C. Knobler, M. O'Keeffe, O. Yaghi, *Acc. Chem. Res.* **2010**, *43*, 58–67.
[17] R. Banerjee, A. Phan, B. Wang, C. Knobler, H. Furukawa, M. O'Keeffe, O. Yaghi, *Science* **2008**, *319*, 939–943.
[18] B. Wang, A. Côté, H. Furukawa, M. O'Keeffe, O. Yaghi, *Nature* **2008**, *453*, 207–211.

[19] W. Morris, C. Doonan, H. Furukawa, R. Banerjee, O. Yaghi, *J. Am. Chem. Soc.* **2008**, *130*, 12626–12627.
[20] S. Yang, X. Lin, A. J. Blake, G. Walker, P. Hubberstey, N. Champness, M. Schröder, *Nature Chem.* **2009**, *1*, 487–493.
[21] T. Maji, G. Mostafa, R. Matsuda, S. Kitagawa, *J. Am. Chem. Soc.* **2005**, *127*, 17152–17153.
[22] D. Tanaka, K. Nakagawa, M. Higuchi, S. Horike, Y. Kubota, T. Kobayashi, M. Takata, S. Kitagawa, *Angew. Chem.* **2008**, *120*, 3978; *Angew. Chem. Int. Ed.* **2008**, *47*, 3914–3918.
[23] S. Shimomura, R. Matsuda, T. Tsujino, T. Kawamura, S. Kitagawa, *J. Am. Chem. Soc.* **2006**, *128*, 16416–16417.
[24] V. Niel, J. Martinez-Agudo, M. Muñoz, A. Gaspar, J. Real, *Inorg. Chem.* **2001**, *40*, 3838–3839.
[25] A. Modrow, D. Zargarani, R. Herges, N. Stock, *Dalton Trans.* **2011**, *40*, 4217–4222.
[26] J. Griffiths, *Chem. Soc. Rev.* **1972**, *1*, 481–493.
[27] H. Dürr, H. Bouas-Laurent, in: *Photochromism*, Elsevier, Amsterdam **1990**, vol 1.
[28] J. Otsuki, K. Suwa, K. Narutaki, C. Sinha, I. Yoshikawa, K. Araki, *J. Phys. Chem. A* **2005**, *109*, 8064–8069.
[29] J. Otsuki, K. Suwa, K. Sarker, C. Sinha, *J. Phys. Chem. A* **2007**, *111*, 1403–1409.
[30] T. Reineke, M. Eddaoudi, D. Moler, M. O'Keeffe, O. Yaghi, *J. Am. Chem. Soc.* **2000**, *122*, 4843–4844.
[31] Z.-F. Chen, R.-G. Xiong, B. Abrahams, X.-Z. You, C.-M. Che, *J. Chem. Soc., Dalton Trans.* **2001**, *17*, 2453–2455.
[32] V. Zeleňák, Z. Vargová, M. Almáši, A. Zeleňáková, J. Kuchár, *Microporous Mesoporous Mater.* **2010**, *129*, 354–359.
[33] C.-M. Jun, Z. Zhu, Z.-F. Chen, Y.-J. Hu, X.-G. Meng, *Cryst. Growth Des.* **2010**, *10*, 2054–2056.
[34] R. Verma, M. Aggarwal, M. Bansal, I. Kaur, *Med. Chem. Res.* **2007**, *15*, 483–491.
[35] N. Stock, *Microporous Mesoporous Mater.* **2010**, *129*, 287–295.
[36] H. F. Clausen, R. D. Poulsen, A. D. Bond, M.-A. S. Chevallier, B. Brummerstedt Iversen, *J. Solid State Chem.* **2005**, *178*, 3343–3351.
[37] K. Park, Z. Ni, A. Côté, J. Choi, R. Huang, F. Uribe-Romo, H. Chae, M. O'Keeffe, O. Yaghi, *Proc. Natl. Acad. Sci. USA* **2006**, *103*, 10186–10191.
[38] A. Phan, C. Doonan, F. Uribe-Romo, C. Knobler, M. O'Keeffe, O. Yaghi, *Acc. Chem. Res.* **2010**, *43*, 58–67.

Received: July 28, 2011
Published Online: October 26, 2011

Eur. J. Inorg. Chem. **2011** · © WILEY-VCH Verlag GmbH & Co. KGaA, 69451 Weinheim, 2011 · ISSN 1434–1948

SUPPORTING INFORMATION

DOI: 10.1002/ejic.201100789
Title: [$Zn(C_3H_3N_2)(C_3H_2N_2–N=N–C_6H_5)$], a Mixed-Linker ZIF Containing a Photoswitchable Phenylazo Group
Author(s): Stephan Bernt, Mark Feyand, Antje Modrow, Julia Wack, Jürgen Senker, Norbert Stock*

(S1) High-throughput synthesis

[Zn(Im)(aIm)] was discovered using our high-throughput (HT) methodology.[1] Our high-throughput reactors are based on the 96 well plate format and contain 24 or 48 teflon inserts. Thus a total volume of 200 µL (48 reactor block) and 2 mL (24 reactor block) is used.

For the systematic investigation a 24 reactor block was used. Methanol and DMF were chosen since numerous ZIFs have been synthesized in these solvents. A 0.3 M solution of imidazole, a 0.3 M solution of 2-phenylazoimidazole and a 0.3 M solution of $Zn(NO_3)_2 \cdot 6\ H_2O$ in DMF and methanol were used as stock solutions. The exact amounts of starting materials are given in table S2. The reactants were mixed without stirring in the following order: 2-phenylazoimidazole, imidazole, $Zn(NO_3)_2 \cdot 6\ H_2O$ and solvent. The reaction block was covered with a teflon foil, sealed with the top plate of the reactor and heated in an oven at 85 °C for 96 h. A cooling ramp of 12 h was chosen to form highly crystalline material. After the reaction the crystals were filtered, washed with 2 mL DMF, twice with 5 mL acetone and dried at 200 °C in vacuo. The samples were automatically characterized using a STOE HT X-ray powder diffractometer (Cu $K_{\alpha 1}$ radiation) equipped with an image plate detector.

[1] N. Stock, *Miroporous Mesoporous Mater.* **2010**, *129*, 287-295.

(S2) Discovery library where 1 was found

The following stock solutions were prepared:

$Zn(NO_3)_2 \cdot 6\ H_2O$: 0.3 M in DMF / MeOH

2-Phenylazoimidazole: 0.3 M in DMF / MeOH

Imidazole: 0.3 M in DMF / MeOH

These solutions were directly used in the HT synthesis. The exact amounts are given in table S2:

Table S2: Amounts of reactants used in the high-throughput study (**1** = title compound).

	molar ratios			dispensed amounts (µL)					
#	$Zn(NO_3)_2 \cdot 6H_2O$	HaIm	HIm	$Zn(NO_3)_2 \cdot 6\ H_2O$	HaIm	Him	DMF	EtOH	result
1	3	1	-	656	219	-	525	-	clear solution
2	2	1	-	545.5	274	-	580.5	-	Zn-formate*
3	1	1	-	438	438	-	524.5	-	Zn-formate*
4	1	2	-	328	657	-	415	-	Zn-formate*
5	1	3	-	284.5	854	-	261.5	-	Zn-formate*
6	1	4	-	219	876	-	305	-	Zn-formate*
7	3	1	-	656	219	-	-	525	clear solution
8	2	1	-	545.5	274	-	-	580.5	clear solution
9	1	1	-	438	438	-	-	524.5	clear solution
10	1	2	-	328	657	-	-	415	clear solution
11	1	3	-	284.5	854	-	-	261.5	clear solution
12	1	4	-	219	876	-	-	305	clear solution
13	1	1	1	193.3	193.3	193.3	820	-	**1**
14	1	2	1	193.3	386.7	193.3	626.7	-	**1**
15	1	1	2	193.3	193.3	386.7	626.7	-	**1**
16	1	1	3	193.3	193.3	580	433.7	-	**1**
17	1	3	1	193.3	580	193.3	433.7	-	**1**
18	1	2	2	193.3	386.7	386.7	433.7	-	**1**
19	1	1	1	193.3	193.3	193.3	-	820	clear solution
20	1	2	1	193.3	386.7	193.3	-	626.7	clear solution
21	1	1	2	193.3	193.3	386.7	-	626.7	clear solution
22	1	1	3	193.3	193.3	580	-	433.7	clear solution
23	1	3	1	193.3	580	193.3	-	433.7	clear solution
24	1	2	2	193.3	386.7	386.7	-	433.7	clear solution

* Zn-formate was obtained as described in the literature[2] (CCDC: 266350).

[2] H. F. Clausen, R. D. Poulsen, A. D. Bond, M.-A. S. Chevallier, B. Brummerstedt Iversen, *J. Solid State Chem.* **2005**, *178*, 3343-3351.

(S3) SEM-picture of single crystals of the title compound

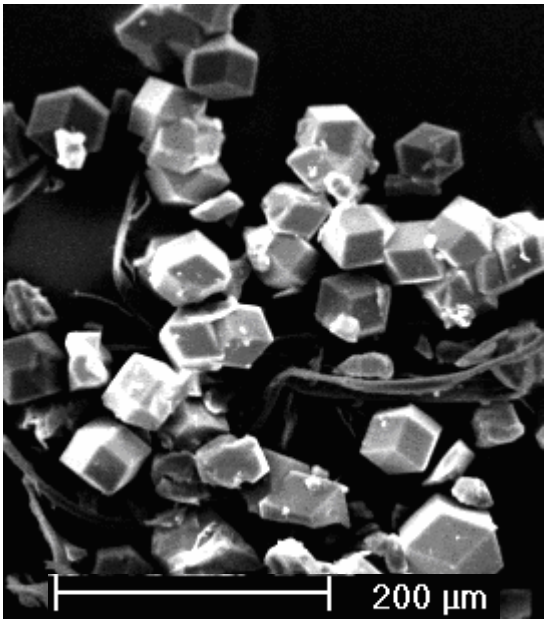

Fig. S3. SEM image of single crystals of the compound Zn(Im)(aIm).

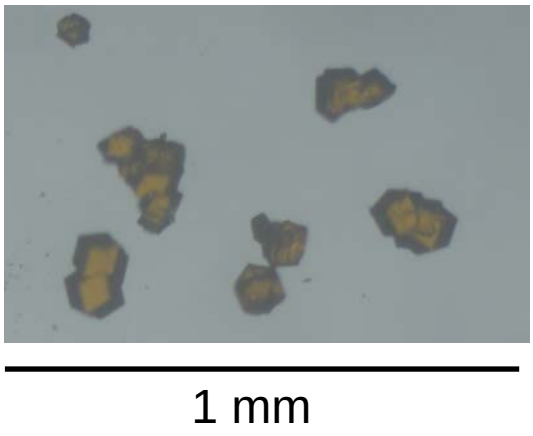

Fig. S3b. Optical micrograph of the title compound.

(S4) Crystal structure of [Zn(Im)(aIm)]

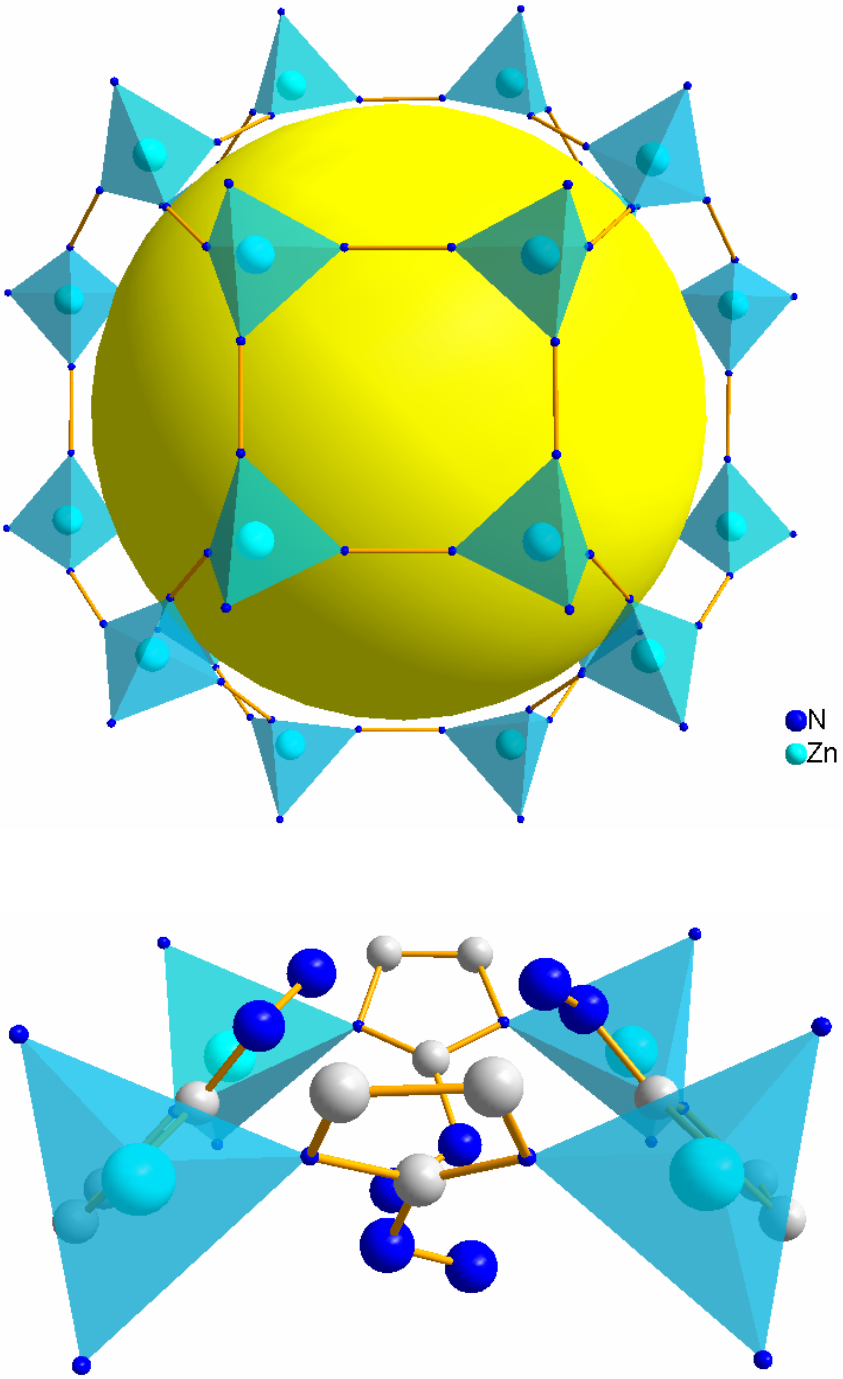

Fig. S4a. Top: SOD cage of [Zn(Im)(aIm)] with a view at a four ring which is composed of four Zn^{2+} and four imidazolate ions (for clarity the imidazolate ions are replaced by a line between the two coordinating N atoms); bottom: four ring with imidazolate linkers. Due to the statistical disorder only every second imidazolate ion is connected to the azophenyl group. Phenyl rings are omitted for clarity.

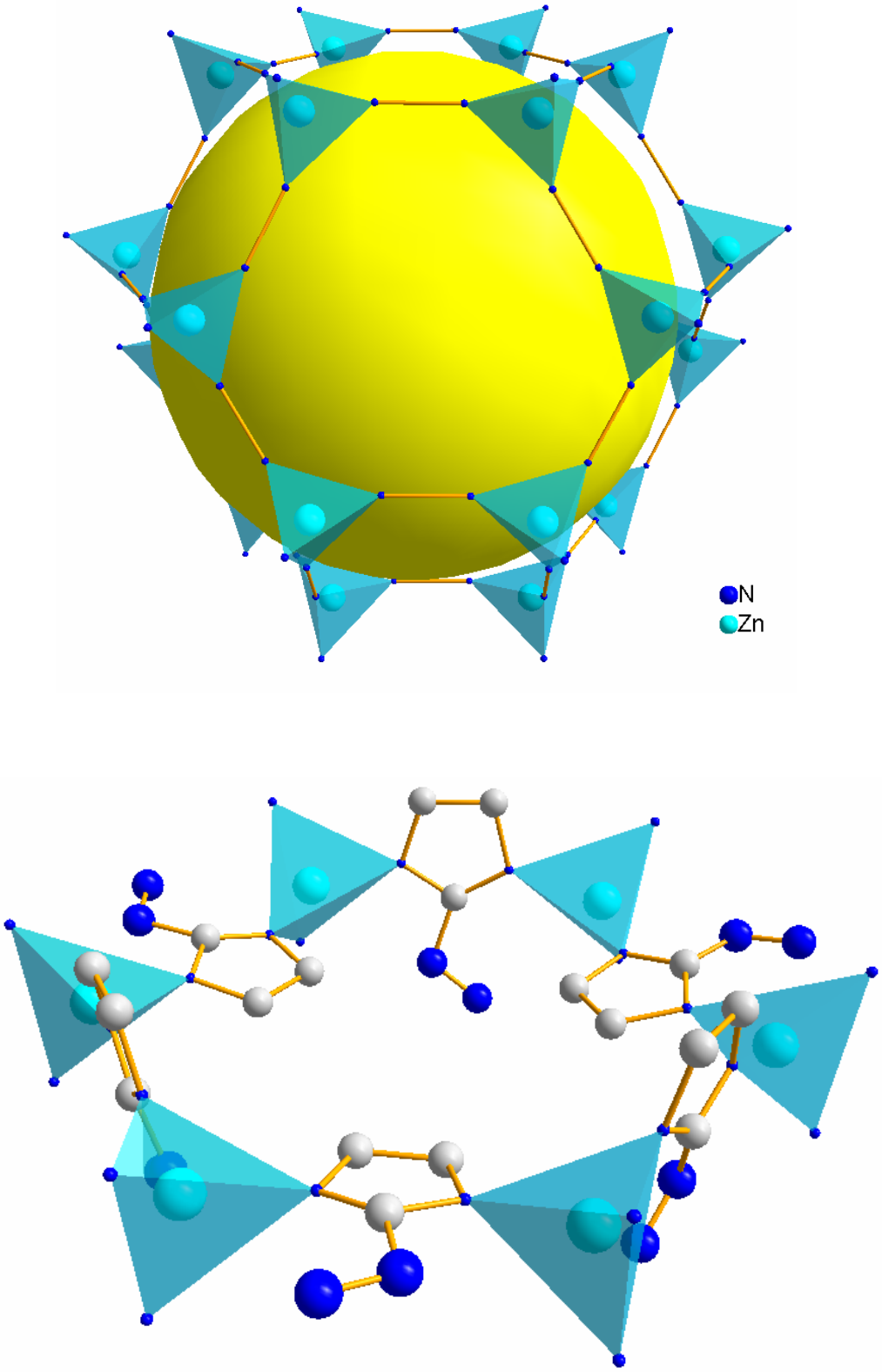

Fig. S4b. Top: SOD cage of [Zn(Im)(aIm)] with a view at a six ring which is composed of six Zn^{2+} and six imidazolate ions (for clarity the imidazolate ions are replaced by a line between the two coordinating N atoms); bottom: six ring with imidazolate linkers. Due to the statistical disorder only every second imidazolate ion is connected to the azophenyl group. Phenyl rings are omitted for clarity.

(S5) Crystallographic data from the XRPD

X-ray powder diffraction data for indexing were collected in reflection mode employing a X'Pert Pro PANalytical diffractometer with Cu $K_{\alpha 1}$ radiation (λ = 1.5418) equipped with a PIXcel detector.

Wavelength: 1.540598

Number of accepted peaks: 31

Symmetry: Cubic I

Refined cell parameters:

Cell_A: 17.009(6)

Cell_Volume: 4921.1(28)

Number of single indexed lines: 31

Number of unindexed lines: 0

2Theta zeropoint: 0.024(11)

Final 2Theta window: 0.0600

N	2Th[obs]	H	K	L	2Th[calc]	obs-calc	Int.	d[obs]	d[calc]
1	7.343	1	1	0	7.344	-0.0013	100.0	12.0295	12.0274
2	10.391	2	0	0	10.393	-0.0026	36.5	8.5068	8.5046
3	12.738	2	1	1	12.738	0.0006	11.4	6.9437	6.9440
4	14.719	2	2	0	14.719	-0.0001	16.6	6.0137	6.0137
5	16.458	3	1	0	16.467	-0.0089	3.5	5.3817	5.3788
6	18.050	2	2	2	18.052	-0.0018	23.1	4.9106	4.9102
7	19.508	3	2	1	19.511	-0.0038	3.8	4.5468	4.5459
8	20.882	4	0	0	20.873	0.0089	5.9	4.2505	4.2523
9	22.154	3	3	0	22.155	-0.0014	7.5	4.0094	4.0091
10	23.419	4	2	0	23.370	0.0490	2.9	3.7955	3.8034
11	24.521	3	3	2	24.528	-0.0064	6.3	3.6273	3.6264
12	25.606	4	2	2	25.637	-0.0303	3.2	3.4760	3.4720
13	26.698	5	1	0	26.702	-0.0042	5.9	3.3363	3.3358

14	28.722	5	2	1	28.724	-0.0020	2.3	3.1057	3.1055
15	29.672	4	4	0	29.687	-0.0151	2.4	3.0083	3.0068
16	30.600	5	3	0	30.623	-0.0228	2.8	2.9192	2.9171
17	31.528	6	0	0	31.534	-0.0053	2.6	2.8353	2.8349
18	32.434	6	1	1	32.421	0.0131	3.2	2.7582	2.7593
19	33.340	6	2	0	33.287	0.0526	1.7	2.6853	2.6894
20	34.158	5	4	1	34.134	0.0233	1.8	2.6229	2.6246
21	34.953	6	2	2	34.963	-0.0101	3.0	2.5650	2.5642
22	36.585	4	4	4	36.572	0.0134	2.1	2.4542	2.4551
23	37.314	7	1	0	37.353	-0.0391	1.9	2.4079	2.4055
24	38.861	7	2	1	38.876	-0.0154	1.4	2.3156	2.3147
25	41.800	6	5	1	41.782	0.0180	1.6	2.1593	2.1602
26	43.170	8	1	1	43.174	-0.0041	1.8	2.0939	2.0937
27	44.562	6	5	3	44.531	0.0310	1.6	2.0317	2.0330
28	45.821	7	5	0	45.856	-0.0345	1.6	1.9787	1.9773
29	49.644	9	2	1	49.666	-0.0219	1.4	1.8349	1.8342
30	50.910	9	3	0	50.888	0.0215	1.4	1.7922	1.7929
31	56.124	10	2	2	56.151	-0.0268	1.1	1.6374	1.6367

Average delta(2Theta) = 0.016

Maximum delta(2Theta) = 0.053 (peak 19) = 3.3 * average

Figure of Merit F(30) = 44.2 (0.015, 44)

Durbin-Watson serial correlation = 2.056 (not significant)

Sqrt[sum(w * delta(q)^2) / (Nobs - Nvar)] = 0.00016027

(S6) TG analysis of [Zn(Im)(aIm)]

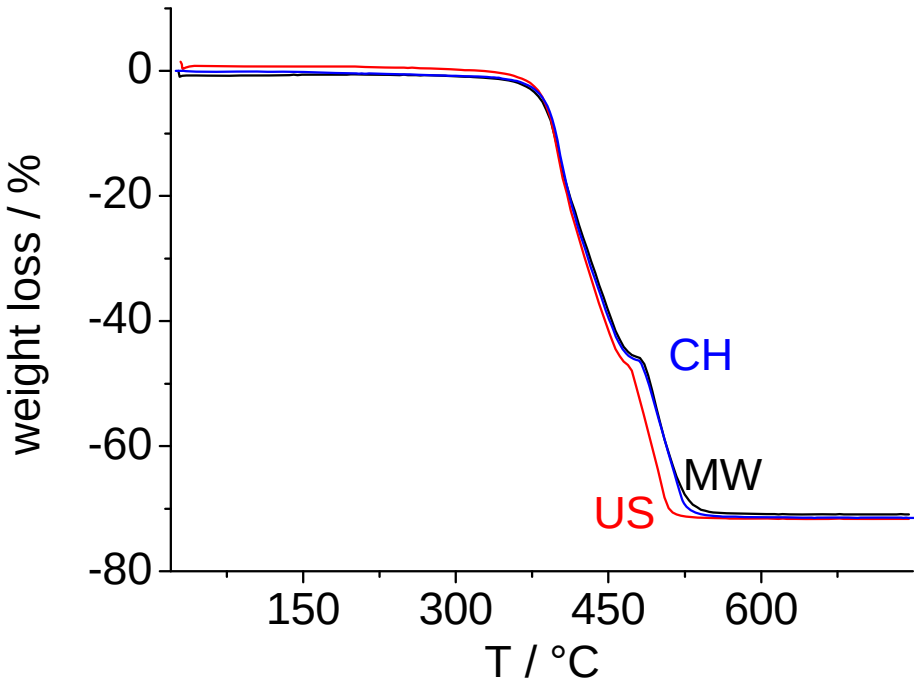

Fig. S6. The TG analyses of the samples synthesized by conventional heating (CH, blue), microwave-assisted heating (MW, black) and by applying ultrasound (US, red) demonstrate the high thermal stability of the title compound. The mass losses of 72.14% for CH, 71.68% for MW and 71.25% for US are in good agreement with the calculated value (73.05 %) where only ZnO remains as decomposition product (verified by X-ray powder diffraction). The difference between the graphs for US (above 400 °C) and CH/MW are due to differences in the particle sizes of the samples.

(S7) FTIR spectrum of the title compound

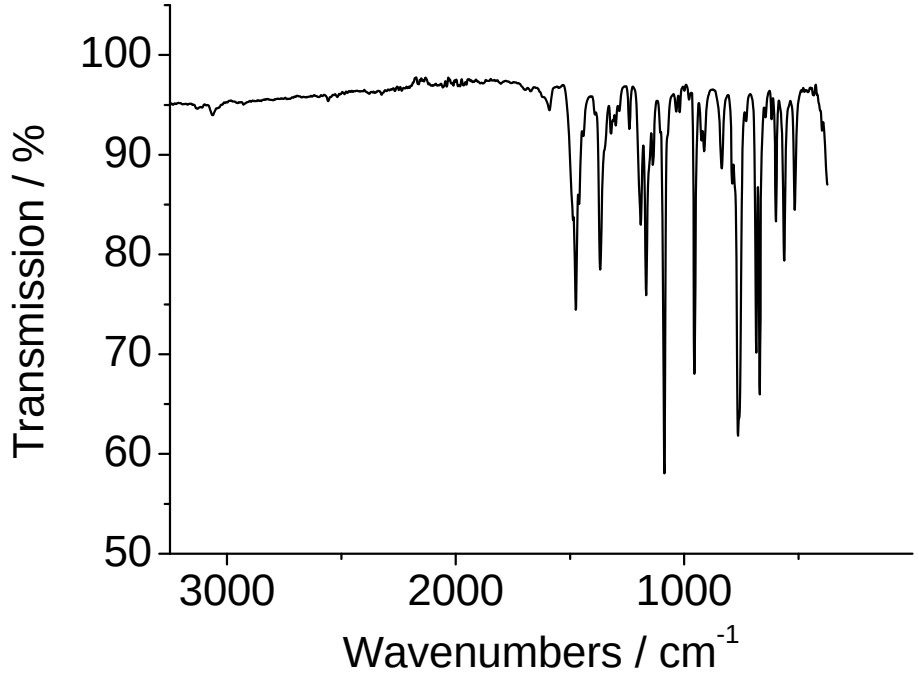

Fig. S7. FTIR spectrum of [Zn(Im)(aIm)].

The signal at 3057 cm^{-1} can be assigned to aromatic =C-H stretching vibrations. Due to the reflection geometry in the measurement (ATR unit), the =C-H stretching signal is very weak. The ring –C=C- stretching vibrations of the phenylgroup are of variable intensity and occur in the region of 1625 cm^{-1} and 1430 cm^{-1}. The ring –C=C- and –C=N- stretching vibrations of the imidazolate groups occur in the region of 1670 cm^{-1} and 1320 cm^{-1}.

(S8) ^{13}C-MAS NMR spectrum with integrals

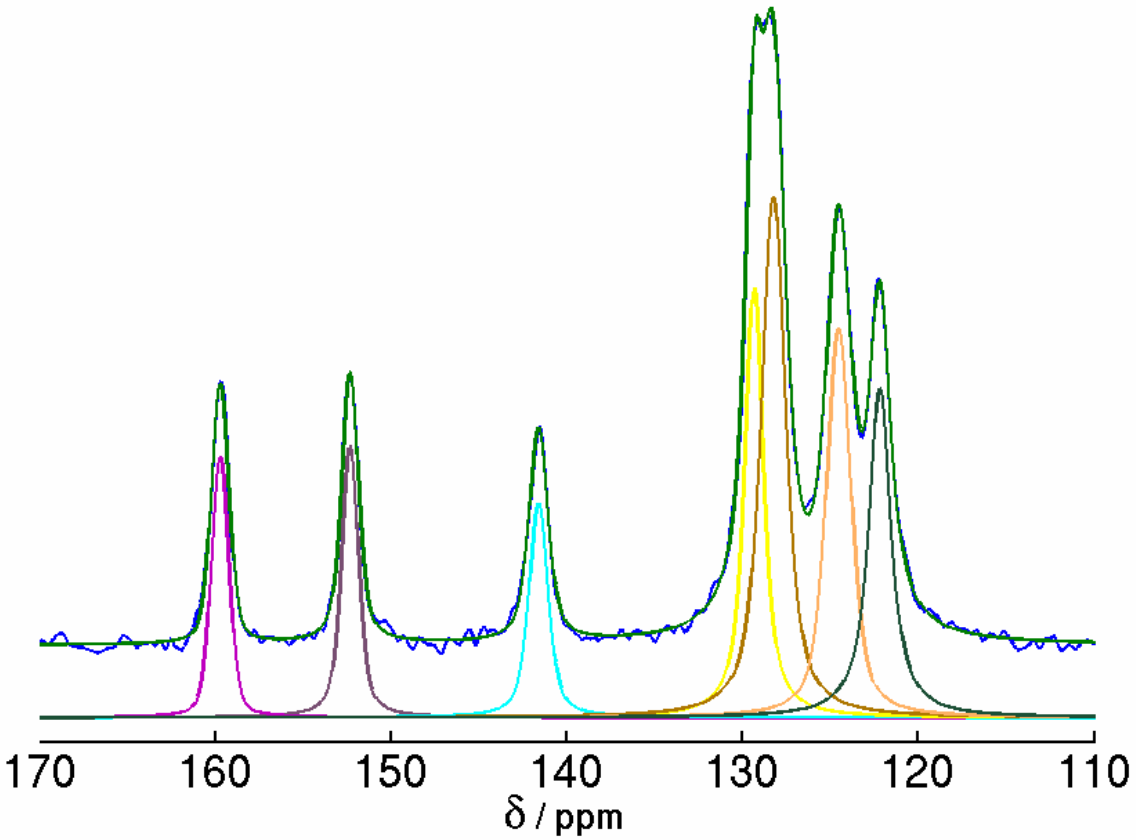

Fig. S8. ^{13}C-MAS-NMR (see also Fig. 3 for assignments) spectrum of the title compound [Zn(Im)(aIm)]. The corresponding integrals are given in table S8.

Table S8. Expected and observed (calculated from the ^{13}C-MAS spectrum) integrals of the ^{13}C-MAS spectrum.

signal	expected integral (amount of C atoms)	observed integral (amount of C atoms)
159.6	1	1.0
152.3	1	1.1
141.5	1	1
129.1	2	2.1
128.5	3	3.3
124.5	2	2.4
122.2	2	2.0

(S9) UV/Vis spectra of the (*trans-cis* and *cis-trans*) isomerization of all cycles

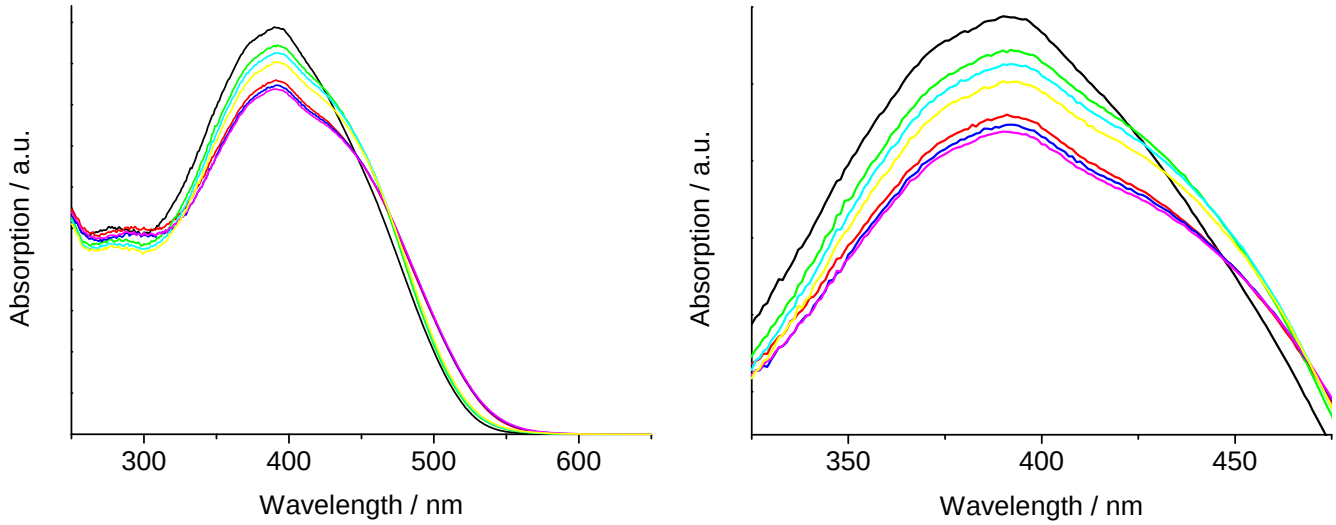

Fig. S9. Results of the UV/vis switching experiments of [Zn(Im)(aIm)]. Left UV/vis spectra recorded from 250–600 nm; right: detailed view from 325–475 nm ($\pi \rightarrow \pi^*$ transition of the *trans* isomer at 392 nm). The assignments of the graphs are given in the table below.

color	isomer	switching cycle
black (initial curve)	-	-
purple	*cis*	1 (355 nm irradiation)
green	*trans*	1 (525 nm irradiation)
blue	*cis*	2 (355 nm irradiation)
turquoise	*trans*	2 (525 nm irradiation)
red	*cis*	3 (355 nm irradiation)
yellow	*trans*	3 (525 nm irradiation)

8 Controlled modification of the inorganic and organic bricks in an Al-based MOF by direct and post-synthetic synthesis routes

Erschienen in:
CrystEngComm **14**, 4126–4136 (2012)

CrystEngComm

Dynamic Article Links

Cite this: *CrystEngComm*, 2012, **14**, 4126–4136

www.rsc.org/crystengcomm

PAPER

Controlled modification of the inorganic and organic bricks in an Al-based MOF by direct and post-synthetic synthesis routes†

Tim Ahnfeldt,[a] Daniel Gunzelmann,[b] Julia Wack,[b] Jürgen Senker*[b] and Norbert Stock*[a]

Received 2nd December 2011, Accepted 26th January 2012
DOI: 10.1039/c2ce06620c

Four new porous CAU-1 derivatives CAU-1–NH_2 ($[Al_4(OH)_2(OCH_3)_4(BDC–NH_2)_3]\cdot xH_2O$, $BDC–NH_2^{2-}$ = aminoterephthalate), CAU-1–NH_2(OH) ($[Al_4(OH)_6(BDC–NH_2)_3]\cdot xH_2O$), CAU-1–$NHCH_3$ ($[Al_4(OH)_2(OCH_3)_4(BDC–NHCH_3)_3]\cdot xH_2O$) and CAU-1–$NHCOCH_3$ ($[Al_4(OH)_2(OCH_3)_4(BDC–NHCOCH_3)_3]\cdot xH_2O$) all containing an octameric $[Al_8(OH)_{4+y}(OCH_3)_{8-y}]^{12+}$ cluster, with y = 0–8, have been obtained by MW-assisted synthesis and post-synthetic modification. The inorganic as well as the organic unit can be modified. Heteronuclear $^1H–^{15}N$, $^1H–^{13}C$ and homonuclear $^1H–^1H$ connectivities determined by solid-state NMR spectroscopy prove the methylation of the NH_2 groups when conventional heating is used. Varying reaction times and temperatures allow controlling the degree of methylation of the amino groups. Short reaction times lead to non-methylated CAU-1 (CAU-1–NH_2), while longer reaction times result in CAU-1–$NHCH_3$. CAU-1–NH_2 can be modified chemically by using acetic anhydride, and the acetamide derivative CAU-1–$NHCOCH_3$ is obtained. Thermal treatment permits us to change the composition of the Al-containing unit. Methoxy groups are gradually exchanged by hydroxy groups at 190 °C in air. Solid-state NMR spectra unequivocally demonstrate the presence of the amino groups, as well as the successful post-synthetic modification. Furthermore $^1H–^1H$ correlation spectra using homonuclear decoupling allow the orientation of the $NHCOCH_3$ groups within the pores to be unravelled. The influence of time and temperature on the synthesis of CAU-1 was studied by X-ray powder diffraction, elemental analyses, and ^1H liquid-state NMR and IR spectroscopy.

1. Introduction

Metal–organic frameworks (MOFs) have evolved over the past decade into the most investigated class of porous materials.[1] Based on their high thermal stability, well defined pore systems and high porosity, some MOFs are suitable for a number of potential applications, such as controlled drug release,[2] storage and separation of gases,[3] as catalysts[4] and in sensing devices.[5] For most of the applications very low framework density and/or additional functional groups in the pores are required. To achieve a low framework density, MOFs which are based on light metals such as magnesium or aluminium are promising.[6] In the last decade aluminium-containing MOFs (Al-MOFs) have been investigated intensively.[7] Al-based MOFs are known for their high thermal and chemical stability, non-toxicity and large apparent specific BET surface areas.[8] Al-MOFs can be synthesised using common linker molecules, such as terephthalic acid,[9] naphthalenedicarboxylic acid[10] and trimesic acid.[11] Starting from the terephthalic acid linker additional functional groups, like hydroxy-, nitro-, chloro-, bromo-, and methyl-groups, were successfully incorporated into Al-MOFs *via* isoreticular synthesis strategies.[12] The modified frameworks show often different sorption[13] and improved catalytic properties,[14] which are based on different host–guest interactions. The most common functional group in Al-MOFs is the amino group. The amino group is chemically inert in most solvents and does not participate in the coordination chemistry of the metal ions. Furthermore, the amino group allows post-synthetic modification reactions on the pore surfaces such as nucleophilic substitution, acid–base reactions or condensation reactions.[15] Modified linker molecules can change properties like the accessibility of the pores and thus sorption behaviour depending on their orientation within the pores. The orientation of linker residues, however, is difficult to determine and mostly unknown. Solid-state NMR spectroscopy is a powerful tool for this task. It enables the determination of distances, angles and orientation correlations. Based on the aminoterephthalic acid linker the amino group could be successfully incorporated into the

[a]*Institut für Anorganische Chemie Christian-Albrechts-Universität, Max-Eyth Strasse 2, 24118 Kiel, Germany. E-mail: stock@ac.uni-kiel.de; Fax: +49 4318801775; Tel: +49 4318801675*
[b]*Anorganische Chemie III, Universität Bayreuth, Universitätsstraße 30, 95447 Bayreuth, Germany. E-mail: juergen.senker@uni-bayreuth.de; Tel: +49 921552532*

† Electronic supplementary information (ESI) available: Additional results of solid state and solution-based NMR spectroscopic studies, X-ray powder diffraction and temperature dependent X-ray powder diffraction patterns and results of the thermogravimetric measurements. See DOI: 10.1039/c2ce06620c

structures of MIL-53 (ref. 16) and MIL-101.[17,18] Very recently we synthesised CAU-1 using the aminotereph-thalic acid linker.[17] The CAU-1 framework[19] contains $[Al_8(OH)_4(OCH_3)_8]^{12+}$ clusters composed of eight distorted AlO_6-octahedra that are connected through hydroxy groups (corner-sharing) and two methoxy groups (edge-sharing). The arrangement of these clusters can be derived from a tetragonally distorted bcc arrangement. These clusters are twelve-fold connected *via* amino terephthalate ions. The structure possesses two kinds of cavities with effective diameters of approximately 1 and 0.45 nm. Twelvefold connected networks, such as UiO-66 (ref. 20) and MIL-125,[21] are known for their stability and high porosity. CAU-1 has been intensively investigated, for example in the field of thin-film crystal growth,[22] N_2-, H_2-, and CO_2-sorption[23,24] and post-synthetic modification,[25] and its formation has been studied by *in situ* EDXRD measurements.[12*a*,26] The first publication on CAU-1 (ref. 17) depicts a signal at ~27 ppm in the ^{13}C CP MAS solid-state NMR spectrum, which could not be assigned at that time. This prompted us to carry out an in-depth investigation which also revealed the origin of the ^{13}C signal. Herein we show that the signal is due to the methylation of the amino group. We also demonstrate the influence of the reaction time and temperature on the *in situ* methylation of CAU-1–NH_2. In addition, the post-synthesis modification by reaction with acetic anhydride is shown and the influence of thermal activation on the composition of the Al-based building unit is identified.

2. Experimental

2.1 Chemicals

$AlCl_3 \cdot 6H_2O$ (Riedel-de Haen, ⩾99%), H_2BDC–NH_2 (Fluka, ⩾98%), methanol (BASF, purum), and acetic anhydride (Fluka, ⩾99%).

2.2 Methods

X-Ray powder diffraction patterns were recorded with a STOE STADI P diffractometer equipped with a linear position sensitive detector using monochromatic Cu-$K_{\alpha 1}$ radiation. Lattice parameters were determined using the DICVOL[27] program and refined using the STOE software package WinXPow.[28] Temperature-dependent X-ray powder diffraction (TD-XRPD) experiments were performed under air with a STOE STADI P diffractometer equipped with an image plate detector and a STOE capillary furnace (version 0.65.1) using monochromatic Cu-$K_{\alpha 1}$ radiation. Each powder pattern was recorded in the 4–35° range (2θ) at intervals of 10 °C up to 350 °C and intervals of 25 °C from 350–400 °C with duration of 15 min per scan. The temperature ramp between two patterns was set to 2 °C min^{-1}.

Thermogravimetric (TG) analysis was carried out in air (75 mL min^{-1}, 25–900 °C, 4 °C min^{-1}) on a Netzsch STA-409CD. Carbon, hydrogen, and nitrogen contents were determined by elemental chemical analysis on an Eurovektor EuroEA Elemental Analyzer. EDX analysis was performed on a Philips ESEM XL 30. IR spectra were recorded on an ATI Matheson Genesis in the spectral range 4000–400 cm^{-1} using the KBr disk method as well as on an ALPHA-ST-IR Bruker spectrometer equipped with an ATR unit.

Several types of adsorption experiments were carried out using three different gases. Based on the TG data, activation at 130 °C under vacuum for 3 h was used for all measurements. The specific surface area of the dehydrated CAU-1 derivatives was determined by measuring the N_2 sorption isotherms at −196 °C using a BELSORP-max apparatus. Approximately 30 mg of sample were used for each experiment. The CO_2 and H_2O adsorption experiments were carried out at 25 °C up to a pressure of 1 bar using the same instrument.

For the NMR study of the CAU-1 samples liquid- and solid-state NMR experiments were performed. Liquid-state NMR spectra were recorded on a Bruker DRX500 operating at 500 MHz for ^1H. Two different procedures were applied to obtain solution samples for the liquid-state NMR investigations. In the first method, the washed CAU-1 material was directly dissolved in a dilute NaOD/D_2O solution. In the second method the linker was isolated by digesting the framework in 2 M NaOH and reprecipitating by neutralising using 2 M HCl. After filtration, the linker was redissolved in a dilute NaOD/D_2O solution.

The 1D solid-state NMR experiments were carried out on commercial BRUKER Avance DSX-300 and Avance II 300 spectrometers operating at 7.05 T with resonance frequencies of 75.47 MHz for carbon and of 30.41 MHz for nitrogen. 2D experiments were measured on a BRUKER Avance III 400 spectrometer operating at 9.4 T with resonance frequencies for ^1H and ^{13}C of 400.13 MHz and 100.62 MHz. The proton and carbon shifts were referenced relative to tetramethylsilane and the nitrogen shifts to nitromethane. The carbon–proton 2D MAS-J-HMQC[29] experiment of solvothermally synthesised CAU-1 was performed using a 4 mm double-resonance probe with the sample restricted to the inner third of the rotor to increase rf field homogeneity and spinning at 10 kHz rotation frequency. The contact time for the cross-polarisation was set to 5 ms and the delay τ equal to 2 ms. The proton rf field strength was set to 83 kHz during τ (FSLG decoupling) and 100 kHz during acquisition (Spinal64 decoupling). All proton–proton homonuclear and carbon–proton heteronuclear correlation experiments were measured accordingly at 12.5 kHz rotation frequency with a ^1H nutation frequency of 76 kHz for excitation and decoupling (using the eDUMBO sequence during t_1 and the windowed wDUMBO sequence during t_2). The 1D ^{13}C and ^{15}N CPMAS spectra were collected in 4 mm or 7 mm triple resonance probes with spinning speeds between 5 and 8 kHz. These spectra were recorded using a cross-polarization sequence with a nutation frequency of the protons of 77 kHz (sweeping from 50 to 100% power) and a Spinal64 proton decoupling of 63 kHz for the ^{13}C spectra and 89 kHz proton nutation frequency and spinal64 proton decoupling of 71 kHz for the ^{15}N spectra. The relaxation times were checked and the recycle delays set accordingly to 5 s for CAU-1–NH_2, 2.5 s for CAU-1–$NHCOCH_3$ and 2.5 s for CAU-1–$NHCH_3$, respectively.

For the microwave reactions the commercially available microwave synthesizer Biotage Initiator was used. The reaction temperature attained within 1 min corresponds to ramp rates of 2–5 °C s^{-1}. Glass reactor vials (Biotage microwave vial 2–5 mL) with an inner diameter of 14 mm and a volume of 10 mL were used. Temperatures were measured by an internal IR sensor.

Conventional syntheses were carried out in glass reactors (DURAN® glass 25 mL) and Teflon-lined steel autoclaves with a maximum volume of 30 mL.

2.3 Systematic investigation of the influence of reaction time and temperature on the methylation of CAU-1

Based on previous results obtained from the *in situ* EDXRD crystallisation studies the reactions were carried out in a microwave (MW) oven (Biotage Initiator) using 5 mL glass vials.[12a,26] For all reactions a mixture of $AlCl_3 \cdot 6H_2O$ (232 mg, 0.961 mmol) and $H_2BDC–NH_2$ (58 mg, 0.312 mmol) was used, which was suspended in methanol (3.175 mL). The influence of reaction time was studied at 135 °C in a time range of 15–638 min and at 145 °C between 2 and 10 min.

2.4 Synthesis of CAU-1–NH_2, $[Al_4(OH)_2(OCH_3)_4(BDC–NH_2)_3]$

The non-methylated compound CAU-1–NH_2 was synthesised using MW-assisted heating. A mixture of $AlCl_3 \cdot 6H_2O$ (232 mg, 0.961 mmol) and $H_2BDC–NH_2$ (58 mg, 0.312 mmol) was suspended in methanol (3.175 mL) in a 5 mL glass vial. After sealing, the reaction mixture was heated under stirring (300 r s^{-1}) at 145 °C for 3 min. The reaction mixture was rapidly cooled to room temperature. A yellow microcrystalline dispersion was obtained. After centrifugation, the product was redispersed in water (25 mL) to remove the Cl^- ions, which may be present due to the formation of $R–NH_3^+$ groups. This procedure was repeated (three times) until no Cl^- ions could be detected anymore. The final product was dried in air to yield CAU-1–NH_2 (75% for the as-synthesised product and 50% for the activated compound based on aminoterephthalic acid). Elemental analysis of the washed phase: observed, C: 41.22, H: 3.65, N: 5.46; calculated (based on $[Al_4(OH)_2(OCH_3)_4(BDC–NH_2)_3]$), C: 41.84, H: 3.64, N: 5.22%.

2.5 Synthesis of CAU-1–$NHCH_3$, $[Al_4(OH)_2(OCH_3)_4(BDC–NHCH_3)_3]$

The methylated compound was synthesised using MW-assisted heating by increasing the reaction time. A mixture of $AlCl_3 \cdot 6H_2O$ (232 mg, 0.961 mmol) and $H_2BDC–NH_2$ (58 mg, 0.312 mmol) was suspended in methanol (3.175 mL) and heated to 135 °C for 10 h. A yellow microcrystalline product was obtained after filtering and drying in air. Like CAU-1–NH_2, the as-synthesized products contain large amounts of Cl^- ions. To remove these, the raw product was washed several times with water to yield CAU-1–$NHCH_3$. Elemental analysis of the washed phase: observed, C: 44.03, H: 4.18, N: 4.97; calculated (based on $[Al_4(OH)_2(OCH_3)_4(BDC–NHCH_3)_3]$), C: 43.31, H: 4.10, N: 4.98%.

2.6 Post-synthetic modification of CAU-1–NH_2

To $[Al_4(OH)_2(OCH_3)_4(BDC–NH_2)_3]$ (500 mg, 0.626 mmol) acetic anhydride (2 mL, 21.197 mmol) was added. The reaction was carried out in an ultrasonic bath (160 W Bandelin Sonorex RK 100) at room temperature for 3 h leading to the formation of the amide derivative. The product was washed with H_2O and heated in air (80 °C, 2 h) to yield CAU-1–$NHCOCH_3$. Elemental analysis: observed, C: 35.59, H: 3.50, N: 3.63; calculated (based on $[Al_4(OH)_2(OCH_3)_4(BDC\text{-}NHCOCH_3)_3] \cdot xH_2O$; $x \approx 12$) C: 35.68, H: 3.59, N: 3.67%.

2.7 Thermal activation of CAU-1–NH_2

To remove solvent molecules from the pores of CAU-1–NH_2, the samples were treated thermally. Depending on the activation conditions (vacuum *vs.* air) and the applied temperatures (120–190 °C), a substitution of methoxy groups by hydroxy groups in the Al-based brick of the CAU-1–NH_2 framework takes place. At an activation temperature of 190 °C the methoxy groups were fully replaced by hydroxy groups after 24 h and CAU-1–NH_2(OH) ($[Al_4(OH)_6(BDC–NH_2)_3] \cdot xH_2O$) is formed.

3. Results and discussion

3.1 Solid-state NMR investigation of CAU-1 synthesised under conventional heating

The unassigned carbon signal at 27 ppm (see Ahnfeldt *et al.*,[17] Fig. S5b†) gave rise to the question whether the product is phase pure. By performing a carbon–proton 2D MAS-J-HMQC experiment the carbon signals are correlated to signals of directly bonded hydrogen nuclei. In the HMQC spectrum (Fig. 1) the signal at 27 ppm correlates with a proton signal at 2.2 ppm, characteristic of a methyl group, the signal at 57 ppm with the methoxy proton signal at 2.8 pm, and the directly proton bonded aromatic carbons (113, 116, and 132 ppm) correlate with proton signals between 7 and 8 ppm. Non-bonded carbons, like the carboxy (174 ppm) or the quaternary aromatic carbons (153, 137 and 115 ppm), show no correlation to protons in this experiment, but can be seen in the top of Fig. 1 for comparison.

The same proton signals were found in proton–proton homonuclear correlation (HOMCOR) spectra (Fig. 2 and S1†) as well as in carbon–proton heteronuclear (HETCOR) spectra (shown in Fig. S2†). All these 2D spectra exhibit cross-peaks

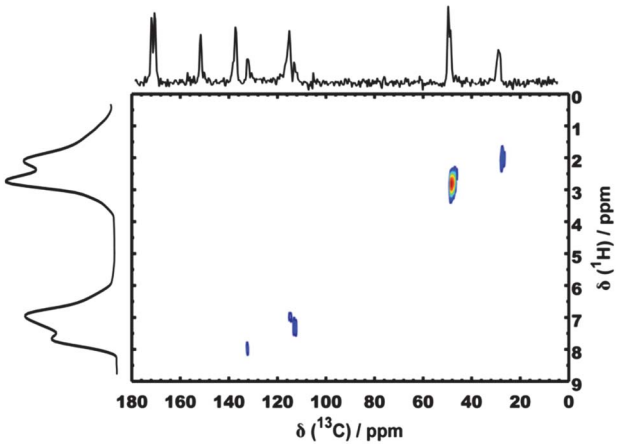

Fig. 1 ^1H-^{13}C-MAS-J-HMQC spectrum of CAU-1 synthesised under conventional heating showing correlations between directly bonded protons to carbon nuclei. For comparison a ^{13}C CP spectrum of the sample, depicting all carbon signals, is shown on top. On the left the homonuclear decoupled ^1H spectrum is shown.

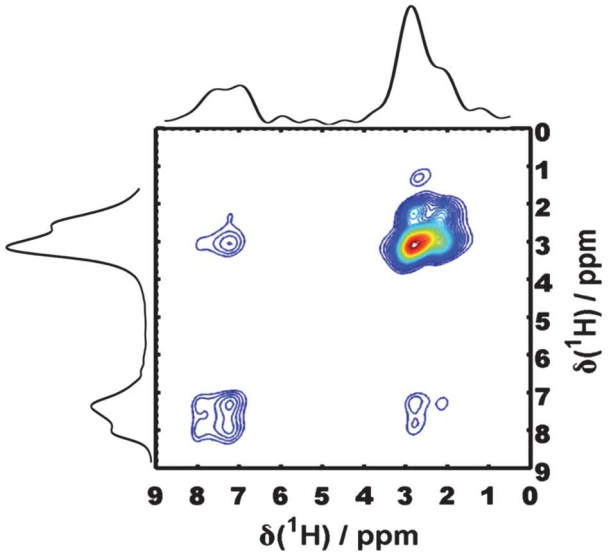

Fig. 2 ^{1}H-^{1}H HOMCOR spectrum of conventionally synthesized CAU-1 with DUMBO decoupling during t_1 and t_2 and a spin diffusion time of 4 ms, showing also longer proton–proton distance correlations.

between either the ^{1}H signal at 2.2 ppm or the ^{13}C signal at 27 ppm and other characteristic resonances. For example in Fig. 2 the ^{1}H signal at 2.2 ppm couples with the resonances in the aromatic region. These experiments therefore allow the assignment of a methyl group as an integral part of the CAU-1 structure. A final clue to its nature is given by the ^{15}N-CPPI experiment (Fig. 3) that shows different nitrogen signals.

The intensity modulation due to a CPPI sequence (Fig. 3, inset) reveals that the ^{15}N resonances at −319 and −323 ppm bear –NH functionalities while the one at −347 ppm seems to be a tertiary N atom. Together with the shift values the signals at −319 and −323 ppm can be assigned to –$NHCH_3$ groups while the one at −347 ppm is probably a –$N(CH_3)_2$ group. By the HMQC experiment we could prove the methyl group to be an integral part of the structure and *via* the CPPI experiment we could prove the methylation of the amino group. The CAU-1 synthesised under conventional heating therefore is methylated at the aminoterephthalic linker molecules. It is worth noting that the occurrence of two different shifts for the $NHCH_3$ groups indicates two different scenarios for the orientation of the functional groups within the pores with one alignment being more probable by a factor of 2. Parameters influencing this methylation reaction are studied in the following.

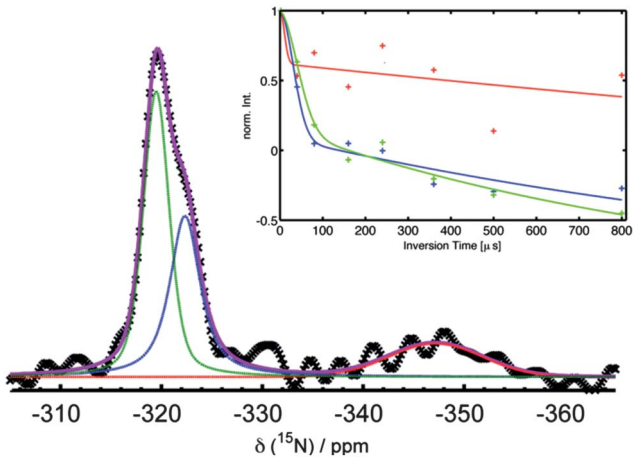

Fig. 3 ^{15}N-CPPI-spectrum and intensity decrease (shown in the inse) for the signals at −319 (green), −323 (blue) and −347 ppm (red).

3.2 Influence of the reaction temperature

The synthesis of CAU-1 under MW-assisted heating was carried out in the temperature range 115–145 °C. The reaction time for each temperature was determined from the *in situ* EDXRD studies on CAU-1 (ref. 26) and corresponds to the time required to reach full crystallisation (ranging from 105 min for 115 °C to 7–9 min for 145 °C, Table S1†). The reaction products were filtered and washed once with water. The XRPD patterns of the reaction products are shown in Fig. S3† and demonstrate that CAU-1 was formed at all reaction temperatures. The corresponding IR spectra of the reaction products are shown in Fig. 4.

The IR spectra of CAU-1 show the characteristic bands for the symmetric and asymmetric stretching modes of the bridging carboxylate group between 1600 and 1400 cm^{-1}. The presence of methoxy groups in the structure of CAU-1 is clearly demonstrated by the asymmetric and symmetric C–H stretching vibrations at 2940 and 2835 cm^{-1} as well as the C–O stretching vibration at ∼1080 cm^{-1}. The typical bands for the NH_2 group at ∼3500 and 3380 cm^{-1} (symmetric and asymmetric N–H vibrations) are not observed, because they are obscured by a broad intensive band between 3200 and 3600 cm^{-1} due to the presence of water molecules. The characteristic double band for the C_{ar}–N (NH_2) (ar = aromatic) vibration at 1254 and 1334 cm^{-1} can be observed in all spectra.[30] The relatively high intensities of these characteristic amino-bands indicate a large quantity of non-methylated NH_2 groups. This suggests that the reaction temperature has no or only minor influence on the methylation of CAU-1.

3.3 Influence of the reaction time on the degree of methylation at the reaction temperature of 135 °C

To study the influence of the reaction time on the degree of methylation, five reactions were carried out under MW-assisted

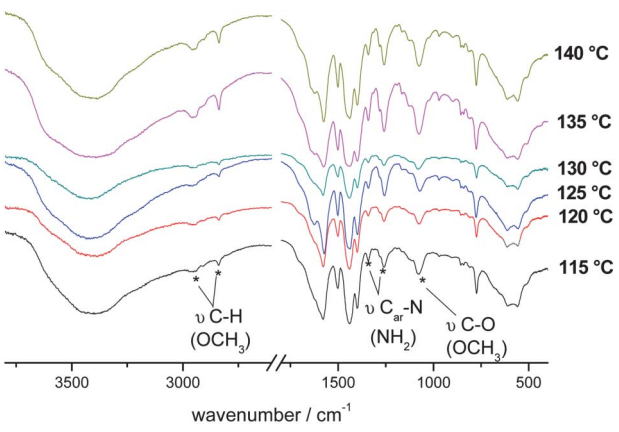

Fig. 4 IR-spectra of the CAU-1 product obtained by MW-assisted heating carried out in the temperature range between 115 and 140 °C.

heating at 135 °C. Reaction times were varied between 15 min and 638 min. The reaction products were characterized by elemental analyses, IR-spectroscopy and ^{1}H liquid-state NMR spectroscopy, which is the most powerful of the three methods. Employing ^{1}H NMR spectroscopy the digested reaction products, which contain only the isolated linker molecules redissolved in a dilute NaOD/D_2O solution, were characterised (Fig. 5). Elemental analyses and IR-spectroscopy were performed on the activated products. Two sets of signals are observed in the ^{1}H NMR spectra which belong to aminoterephthalate and *N*-methylaminoterephthalate ions. The sets of ^{1}H signals are labelled as follows (Scheme 1). The intensity of the resonance corresponding to the protons of the methyl group from the BDC–$NHCH_3^{2-}$ ions at 2.22 ppm in the ^{1}H NMR spectra (Fig. 5) increases with increasing reaction time due to the methylation of the amino groups. The degree of methylation was calculated from the sum of integrals of the aromatic H atoms and the integral of the methyl groups. This procedure is applied to all spectra that are discussed in this study.

The degree of methylation depends strongly on the reaction time. After a reaction time of 15 min only 8% of the amino groups are methylated. This value increases to 47 and 95% after a reaction time of 98 and 638 min, respectively. Furthermore small signals at 2.17 and 2.13 ppm appear in the spectra after a reaction time above 38 min, which indicates some multiple methylation of the amino groups at longer reaction times. Thus, post-synthetic modification, *i.e.* methylation, of CAU-1–NH_2 takes place within the cages. This reaction could be catalysed by Lewis acidic sites of free Al^{3+} ions in the reaction solution.

Focusing on the 6.0–7.3 ppm range the two sets of signals due to the methylated and non-methylated product are clearly distinguishable. Thus the degree of methylation is also visible in the aromatic ^{1}H region. In comparison to CAU-1–NH_2 the ^{1}H signals of the aromatic H atoms of CAU-1–$NHCH_3$ (labelled red) are shifted by about ±0.04 ppm (Fig. 5, left).

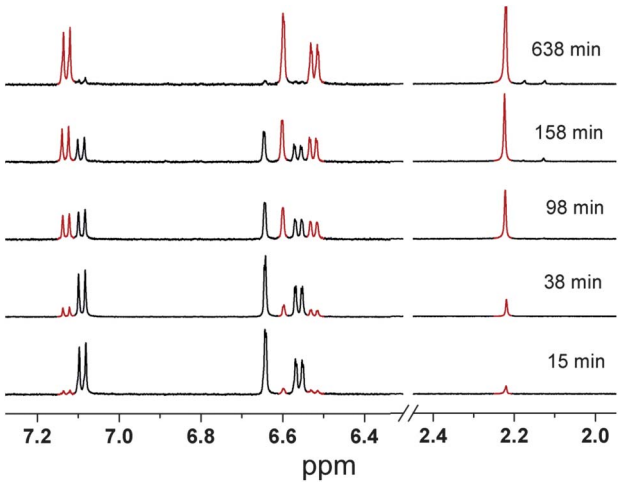

Fig. 5 ^{1}H NMR spectra of the extracted aminoterephthalate linkers collected from the MW-assisted syntheses at 135 °C using reaction times between 15 and 638 min. Each spectrum is normalized to the sum of the aromatic H signals (methylated (black) and non-methylated (red)), the aromatic signals (left) are multiplied by 2.5 relative to the methyl signals (right) for better visualisation.

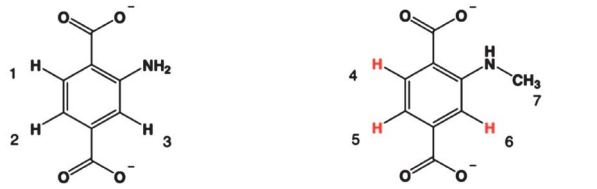

$[Al_4(OH)_2(OCH_3)_4(BDC\text{-}NH_2)_3]$ $[Al_4(OH)_2(OCH_3)_4(BDC\text{-}NHCH_3)_3]$

Scheme 1 Labelling of the ^{1}H signals in methylated and non-methylated aminoterephthalate ions: ^{1}H NMR 500 MHz, (NaOD/D_2O) δ: BDC–NH_2^{2-}: 7.09 (d, 1H, H1 $^3J_{H-H}$ = 8.1 Hz); 6.64 (s, 1H, H3); 6.56 (d, 1H, H2 $^3J_{H-H}$ = 8.1 Hz); BDC–$NHCH_3^{2-}$: 7.13 (d, 1H, H4 $^3J_{H-H}$ = 8.0 Hz); 6.60 (s, 1H, H6); 6.52 (d, 1H, H5 $^3J_{H-H}$ = 8.0 Hz); 2.22 (s, 3H, H7).

The methylation of the amino group leads to a low field shift for the protons in the *meta*-position (H4) and to a high field shift for the protons in *ortho*- and *para*-positions (H5, H6).

The results of the ^{1}H NMR investigation are also in good agreement with the elemental analyses of the compounds. Table 1 shows the experimental and calculated CHN values of the products using a reaction time of 38, 98 and 638 min. It should be noted that after washing no water molecules are enclosed in the framework. In addition, the methylation of the amino groups is also clearly demonstrated by the appearance of new vibrational bands in the IR spectra that are associated with the formation of the methylamine functionality (Fig. 6).

The two possible bands due the symmetric and asymmetric stretching vibration of the amino group (ν N–H) at 3520 and 3390 cm^{-1} are clearly visible in the spectra collected for short reaction times (15, 38 min). The N–H double band vanishes and one broad band at 3393 cm^{-1} due to the N–H vibration of the methylamine is observed for the reactions using a longer reaction time. A new signal at 1285 cm^{-1} is observed, which increases at longer reaction times and can be assigned to the C_{ar}–N stretching vibration of the methylamine group.[30] At the same time, the bands due to the C_{ar}–N (NH_2) vibration at 1260 and 1340 cm^{-1} appear with much lower intensities. This indicates the high degree of methylation of the NH_2 groups at longer reaction times.

The IR spectra confirm the results of the ^{1}H NMR spectroscopy that methylation increases at longer reaction times.

3.4 Influence of the reaction time on the degree of methylation at the reaction temperature of 145 °C

To speed up the crystallisation of CAU-1, the reaction temperature was raised to 145 °C. MW-assisted synthesis was stopped after shorter reaction times (2, 3, 5, and 10 min) in order to minimize the degree of methylation. For the NMR measurements the product was directly dissolved in NaOD/D_2O, which allows detecting the methoxy groups. The ^{1}H NMR spectra of the washed products show at longer reaction times an increase in the degree of methylation of the amino groups, as well as the increase of the amount of methoxy groups (2.64 ppm, Fig. S4†). This signal can be assigned to CH_3OD, which is formed by the release of the incorporated methoxy groups from the Al-based brick of the CAU-1 framework. According to the composition $[Al_4(OH)_2(OCH_3)_4(BDC\text{–}NH_2)_3]$ for CAU-1–NH_2 an integral ratio of methoxy H-atoms to aromatic H-atoms = 4 : 3 (= 1.33)

Table 1 Elemental analysis results of CAU-1 synthesised *via* MW-assisted heating at 135 °C for 38, 98 and 638 min. Calculated values correspond to a composition according to $[Al_4(OH)_2(OCH_3)_4(BDC–NH_{2-x}C_xH_{3x})_3]$

Reaction time/min	Degree of methylation (x) (%)	C_{exp} (calc.) (%)	H_{exp} (calc.) (%)	N_{exp} (calc.) (%)
38	16 (0.16)	42.28 (42.21)	3.72 (3.73)	5.09 (5.18)
98	47 (0.47)	42.90 (42.90)	3.92 (3.90)	5.22 (5.10)
638	95 (0.95)	43.31 (43.92)	4.10 (4.15)	4.98 (4.98)

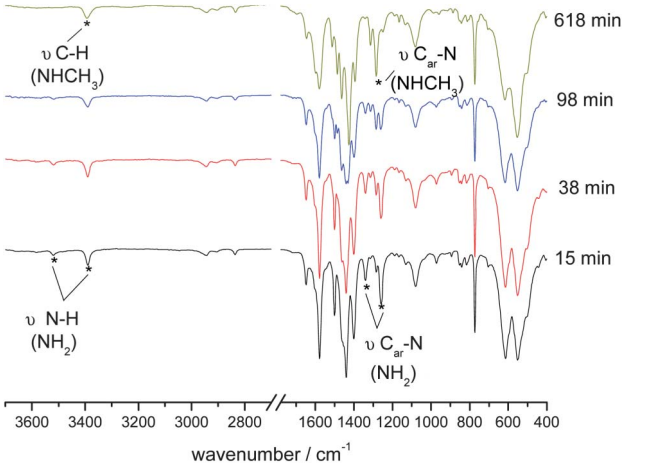

Fig. 6 IR spectra of CAU-1 synthesised *via* MW-assisted heating at the reaction temperature of 135 °C. Four different reaction times were investigated (15, 38, 98 and 638 min).

is expected. Increasing the reaction time from 2 to 10 min leads to integral ratios varying from 1.10 to 1.31, respectively. Thus, short reactions lead only to the partial incorporation of methoxy (83%) groups while after 10 min 99% of the methoxy groups are present. We presume that at very short reaction times structural defects are present. This has also been reported in the synthesis of MOF-5 using short reaction times.[31]

As observed at reaction temperatures of 135 °C, an increase of reaction time leads to a higher degree of methylation of the amino groups, which is clearly visible by an increase of the signal at 2.2 ppm due to the methyl groups. The results are summarized in Table 2.

The lowest degree of methylation of the amino group was found for a reaction time of only two minutes (2%). However, the reaction was not complete and only a very small amount of CAU-1–NH_2 could be obtained (yield < 10% of the washed product, based on aminoterephthalic acid). Using a reaction time of ten minutes leads to a high yield (90%) but also to a much higher degree of methylation (13%).

The results of the NMR investigation fit well with the elemental analyses of the compounds, which are also listed in Table 2. For the products at reaction times of 2 and 3 min water molecules are enclosed within the framework. The best compromise between the product yield and degree of methylation was determined to be at a reaction time of 3 min. In three repeated reactions the dissolved products exhibit the identical degree of methylation (3%), which clearly shows the good reproducibility of the MW-assisted synthesis (Fig. S5†).

3.5 Influence of the heating method and reactor material

In order to investigate the methylation of the amino groups during the CAU-1 synthesis applying conventional heating methods, reactions were performed in Teflon-lined steel autoclaves and glass autoclaves. A mixture of $AlCl_3·6H_2O$ (463.5 mg, 1.920 mmol) and $H_2N–H_2BDC$ (116.60 mg, 0.645 mmol) was suspended in methanol (6.175 mL) and heated at 125 °C for 5 h. The washed products were directly dissolved in a dilute NaOD/D_2O solution and characterized by ^1H NMR spectroscopy (Fig. 7). Three sets of signals can be observed in the spectra, which can be assigned to aminoterephthalate, *N*-methylaminoterephthalate, and *N*,*N*-dimethylaminoterephthalate. The signals are discussed for the reaction products obtained in the glass reactor. The labelling of the sets of ^1H signals is listed in Scheme S1† in the ESI. The reaction carried out in a Teflon-lined steel autoclave led to only a small amount of CAU-1–$NHCH_3$ (12%) compared to the reaction performed in a glass autoclave, which shows that 52% of the amino groups are single methylated and 21.5% of the amino groups are twofold methylated (CAU-1–$N(CH_3)_2$). The variation of the degree of methylated amino groups as a function of the use of different reaction vessels may be caused by different heating or diffusion rates within the reactors.

3.6 Influence of the thermal activation process on the composition of CAU-1–NH_2

The TG analysis of CAU-1–NH_2 was performed on the degassed sample (30 min/130 °C at 1×10^{-3} bar) in air. The TG curve is shown in Fig. S6†. A very flat step, corresponding to a weight loss of 10%, is observed between 50 and 370 °C. This weight loss cannot to be due to the presence of incorporated solvent molecules since this would lead to a well defined step in the TG curve. At higher temperatures, above 370 °C, the decomposition of the frameworks takes place and Al_2O_3 is formed. The observed and calculated total weight loss, based on the final mass of Al_2O_3, fit well (obs. 25.1%, calc. 25.5%). To investigate

Table 2 Elemental analyses, degree of incorporation of methoxy and methyl groups in CAU-1 synthesised by MW-assisted heating at 145 °C. Reaction times of 2 to 10 min were used. Calculated values are based on a composition according to $[Al_4(OH)_{2+y}(OCH_3)_{4-y}(BDC–NH_{2-x}C_xH_{3x})_3]·wH_2O$

Time/min	Methoxy groups (y) (%)	Degree of methylation (x) (%)	H_2O formula (w)	C_{exp} (calc.) (%)	H_{exp} (calc.) (%)	N_{exp} (calc.) (%)
2	83 (0.68)	2 (0.02)	2.3	39.31 (39.34)	3.47 (3.84)	5.34 (5.28)
3	88 (0.48)	3 (0.03)	1.3	40.36 (40.37)	3.53 (3.82)	5.14 (5.12)
5	96 (0.16)	6 (0.06)	—	42.84 (41.84)	3.69 (3.69)	5.34 (5.22)
10	99 (0.04)	13 (0.13)	—	41.81 (42.11)	3.70 (3.71)	5.22 (5.19)

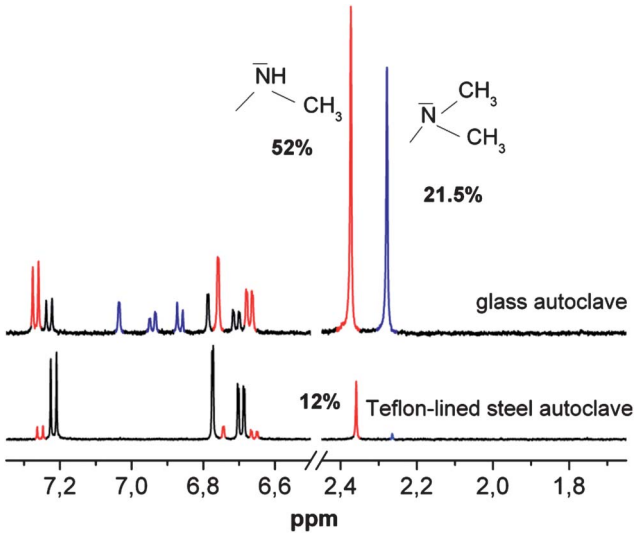

Fig. 7 ^{1}H NMR spectra of CAU-1 prepared by conventional synthesis using a Teflon-lined autoclave (bottom) or a glass autoclave (top). After the washing process both compounds were directly dissolved in a dilute NaOD/D_2O solution. Each spectrum is normalized to the H3, H6, and H10 signals, respectively. Signals due to the linker molecules are coloured as follows: blue: dimethylated, red: methylated and black: non-methylated.

the processes taking place up to 370 °C the influence of the thermal activation process on the composition of CAU-1–NH_2 was studied using the product obtained by MW-assisted synthesis (3 min/145 °C). In the course of this study different activation times, temperatures and atmospheres (vacuum *vs.* air) were used. After thermal treatment the samples were characterized by elemental analyses, IR-spectroscopy and ^{1}H-liquid-state NMR spectroscopy. For the ^{1}H-liquid-state NMR spectroscopy investigations the samples were directly dissolved in a dilute NaOD/D_2O solution. Elemental analyses and IR spectroscopy were performed on the thermally activated products without any further treatment. Fig. S7† shows the ^{1}H spectra of the dissolved CAU-1–NH_2 compounds after thermal treatment under different temperatures, activation times, and activation atmospheres (vacuum *vs.* air). For all five activation procedures, we observed a decrease in the fraction of incorporated methoxy groups retained within the framework (see Table 3). Heating under vacuum at 130 °C for 12 h leads only to the release of a very small fraction of methoxy groups (83% retained) compared to similar heating procedures at 120 °C (55% retained) in air. Even a very short thermal treatment of 30 min at 120 °C leads to a significant removal of methoxy groups (73% retained). While an activation temperature of 190 °C for 12 h leads to an almost complete removal of the incorporated methoxy groups (8% retained), no signal is observed after an activation time of 24 h. Thus methoxy groups are fully replaced by hydroxy groups.

The resulting compound $[Al_4(OH)_6(BDC–NH_2)_3]\cdot xH_2O$, denoted as CAU-1–$NH_2$(OH), contains large amounts of adsorbed water molecules, due to a higher hydrophilicity of the framework. Water molecules from the air are necessary for the substitution of methoxy groups by hydroxy groups. This has also been observed previously for thermal activation procedures of acidic zeolite catalysts, which contain surface methoxy species.[32,33] The removal of the methoxy groups is also observed by IR spectroscopy.

Table 3 Percentage of incorporated methoxy groups within the structure of CAU-1–NH_2, $[Al_4(OH)_{2+y}(OCH_3)_{4-y}(BDC–NH_{2-x}C_xH_{3x})_3]$, after thermal treatment. The CAU-1 products were synthesised by MW-assisted heating using a reaction time of 3 min at 145 °C

Activation procedure	Methoxy groups (%)	Composition in y and x
—	88	y = 0.48; x = 0.03
130 °C/12 h (3 mbar)	83	y = 0.68; x = 0.03
120 °C/0.5 h	73	y = 1.08; x = 0.03
120 °C/12 h	55	y = 1.80; x = 0.03
190 °C/12 h	8	y = 3.68; x = 0.03
190 °C/24 h	0	y = 4.00; x = 0.03
190 °C/12 h (3 mbar)	83	y = 0.68; x = 0.03

The IR spectra of CAU-1–NH_2 before and after the thermal treatment in air (190 °C/24 h) are shown in Fig. 8. The two broad bands due to the symmetric and asymmetric modes of C–H stretching vibration of the bridging methoxy groups at 2940 and 2840 cm^{-1} and the C–O stretching vibration of the incorporated methoxy groups at ~1080 cm^{-1} vanish in the spectrum of the heated sample. At the same time, the intensity of the weak signal at ~3700 cm^{-1} due to the bridging OH groups increases. The powder pattern of the washed sample exhibits no significant change in crystallinity after thermal treatment (see Section 3.8 and Fig. 13).

3.7 Post-synthetic modification of CAU-1–NH_2

Using MW-assisted heating for the syntheses of CAU-1 led to non-methylated amino groups at very short reaction times. This should allow the post-synthetic modification of the amino functionality, which has been previously reported, for example, for Al-MIL-53–NH_2 and IRMOF-3.[16,34] For the proof of principle we reacted CAU-1–NH_2 with acetic anhydride, which led to the fully acylated compound CAU-1–$NHCOCH_3$ ($[Al_4(OH)_2(OCH_3)_4(BDC–NHCOCH_3)_3]\cdot xH_2O$) (Scheme 2).

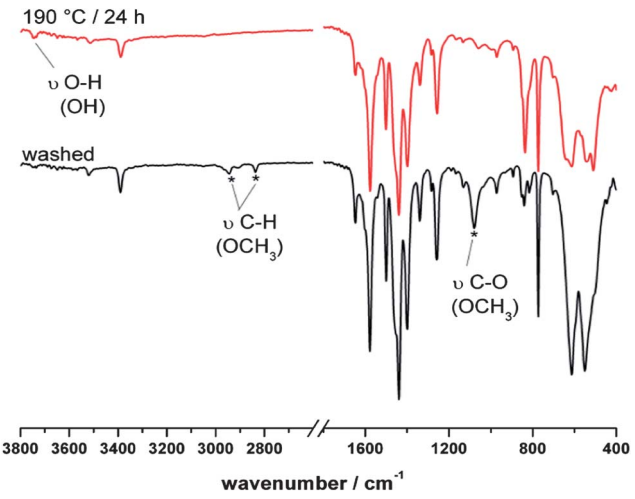

Fig. 8 Comparison of the IR-spectra of washed CAU-1 before (black) and after thermal treatment (190 °C for 24 h in air) (red).

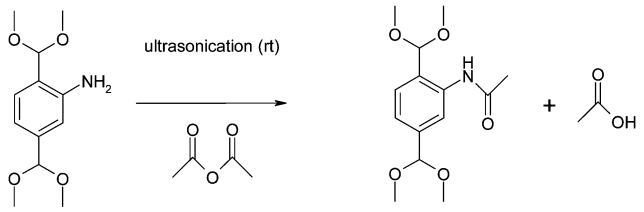

Scheme 2 Post-synthetic modification of CAU-1–NH_2 by reaction with acetic anhydride.

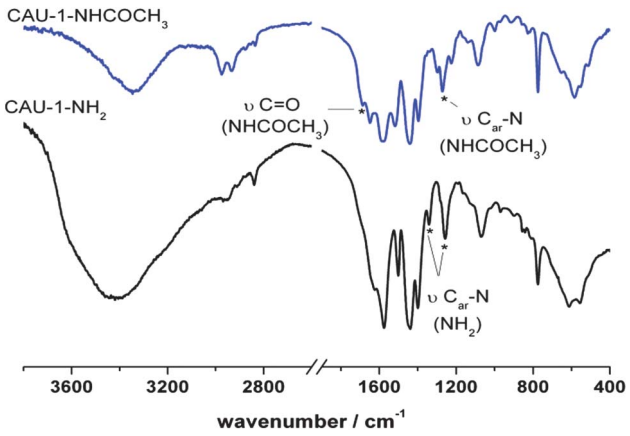

Fig. 9 IR spectra of modified CAU-1 (blue) and unmodified CAU-1–NH_2 (black). The characteristic bands in the spectra are marked with black stars.

Fig. 9 shows the IR spectra of the CAU-1–NH_2 and CAU-1–$NHCOCH_3$. New signals at 1690 and 1274 cm^{-1} in the spectrum of CAU-1–$NHCOCH_3$ are caused by the C=O and the C_{ar}–N stretching vibrations of the amide group respectively.[30] At the same time, the bands due to the C_{ar}–N (NH_2) stretching vibration at 1258 and 1341 cm^{-1} do not appear in the spectrum anymore. This indicates a nearly complete modification of the NH_2 groups.

The results of the IR-spectroscopic measurements of the post-synthetic modification of CAU-1–NH_2 are also confirmed by solid-state ^{13}C and ^{15}N MAS NMR experiments (Fig. 10 and 11).

In contrast to the material obtained by conventional heating (see Ahnfeldt *et al.*,[17] Fig. S5b†), the ^{13}C spectrum of CAU-1–NH_2 shows no signal at 27 ppm (Fig. 10, top). This depicts that there are no –$NHCH_3$ groups present. Upon post-synthetic modification, two new signals at 24 ppm and 178 ppm are observed, which can be assigned to the methyl group of the acetamide and the carbonyl ^{13}C atom, respectively. The signal of the ipso carbon atom, which is closest to the newly formed amide bond, shifts from 150 ppm to 141 ppm.

The ^{15}N CPMAS-NMR spectrum of CAU-1–NH_2 (Fig. 11) exhibits a signal at −316 ppm, which we assigned to the –NH_2 group. The signal due to the N-atom of the amino group shifts in the spectrum of CAU-1–$NHCOCH_3$ to −253 ppm caused by the formation of the amide group. There is no signal left at −316 ppm which confirms a complete modification of the –NH_2 group.

Further structural information for CAU-1–$NHCOCH_3$ could be gained by a series of solid-state NMR experiments like ^{1}H–^{1}H spin diffusion spectra and carbon–proton HETCOR spectra. In Fig. 12 different ^{1}H spin diffusion spectra of CAU-1–$NHCOCH_3$ as a function of the mixing times are shown. The signal assignment for these spectra is as follows: at 0.8 and 1.5 ppm two signals for the methyl protons of the acetyl residue, at 3.0 ppm a signal for the methoxy groups, at 7–8 ppm a broad signal for the aromatic protons and at 9 ppm the NH proton signal.

For very short spin diffusion mixing times (1 μs) no correlation occurs, at short mixing times (700 μs) first spatial proximity can be observed between the signal at 3.0 ppm and 1.5 ppm which we assign to the methoxy groups of the inorganic brick and the methyl group of the acetamide, respectively. This can only be explained by a short distance between the methoxy groups and a part of the linker residues. At medium mixing times (1500 μs) the other correlations begin to develop, whereas even at longer mixing times (4000 μs) the correlation between the signal

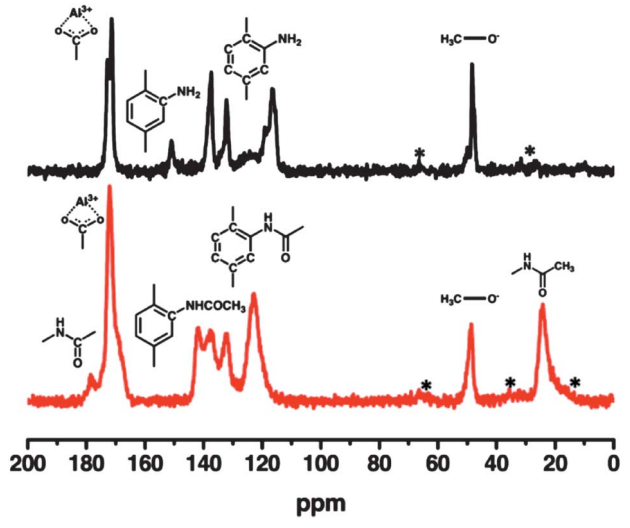

Fig. 10 ^{13}C MAS NMR spectra of CAU-1–NH_2 (black) and CAU-1–$NHCOCH_3$ (red). The signals marked by an asterisk (*) are due to spinning side bands.

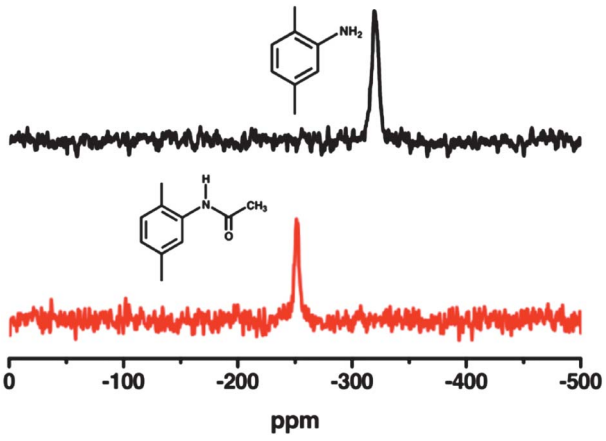

Fig. 11 ^{15}N CPMAS NMR spectra of CAU-1–NH_2 (black) and CAU-1–$NHCOCH_3$ (red).

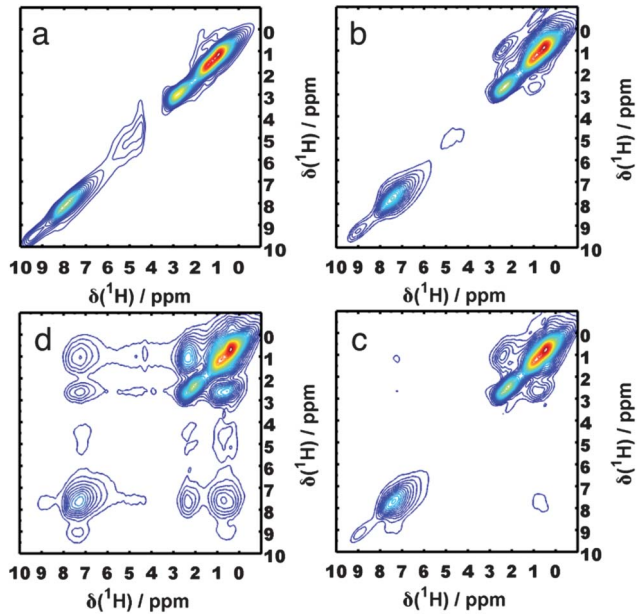

Fig. 12 2D spin diffusion spectra of CAU-1–$NHCOCH_3$ at mixing times of 1 μs (a), 700 μs (b), 1500 μs (c) and 4000 μs (d).

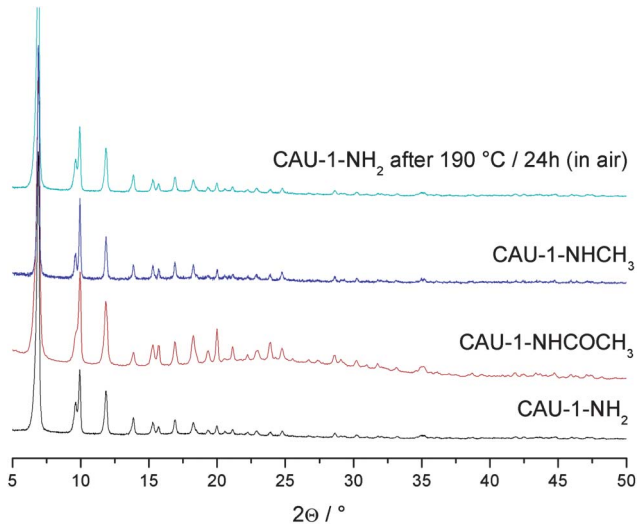

Fig. 13 XRPD patterns of CAU-1–NH_2 (black), CAU-1–$NHCOCH_3$ (red), CAU-1–$NHCH_3$ (blue), and CAU-1–NH_2 after thermal treatment at 190 °C for 24 h in air (green).

Table 4 Refined lattice parameters determined from XRPD data of CAU-1–X (X = –NH_2, –$NHCH_3$, –$NHCOCH_3$) and CAU-1–NH_2(OH), which was heated before the measurement to exchange the incorporated methoxy groups by hydroxy groups (190 °C/24 h in air)

Compound	*a*/Å	*b*/Å	*c*/Å	*V*/Å^3
CAU-1–NH_2	18.319(4)	18.319(4)	17.753(7)	5958(1)
CAU-1–$NHCH_3$	18.331(5)	18.331(5)	17.739(7)	5960(2)
CAU-1–$NHCOCH_3$	18.341(5)	18.341(5)	17.735(4)	5966(1)
CAU-1–NH_2(OH)	18.330(6)	18.330(6)	17.761(7)	5968(1)

at 3.0 and 0.8 ppm is still weak. We interpret this behaviour as a long distance between methoxy groups and methyl groups of these linker residues. This is only possible if there are different positions for the methyl residues available, like an orientation dependence between an alignment of the linker into the smaller pores (short distances) and into the bigger pores (longer distances). For this model we estimate *via* the intensity ratio of the signals at 1.5 and 0.8 ppm one-third of the linker molecules to be oriented into the small pores and two-thirds into the bigger pores as a possible scenario.

Similar experiments were conducted for CAU-1–$NHCH_3$, but no such behaviour could be observed (see Fig. S1†). This could be explained by the smaller volume of the methyl residues relative to the acetyl residue of CAU-1–$NHCOCH_3$.

3.8 XRPD studies on CAU-1–NH_2, CAU-1–$NHCH_3$, CAU-1–$NHCOCH_3$ and CAU-1–NH_2(OH)

CAU-1–NH_2, CAU-1–$NHCH_3$, and CAU-1–$NHCOCH_3$ could be synthesized with high crystallinity and without crystalline impurities. The thermal treatment of CAU-1–NH_2 at 190 °C for 24 h in air led to a complete replacement of the methoxy by the hydroxy groups. Fig. 13 shows powder patterns of all three products, as well as the one of CAU-1–NH_2 after thermal treatment (190 °C/24 h in air).

To determine the influence of the composition on the crystal structure, the lattice parameters were determined by using WinXPow.[28] Lattice parameter refinements and systematic extinctions led for all compounds to a tetragonal body-centred unit cell with very similar lattice parameters in all four cases (Table 4).

3.9 Temperature-dependent X-ray powder diffraction measurement (TD-XRPD)

For investigating the influence of the different compositions of the compounds on the thermal properties TD-XRPD measurements of all four compounds were performed. The TD-XRPD measurements of CAU-1–NH_2, CAU-1–NH_2(OH), CAU-1–$NHCH_3$ and CAU-1–$NHCOCH_3$ are shown in Fig. 14 and S8–S10†, respectively. In good agreement with the results of the TG analysis of CAU-1–NH_2 (Fig. S6†), all investigated

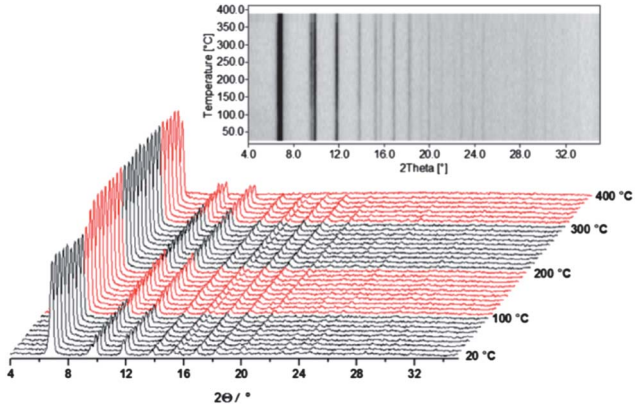

Fig. 14 Temperature-dependent X-ray powder diffraction patterns of CAU-1–NH_2 in air (20–400 °C).

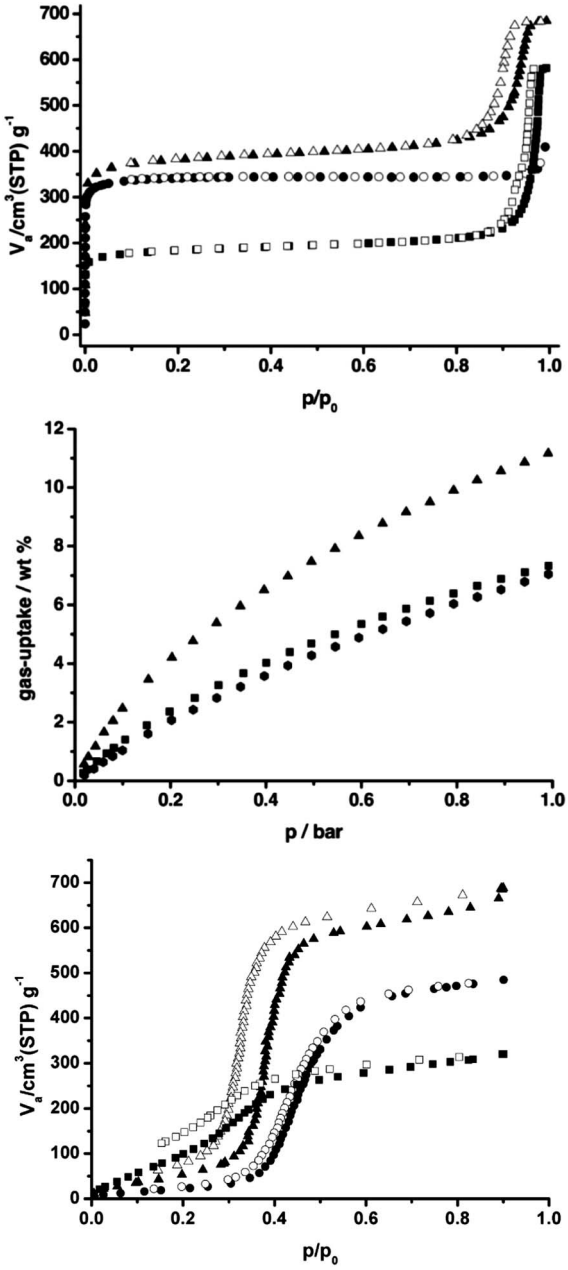

Fig. 15 N_2 (top), CO_2 (middle) and H_2O (bottom) sorption isotherms for CAU-1–NH_2 (● = adsorption, ○ = desorption), CAU-1–$NHCH_3$ (▲ = adsorption, △ = desorption) and CAU-1–$NHCOCH_3$ (■ = adsorption, □ = desorption). The H_2O and CO_2 sorption isotherms were collected at 298 K, N_2 sorption experiments at 77 K.

compounds show a high thermal stability at least up to 350 °C. At around 100 °C, increased reflection intensities were observed in the TD-XRPD measurements, which are accompanied by the removal of absorbed water molecules. Up to the decomposition of the framework, no changes of the reflection positions are detectable.

However, a comparison of the TD-XRPD measurement of all four CAU-1 derivatives led to the conclusion that the different compositions have no or only a minor influence on their thermal behaviour.

Table 5 Comparison of specific surface area S_A, total pore volume $V(N_2)$ and total pore volume $V(H_2O)$ of CAU-1–NH_2, CAU-1–$NHCH_3$, and CAU-1–$NHCOCH_3$

CAU-1–X	–NH_2	–$NHCH_3$	–$NHCOCH_3$
$S_A/m^2\ g^{-1}$	1530	1340	680
$V(N_2)^a/cm^3\ g^{-1}$	0.64	0.53	0.30
$V(H_2O)^b/cm^3\ g^{-1}$	0.55	0.48	0.25
wt $CO_2{}^c$ (%)	11.2	7.0	7.3

[a] Calculated at p/p_0 = 0.5 from the nitrogen adsorption isotherm and 77 K. [b] Calculated at p/p_0 = 0.9 from the water adsorption isotherm and 298 K. [c] Calculated at 1 bar and 298 K.

3.10 Sorption study on CAU-1

The three CAU-1 derivatives, CAU-1–NH_2, CAU-1–$NHCH_3$, and CAU-1–$NHCOCH_3$, show different sorption properties depending on the functional group and the adsorptive employed (Fig. 15).

Using nitrogen (Fig. 15, top), Type 1 isotherms are observed for all three compounds. The apparent specific surface area, calculated using the BET equation, decreases strongly from 1530 $m^2\ g^{-1}$ (CAU-1–NH_2) to 680 $m^2\ g^{-1}$ (CAU-1–$NHCOCH_3$) depending on the size of the functional group. Accordingly, the micropore volume also decreases from 0.64 $cm^3\ g^{-1}$ (CAU-1–NH_2) to 0.30 $cm^3\ g^{-1}$ (CAU-1–$NHCOCH_3$). Adsorption experiments with water vapour show a higher uptake for CAU-1–$NHCOCH_3$ at low p/p_0 values compared to CAU-1–NH_2 and CAU-1–$NHCH_3$. This may be due to hydrogen bonding interactions of the amide group, which decrease in the order –$NHCOCH_3$ > –NH_2 > –$NHCH_3$, as well as a higher adsorption potential due to narrower pore sizes. The order is in agreement with the desorption curves of CAU-1–$NHCOCH_3$ and CAU-1–NH_2, where a slight hysteresis due to these stronger interactions with the adsorbate is observed. The micropore volume calculated from the water adsorption isotherms (Fig. 15, bottom) is smaller than the calculated micropore volume from the nitrogen isotherms, as observed for other MOFs like DUT-4 and HKUST-1.[35] The CO_2 sorption measurements of the three compounds (Fig. 15, middle) were carried out at 298 K and up to 1 bar. Under this condition, the maximum uptake was not accomplished. However, the isotherm of CAU-1–NH_2 shows a higher uptake of CO_2 (11.2 wt%) than the isotherms of CAU-1–$NHCOCH_3$ (7.3 wt%) and CAU-1–$NHCH_3$ (7.0 wt%). The higher uptake of CO_2 from the amide functionalized CAU-1 compared to CAU-1–$NHCH_3$ could be explained by stronger host–guest interactions of the adsorbent with CO_2. The results of all sorption measurements are summarised in Table 5.

4. Conclusion

In summary, we have demonstrated that in the field of porous materials the presence of guest molecules, like solvent or uncoordinated linker molecules, can easily result in a misinterpretation of the data. Thus, an extensive characterisation of the reaction products of MOF syntheses is mandatory to fully understand structure–property relationships.

In the case of CAU-1, X-ray diffraction, IR- as well as liquid-state and solid-state NMR-spectroscopy, *in situ* EDXRD,

TD-XRPD, thermogravimetric and elemental analysis, sorption experiments and dynamic light scattering have been applied. Surprisingly, not only the synthesis conditions during the product formation lead to isoreticular products of different compositions, *i.e.*, variation of the degree of methylation, but also the activation procedure needs to be controlled in detail.

We showed the various modifications of the organic linker. By conventional heating methylation of the amino residue occurs depending on the reaction time, whereas by MW-assisted synthesis and short reaction times methylation can be suppressed completely. Even post-synthesis modification is possible *via* acetylation of the amino group.

Also the modification of the inorganic brick is possible during the activation process in air *via* substitution of the methoxy by hydroxy groups.

Liquid- and solid-state NMR spectroscopy proved to be an essential tool for the thorough investigation of the synthesis routes. *Via* solid-state NMR spectroscopy the methylation reaction under conventional synthesis conditions was discovered and the post-synthetic modification as well as the linker orientation were studied.

Acknowledgements

The authors thank Michael Wharmby for cross-reading this article and fruitful discussions. The state of Schleswig-Holstein and the Deutsche Forschungsgemeinschaft (DFG, SPP 1362) "Porous Metal–Organic Frameworks" under the grant STO 643/5-2 and SE 1417/3-2 are gratefully acknowledged for the financial support. The research leading to these results has received funding from the European Community's Seventh Framework Programme (FP7/2007-2013) under grant agreement no. 228862.

Notes and references

1 U. Mueller, M. Schubert, F. Teich, H. Puetter, K. Schierle-Arndt and J. Pastre, *J. Mater. Chem.*, 2006, **16**, 626.
2 P. Horcajada, C. Serre, M. Vallet-Reg, M. Sebban, F. Taulelle and G. Férey, *Angew. Chem., Int. Ed.*, 2006, **45**, 5974.
3 J. Li, R. Kuppler and H. Zhou, *Chem. Soc. Rev.*, 2009, **38**, 1477.
4 J. Y. Lee, O. K. Farha, J. Roberts, K. A. Scheidt, S. T. Nguyen and J. T. Hupp, *Chem. Soc. Rev.*, 2009, **38**, 1450.
5 G. Lu and J. T. Hupp, *J. Am. Chem. Soc.*, 2010, **132**, 7832.
6 M. Gaab, N. Trukhan, S. Maurer, R. Gummaraju and U. Müller, *Microporous Mesoporous Mater.*, 2011, DOI: 10.1016/j.micromeso.2011.08.016.
7 (*a*) H. Reinsch, M. Krüger, J. Wack, J. Senker, F. Salles, G. Maurin and N. Stock, *Microporous Mesoporous Mater.* DOI: 10.1016/j.micromeso.2011.05.029; (*b*) C. Volkringer, T. Loiseau, M. Haouas, F. Taulelle, D. Popov, M. Burghammer, C. Riekel, C. Zlotea, F. Cuevas, M. Latroche, D. Phanon, C. Knöfelv, P. L. Llewellyn and G. Férey, *Chem. Mater.*, 2009, **21**, 5783; (*c*) A. Comotti, S. Bracco, P. Sozzani, S. Horike, R. Matsuda, J. Chen, M. Takata, Y. Kubota and S. Kitagawa, *J. Am. Chem. Soc.*, 2008, **130**, 13664.
8 C. Volkringer, T. Loiseau, N. Guillou, G. Férey, M. Haouas, F. Taulelle, N. Audebrand, I. Margiolaki, D. Popov, M. Burghammer and C. Riekel, *Cryst. Growth Des.*, 2009, **9**, 2927.
9 T. Loiseau, C. Serre, C. Huguenard, G. Fink, F. Taulelle, M. Henry, T. Bataille and G. Férey, *Chem.–Eur. J.*, 2004, **10**, 1373.
10 (*a*) T. Loiseau, C. Mellot-Draznieks, H. Muguerra, G. Férey, M. Haouas and F. Taulelle, *C. R. Chim.*, 2005, **8**, 765; (*b*) I. Senkovska, F. Hoffmann, M. Fröba, J. Getzschmann, W. Böhlmann and S. Kaskel, *Microporous Mesoporous Mater.*, 2009, **122**, 93.
11 (*a*) T. Loiseau, L. Lecroq, C. Volkringer, J. Marrot, G. Férey, M. Haouas, F. Taulelle, S. Bourrelly, P. L. Llewellyn and M. Latroche, *J. Am. Chem. Soc.*, 2006, **128**, 10223; (*b*) C. Volkringer, D. Popov, T. Loiseau, G. Férey, M. Burghammer, C. Riekel, M. Haouas and F. Taulelle, *Chem. Mater.*, 2009, **21**, 5695.
12 (*a*) T. Ahnfeldt, J. Moellmer, V. Guillerm, R. Staudt, C. Serre and N. Stock, *Chem.–Eur. J.*, 2011, **23**, 6462; (*b*) S. Biswas, T. Ahnfeldt and N. Stock, *Inorg. Chem.*, 2011, **50**, 9518; (*c*) D. Himsl, D. Wallacher and M. Hartmann, *Angew. Chem., Int. Ed.*, 2009, **48**, 4639.
13 A. Boutina, S. Couck, F.-X. Coudert, P. Serra-Crespo, J. Gascon, F. Kapteijn, A. H. Fuchs and J. F. M. Denayer, *Microporous Mesoporous Mater.*, 2011, **140**, 108.
14 P. Serra-Crespo, E. V. Ramos-Fernandez, J. Gascon and F. Kapteijn, *Chem. Commun.*, 2011, **47**, 8578.
15 K. K. Tanabe and S. M. Cohen, *Chem. Soc. Rev.*, 2011, **40**, 498.
16 (*a*) T. Ahnfeldt, D. Gunzelmann, T. Loiseau, D. Hirsemann, J. Senker, G. Férey and N. Stock, *Inorg. Chem.*, 2009, **48**, 3057; (*b*) J. Gascon, U. Aktay, M. D. Hernandez-Alonso, G. P. M. van Klink and F. Kapteijn, *J. Catal.*, 2009, **261**, 75.
17 T. Ahnfeldt, N. Guillou, D. Gunzelmann, I. Margiolaki, T. Loiseau, G. Férey, J. Senker and N. Stock, *Angew. Chem., Int. Ed.*, 2009, **48**, 5163.
18 P. Serra-Crespo, E. V. Ramos-Fernandez, J. Gascon and F. Kapteijn, *Chem. Mater.*, 2011, **23**, 2565.
19 Comment: CAU-1 refers to the general framework structure of these compounds. In the following the functionalisation of the $-NH_2$ groups ($-NH_2$, $NHCH_3$, $-N(CH_3)_2$) is explicitly stated to prevent further confusion.
20 J. H. Cavka, S. Jakobsen, U. Olsbye, N. Guillou, C. Lamberti, S. Bordiga and K. P. Lillerud, *J. Am. Chem. Soc.*, 2008, **130**, 13850.
21 M. Dan-Hardi, C. Serre, T. Frot, L. Rozes, G. Maurin, C. Sanchez and G. Ferey, *J. Am. Chem. Soc.*, 2009, **131**, 10857.
22 F. Hinterholzinger, C. Scherb, T. Ahnfeldt, N. Stock and T. Bein, *Phys. Chem. Chem. Phys.*, 2010, **12**, 4515.
23 X. Si, C. Jiao, F. Li, J. Zhang, S. Wang, S. Liu, Z. Li, L. Sun, F. Xu, Z. Gabelica and C. Schick, *Energy Environ. Sci.*, 2011, **4**, 4522.
24 M. Pera-Titus, M. Savonnet and D. Farrusseng, *J. Phys. Chem. C*, 2010, **114**, 17665.
25 M. Savonnet, E. Kockrick, A. Camarata, D. Bazer-Bachi, N. Bats, V. Lecocq, C. Pinela and D. Farrusseng, *New J. Chem.*, 2011, **35**, 1892.
26 T. Ahnfeldt and N. Stock, *CrystEngComm*, 2012, **14**, 505.
27 A. Boultif and D. Louer, *J. Appl. Crystallogr.*, 1991, **24**, 987.
28 *STOE WinXPOW version 2.11*, Stoe & Cie GmbH, Darmstadt, Germany, 2005.
29 A. Lesage and L. Emsley, *J. Magn. Reson.*, 2001, **148**, 449.
30 G. Socrates, *Infrared and Raman Characteristic Group Frequencies: Tables and Charts*, Wiley & Sons, West Sussex, UK, 3rd edn, 2004.
31 U. Ravon, M. Savonnet, S. Aguado, M. E. Domine, E. Janneau and D. Farrusseng, *Microporous Mesoporous Mater.*, 2010, **129**, 319.
32 W. Wang, A. Buchholz, M. Seiler and M. Hunger, *J. Am. Chem. Soc.*, 2003, **125**, 15260.
33 W. Wang and M. Hunger, *Acc. Chem. Res.*, 2008, **41**, 895.
34 Z. Wang and S. M. Cohen, *J. Am. Chem. Soc.*, 2007, **129**, 12368.
35 P. Küsgens, M. Rose, I. Senkovska, H. Fröde, A. Henschel, S. Siegle and S. Kaskel, *Microporous Mesoporous Mater.*, 2009, **120**, 325.

Electronic Supplementary Material (ESI) for CrystEngComm

Supporting Information

Controlled modification of the inorganic and organic brick in an Al-based MOF by direct and post-synthetic synthesis routes

Tim Ahnfeldt,[a] Daniel Gunzelmann,[b] Julia Wack,[b] Jürgen Senker[b,*] and Norbert Stock[a,*]

[a]Insitut für Anorganische Chemie, Christian-Albrechts-Universität, Max-Eyth Straße 2, 24118 Kiel, Germany

[b]Anorganische Chemie III, Universität Bayreuth, Universitätsstraße 30, 95447 Bayreuth, Germany

1. Proton-proton homonuclear spin diffusion spectra of CAU-1-NHCH$_3$, and CAU-1-NH$_2$

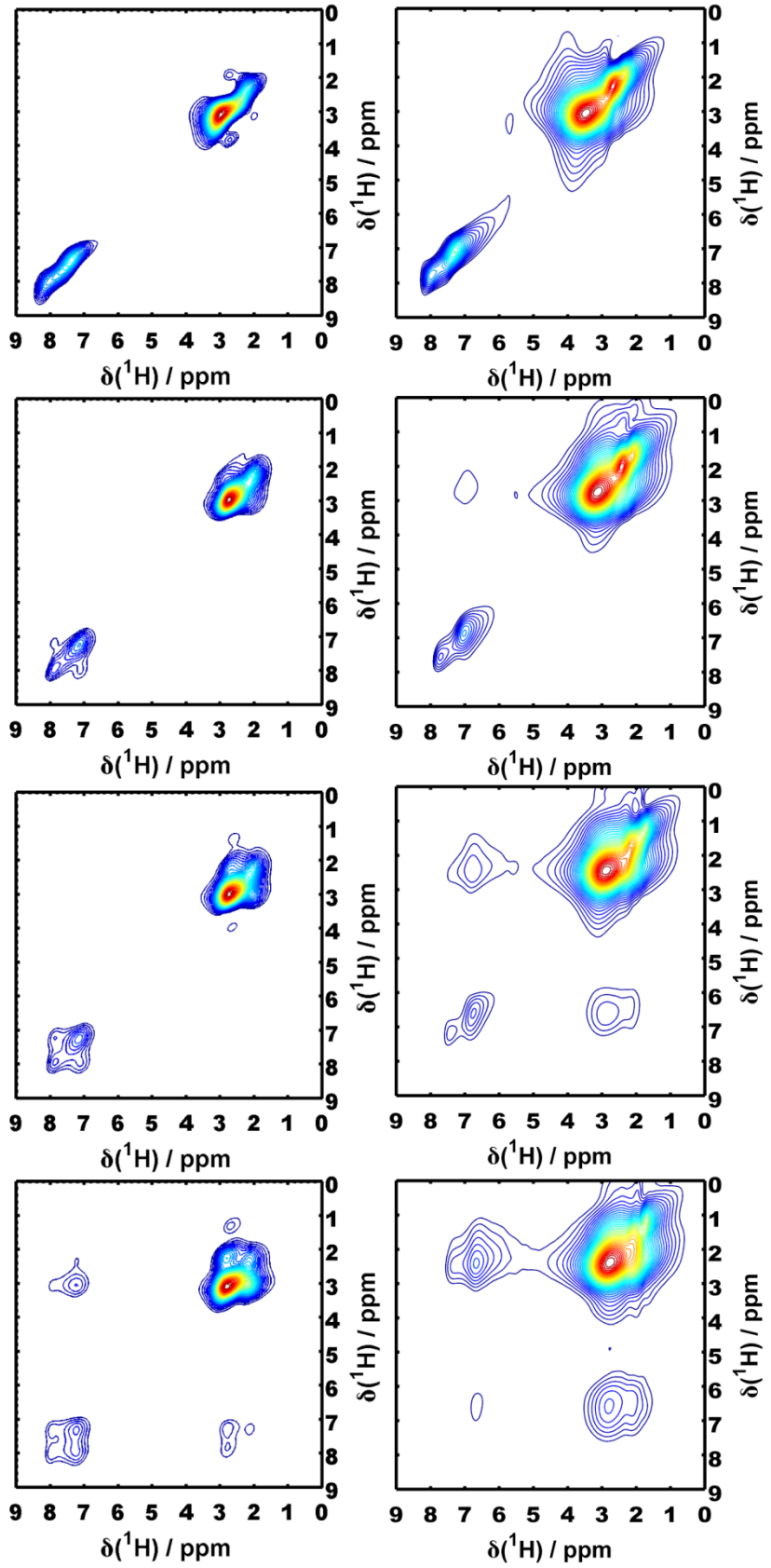

Fig. S1 Proton-Proton Spin-Diffusion Spectra of CAU-1-NHCH$_3$ (left), and CAU-1-NH$_2$ (right) at Spin Diffusion mixing times of 1 µs (top), 700 µs, 1500 µs and 4000 µs (from top to bottom).

2. Carbon-proton HETCOR spectra of CAU-1-$NHCH_3$ and CAU-1-$NHCOCH_3$

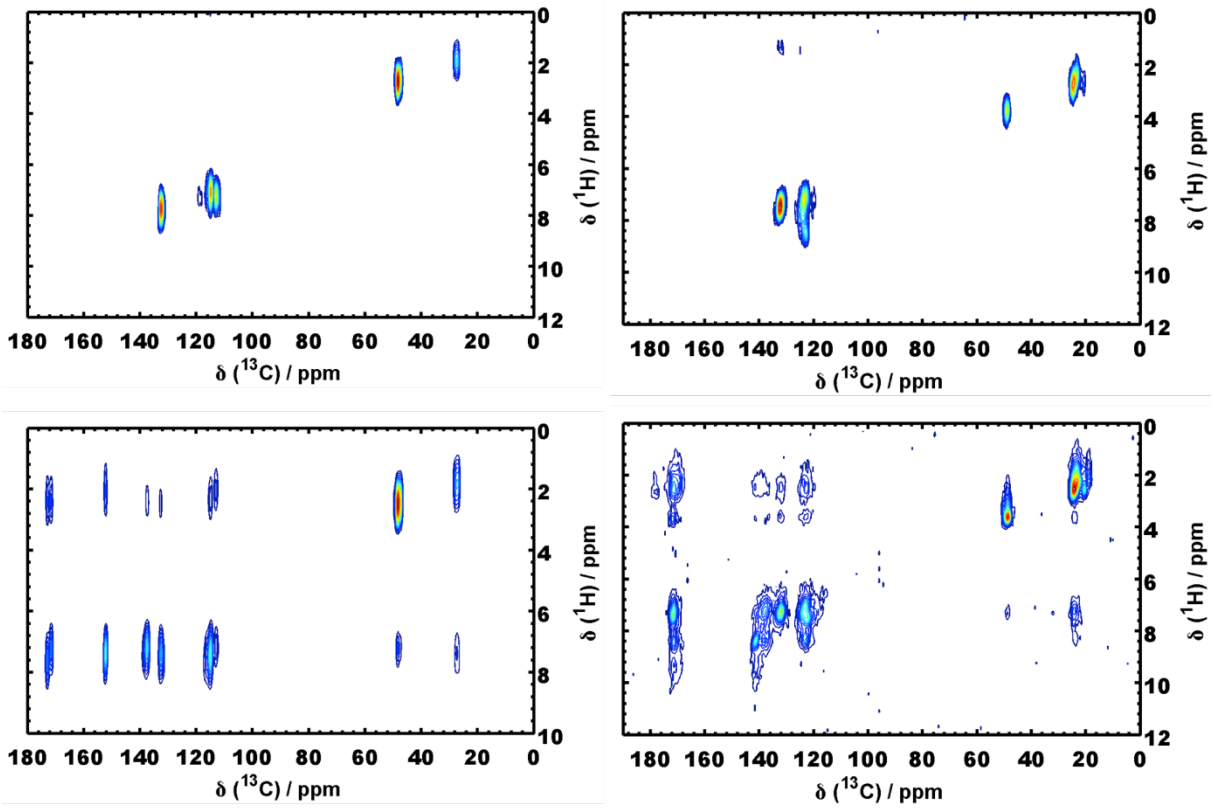

Fig. S2 Carbon-proton HETCOR spectra of CAU-1-$NHCH_3$ (left) and CAU-1-$NHCOCH_3$ (right) at contact times of 75 µs (top) and 1000 µs (bottom) showing short and long distance correlations, respectively.

3. Reaction times to reach full crystallisation (α = 1) determined from the EDXRD studies for MW-assisted reactions

CAU-1 was synthesized by MW-assisted heating in the temperature range 115 - 145 °C. The reaction time for each temperature was determined from EDXRD studies on the product formation of CAU-1-NH_2 and corresponds to the time required to reach full crystallisation, i.e. extent of crystallisation, α = 1 (Table S1).[1]

Tab. S1 Reaction times to reach full crystallisation (α = 1) determined from the EDXRD studies for MW-reactions carried out in the temperature range between 115-145 °C. Values taken form reference [1].

reaction temperature / °C	reaction time / min
115	105
120	65-70
125	42
130	25
135	16
140	10
145	7-9

4. X-ray powder diffraction (XRPD) patterns of CAU-1 obtained by MW-assisted heating at different temperatures

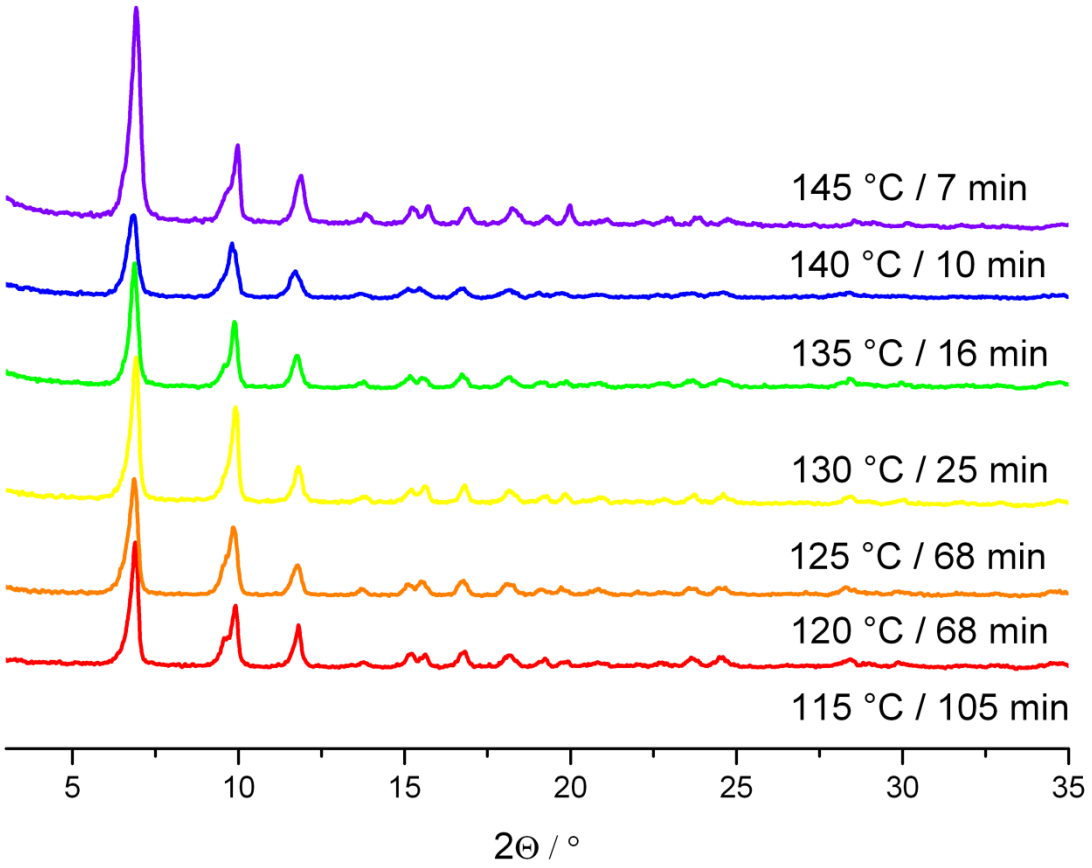

Fig. S3 X-ray powder diffraction (XRPD) patterns for CAU-1 obtained by MW-assisted heating carried out in the temperature range between 115 °C – 145 °C.

5. Time dependence of the methylation of the MW-assisted synthesis at 145 °C

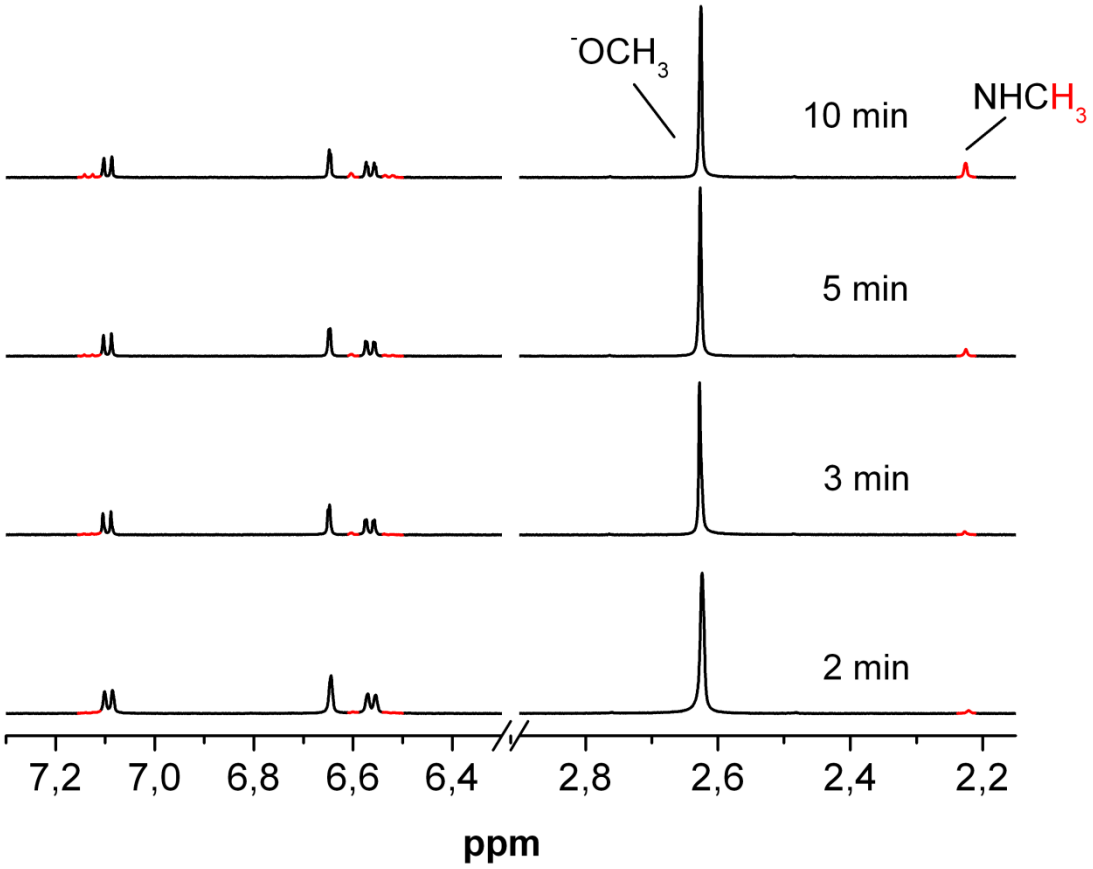

Fig. S4 ^{1}H NMR spectra of the dissolved CAU-1 samples collected from MW-assisted syntheses at 145 °C using reaction times between 2 and 15 min. Each spectrum is normalized to the sum of the aromatic H signals (methylated and non-methylated). Signals due to methylated CAU-1 are highlighted red.

6. Accuracy of ^{1}H NMR spectra and reproducibility of the MW-assisted synthesis of CAU-1-NH_2

In three repeated reactions under identical condition (3min a-c) all directly dissolved products exhibit the identical degree of methylation in the ^{1}H NMR spectra, which clearly shows the good reproducibility of the synthesis and the measurements.

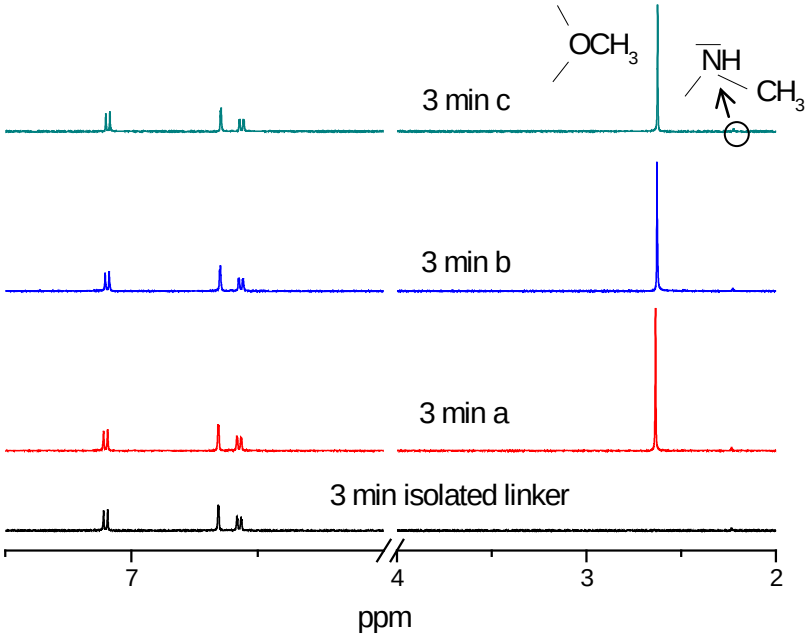

Fig. S5 ^{1}H NMR spectra of the isolated aminoterephthalic acid linker (black) and directly dissolved CAU-1 (red, blue and green) prepared by MW-assisted synthesis at 145 °C using a reaction time of 3 min. Each spectrum is normalized to the sum of aromatic H signals (methylated and unmethylated).

The integral ratios methoxy H-atoms : aromatic H-atoms of the products (3 min a-c) are between 1.14 and 1.21 (1.33 calc.). Thus, approximately 88% of the methoxy groups are incorporated in the framework after this reaction time according to the formula sum. We presume that syntheses at very short reaction times may lead to CAU-1-NH_2 for which a small fraction (12%) of the methoxy groups is replaced by OH-groups. Nevertheless, the product is still very crystalline and exhibits high thermal and chemical stability, such as CAU-1-CH_3 and CAU-1-$CHCOCH_3$.

7. Labelling of the set of ^{1}H signals of the reaction product carrying out under conventional heating method using a glass reactor

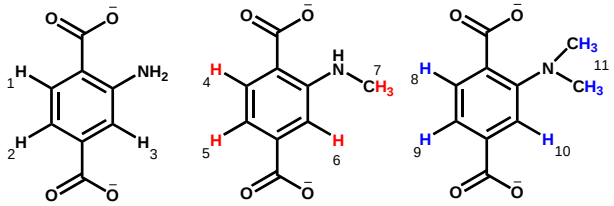

Scheme S1 Labelling of the ^{1}H signals in dimethylated, methylated and non-methylated CAU-1. ^{1}H NMR 500 MHz, (NaOD/D_2O) δ: **BDC-NH_2^{2-}:** 7.23 (d, 1H, H_1 $^{3}J_{H\text{-}H}$ = 8.2Hz); 6.79 (s, 1H, H_3); 6.71 (d, 1H, H_2 $^{3}J_{H\text{-}H}$ = 8.1Hz); **BDC-$NHCH_3^{2-}$:** 7.27 (d, 1H, H_5 $^{3}J_{H\text{-}H}$ = 8.0Hz); 6.76 (s, 1H, H_6); 6.52 (d, 1H, H_5 $^{3}J_{H\text{-}H}$ = 8.0Hz); 2.37 (s,3H,H_7); **BDC-$N(CH_3)_2^{2-}$:** 7.04 (s, 1H, H_{10}); 6.94 (d, 1H, H_9 $^{3}J_{H\text{-}H}$ = 8.0Hz); 6.87 (d, 1H, H_8 $^{3}J_{H\text{-}H}$ = 7.9Hz); 2.28 (s, 6H, H_{11})

8. TG-curve of CAU-1-NH_2

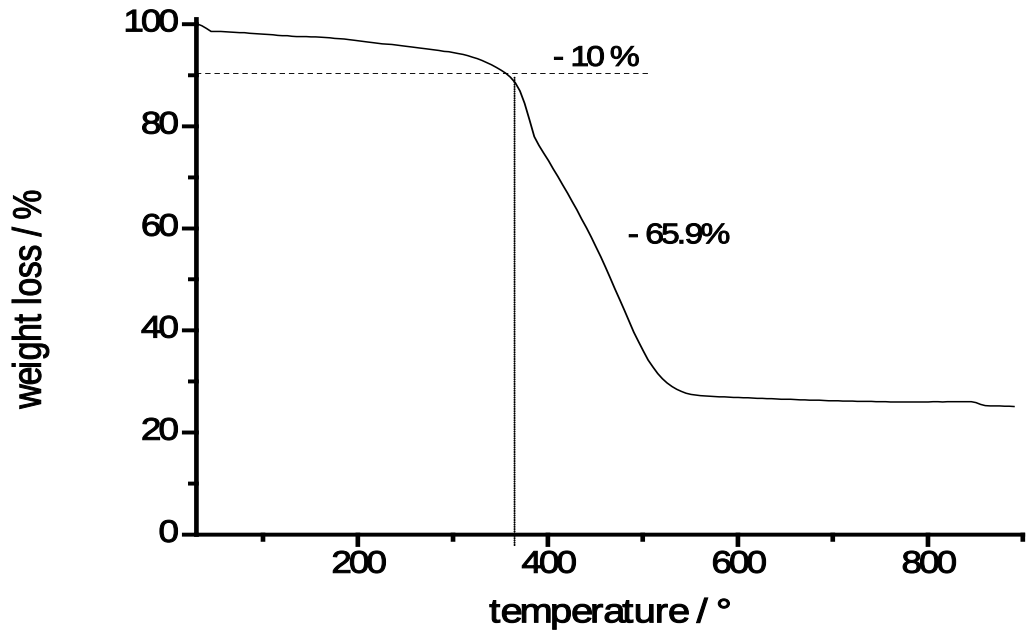

Fig. S6 TG-curve of CAU-1-NH_2 synthesized via MW-heating (3min / 145°C). The sample was measured in air with a heating rate of 4K / min and was degassed (30 min / 130 °C) before the measurement.

9. Activation process screened by ^{1}H NMR

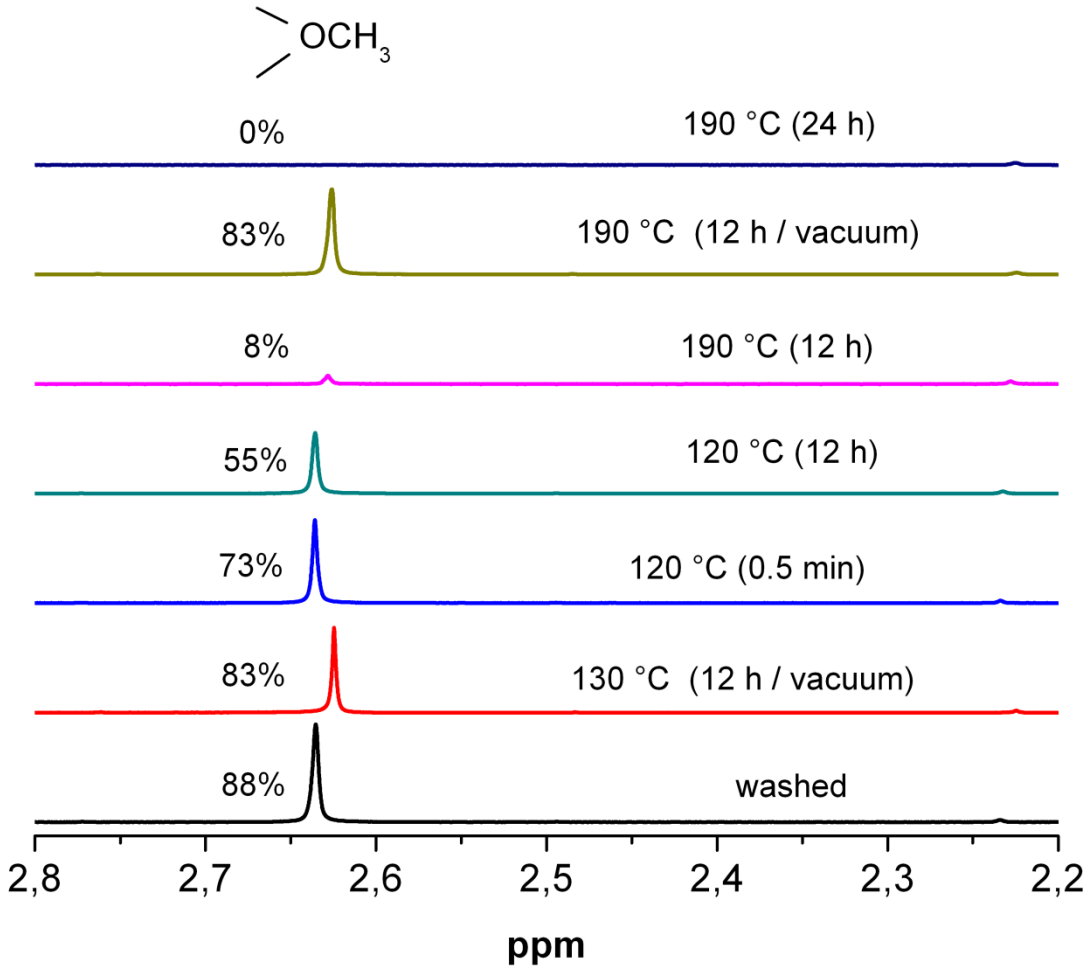

Fig. S7 ^{1}H NMR spectra of differently activated CAU-1-NH_2 compounds prepared by MW-synthesis. After the washing process the compounds were treated using different activation procedures. Each spectrum is normalized to the sum of aromatic H signals (methylated and non-methylated, not shown).

10. Temperature-dependent X-ray powder diffraction measurements (TD-XRPD)

The TD-XRPD measurements of CAU-1-NH_2(OH), CAU-1-$NHCH_3$ and CAU-1-$NHCOCH_3$ are shown in Figure S8-S10. The data were obtained under air with a STOE STADI P diffractometer equipped with an image plate detector and a STOE capillary furnace (version 0.65.1) using monochromated Cu-$K_{\alpha 1}$ radiation. Each powder pattern was recorded in the 4-35° range (2θ) at intervals of 10 °C up to 350 °C, and interval of 25 °C from 350-400 °C with duration of 15 min per scan. The temperature ramp between two patterns was set to 2 °C min^{-1}.

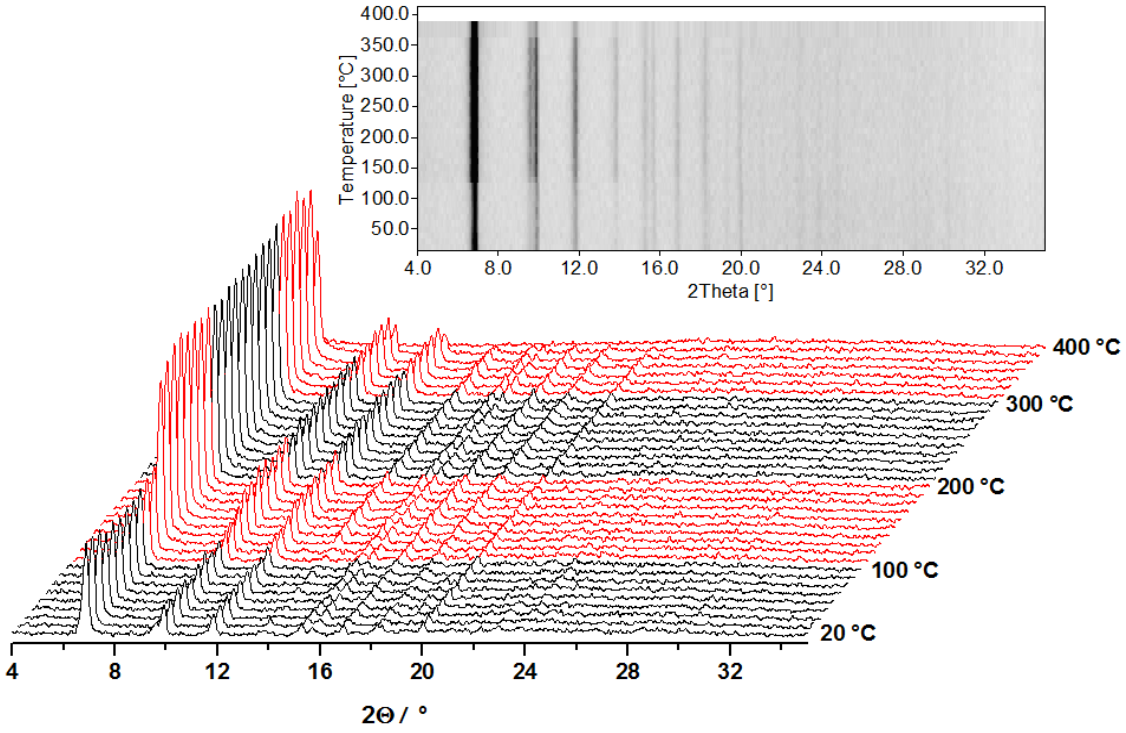

Fig. S8 Temperature-dependent X-ray powder diffraction patterns of CAU-1-NH_2(OH), $[Al_4(OH)_6((BDC\text{-}NH_2)_3]\cdot xH_2O$, in air (20 - 400 °C).

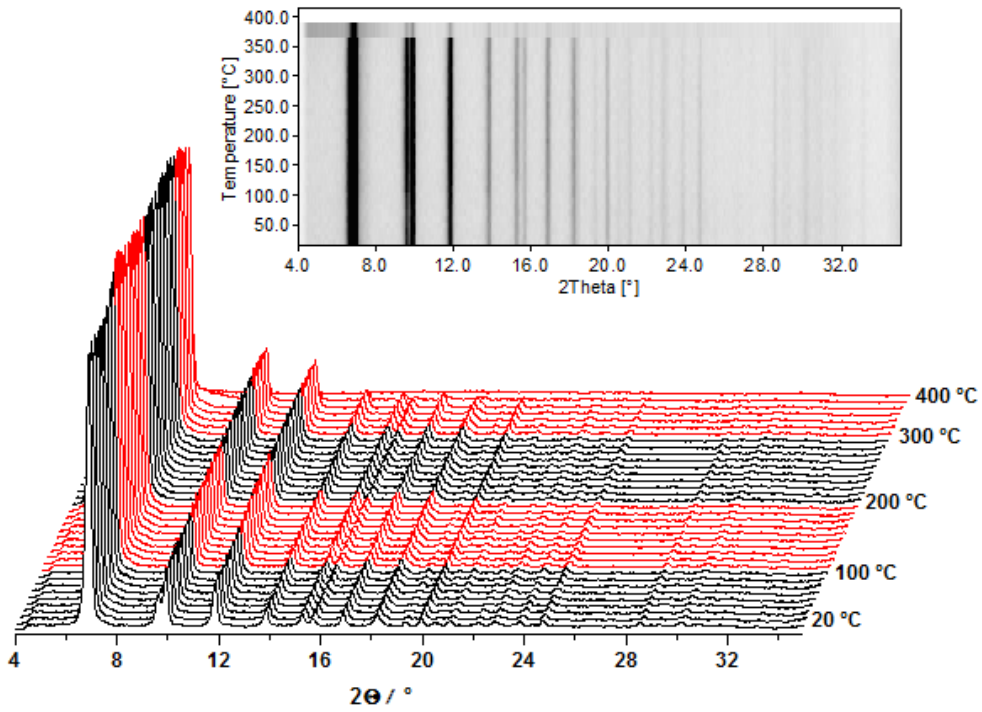

Fig. S9 Temperature-dependent X-ray powder diffraction patterns of CAU-1-NHCH$_3$, $[Al_4(OH)_2(OCH_3)_4(BDC\text{-}NHCH_3)_3]\cdot xH_2O$, in air (20 - 400 °C).

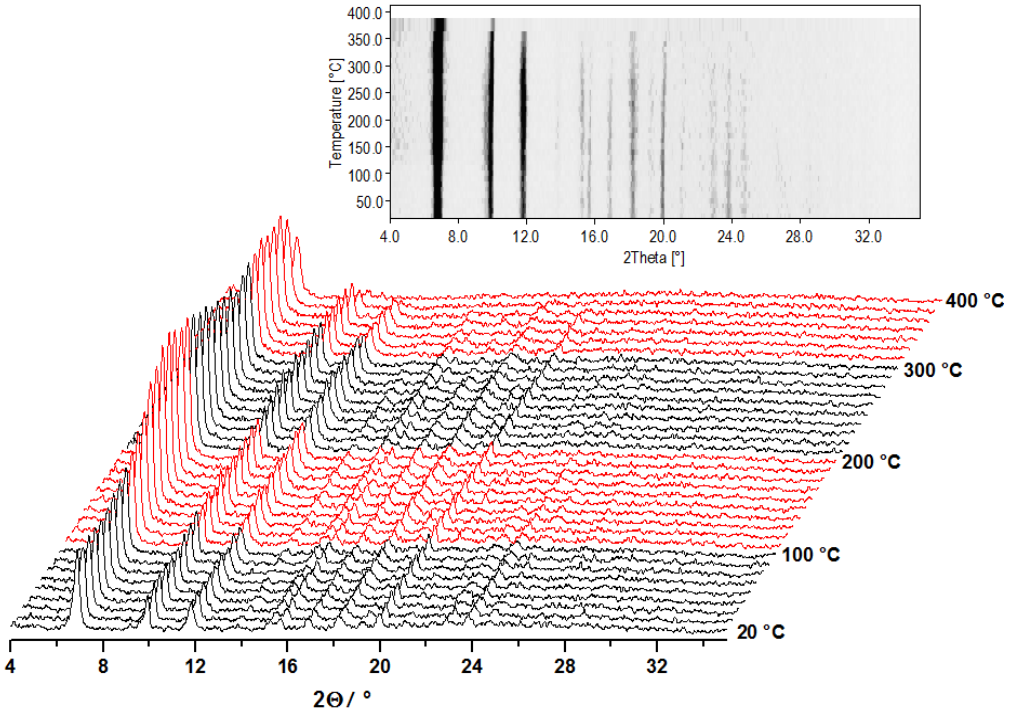

Fig. S10 Temperature-dependent X-ray powder diffraction patterns of CAU-1-NHCOCH$_3$, $[Al_4(OH)_2(OCH_3)_4(BDC\text{-}NHCOCH_3)_3]\cdot xH_2O$, in air (20 - 400 °C).

Literature

[1] T. Ahnfeldt, N. Stock, *CrystEngComm*, **2011**, doi:110.1039/c1ce05956d

9 Preferred orientation of the formamido hydrogen bond anchor in MIL-53-NHCHO

Preferred orientation of the formamido hydrogen bond anchor in MIL-53-NHCHO

Julia Wack,[†] Tim Ahnfeldt,[†] Carsten B. L. Tschense,[†] Norbert Stock,[‡] and Juergen Senker[*,†]

Department of Inorganic Chemistry III,University of Bayreuth, Bayreuth, and Department of Chemistry, Christian Albrechts University Kiel, Kiel

E-mail: juergen.senker@uni-bayreuth.de

Phone: +49(0)921 / 55-2532. Fax: +49 (0)921/55-2788

Abstract

Functional groups are introduced in porous materials to enhance selective interactions of the pore walls with adsorbed guest molecules. Usually a statistical distribution of functional groups in the pores is assumed, which results that the functional groups are accessible from all sites. Using NMR crystallography strategies we demonstrate the clustering of the formamido groups in the pores of postsynthetically modified MIL-53-NHCHO, leading to partially blocked anchor groups. To yield a NMR active sensor, ^{13}C labels are introduced in the functional groups during the PSM of the MOF framework. In this contribution, the alignment of of the formamido groups in the pores of MIL-53-NH^{13}CHO is probed by a combination of DQ build up curves, static wideline experiments and DFT calculations. These investigations were performed on two systems MIL-53-NH^{13}CHO/acetone and MIL-53-NH^{13}CHO/water to determine whether

*To whom correspondence should be addressed
[†]University of Bayreuth
[‡]Christian-Albrechts-Universität zu Kiel

the incorporated guest molecules introduce or influence the alignment of the formamido groups. It was previously shown that the acetone molecules are hydrogen bound to the formamido group while the water molecules do not participate in a selective host guest interaction. We can show that the guest molecules have no influence on the orientation of the functional group in MIL-53-NH13CHO, which hints at a preorientation during synthesis.

Introduction

Metal-organic frameworks (MOFs) are a class of highly crystalline and porous materials, which offer a large potential for different applications like drug delivery,[1–4] gas separation,[5–7] gas storage[8,9] and as sensor devices.[10–12] All these applications rely crucially on the interaction between the frameworks pore wall and the incorporated guest molecules. To enhance these interactions the introduction of functionality into the pores of MOFs has become a vividly investigated field in the last 20 years.[13–15] Meanwhile several strategies for the modification of the pore wall have been developed, like premodification via isoreticular linker molecules,[16,17] mixed linker approach[18,19] and postsynthetic modification (PSM).[20,21] The isoreticular synthesis is limited to functional groups, which remain stable during solvothermal synthesis, while the mixed linker approach limits the amount of functional groups in the pore. The most promising candidate for the synthesis of groups with multifunctionality is the PSM. A good starting point for PSM is a MOF containing free amino groups.

The isoreticular synthesis of many MOFs, to yield the corresponding amino MOF (eg. IRMOF-3,[22] MIL-53-NH2[16] and CAU-1[23]) is very common, since the amino functionality provides many possibilities for covalent PSM. The formation of amides can be achieved by using linear alkyl chain anhydrides[15] or formic acid,[16] while urea groups are formed when isocyanates[24,25] are used for the modification. For the formation of secondary or ternary amines a tandem condensation-reduction reaction is used.[26] The effects of the functionalization on the host-guest interactions is so far measured indirectly in adsorption studies[17] or

theoretically via molecular modeling.[27]

Recently, we could demonstrate that if the guest molecules have the right size (van der waals interaction with the pore wall) and bonding motive (hydrogen bond with the functional group) a specific interaction with the framework is achieved. This means for an interaction with a guest molecule the functional group has to have a high selectivity but also has to be accessible freely by the guest molecules. Therefore, the correlation between the anchor groups has to be minimized.

To study the local ordering of functional groups in MOFS, NMR (Nuclear Magnetic Resonance) crystallography provides a powerful tool to investigate local order/disorder on the length scale even on a molecular level.[28–30] The power of this approach lies in the combination of complementary methods. To fully exploit all information an approach combining solid-state NMR experiments with computational methods is advantageous.[31] Since the use of calculations allows for the connection between structure models and measured data. The possibilities of this approach was recently published in a review article.[32]

In principle there are two methods for DFT calculations, the local ones of single molecules or clusters and the plane wave (pw) approach, which accounts for the periodic nature of crystals. Since the computational cost of pw calculations is rather high, often cluster models are used to interpret solid-state NMR experiments.[33,34]

Whereas in the majority of investigations the focus is on evaluation of the isotropic chemical shift for the investigations on structural effects, we focus on the full CSA (chemical shift anisotropy) tensor. The calculations of the anisotropic parameters offer a method, which is highly accurate at low cost.[35] Furthermore, it was shown in literature that e.g. all ^{13}C tensors for α-glucose and α-glucose$\cdot H_2O$ could be reproduced correctly by pw DFT calculations[36] or the effect of hydrogen bonding on the ^{15}N tensors of benzamide could be followed by DFT calculations.[37]

On the solid-state NMR site, the lineshape of slow MAS or static spectra for spin=1/2 nuclei allows to provide information on the full CSA tensors of one functional groups. First

step to get insights into the local arrangement of anchor groups towards each other a distance measurement between groups is helpful. The distance measurement in solid-sate NMR relies on the dipolar interactions $D_{dip} \propto 1/r^3$. To measure homonuclear distances double quantum filtered experiments enjoy a great popularity. They are applied for a wide range of different materials. Recently for the investigation of the photointermediate of rhodopsin,[38] but also for inorganic phosphates and phosphorous sulfides[39] or for medium range distances in small organic molecules[40] and for very long distances in polymers[41–43] and even for the investigation of host-guest interactions in inclusion compounds the distance between ^{129}Xe atoms.[44]

In this work we use NMR crystallography to determine the orientation of the formamido groups in functionalized MIL-53-NHCHO dependent on the guest molecules water and acetone. DQ filtered build-up experimentss reveal the position, where the bdc linker molecules are functionalized via distance measurements.

Experimental Details

Synthesis

MIL-53-NH_2 was synthesized according to a previously published procedure.[16] 1.0 g of the as-synthesized product MIL-53-NH_2-as was heated in N,N'-dimethylformamide (DMF; 60 mL) at 150 °C for 24 h in a conventional oven to remove the excess terephthalic acid. The filtered solid was heated four times at 130 °C for 4 h in a methanol/water mixture (1:1, 100mL) in a conventional oven to remove DMF from the pore space. This activation procedure is crucial for the PSM of MIL-53-NH_2. Even small traces of DMF within the pores lead to a decreased amount of modified amino groups. The yellow solid was collected by filtration, washed with water ((Al)MIL-53-NH_2-lt) and annealed at 130 °C for 12 h in a conventional oven. The product was characterized with the standard methods (XRD, NMR and elemental analysis).

Postsynthetic Modification of MIL-53-NH_2(lt):

To 500 mg of Al(OH)[H_2N-BDC]·0.9H2O (2.0 mmol), 500 μL of ^{13}C- enriched formic

acid (13.3 mmol) was added in a 100 mL beaker. The reaction at 70 °C for 5 h, followed by washing with H_2O and heating in air (100 °C, 2 h), leads to the formation of formamido groups ((Al)MIL-53-NH^{13}CHO, Al(OH)[OH^{13}CN-BDC] ·H_2O).

Loading with guest molecules:

150 mg of MIL-53 (synthesized according to ref.,[45] $AlCl_3$· 6 H_2O was used instead of $Al(NO_3)_3$· $9H_2O$), MIL-53-NH_2 (synthesized according to ref.[16]), MIL-53-NO_2 (synthesized according to ref.[17]) and MIL-53-NH^{13}CHO were put into schlenk flasks and dried for 8 hours at 120 °C under HV. With argon passing through the reaction zone counter-current to the functionalized MOFs dry acetone was added in excess. For three hours the system was equilibrated, afterward the excess acetone was evaporated at room temperature under argon. The samples with the guest molecules inside were handled for all measurements under argon.

Solid-State NMR

The solid-state NMR experiments were performed on an AVANCE II 300 Bruker wide-bore spectrometer (B_0 = 7.05 T). All samples were packed in 4 mm CRAMPS MAS ZrO_2 rotors under inert gas atmosphere and measured with a triple resonance Bruker 4 mm probe. The ^{13}C chemical shifts were referenced relative to TMS while the ^{15}N chemical shifts were referenced relative to CH_3NO_2. The excitation of ^{13}C and ^{15}N in the MAS experiments was achieved via a ramped cross polarization (CP) transfer using the polarization of the proton bath.[46] Meanwhile the power on the proton channel was varied from 100 % to 50 %. For the CP measurements a five times saturation cycle with five 90 pulses was applied on the proton and for the direct experiments on the carbon channel. All MAS and DQ experiments were measured with proton decoupling using the SPINAL-64 decoupling scheme[47] and a nutation frequency between 70 kHz - 80 kHz during acquisition.

1D CP spectra for MIL-53-NH_2 and MIL-53-NH^{13}CHO were carried out at a spinning frequency ν_{rot} of 12.5 kHz with a CP contact time of 3 ms and a recycle delay of 2 s.

For the determination of the full chemical shift tensor a static 1D ^{13}C was recorded with the hahn-echo sequence. For shorter measurement times the carbon nuclei were excited via CP. During acquisition a continuous wave decoupling with a strength of 70 kHz was applied.

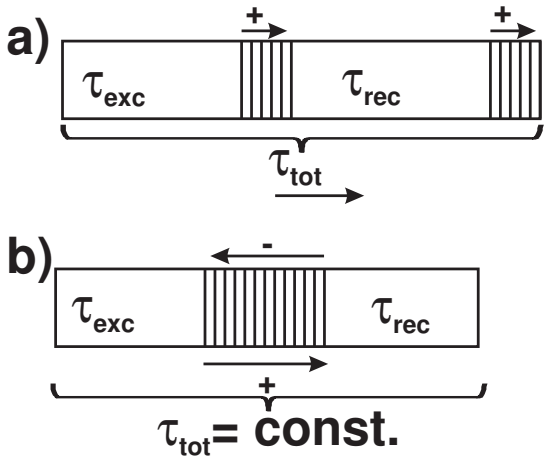

Figure 1: Difference between the symmetrical (a)) and CT (b)) build up procedures.The arrows are indicating the direction in which the incrementation of the recoupling time is incremented during the experiment.

To measure the distances between the functional groups we used DQ build up experiments. For the calibration of all experiments 1,3-$^{13}C_2$-malonic acid was used. (see Figure S1-S5 in the ESI) The framework geometry of MIL-53 suggests rather long distances up to 8 Å. Therefore, we use the $SR26_4^{11}$ recoupling sequence designed for small dipolar couplings. For the measurement of small couplings the excitation time often gets quite long. The challenge with long mixing time is the problem with the damping of the DQ signal due to small rf inhomogeneities of the RN pulse train, which leads to residual CSA and the remaining of interactions with covalently bond protons even under high proton decoupling and due to the T_2 relaxation.[39,48] There are three different experimental procedures to get around this problem. The two which were measured here are displayed in figure 1. In the case of an symmetrical measured experiment (see figure 1 b) a reference experiment with the antiphasecycle, which selects zero quantum coherences, has to be taken, to allow for the compensation of T_2 damping. Another possibility to overcome this challenge is the constant

time (CT) protocol which was designed to keep the overall recoupling time constant (see figure 1 b), in order to remove the influence of the T_2 relaxation on the curve. Thus no reference experiment has to be taken and the curve can only be multiplied with a scalar value.

For all 1D DQ filtered ^{13}C experiments a $SR26_4^{11}$ recoupling sequence[49] with the classical 16 times phase cycle was used. The MAS rotation frequency was set to $\nu_{rot} = 6.25$ kHz, which results in a ^{13}C nutation frequency of 40.625 kHz for the DQ excitation and reconversion. Parallel to the total recoupling time, continuous wave (cw) proton decoupling applied with a nutation frequency ν_{nut} of approximately 110 kHz was used. The z-filter in these experiments was set to 5 ms and the recycle delay to 5 s. All 2D experiments were recorded applying the STATES-TPPI method. The here presented CT build up curve of MIL-53-NH^{13}CHO was measured at a total recoupling time of $\tau_{mix} = 30.72$ ms. For the 2D build-up curve a row of 14 2D spectra at a MAS rotation frequency $\nu_{rot} = 8.0$ kHz ($\nu_{nut}(^{13}C) = 52$ kHz) was measured with τ_{exc} from 0 ms to 13 ms.

Simulation

Simulation of the DQ build-up curves: The simulations of the DQ build-up curves were performed with the SIMPSON simulation program version 3.1.0.[50] Beforehand convergence was determined to 320 crystal orientations and 15 γ-angles, for a symmetrical build up curve at 4.00 Å. The fit of the simulation to the experimental data was performed with self-written python scripts using NumPy and SciPy. For these fits the RMSD was minimized using the L-BFGS-B algorithm.[51] For ideal spin pairs the build up can be solved analytically with the following Bessel functions[52] for the symmetrical protocol it equals:

$$f_{DQ}^{sym}(\tau) = 1/2 - \frac{\sqrt{2}\pi}{8} J_{1/4}(3/2\,|\kappa|\,b_{jk}\tau)\, J_{-1/4}(3/2\,|\kappa|\,b_{jk}\tau) \tag{1}$$

and for the CT protocol (with $-T/2 \leq \tau \leq T/2$):

$$f_{DQ}^{CT}(\tau, T) = \frac{\sqrt{2}\pi}{8}\left\{J_{1/4}(3/2\,|\kappa|\,b_{jk}\tau)\,J_{-1/4}(3/2\,|\kappa|\,b_{jk}\tau) - J_{1/4}(3/4\,|\kappa|\,b_{jk}\tau)\,J_{-1/4}(3/4\,|\kappa|\,b_{jk}\tau)\right\} \tag{2}$$

Simulation of the static 1D spectrum For the simulation of the 1D ^{13}C spectrum the SIMPSON[50] simulation program version 3.1.0 was used. The powder averaging was achieved with a *repulsion*-file containing 8000 crystallite orientations and the linebroadening was set to 1000 Hz.

DFT calculations

All plane wave calculations were carried out with the CASTEP[53] and the CASTEP NMR[54,55] simulation package version 6.01, using the PBE functional for the correlation-exchange energy approximation. For the corrections of the dispersion interactions the module DFT-SEDC[56] was included. No symmetry detection was used, and all the structures were given in P1. NMR parameters calculations dependent on the torsion angle (α) between the formamido functional group and the aromatic ring were performed. Therefore, starting from a minimized MIL-53 with one functional group within one unit cell, structures with α set to 0°, 40°, 80°, 120°, 160°, 200°, 240°, 280°, 320° were built. These structure were first geometry optimized with this torsion angle biased. For the minimized structure the NMR parameter were calculated. Beforehand the optimum accuracy of the calculation were derived in a convergence study. Therefore, a row of these calculations were performed as a function of the cutoff energy (600 - 1200 eV) and another row as a function of the k-point spacing (0.04 - 0.08). For a cutoff energy of 1000 eV and a k-point spacing of (0.07 ≡ number of k-point = 3) the change in the principle values of CSA tensor were less than 0.01 % compared to the calculation with the lower parameters (900 eV and k-point spacing = 0.08). Consequently a cut off energy of 1000 eV and a k-point spacing of 0.07 was used throughout all the pw calculations.

Results and Discussion

Isotope enrichment of the functional groups.

With the introduction of functional groups into the pores, the question arises if these groups are oriented preferentially in the pore space. In the case of formamido functionalized MIL-53 there are many possibilities how the functional groups could arrange. Since there is only one functional groups bound to the terephthalic acid linker which offers four possible sites for functionalization and there are two different functional groups in one pore there are many possible isomers. These isomers are distinguishable by the distances between the formamido functional groups. Figure 2 shows schematically the different possible distances between the formamido groups in one pore of MIL-53-NHCHO, measured from formamido carbon to formamido carbon. These distances within one pore are between 4.0 Å and 8.5 Å. Additionally, the groups can have different conformations, which could vary these distances by $\approx$ 0.5 Å.

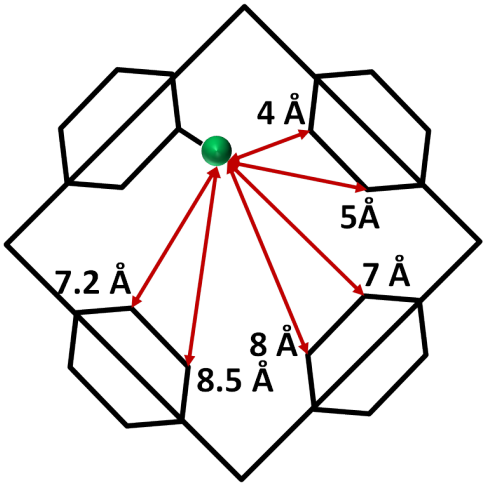

Figure 2: Possible distances between the formamido functional groups in MIL-53-NHCHO.

NMR crystallography offers the opportunity to determine, which orientation the functional groups in the pore have. DQ build up curves provide a tool for measuring the distances between the anchor groups, while a combination of static solid state NMR with DFT calculations gives information about the conformation of the functional groups.

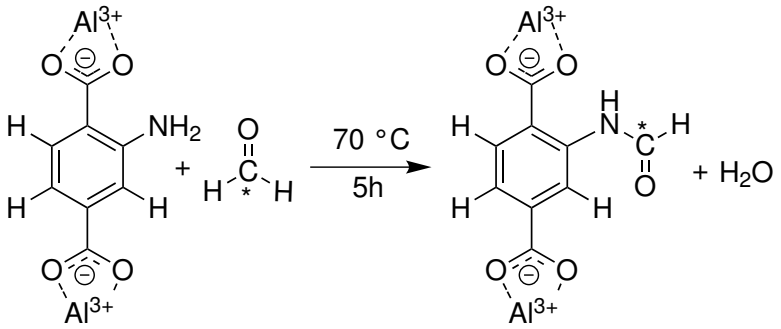

Figure 3: Reaction scheme for the postsynthetic modification of MIL-53-NH_2 with ^{13}C formic acid to form MIL-53-$NH^{13}CHO$.

For these investigations the introduction of a ^{13}C label as NMR active sensor in the anchor groups is necessary. This is achieved by using ^{13}C -enriched formic acid for the PSM of MIL-53-NH_2. The scheme for this reaction is provided in Figure 3. The degree of functionalization was followed using solid-state NMR spectroscopy. To investigate the influence of the guest molecules on the orientation of the functional groups MIL-53-$NH^{13}CHO$ with two different guest molecules was investigated. At ambient conditions, water molecules are adsorbed, which perform no selective interactions with the functional groups. For the second sample, after removing the water, we adsorbed acetone molecules at the pore wall of MIL-53-$NH^{13}CHO$, since the acetone molecules are selectively bound to the formamido groups.

In Figure 4 a comparison of the ^{13}C CP MAS spectra of the MOF before and after the PSM is shown. The signal for the carbon atom carrying the amino group occurs typically at 150 ppm and shifts with the amide formation completely to 140 ppm. Additionally, the signal in the ^{15}N CP MAS spectrum is completely shifted to -249 ppm (NH) (see Figure S6 supporting information), while in MIL-53-NH_2 the signal occurs at -315 ppm (NH_2).[16] This leads to the conclusion that 100 % of the NH_2-groups are converted into formamido-groups, which is the so far highest reported degree of conversion for PSM in this compound.

The formamido signal of both samples, MIL-53-^{13}CHO/water and MIL-53-$NH^{13}CHO$/acetone (see Figure 4 inset and Figure S7, respectively), shows a splitting into two resonances. Indi-

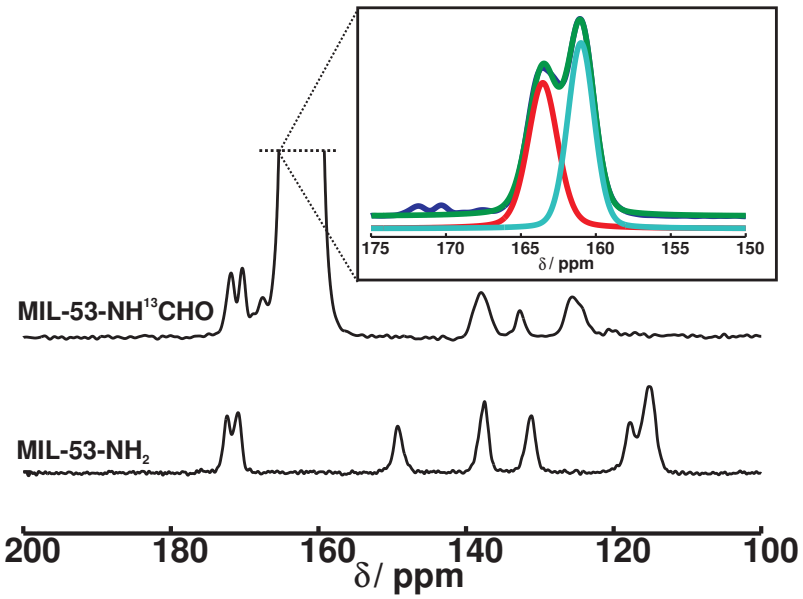

Figure 4: ^{13}C CP MAS spectrum of MIL-53-NH_2/water and the postsynthetically modified enriched MIL-53-NH^{13}CHO/water (ν_{rot} = 12.5 kHz; B0 = 7.05 T). The insert shows the deconvolution of the enriched formamido signal into two ^{13}C resonances with an intensity ratio of 1.00(2):0.93(2).

cating that there are at least two different environments for the functional groups in MIL-53-NH^{13}CHO independent from the adsorbed guest molecules.

Determining the torsion angle of the formamido group

First we determined the conformation of the formamido groups within the pores of MIL-53-NH^{13}CHO based on the analysis of the full ^{13}C chemical shift tensor of the enriched amide carbon. For the extraction of the CSA tensor parameters the static ^{13}C 1D CP spectrum in Figure 5 was used. By refining the lineshape of the measured spectrum we could derive the principal values of the CSA Tensor to δ_{aniso} = 86 ppm for the anisotropy parameter and to η = 0.65 for the asymmetry. The CSA tensor parameters are dependent on the chemical surrounding and the orientation of a nucleus.

With the help of DFT calculations we evaluated different structure models of MIL-53-NH^{13}CHO regarding to match with the experimental values. Therefore, plane wave (pw) calculation were performed, to take into account the influence of the MOF network on the CSA tensors.

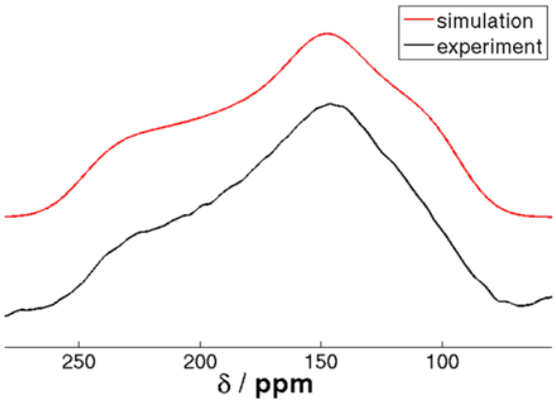

Figure 5: Static ^{13}C CP 1D wideline spectrum of MIL-53-NH^{13}CHO (black) and simulation of the lineshape with SIMPSON (red).

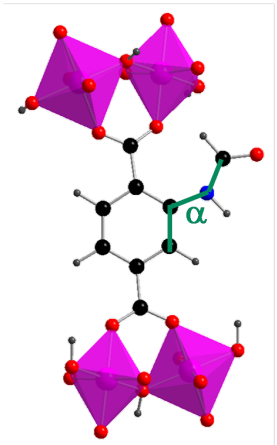

Figure 6: Torsion angle varied for the calculation of the CSA parameters.

Since the aromatic ring and the peptide bond are both planar due to delocalized π-systems, the only degree of freedom is the torsion angle between the aromatic ring and the functional group (see Figure 6). Therefore, we performed a row of calculations as a function of this torsion angle α. On account of the isomerism of the peptide bond two different sets of calculations, one for the CIS and one for the TRANS isomer, were carried out.

Therefore, we again carried out the calculations on an structure model containing one unit cell of the MIL-53 network with one functional group attached to the bdc molecule. Using this nine structures varying the torsion angle α shown in Figure 6 in steps of 40° were built for each isomer. In Figure 7 the resulting CSA parameters as a function of α are

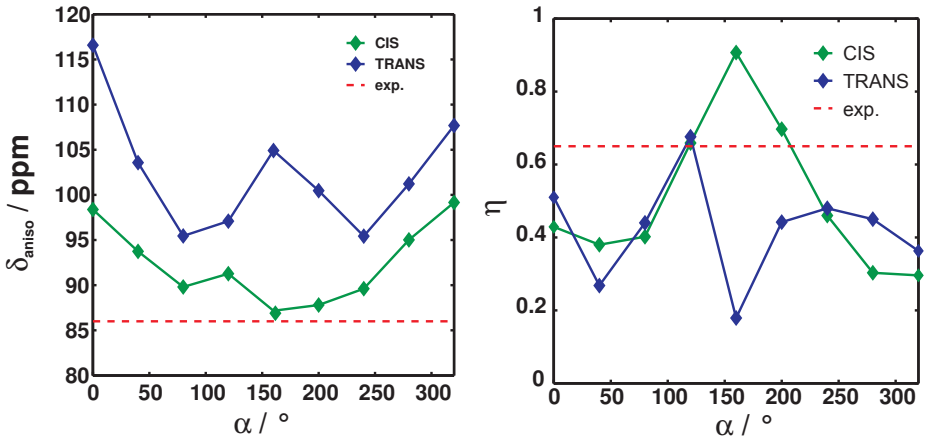

Figure 7: Dependance of δ_{aniso} on α for MIL-53-NH^{13}CHO determined by pw DFT calculations.

shown. The distribution of both parameters are ranging from 87.2 -99.2 ppm for δ_{aniso} and 0.27 - 0.91 for η using the CIS form and from 95.4 -116.6 ppm for δ_{aniso} and 0.18 - 0.68 for η using the TRANS isomer. To match the experimental values the structure with $\alpha = 200°$ is suited best, since $\delta_{aniso} = 87.8$ ppm (2.1 %) and $\eta = 0.69$ (6.1 %). Astonishingly, the best fits between calculations and experiment are achieved by the structure models including the naturally less abundant CIS isomer. This leads to the conclusion that the amide groups in MIL-53-NHCHO have CIS configuration and are twisted by 200° to the aromatic core of the linker molecule.

Double Quantum Build up Curves

To shed light on the configuration of the functional groups within the pores of MIL-53-NH^{13}CHO, we made use of distance measurements with DQ build up curves. To test the robustness and accuracy of the chosen SR26$_4^{11}$ recoupling sequence we used 1,3-$^{13}C_2$-malonic acid as a model (see Figure S1 – S5 in the supporting information). The distance between the enriched carbons in malonic acid could be derived by the DQ experiment and simulation with a spin pair with an error of 0.1 Å to 2.5 Å.

In the CP spectrum of MIL-53-NH^{13}CHO the signal of the formamido group is split into two signals (Figure 4). Thus, three DQ correlations can be excited. To measure all of the correlation we performed a row of 2D ^{13}C-^{13}C DQ-SQ spectra as a function of the

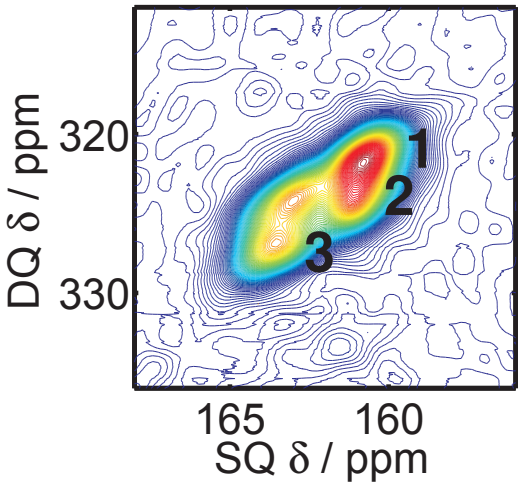

Figure 8: ^{13}C DQ filtered 2D experiment MIL-53-NH^{13}CHO at τ_{exc} = 7.0 ms.

excitation time τ_{exc}, which were afterward deconvoluted using 2D Gauss/Lorentz functions. Representative, the spectrum at τ_{exc} = 7.0 ms is displayed in Figure 8. For all 2D spectra the three possible coherences, two self and one cross coherence, are observed. The two DQ auto correlation peaks occur at 161 + 161 = 322 ppm (see Figure 8 peak 1) and 163 +163 = 326 ppm (see Figure 8 peak 3) as well as a DQ cross peak at 161 + 163 =324 ppm (see Figure 8 peak 2). Since the peaks are all overlapping it is necessary to fit all spectra with 2D Gauss and Lorentz functions (see Figure S8) to derive the intensity of each signal at each mixing time. The resulting intensity build-up is shown in figure 9.

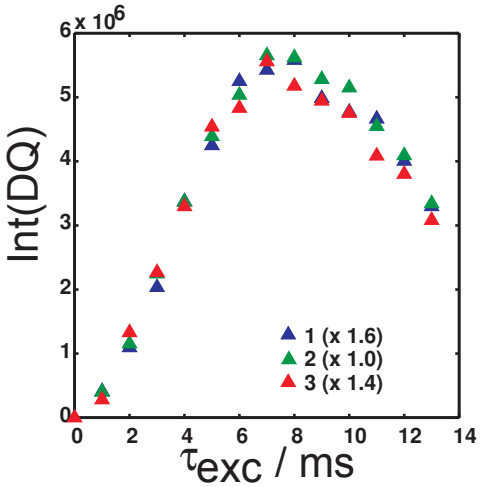

Figure 9: ^{13}C build-up curve derived from a row of 2D spectra for MIL-53-NH^{13}CHO for the three signal indicated in Figure 8. The values in the legend show the factor for the intensity.

Although the individual intensities differ the observed build up behavior for all three coherences is similar. This indicates that there are two different functional groups in two different scenarios but still the functional groups between each other exhibit similar distances. Since all signals show the same build up, we can use the build-up in a 1D fashion for simulating the curves, and can so extract the distance between the ^{13}C enriched groups.

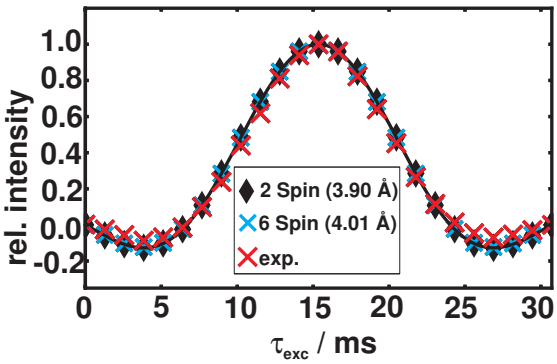

Figure 10: 1D ^{13}C CT build-up curve for MIL-53-NH^{13}CHO/water at τ_{tot} = 30.72 ms (red cross). The SIMPSON simulation for a spin pair with 3.9 Å (black diamonds) and a spin pair of 4.01 Å with four additional spins 6.6 Å away (blue cross). The black solid line displays the Bessel function for 3.9Å

.

Therefore, we recorded for both samples, MIL-53-NH^{13}CHO/water and NH^{13}CHO/acetone 1D CT build-up curves. In figure 10 the 1D CT build-up curve at τ_{tot} = 30.72 ms for MIL-53-NH^{13}CHO with water is shown. For the extraction of the distances we simulated the build-up curve with the SIMPSON simulation package.[50] First we used the most basic spinsystem, containing two ^{13}C spins, for the fitting of the curve. This resulted in a distance of 3.91 Å (RMSD = 0.031) for the ^{13}C nuclei in the functional groups. To check the influence of other functional groups in the vicinity of the spin pair, we used simulations containing 6 ^{13}C spins, a spin pair with variable distance and four spins being 6.6 Å (lattice parameter c) away. Since the distance to the next pores (above and below) is shorter than the possible distances within one pore (see figure 2). The result of this simulation is show in figure 10 displayed by the blue crosses, showing that the system is dominated by two spins thus bigger spin systems are not necessary to describe the ordering in MIL-53-NH^{13}CHO/water. (RMSD(fit with 2

spins)= 0.031 and RMSD(fit with 6 spins)=0.030). This means that the functional groups in MIL-53-NH^{13}CHO with water in the pores are arranged into pairs with distances of 3.9 Å ± 0.1 Å. Now we want to determine if this ordering of the functional groups into pairs is dependent on the guest molecule incorporated in the pores of the MOF framework. Therefore we tempered the MOF in vacuum to evaporate the water and the loaded the framework with acetone molecules and measured DQ build up curves. The resulting 1D CT build-up curve at τ_{tot} = 30.72 ms for MIL-53-NH^{13}CHO/acetone is shown in figure 11. We again performed a simulation using two ^{13} spins wit the SIMPSON simulation package to fit the curve of for MIL-53-NH^{13}CHO/acetone (see Figure 10 black diamonds). This resulted in a distance of 3.84 Å (RMSD = 0.036) for the functional groups . Compared with the distance of the functional groups in the MOF with water in the groups the distances are equal. So we can conclude that the ordering on the functional groups is not depended on the guest molecules insight the framework and stay stable during heating at 8 hours at 120 °C under HV. This leads to the assumption that the functional groups already arranged into pairs during the post-synthetic modification of the of the network.

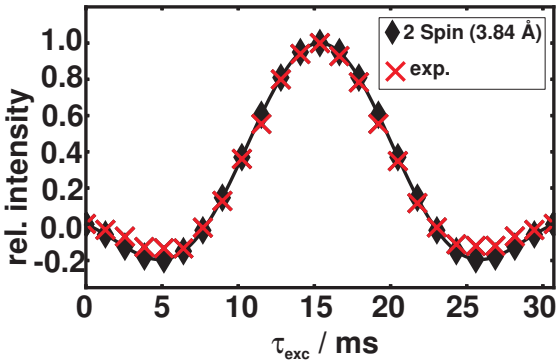

Figure 11: 1D ^{13}C CT build-up curve for MIL-53-NH^{13}CHO/acetone at τ_{tot} = 30.72 ms (red crosses). The simulation with the SIMPSON simulation package of a spin pair with 3.84 Å is displayed by the black diamonds.

The symmetric build-up curve for MIL-53-NH^{13}CHO/water and MIL-53-NH^{13}CHO/acetone, with the corresponding Bessel function fit is shown in figure 12. It is noticeable that the DQ efficiency for both curves does not reach the value of 0.5. The reason could be experimental

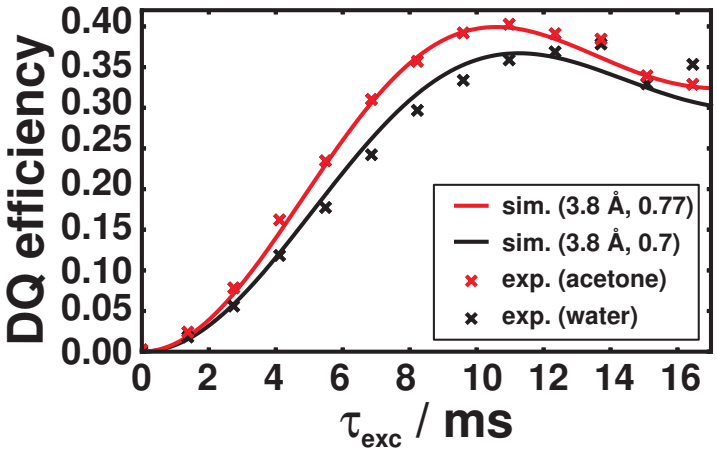

Figure 12: ^{13}C symmetric DQ build-up curve for MIL-53-NH^{13}CHO/water (black) and MIL-53-NH^{13}CHO/acetone (red). The solid lines correspond to Bessel function fit with 3.8 Å and a scaling factor for the intensity of 0.7 (MIL-53-NH^{13}CHO/water) and 0.77 (MIL-53-NH^{13}CHO/acetone).

errors, but the symmetric build-up curve of 1,3-$^{13}C_2$-malonic acid (Figure S8) reaches 0.5 in DQ efficiency and is measured with the exact same parameters. More likely only a part of the nuclei are arranged close enough to allow for the excitation of DQ coherences.

For the fits with the Bessel functions a scaling factor of 0.7 (MIL-53-NH^{13}CHO/water) and 0.77 (MIL-53-NH^{13}CHO/acetone) in intensity was derived. This reflects the ratio between isolated spins and coupled spin pairs, resulting that 70 -77 % of all functional groups in MIL-53-NH^{13}CHO align into pairs.

The short distance of r = 3.9±0.1 Å in MIL-53-NH^{13}CHO/acetone and MIL-53-NH^{13}CHO/water in comparison with Figure 2 suggests 77 %/70 % of the functional groups in the MOF are in the closest possible neighborhood within the pore.

With the information from the calculations and the evaluation of the DQ build-up behaviour of the MIL-53-NH^{13}CHO we can develope the structure model displayed in figure 13. It shows that the functional groups are arranged in the closest possible pairs additionally have cis configuration and are distorted towards the aromatic ring by $\alpha = 200°$.

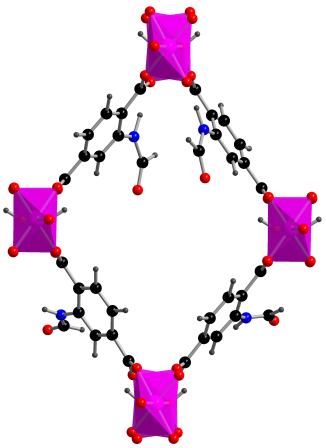

Figure 13: Structure model for the arrangemnet of the functional groups in MIL-53-NH[13]CHO. The formamido groups have cis configuration, a torsion angle of 200° towards the aromatic ring and are 3.9 Å close.

Conclusion

We successfully optimized the PSM of MIL-53-NH_2 with ^{13}C formic acid into MIL-53-$NH^{13}CHO$ to reach a degree of conversion of 100 %, which could be proven by 1D solid-state NMR experiments. For MIL-53-$NH^{13}CHO$ we could determine the local order of functional groups in the pores of an functionalized MOF for the first time. We determined the distance between a pair of formamido groups in MIL-53-$NH^{13}CHO$/water and MIL-53-$NH^{13}CHO$/acetone to be r = 3.9±0.1 Å. The ratio of the functional groups which are that close is 70 % for MIL-53-$NH^{13}CHO$/water and 77 % for MIL-53-$NH^{13}CHO$/acetone. This close distance leads to a arrangement in the MOF pores, where the bdc linker molecules are functionalized in the closest possible neighboring position. This ordering effect is almost not influenced by the adsorbed guest molecules, thus has to be formed during synthesis of the framework. With a static 1D wideline ^{13}C experiment we derived the full CSA tensor parameters for the formamido group. The calculations describe a structure model with the formamido functionalization being CIS and having a torsion angle towards the aromatic ring of 200°.

Acknowledgement

We gratefully thank the ENB Graduate School "*Structure, Reactivity and Properties of Oxide Materials*" and the DFG (SPP1362, Se 1417/3-1, 1417/3-2) for funding.

Supporting Information Available

This will usually read something like: "Experimental procedures and characterization data for all new compounds. The class will automatically add a sentence pointing to the information on-line:

This material is available free of charge via the Internet at `http://pubs.acs.org/`.

References

(1) Miller, S. R.; Heurtaux, D.; Baati, T.; Horcajada, P.; Greneche, J. M.; Serre, C. *Chem. Commun.* **2010**, *46*, 4526–4528.

(2) Horcajada, P. et al. *Nat. Mater.* **2010**, *9*, 172–178.

(3) Chalati, T.; Horcajada, P.; Couvreur, P.; Serre, C.; Ben Yahia, M.; Maurin, G.; Gref, R. *Nanomedicine (Lond)* **2011**, *6*, 1683–95.

(4) Della Rocca, J.; Liu, D. M.; Lin, W. B. *Acc. Chem. Res.* **2011**, *44*, 957–968.

(5) Li, J. R.; Kuppler, R. J.; Zhou, H. C. *Chem. Soc. Rev.* **2009**, *38*, 1477–1504.

(6) Liu, X.; Oh, M.; Lah, M. S. *Crystal Growth & Design* **2011**, *11*, 5064–5071.

(7) Xie, S. M.; Zhang, Z. J.; Wang, Z. Y.; Yuan, L. M. *J. Am. Chem. Soc.* **2011**, *133*, 11892–11895.

(8) Dinca, M.; Long, J. R. *Angew. Chem. Int. Ed.* **2008**, *47*, 6766–6779.

(9) Rowsell, J. L. C.; Yaghi, O. M. *Angew. Chem. Int. Ed.* **2005**, *44*, 4670–4679.

(10) Xie, Z. G.; Ma, L. Q.; deKrafft, K. E.; Jin, A.; Lin, W. B. *J. Am. Chem. Soc.* **2010**, *132*, 922–923.

(11) Chen, B. L.; Xiang, S. C.; Qian, G. D. *Acc. Chem. Res.* **2010**, *43*, 1115–1124.

(12) Lu, G.; Farha, O. K.; Kreno, L. E.; Schoenecker, P. M.; Walton, K. S.; Van Duyne, R. P.; Hupp, J. T. *Adv. Mater.* **2011**, *23*, 4449–4452.

(13) Ferey, G. *Chem. Soc. Rev.* **2008**, *37*, 191–214.

(14) Kitagawa, S.; Kitaura, R.; Noro, S. *Angewandte Chemie-international Edition* **2004**, *43*, 2334–2375.

(15) Wang, Z. Q.; Cohen, S. M. *J. Am. Chem. Soc.* **2009**, *131*, 16675–+.

(16) Ahnfeldt, T.; Gunzelmann, D.; Loiseau, T.; Hirsemann, D.; Senker, J.; Ferey, G.; Stock, N. *Inorg. Chem.* **2009**, *48*, 3057–3064.

(17) Biswas, S.; Ahnfeldt, T.; Stock, N. *Inorg. Chem.* **2011**, *50*, 9518–9526.

(18) Bunck, D. N.; Dichtel, W. R. *Chem. Eur. J.* **2013**, *19*, 818–827.

(19) Bernt, S.; Feyand, M.; Modrow, A.; Wack, J.; Senker, J.; Stock, N. *Eur. J. Inorg. Chem.* **2011**, 5378–5383.

(20) Wang, C.; Xie, Z. G.; deKrafft, K. E.; Lin, W. L. *J. Am. Chem. Soc.* **2011**, *133*, 13445–13454.

(21) Roy, P.; Schaate, A.; Behrens, P.; Godt, A. *Chem. Eur. J.* **2012**, *18*, 6979–6985.

(22) Rowsell, J. L. C.; Yaghi, O. M. *J. Am. Chem. Soc.* **2006**, *128*, 1304–1315.

(23) Ahnfeldt, T.; Guillou, N.; Gunzelmann, D.; Margiolaki, I.; Loiseau, T.; Ferey, G.; Senker, J.; Stock, N. *Angewandte Chemie-International Edition* **2009**, *48*, 5163–5166.

(24) Wang, Z. Q.; Cohen, S. M. *J. Am. Chem. Soc.* **2007**, *129*, 12368–+.

(25) Wang, Z. Q.; Cohen, S. M. *Angewandte Chemie-international Edition* **2008**, *47*, 4699–4702.

(26) Burrows, A. D.; Keenan, L. L. *CrystEngComm* **2012**, *14*, 4112–4114.

(27) Stavitski, E.; Pidko, E. A.; Couck, S.; Remy, T.; Hensen, E. J. M.; Weckhuysen, B. M.; Denayer, J.; Gascon, J.; Kapteijn, F. *Langmuir* **2011**, *27*, 3970–3976.

(28) Cadars, S.; Mifsud, N.; Lesage, A.; Epping, J. D.; Hedin, N.; Chmelka, B. F.; Emsley, L. *J. Phys. Chem. C* **2008**, *112*, 9145–9154.

(29) Senker, J.; Sehnert, J.; Correll, S. *J. Am. Chem. Soc.* **2005**, *127*, 337–349.

(30) Seyfarth, L.; Seyfarth, J.; Lotsch, B. V.; Schnick, W.; Senker, J. *Phys. Chem. Chem. Phys.* **2010**, *12*, 2227–2237.

(31) Dudenko, D. V.; Williams, P. A.; Hughes, C. E.; Antzutkin, O. N.; Velaga, S. P.; Brown, S. P.; Harris, K. D. M. *J. Phys. Chem. C* **2013**, *117*, 12258–12265.

(32) Bonhomme, C.; Gervais, C.; Babonneau, F.; Coelho, C.; Pourpoint, F.; Azais, T.; Ashbrook, S. E.; Griffin, J. M.; Yates, J. R.; Mauri, F.; Pickard, C. J. *Chem. Rev.* **2012**, *112*, 5733–5779.

(33) Tossell, J. A. *Chem. Phys. Lett.* **1999**, *303*, 435–440.

(34) Valerio, G.; Goursot, A. *J. Phys. Chem. B* **1999**, *103*, 51–58.

(35) Zheng, A.; Liu, S. B.; Deng, F. *J. Comput. Chem.* **2009**, *30*, 222–235.

(36) Brouwer, D. H.; Langendoen, K. P.; Ferrant, Q. *Canadian Journal of Chemistry-revue Canadienne De Chimie* **2011**, *89*, 737–744.

(37) Facelli, J. C.; Pugmire, R. J.; Grant, D. M. *J. Am. Chem. Soc.* **1996**, *118*, 5488–5489.

(38) Concistre, M.; Johannessen, O. G.; McLean, N.; Bovee-Geurts, P. H. M.; Brown, R. C. D.; DeGrip, W. J.; Levitt, M. H. *J. Biomol. NMR* **2012**, *53*, 247–256.

(39) auf der Günne, J. S. *J. Magn. Reson.* **2003**, *165*, 18 – 32.

(40) Carravetta, M.; Eden, M.; Johannessen, O. G.; Luthman, H.; Verdegem, P. J. E.; Lugtenburg, J.; Sebald, A.; Levitt, M. H. *J. Am. Chem. Soc.* **2001**, *123*, 10628–10638.

(41) Graf, R.; Demco, D. E.; Gottwald, J.; Hafner, S.; Spiess, H. W. *J. Chem. Phys.* **1997**, *106*, 885–895.

(42) Schmidt, M.; Wittmann, J. J.; Kress, R.; Schneider, D.; Steuernagel, S.; Schmidt, H.-W.; Senker, J. *Cryst. Growth Des.* **2012**, *12*, 2543–2551.

(43) Schmidt, M.; Wittmann, J. J.; Kress, R.; Schmidt, H. W.; Senker, J. *Chem. Commun.* **2013**, *49*, 267–269.

(44) Brouwer, D. H.; Alavi, S.; Ripmeester, J. A. *Phys. Chem. Chem. Phys.* **2007**, *9*, 1093–1098.

(45) Loiseau, T.; Serre, C.; Huguenard, C.; Fink, G.; Taulelle, F.; Henry, M.; Bataille, T.; Ferey, G. *Chemistry-A European Journal* **2004**, *10*, 1373–1382.

(46) Pines, A.; Gibby, M. G.; Waugh, J. S. *J. Chem. Phys.* **1973**, *59*, 569–590.

(47) Fung, B. M.; Khitrin, A. K.; Ermolaev, K. *J. Magn. Reson.* **2000**, *142*, 97–101.

(48) Bennett, A. E.; Weliky, D. P.; Tycko, R. *J. Am. Chem. Soc.* **1998**, *120*, 4897–4898.

(49) Kristiansen, P. E.; Carravetta, M.; Lai, W. C.; Levitt, M. H. *Chem. Phys. Lett.* **2004**, *390*, 1–7.

(50) Bak, M.; Rasmussen, J. T.; Nielsen, N. C. *J. Magn. Reson.* **2000**, *147*, 296–330.

(51) Zhu, C. Y.; Byrd, R. H.; Lu, P. H.; Nocedal, J. *Acm Trans. o. Math.* **1997**, *23*, 550–560.

(52) Kristiansen, P. E.; Carravetta, M.; van Beek, J. D.; Lai, W. C.; Levitt, M. H. *J. Chem. Phys.* **2006**, *124*, 234510.

(53) Clark, S. J.; Segall, M. D.; Pickard, C. J.; Hasnip, P. J.; Probert, M. J.; Refson, K.; Payne, M. C. *Z. Kristallogr.* **2005**, *220*, 567–570.

(54) Yates, J. R.; Pickard, C. J.; Mauri, F. *Phys. Rev. B* **2007**, *76*, 024401.

(55) Harris, R. K.; Hodgkinson, P.; Pickard, C. J.; Yates, J. R.; Zorin, V. *Magn. Reson. Chem.* **2007**, *45*, S174–S186.

(56) McNellis, E. R.; Meyer, J.; Reuter, K. *Phys. Rev. B* **2009**, *80*, 205414.

Preferred orientation of the formamido hydrogen bond anchor in MIL-53-NHCHO

Julia Wack,[†] Tim Ahnfeldt,[†] Carsten B. L. Tschense,[†] Norbert Stock,[‡] and Juergen Senker[*,†]

Department of Inorganic Chemistry III, University of Bayreuth, Bayreuth, and Department of Chemistry, Christian Albrechts University Kiel, Kiel

E-mail: juergen.senker@uni-bayreuth.de

Phone: +49(0)921 / 55-2532. Fax: +49 (0)921/55-2788

Section: Calibration of the DQ experiments with malonic acid

Section: Following the PSM of MIL-53-NH$_2$ to MIL-53-NH^{13}CHO.

[*]To whom correspondence should be addressed

[†]University of Bayreuth

[‡]Christian-Albrechts-Universität zu Kiel

Section: 2D fit for the ^{13}C-^{13}C DQ-SQ spectrum of MIL-53-NH^{13}CHO.

Figure S8: 2D deconvolution of the 2D ^{13}C-^{13}C DQ-SQ spectrum for MIL-53-NH^{13}CHO at τ_{tot} = 7.0 ms.

Calibration of the DQ experiments with malonic acid

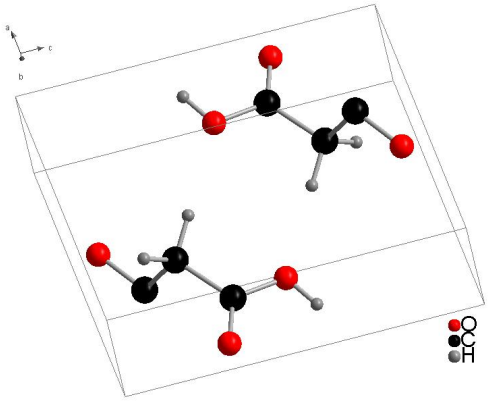

Figure S1: Structure of β-malonic acid.[1]

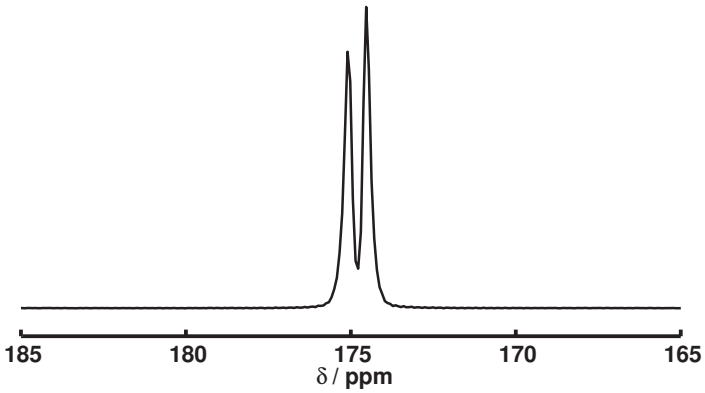

Figure S2: ^{13}C CP MAS spectrum for 1,3-$^{13}C_2$-malonic acid.

1,3-$^{13}C_2$-malonic acid was chosen as model system to calibrate the experiments and determine the accuracy of the results. From the crystal structure of 1,3-$^{13}C_2$-malonic acid (see

Figure S1) we now that there is one molecule in the assymetric unit. The intramolecular distance between the enriched carboxyl atoms is with 2.5 Å in the medium range. The shortest intermolecular distances are 3.6 Å. This means that the difference from the shortest spinpair to the next spins is 25 % the same as in MIL-53-NHCHO from the spinpair of 3.9 Å to 6.6 Å. In Figure S2 the ^{13}C CP MAS spectrum of 1,3-$^{13}C_2$-malonic acid is shown. 1,3-$^{13}C_2$-malonic acid exhibits two different resonaces for the enriched carboxyl groups in one malonic acid molecule due to space symmetry.

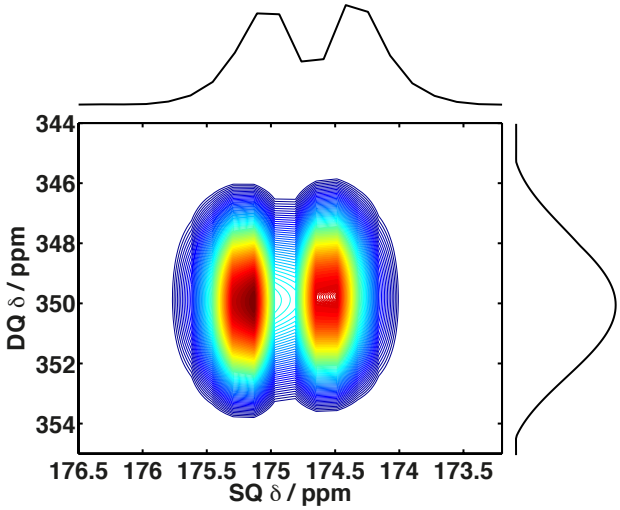

Figure S3: 2D ^{13}C-^{13}C DQ-SQ spectrum for 1,3-$^{13}C_2$-malonic acid at τ_{tot} = 5.2 ms.

The 2D ^{13}C-^{13}C DQ-SQ spectrum for 1,3-$^{13}C_2$-malonic acid at excitation time of 2.56 ms, which corresponds to a time at the maximum intensity, is shown in figure S3. In the spectrum in figure S3 only a DQ cross peaks but no DQ auto correlation peaks occur. Thus an overlapping of the signals in the F2-domain of the spectrum is not possible and we can perform the build up curves in a row of 1D experiments. To yield a CT build-up curve which is reliable for distance evaluation a zero crossing of the curve has to be detected.[2] Since a zero-crossing only occurs when the total mixing time is considerably longer than the excitation time where the build-up reaches maximum DQ efficiency. Thus first an symmetric build-up curve has to be measured. This ^{13}C symmetric build-up curve is shown in Figure S4. The maximum DQ efficiency is reached at an excitation time of 2.52 ms. To fit the

shortest distance in the system the first increase in the curves is used, the Bessel function fit of resulted in a distance of 2.6 Å. However, since the first increase only consists of 3 points these result is not very reliable. Since the CT build-up curves have more points due to their longer used total mixing time, they are more useful for an accurate evaluation.

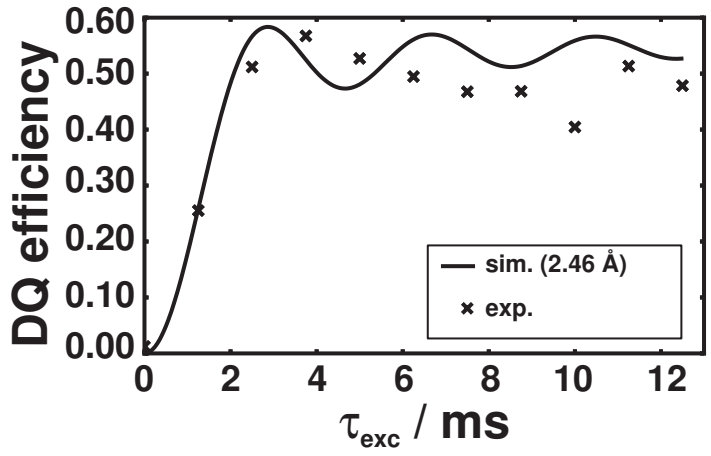

Figure S4: ^{13}C symmetric build-up curve for 1,3-$^{13}C_2$-malonic acid for the two resonances.

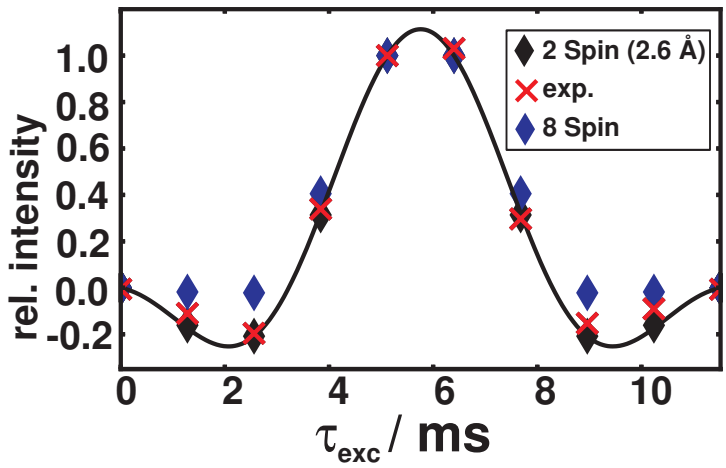

Figure S5: ^{13}C CT build-up curve for 1,3-$^{13}C_2$-malonic acid at τ_{tot} = 11.52 ms.

The CT build-up curve at a total mixing time τ_{mix} of 11.52 ms is shown in figure S5 together with two Simpson simulation with 2 and 8 Spins. As the difference in the symmetric build-up of the two resonances was marginal and the derived distance the same, we abstained from deconvolution and integrated both signals together. The build-up curve was fitted with

a 2 Spins system and the returned distance from this fit was 2.6 Å ± 0.1 Å (RMSD = 0.028) corresponding to a coupling constant -432.308 ± 50 Hz. A second simulation with an 8 Spins system taking into account all the nuclei in the crystal structure within a distance up to 5 Å, returned a value for the closest intramolecular distance of 2.6 Åand a RMSD of 0.07. The RMSD and figure S5 clearly depict that the 2 Spin system fits the experiments better, meaning that there is no influence of Spins at a distance between 3.2 Å and 5 Å to the CT build-up curve.

Following the PSM of MIL-53-NH_2 to MIL-53-$NH^{13}CHO$

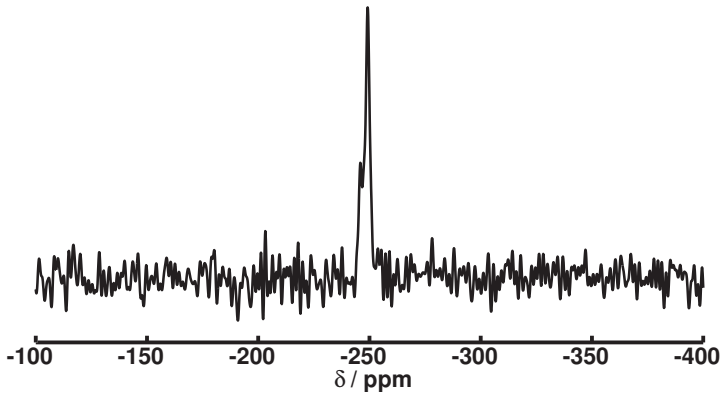

Figure S6: ^{15}N CP MAS spectrum for MIL-53-$NH^{13}CHO$.

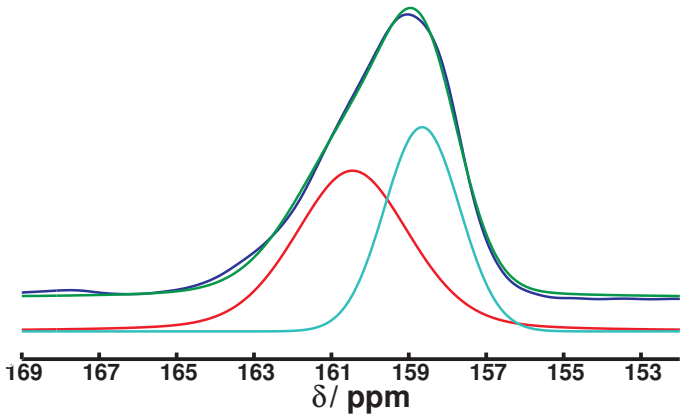

Figure S7: ^{13}C CP MAS spectrum of MIL-53-$NH^{13}CHO$ with acetone in the pores with. The colored lines give the deconvolution of the formamido signal.

2D deconvolution of the 2D ^{13}C-^{13}C DQ-SQ for MIL-53-NH^{13}CHO

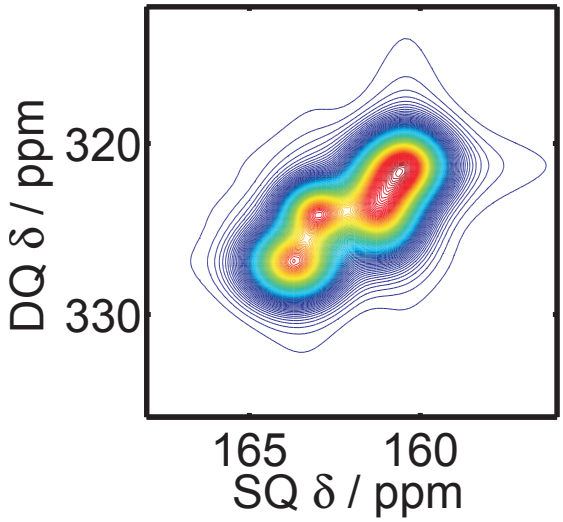

Figure S8: 2D deconvolution of the 2D ^{13}C-^{13}C DQ-SQ spectrum for MIL-53-NH^{13}CHO at τ_{tot} = 7.0 ms.

References

(1) Thalladi, V. R.; Nusse, M.; Boese, R. *J. Am. Chem. Soc.* **2000**, *122*, 9227–9236.

(2) auf der Guenne, J. S. *J. Magn. Reson.* **2003**, *165*, 18 – 32.

10 Identifying selective host-guest interactions based on hydrogen bond donor acceptor pattern in functionalized Al-MIL-53 metal-organic frameworks

Erschienen in:
The Journal of Physical Chemistry C **117**, 19991–20001 (2013)

THE JOURNAL OF PHYSICAL CHEMISTRY C

Article

pubs.acs.org/JPCC

Identifying Selective Host–Guest Interactions Based on Hydrogen Bond Donor–Acceptor Pattern in Functionalized Al-MIL-53 Metal–Organic Frameworks

Julia Wack,[†] Renée Siegel,[†,‡] Tim Ahnfeldt,[†,§] Norbert Stock,[§] Luís Mafra,*[,‡] and Juergen Senker*[,†]

[†]Department of Inorganic Chemistry III, University of Bayreuth, 95440 Bayreuth, Germany

[‡]Department of Chemistry, CICECO, 3810-193 Aveiro, Portugal

[§]Department of Chemistry, Christian Albrechts University Kiel, 24118 Kiel, Germany

Supporting Information

ABSTRACT: We present a study analyzing the selectivity of host–guest interactions in a series of functionalized Al-MIL-53-X metal–organic frameworks with X = H, NH_2, and NHCHO using acetone, ethanol, and water as probe molecules. While the amino group introduces additional hydrogen bond donor centers the NHCHO anchors function as donor and acceptor. The guests were chosen due to their ability to act solely as an acceptor in the case of acetone, whereas ethanol and water provide acceptor and donor qualities with a gradual decrease of the acceptor strength toward ethanol. The characterization of the host–guest interactions includes a comprehensive solid-state NMR spectroscopic study based on a full assignment of ^{1}H and ^{13}C high-resolution spectra using CRAMPS decoupling schemes to enhance ^{1}H resolution combined with advanced 2D HETCOR ($^{1}H-^{13}C$, $^{1}H-^{27}Al$, and $^{1}H-^{14}N$) spectra at high magnetic fields. In spite of a pronounced dynamical disorder of the guests, we could identify a preferred binding of the acetone via a NH···OC hydrogen bond for the NH_2 and the NHCHO anchor groups by analyzing trends in the ^{13}C isotropic chemical shifts. At the same time $^{1}H-^{1}H$ through-space connectivities reveal a close vicinity of the acetone methyl groups to the benzene rings of the linkers. In contrast, for ethanol and water, the interaction with the anchor groups is too weak to compete with the thermal disorder at room temperature.

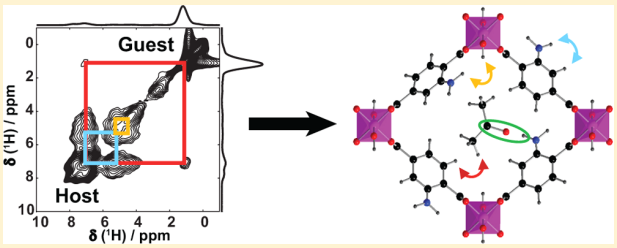

INTRODUCTION

Metal–organic frameworks (MOFs) offer potential for different applications like drug delivery,[1−4] gas separation[5−8] and storage,[9,10] catalysis,[11−13] and sensor design.[14−16] These applications rely crucially on the interaction between the framework and the incorporated guest molecules. As a consequence, substantial effort was recently put into the synthesis of MOFs bearing chemical functionalities which allow for an enhanced uptake of targeted guests by introducing selectivity into host–guest interactions. The selectivity might be established by tuning cavity size and shape,[17] by introducing metal centers with at least one free coordination site,[5,6,9,10] and by using chiral linkers and connectors[6,8] as well as Lewis and Brønsted acid/base binding sites, respectively.[3−6,18−20]

Two main synthetic routes have been established so far. While the direct synthesis[5,8,10] led to a large variety of different classes of MOFs with an impressive range of properties, a fine-tuning of host–guest interactions is limited since the framework formation cannot be controlled during hydrothermal treatment. A promising alternative is the postsynthetic modification (PSM)[17,21−26] where the framework formation and the introduction of targeted functionalities are decoupled. In this way, remarkably high selectivities for CO_2 capture from CO_2/N_2 mixtures for a series of Zn-paddle-wheel MOFs could be reached.[17,21] Tuning the pore space of IRMOF-3, UMCM-1-NH_2, and DMOF-1-NH_2 by PSM, furthermore, resulted in an enhanced H_2 uptake up to two additional molecules per modified linker unit.[27]

Although the potential for tailoring host–guest interactions is obvious considering the above-mentioned investigations which are mainly based on an explorative characterization of the macroscopic sorption properties, only very few experimental studies focus on unraveling the microscopic adsorption mechanism.[28] While the topology of the frameworks itself can be determined based on conventional diffraction methods, information about local properties like binding sites or preferred orientations of guests within the cavities are masked by a pronounced structural and dynamical disorder, for both the frameworks and the incorporated guest molecules.[29,30] In such cases, solid-state NMR spectroscopy is a particularly powerful tool to characterize host–guest interactions due to its ability to shed light on both local structural arrangements and

Received: June 26, 2013
Revised: August 30, 2013
Published: September 4, 2013

dynamical disorder of host and guest. Until now, studies were performed on guest molecules in mesoporous silica[31] or zeolites,[32−34] and on the properties of liquids in confinement.[35] For MOFs, solid-state NMR spectroscopy supported the ab initio structure determination of framework topologies including a comprehensive characterization of the motional processes of the linkers.[29,36,37] Additionally, the reorientational as well as translational dynamics of guest molecules[30] like benzene in MOF-5,[38] CO_2 in CD-MOF-2,[39] and Xe in DUT-8(Ni)[40] was studied. To the best of our knowledge, however, no comprehensive study on the selective binding of guest molecules in postsynthetically functionalized MOFs has been conducted so far.

To obtain information about the location and alignment of guest molecules within the framework, homo- and heteronuclear connectivities and distances as well as the orientation correlation of neighboring chemical shift tensors have to be obtained. For this purpose, a variety of one- and two-dimensional (2D) NMR experiments might be used, ranging from cross-polarization schemes with and without homonuclear decoupling on the I spin system[41−44] over high-resolution double-quantum[45−50] and zero-quantum[51−53] experiments up to wide-line radio frequency driven spin-diffusion techniques.[54,55] In any case, a prerequisite for such studies is an unequivocal assignment of individual resonances to characteristic building units. For MOFs, this is usually straightforward for heteronuclei with a large chemical shift range like ^{13}C and ^{15}N. Typically, such nuclei possess a low natural abundance combined with a small gyromagnetic ratio γ. As a consequence, quantitative NMR spectroscopic experiments require expensive and cumbersome isotope enrichment and are limited to medium range distances well below 1 nm.[48−50] In contrast, protons feature 100% natural abundance and a large γ, principally allowing to exploit the full capacity of modern NMR spectroscopy.[45,51,53] Nevertheless, even today, achieving a full ^1H assignment is demanding. The main reason for this is the small chemical shift range of protons, their chemical diversity within the MOFs, and broad signals on the order of some kHz caused by strong ^1H homonuclear dipolar couplings. To reduce the heavy overlap of individual ^1H resonances, the combined use of very high magnetic fields with so-called CRAMPS (*combined rotation and multiple pulse spectroscopy*)[56−59] methods like PMLG[60−62] and DUMBO,[63] respectively, have been introduced and are meanwhile well-established in the study of small molecules and extended systems.[51]

For the here presented study, we apply a similar strategy on a series of functionalized MOFs with Al-MIL-53 topology[64] loaded with the guests acetone, ethanol, and water. This allows for a detailed analysis of the individual host−guest interactions with the aim to develop a deeper understanding of the underlying selectivity.

Al-MIL-53 exhibits a pore structure composed of one-dimensional rhombohedral channels with a mean diameter of roughly 8.5 × 8.5 Å which are well suited to take up small polar molecules (Figure 1 bottom). The inorganic part of Al-MIL-53 is built of AlO_6 polyhedra (Figure 1 top). These octahedra share corners via *trans* bridging μ-OH-groups and are arranged into chains. They are interconnected through functionalized terephthalate units, forming a three-dimensional network (Figure 1).

Besides the unfunctionalized MIL-53 and MIL-53-NH_2, which were both synthesized directly following recipes of Loiseau et al.[64] and Ahnfeldt et al.,[22] PSM enabled us,

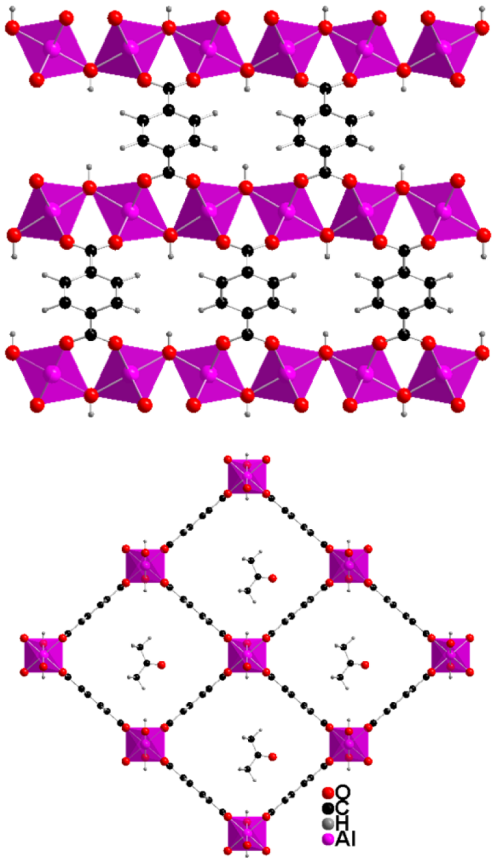

Figure 1. Viewing toward (010) plane (top) and toward (100) plane (bottom) of the structure of Al-MIL-53.[64] The bottom picture contains acetone guest molecules in the pores.

additionally, to introduce a formamido group into the framework.[22] While the unfunctionalized terephthalic acid (H_2bdc) sets the reference level based on unspecific dispersion forces, 2-amino- and 2-formamido-bdc linkers are able to form hydrogen bonds. Whereas NH_2 solely acts as donor, the NHCHO functionality provides both hydrogen bond donor and acceptor qualities. Acetone was chosen as guest molecule because of its ability to act specifically as hydrogen bonding acceptor. In particular, the sensitivity of the ^{13}C chemical shift of the acetone carbonyl groups on hydrogen bond formation[65,66] provides an easy tool to classify the frameworks according to their hydrogen bond donor strength. In contrast, both ethanol and water might interact with donor and acceptor functionalities of the framework.

We first derived a full assignment for all resonances in the high-resolution ^1H NMR spectra of MIL-53/acetone, MIL-53-NH_2/acetone, MIL-53-NHCHO/acetone, MIL-53-NHCHO/ethanol, and MIL-53-NHCHO/H_2O by means of 2D heteronuclear correlation (HETCOR) experiments based on spectral editing techniques such as ^1H-X PRESTO recoupling[67] and ^1H-X *D*-HMQC[68−70] to obtain information about the strongest connectivities of protons to carbon, nitrogen, and aluminum atoms, respectively. Afterward, we analyzed spatial proximities between guest and host molecules in the above-mentioned systems using $^1H-^1H$ high-resolution spin-diffusion experiments with homonuclear decoupling[51] applied in the direct and indirect dimensions.

dx.doi.org/10.1021/jp4063252 | *J. Phys. Chem. C* 2013, 117, 19991−20001

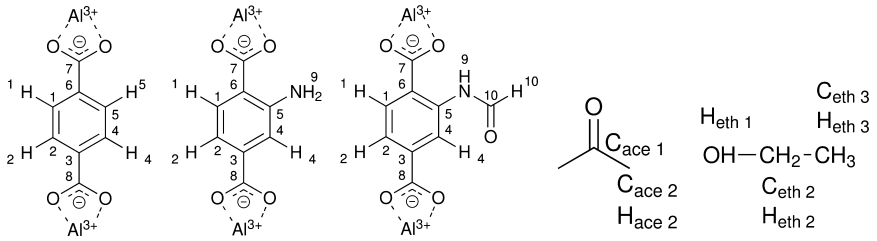

Figure 2. Atom labeling used to assign the NMR data for the linkers of MIL-53, MIL-53-NH_2, and MIL-53-NHCHO as well as the guest molecules (acetone and ethanol).

METHODS, EXPERIMENTAL DETAILS, AND THEORY

Sample Preparation. The synthesis of MIL-53 was done as described by Loiseau et al.[64] while the synthesis of MIL-53-NH_2 and the PSM with formic acid was carried out according to Ahnfeldt et al..[22] All the samples were activated using high vacuum for 8 h at 150 °C. Afterward, liquid acetone, ethanol or water was added in excess. The samples were equilibrated for 8 h, to make sure that the guest molecules are evenly distributed in all MOF pores. Finally, the remaining liquid was evaporated, by exposing to vacuum.

Solid-State NMR Spectroscopy. All experiments were performed on a Bruker Avance III standard-bore 800 spectrometer operating at 18.8 T resulting in Larmor frequencies of 800.13 MHz (^{1}H), 201.19 MHz (^{13}C), 208.49 MHz (^{27}Al), and 57.82 MHz (^{14}N). All samples were packed in air as fast as possible, since at the high-field facility (CERMAX, ITQB Lisbon) no glovebox was available, in ZrO_2 rotors with an outer diameter of 3.2 mm. The ^{1}H−^{27}Al-, and the ^{1}H−^{14}N *D*-HMQC measurements were carried out in a commercial Bruker MAS HX low-gamma probe at a rotation frequency of ν_{rot} = 20 kHz, while all of the other experiments were performed in a commercial Bruker HXY probe with a rotation frequency of ν_{rot} = 16 kHz. The chemical shifts of ^{1}H and ^{13}C were referenced relative to tetramethylsilane (TMS), the ones of ^{27}Al and ^{14}N relative to an acidic solution of aluminum nitrate hexahydrate and to NH_4Cl, respectively.

To study the field dependence of the ^{1}H resolution, additional proton 1D spectra were recorded on a Bruker Avance III wide-bore 400 spectrometer, operated at a Lamor frequency of 400.130 MHz, using a 4 mm double resonance MAS probe. The samples were spun at a frequency ν_{rot} of 10 kHz.

1D Experiments. For all samples, ^{1}H NMR spectra where recorded employing a standard one-pulse sequence and a homonuclear windowed decoupling scheme, wDUMBO[71] with z-rotation supercycling.[72,73] Both experiments were carried out at two distinct external magnetic fields (9.4 and 18.8 T). A rf field strength of 85 kHz was employed for the proton 90° excitation pulse. The best DUMBO decoupling conditions for all experiments was determined using the proton signals of glycine, and the strength of the decoupling was set to 100 kHz. The comparison of the single pulse spectrum with the homonuclear decoupled one revealed a scaling factor of λ_{dec} = 0.53 and a reduction of the line widths by roughly a factor of 2 (determined for MIL-53 compare Supporting Information Figure S1). Additionally, a factor of 2 in resolution is gained since the high field spectrometer was used (800 MHz compared to 400 MHz).

The ^{13}C MAS spectra were acquired using a ramped cross-polarization (CP) transfer via the proton bath with a contact time of 2 ms.[74] The detection of the ^{13}C CP-MAS NMR signal was attained under broadband proton decoupling using the SPINAL-64 sequence[75] employing a rf field strength of 75 kHz. The ^{27}Al NMR spectra were recorded with a Hahn echo pulse sequence with central transition selective excitation pulses of 8 and 16 μs for the 90° and 180° flip angles, respectively.

2D Experiments. The correlation between the proton and the carbon nuclei was achieved by recoupling the ^{1}H−^{13}C heteronuclear dipolar interaction using the rotor-synchronized symmetry based R-sequence $R10_1^3$, applied in a selective PRESTO-II[67] experiment. The recoupling time was optimized to τ_{rec} = 62.5 μs for all five samples (the optimum excitation, where only covalently bound CH_n are polarized, was checked with the sample of MIL-53/acetone (see Figure S2 in the Supporting Information)), and the power was set to a rf field strength of 80 kHz during the R sequence. During the t_1 evolution period, an eDUMBO-1_{22}[76,77] homonuclear decoupling with a rf field strength of 105 kHz was used. The signal acquisition was performed with a SPINAL-64 heteronuclear decoupling using a rf field strength of 75 kHz. The scaling factor of the F1-domain was again determined to λ_{dec} = 0.53.

^{1}H−^{27}Al and ^{1}H−^{14}N HETCOR spectra were recorded using a *D*-HMQC sequence.[68−70] The transfer of polarization between the quadrupolar nuclei and the protons was performed with the supercycled symmetry based $SR4_1^2$ pulse scheme[78−81] using a recoupling time of 300 μs for the transfer to ^{27}Al (the optimum recoupling, where only the protons in the first coordination sphere around the aluminum atoms are polarized, was checked with the sample of MIL-53/acetone (see Figure S3 in the Supporting Information)) and 200 μs for the transfer from ^{1}H to ^{14}N. For the two pulses on the ^{14}N channel the pulse length was adjusted to 35 μs at a rf field strength of 67 kHz (calibrated from NH_4Cl), corresponding to the maximum ^{14}N signal intensity. The t_1 evolution was rotor synchronized using a dwell time of 50 μs. In the case of the ^{1}H−^{27}Al *D*-HMQC NMR experiment, the two central transition selective 90° pulses were set to 7.25 μs using a rf field strength of 11.5 kHz (calibrated from $Al(NO_3)_3$). The experimental setup did not allow for active rotor synchronization, which lead to t_1-noise. It can be identified due to the sinusoidal behavior with alternating positive and negative intensity along the whole F1-domain. This noise often occurs in the spectra of indirect experiments either due to temperature, spinning, or rf fluctuations.[82−84]

The ^{1}H−^{1}H-spin-diffusion spectra were measured with eDUMBO-1_{22} decoupling set to 105 kHz during t_1 and t_2 evolution times using the same parameters as in the HETCOR spectra. The two 90° pulses were set to 2.9 μs.

dx.doi.org/10.1021/jp4063252 | J. Phys. Chem. C 2013, 117, 19991−20001

RESULTS AND DISCUSSION

Figure 2 shows the labeling which is used for the description of the NMR spectra for the linker molecules. The heteroatoms were numbered consecutively, and the hydrogen atoms were then numbered according to the heteroatom to which they are bound. The water molecules in the samples with water in the pores are always labeled H_2O. In addition to the linker molecules, the ^1H atom of μ-connecting OH-groups of the inorganic building unit is labeled OH.

Assignment of the NMR Resonances. To determine the closest contacts between different functionalized frameworks and their guest molecules, we rely on $^1H-^1H$ correlation experiments. Therefore, we first have to assign the proton resonances. The signal assignment of the guest molecules (acetone, ethanol, and water) is certain since their ^1H resonances usually are observed below 4 ppm[85] and thus do not overlap with the signals of the framework. The assignment of the ^1H signals of the framework is more challenging because significantly different environments for proton nuclei with similar shifts do occur. In Figure S4 (Supporting Information), the proton spectra of MIL-53/acetone (a), MIL-53-NH_2/acetone (b), MIL-53-NHCHO/acetone (c), MIL-53-NHCHO/ethanol (d), and MIL-53-NHCHO/water (e) are shown. These systems were chosen to explore a range of different possible hydrogen bond interactions, with the goal to probe whether a selective binding of molecules to the functional group of the framework is formed. While the MIL-53/acetone system exhibits only three signals, which are already known from literature,[64] for the functionalized samples at least six signals can be distinguished, which cannot be assigned without measuring heteronuclear connectivities. We show in the following a detailed assignment strategy for MIL-53-NH_2/acetone (Figures 3 and 6) and MIL-53-NHCHO/acetone

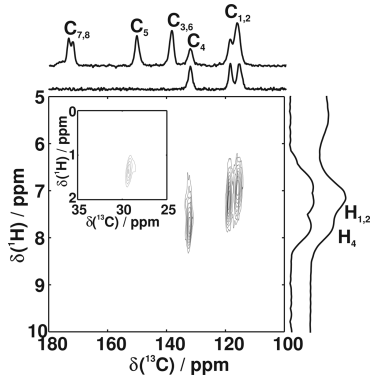

Figure 3. $^1H-^{13}C$ 2D HETCOR MAS spectrum with the respective projections using a selective PRESTO transfer (τ_{rec} = 62.5 μs) for MIL-53-NH_2/acetone, identifying the strongest carbon proton couplings. On the top of each projection, the corresponding 1D experiment is displayed. The inset exhibits the region of the correlation peaks for the methyl group of the acetone molecules.

(Figures 4–7), while the analysis for MIL-53-NHCHO with ethanol and water is presented in the Supporting Information (see Figures S5–S7 for MIL-53-NHCHO/ethanol and Figures S8–S10 for MIL-53-NHCHO/water).

The assignment strategy is based on the resonances of the carbon, nitrogen and aluminum atoms to correlate them with the unknown ^1H resonances of nearby proton nuclei. For the $^1H-^{13}C$ HETCOR we used a PRESTO-II sequence.[67] It is

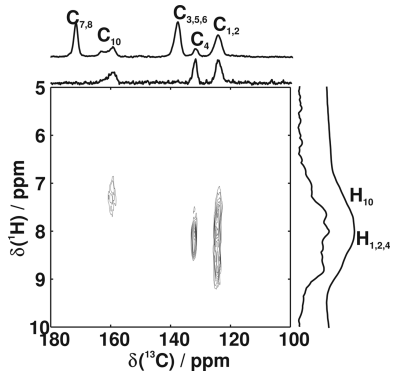

Figure 4. $^1H-^{13}C$ 2D HETCOR MAS spectrum with the respective projections using a selective PRESTO transfer (τ_{rec} = 62.5 μs) for MIL-53-NHCHO/acetone, identifying the strongest carbon proton couplings. On the top of each projection, the corresponding 1D experiment is displayed.

based on a γ-encoded RN sequence which simultaneously suppresses proton spin-diffusion during the polarization transfer. In contrast to a conventional CP, this allows to select specifically the strongest dipolar couplings and thus to polarize only covalently bonded CH_n exchange peaks. In particular, when short transfer times are used.

The $^1H-^{13}C$ HETCOR spectrum for MIL-53-NH_2/acetone (Figure 3) exhibits a proton resonance at 7.7 ppm (H4) which is correlated to a carbon signal at 132 ppm (C4). The proton signals of the CH (C1 and C2 at 119 and 115.8 ppm) occur at 7.2 and 6.9 ppm (H1/H2). The $^1H-^{13}C$ HETCOR of MIL-53-NHCHO (Figure 4) depicts correlation peaks for the aromatic carbon and proton atoms H1/C1 and H2/C2 at (6.8–8.2 ppm/125.0 ppm), while carbon atom C4 leads to a cross peak at 8.0/132.1 ppm (H4/C4). The most important assignment for the following analysis is the one for the proton attached to the carbon in the formamido-group (H10) which is represented in the HETCOR spectrum with two cross peaks at 7.0/159.9 ppm and 7.5/161.8 ppm. From the fact that two different cross peaks can be distinguished for the formamido-group, we conclude that different crystallographic sites for the functional group exist. In the $^1H-^{13}C$ correlation spectra, only in the case of MIL-53-NH_2/acetone (Figure 3 inset) a proton-carbon correlation peak for the methyl proton and methyl carbon atoms in acetone are found, while in all other samples (MIL-53/acetone, MIL-53-NHCHO/acetone, and MIL-53-NCHO/ethanol) these correlations were not observed. This may perhaps indicate that the guest molecules are mobile which, at least, partially averages the $^1H-^{13}C$ dipolar couplings, thus dampening the polarization transfer at room temperature.

The only protons remaining unassigned are H9 of the linker molecules which are covalently bound to nitrogen atoms and the ones of the μ–OH groups which are close to the aluminum core. H9 can be assigned collecting connectivities between N and H while the OH will be identified via $^1H-^{27}Al$ HETCOR experiments. For nitrogen two stable isotopes exist ^{14}N and ^{15}N. ^{15}N is a I = 1/2 nucleus and exhibits a low natural abundance (NA = 0.364%) as well as a small gyromagnetic ratio (γ = -2.713×10^7 rad s^{-1} T^{-1}). The measurement of 2D correlation spectra thus require very long measuring times or isotopic enrichment. In contrast, ^{14}N has a markedly high natural abundance (NA = 99.634%) which reduces the measuring time significantly. By using indirect detection for

dx.doi.org/10.1021/jp4063252 | J. Phys. Chem. C 2013, 117, 19991–20001

the ^{14}N, the sensitivity can be improved even further due to the high γ of protons. We choose the ^{1}H−^{14}N *D*-HMQC experiment since it has provided good results for similar bonding scenarios, recently.[86] ^{14}N has a spin quantum number of I = 1, and its line shape is dominated by first order quadrupolar interaction, leading to signals spanning over several MHz. Furthermore, higher-order quadrupolar interactions introduce a typical line shape to every spinning sideband. These lineshapes are often distorted further due to the impossibility of correctly exciting the whole powder pattern and, additionally, due to their high sensitivity with respect to the magic-angle and rotor synchronization. Thus, it is hardly possible to evaluate the line shape of the F1 projection (^{14}N).[86] Therefore, after dismissing the signal from the t_1-noise, the assignment is done by analyzing the F2 projection.

The ^{1}H−^{14}N *D*-HMQC spectrum of MIL-53-NHCHO/acetone (Figure 5) displays two different ^{1}H−^{14}N correlations

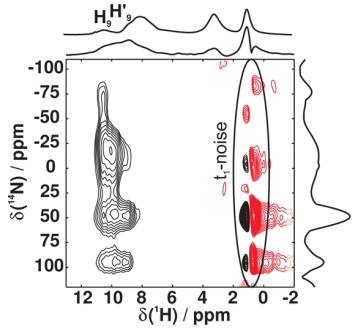

Figure 5. ^{1}H−^{14}N 2D *D*-HMQC with the corresponding projections for MIL-53-NHCHO with acetone in the pores. On top of the F2 projection, the 1D homonuclear decoupled proton spectrum is displayed. Positive and negative intensities are color coded in black and red, respectively.

in two overlapping cross peaks at 9.6 and 10.1 ppm in the F2 projection. The strongly dephased signal at ≈1 ppm is caused by t_1-noise (compare experimental section). The two correlation peaks reveal two different environments for the formamido protons bound to the nitrogen group, which is in good agreement with the result of the ^{1}H−^{13}C HETCOR spectrum, where also two different sites for the carbon atom of the formamido-group were observed. This can be explained mainly by two different scenarios which could not be distinguished further. (i) Only a part of the formamido groups is involved in hydrogen bonds with acetone. (ii) All anchors bind to the guests, but the functional groups exhibit significantly different orientations within the framework.

In the case of MIL-53-NH$_2$/acetone, no ^{1}H−^{14}N *D*-HMQC spectrum could be obtained (data not shown) probably due to the fast spin−spin relaxation and the large second-order quadrupole interaction of the ^{14}N nucleus.

Finally, the μ-OH-groups between the aluminum octahedra for all systems have to be assigned. The 1D ^{27}Al spectra (see Figures S11−S15 in the Supporting Information) exhibit the typical broad shape of an Al nucleus in a distorted octahedral environment. They were deconvoluted with a spin system containing only one ^{27}Al nucleus taking into account an isotropic shift as well as the second order quadrupolar interaction. All relevant refinement parameters are given in Table S1 in the Supporting Information. Summarizing, the chemical shift δ_{iso} varies between 1.9 and 3.6 ppm, while the asymmetry parameter η_Q is close to zero (0.05 −0.12) for all samples and the quadrupolar coupling constant C_Q is observed in the range of 8.6−10.4 MHz. These values are in good agreement with the literature[64] for MIL-53 without guest and with water molecules adsorbed. In particular, C_Q in the formamido-functionalized MIL-53 is independent of the adsorbed guest molecules suggesting that no selective interaction with the inorganic building block occurs.

In Figures 6 and 7, the ^{1}H−^{27}Al-*D*-HMQC spectra are displayed for MIL-53-NH$_2$/acetone and MIL-53-NHCHO/

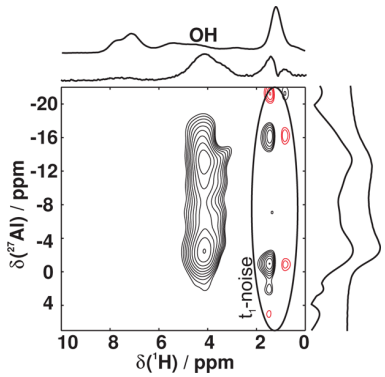

Figure 6. ^{1}H−^{27}Al 2D HETCOR MAS spectrum with the respective projections for MIL-53-NH$_2$ with acetone in the pores. On top of each projection, the corresponding 1D experiment is displayed. Positive and negative intensities are color coded in black and red, respectively.

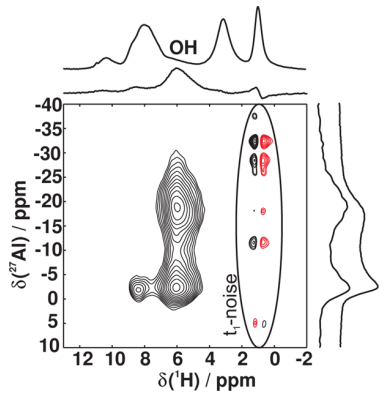

Figure 7. ^{1}H−^{27}Al 2D HETCOR MAS spectrum with the respective projections for MIL-53-NHCHO with acetone in the pores. On top of each projection, the corresponding 1D experiment is displayed. Positive and negative intensities are color coded in black and red, respectively.

acetone, respectively. The proton signal at 4.2 ppm corresponds to the μ-OH groups of the inorganic building unit in MIL-53-NH$_2$ (Figure 6), whereas the protons of the μ-OH groups in case of MIL-53-NHCHO resonate at 6.0 ppm (Figure 7). While the value for the MIL-53-NH$_2$ system is similar to the one of the unfunctionalized sample (compare Table 1), the OH group in MIL-53-NHCHO is strongly shifted downfield. The very sharp and small signal in the spectrum of MIL-53-NHCHO/acetone (Figure 7) at 8.0 ppm (^{1}H)/0.0 ppm (^{27}Al) is caused by a small amount of aluminum hydroxide (Al(OH)$_3$), which forms during the PSM of MIL-53-NH$_2$. Again some t_1-noise is observed at around 1 ppm.

dx.doi.org/10.1021/jp4063252 | J. Phys. Chem. C 2013, 117, 19991−20001

Table 1. Summary of ^{1}H and ^{13}C Chemical Shifts in the Different Host−Guest Systems[a]

δ_{iso}/ppm	chemical unit	MIL-53/acetone	NH_2/acetone	NHCHO/acetone	NHCHO/ethanol	NHCHO/water
C_1	aromatic	129.3	119.0	125.0	125.0	125.0
C_2	aromatic	129.3	115.8	125.0	125.0	125.0
$C_{3,6}$	aromatic	137.2	138.6	138.0	138.0	138.0
C_4	aromatic	129.3	132.0	132.1	132.2	132.2
C_5	aromatic	129.3	150.4	138.0	138.0	138.0
$C_{7,8}$	carboxyl	171.3	172.5	171.6	171.6	171.6
C_{10}	formamido			161.8/159.9	162.8/159.1	162.5/160.4
C_{ace2}	methyl	28.7	29.4	29.0		
C_{ace1}	carbonyl	206.4	208.3	209.45		
C_{eth3}	methyl				16.8	
C_{eth2}	methylene				57.2	
H_1	aromatic	7.9	7.2	8.2	8.7	8.6
H_2	aromatic	7.9	6.9	7.6	7.8	7.6
H_4	aromatic	7.9	7.7	8.0	8.3	7.9
H_5	aromatic	7.9				
H_9	amino/formamido		5.5	10.1	10.3/9.4	10.5
H'_9	amino/formamido			8.6	8.5	8.9
H_{10}	formamido CH			7.0/7.5	7.3/8.1	6.8/7.4
OH	hydroxyl (μ-OH)	4.5	4.2	6.0	6.1	6.1
H_{ace2}	methyl	0.92	1.2	0.97		
H_{eth3}	methyl				0.0	
H_{eth2}	CH_2				2.6	
H_{eth1}	alcohol				≈ 2.8	
H_2O	water		2.8	2.8	≈ 2.8	2.8

[a]All the chemical shifts are expected to be measured with an accuracy of about or better than 0.1 ppm.

In the proton spectrum of MIL-53-NHCHO/acetone, MIL-53-NH_2/acetone, and MIL-53-NHCHO/ethanol (Figure 8a−c), an additional signal at 2.8 ppm occurs, which is characteristic for water molecules (see Figure 8d). This indicates that water molecules are coadsorbed during the sample preparation for the NMR experiments.

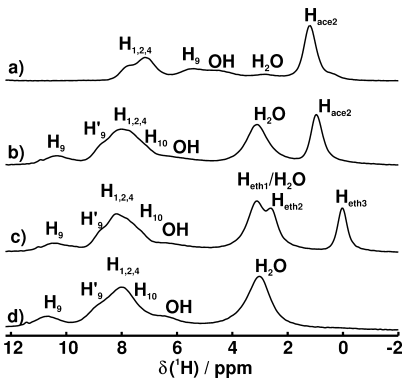

Figure 8. Comparison of 1D proton spectra of MIL-53-NH_2/acetone (a), MIL-53-NHCHO/acetone (b), MIL-53-NHCHO/ethanol (c), and MIL-53-NHCHO/water (d) all measured at a magnetic field of B_0 = 18.8 T with ^{1}H homonuclear decoupling. The assignment of all the resonances is included on top of the individual resonance.

The only signal remaining unassigned is the one at 5.5 ppm in the spectrum of MIL-53-NH_2/acetone (Figure 8a), which consequently belongs to the protons H9 of the NH_2 group. For comparison all the shifts for the different samples are summarized in Table 1. All ^{13}C CP spectra are shown in the Supporting Information (Figures S16−S20). Additionally, the assignment of the ^{1}H signals is displayed on top of the 1D spectra in Figure 8.

Host−Guest Interactions in Functionalized MIL-53. As summarized in Table 1, the ^{13}C and ^{1}H shifts of the host frameworks are not strongly influenced by the adsorbed guest molecules (e.g., of C_1−C_8 and H_1−H_4). For example, the ^{1}H chemical shift of the μ-OH groups varies only with the functionalization of the framework (MIL-53-NH_2/acetone = 4.2 ppm, MIL-53/acetone = 4.5 ppm, and MIL-53-NHCHO-[acetone/ethanol/water] = 6.0/6.1/6.1 ppm) but does not depend on the guest molecules. This again implies that the guest molecules are not bound to the inorganic part of the MOF and do not interact specifically with the benzene ring of the linker molecules. Nevertheless, the carbon shift C_{10} and proton shifts (H_9/H'_9 and H_{10}) of the formamido functionalized MIL-53 vary about ≈1 ppm (C_{10}) and ≈0.5 ppm (H_9/H'_9 and H_{10}) from MIL-53-NHCHO/acetone to MIL-53-NHCHO/ethanol and MIL-53-NHCHO/water, indicating an interaction between the guest molecules and the functional groups of the linker molecules.

From solution-state, it is known that the ^{1}H shift depends on the polarity of the solvent.[85] In the case of ethanol molecules, the methyl shift varies from 0.96 ppm in benzene to 1.25 ppm in chloroform while the methylene groups are observed at 3.34 ppm in benzene and 3.72 ppm in chloroform. For acetone molecules, the methyl groups shift from 1.57 ppm in benzene to 2.22 ppm in water.[85] Adsorbed in the individual frameworks, both guests are highfield shifted compared to these values (see Table 1), reflecting their confined environment.[35,85] For water molecules, the solvent dependent chemical shift is even more pronounced. Its ^{1}H shift varies from 0.4 ppm in benzene up to 4.9 in methanol and water.[85] The medium chemical shift of 2.8 ppm within the framework is too low for specific hydrogen bonding but nevertheless again accounts for its confine-

dx.doi.org/10.1021/jp4063252 | J. Phys. Chem. C 2013, 117, 19991−20001

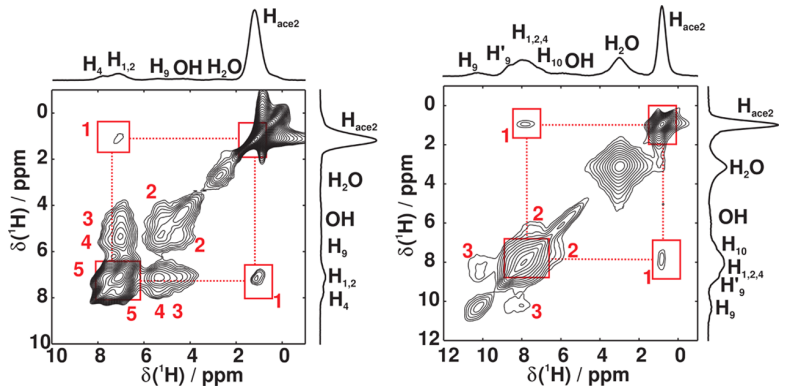

Figure 9. $^{1}H-^{1}H$ spin-diffusion spectra of MIL-53-NH_2 (left) and MIL-53-NHCHO (right) with acetone in the pores. The mixing time was set to 2 ms to see the first correlation peaks between the guest molecules and the framework. On top and on the right sides of the 2D spectra, the F2 and F1 projections, including the preceding full assignment of the proton resonances, are shown.

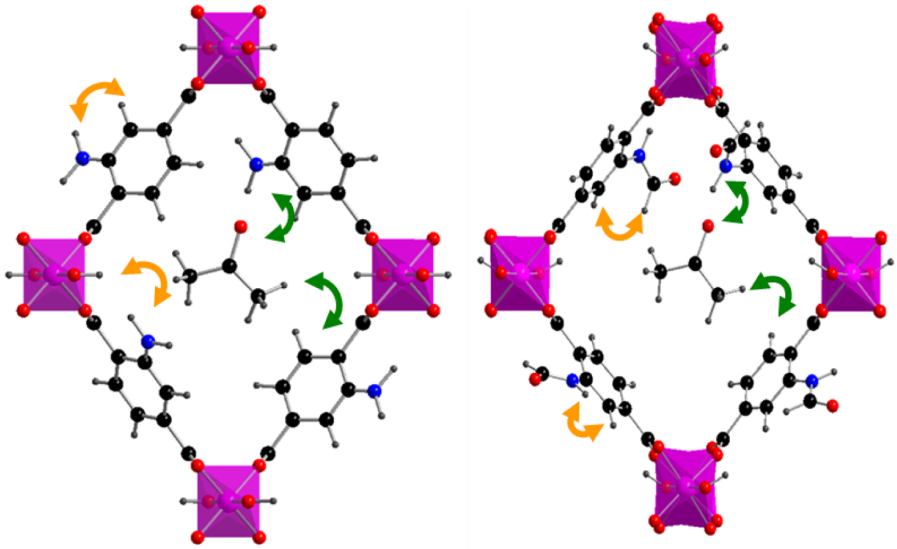

Figure 10. Structure model for the binding site of the acetone molecule in the pores of MIL-53-NH_2 (left) and MIL-53-NHCHO (right). The carbonyl groups of the acetone molecules are hydrogen bonded to the NH_2/NH-groups of the functionalized linker molecules and its methyl protons point to the aromatic protons of the linker molecules (indicated by the green arrows). The orange arrows show the connections within the framework derived from Figure 9.

ment.[31,35] Here the contacts with the inner surfaces reduces the electron density on the hydrogen atoms of the guest molecules which leads to a deshielding. Furthermore, we did not observe any differences as a function of the anchor groups, implying that no selective interactions between the amino and formamido groups and the water molecules are established at room temperature. In cases where water is coadsorbed, consequently, no interference with other guest molecules is expected.

With the exception of the carbonyl chemical shift of acetone, the aliphatic carbon shifts are less sensitive to the solvent in liquid-state. In our case, the CH_3 and CH_2 groups of the guest molecules are in the same range as in the liquid-state. The methylene groups of ethanol resonate at 57.2 ppm which is exactly in the range of liquids (56−58 ppm), while the methyl groups of the guest molecules resonate marginally more downfield (compare in Table 1 C_{ace2} and C_{eth3}) in the framework than in solution (30−31 ppm for acetone in solution and 17−19 ppm for ethanol).

In particular, the carbonyl chemical shift has been proven to be quite sensitive to the hydrogen bond environment due to an easy polarizability of the C═O π-system. This provides further insight into the binding nature of the acetone molecules (compare in Table 1 C_{ace1}). The chemical shift of the C═O-group of acetone molecules in $CDCl_3$, without hydrogen bonds, is observed at 206.2 ppm.[66] Protonated acetone molecules in a superacid solution resonate at 250 ppm.[87] In MIL-53/acetone, the corresponding chemical shift is found at 206.4 ppm, strongly suggesting that the acetone molecules are not engaged in hydrogen bonds. In contrast, the carbonyl chemical shifts of acetone molecules in the pores of the functionalized frameworks are shifted to 209.5 ppm (MIL-53-NHCHO) and 208.3 ppm (MIL-53-NH_2). This indicates that acetone molecules form hydrogen bonds in both cases. The stronger downfield shift for MIL-53-NHCHO/acetone suggests a stronger hydrogen bond than for MIL-53-NH_2/acetone. This is in agreement with the literature, where the hydrogen bond length for $C(sp^2)$-

dx.doi.org/10.1021/jp4063252 | J. Phys. Chem. C 2013, 117, 19991−20001

NH_2 is reported as 2.016 Å as opposed to 1.99 Å for peptide-NH (both bonded to water).[88]

Based on the preceding assignment, one can make use of $^1H-^1H$ spin-diffusion exchange measurements with DUMBO decoupling during t_1 and t_2 as a function of the mixing time, to obtain information about the structural arrangement of the guest molecules within the pores. Due to the large γ of protons, they provide a tool for observing long distances even in the case of a dynamical disorder of the guest molecules. We measured $^1H-^1H$ exchange spectra as a function of mixing times (τ_{mix}). For τ_{mix} = 2 ms, the first cross intensities between host and guest are observed. This allows us to determine the closest spacial proximities in the pores. The corresponding spectra for MIL-53-NH_2/acetone (left) and MIL-53-NHCHO/acetone (right) are shown in Figure 9.

The spectrum of MIL-53-NH_2/acetone (Figure 9 left) exhibits cross peaks between the different aromatic protons (5) and between the amino group and the aromatic protons (4). This reflects the connectivities within one linker molecule. The cross peaks between the OH protons and the NH_2 protons (2) and the OH protons to the aromatic protons (3), which demonstrates a spatial proximity between the functional group of the linker and the μ-OH-group of the framework, which proves the presence of a hydrogen bond between the metal oxide cluster of the framework and the NH_2 group of the linker molecules. This scenario was already suggested in the literature.[89] The methyl protons of the acetone molecule show exclusively cross peaks with the aromatic protons of the bdc molecules of the MOF framework (1), which indicates that the methyl protons point toward the aromatic protons of the bdc linker molecules (compare Figure 10 left).

For MIL-53-NHCHO/acetone, similar results are obtained (see Figure 9 right). The first exchange peak between the host and the guest molecules occurs between the aromatic protons of the terephthalic acid and the methyl protons of acetone (1), proving that the methyl groups of the acetone molecules are again close to the aromatic protons of the linker molecules (compare Figure 10 right). In contrast to the spectrum of MIL-53-NH_2, the latter one contains no cross peaks between the functional group and the μ-OH-groups, indicating that no hydrogen bond is formed between the metal oxide chain and the linker molecule. As the NH-group is covalently bound to the aromatic ring its proton correlates with the aromatic protons in ortho position leading to cross peak (3). Cross peak (2) demonstrates that the CHO proton of the functional group is close to the aromatic protons of the bdc linker molecule.

In both cases, the $^1H-^1H$ spin-diffusion exchange measurements indicate that the methyl groups of the acetone molecules are spatially close to the aromatic protons. Their cross peaks emerge together with the cross peaks between the framework protons, suggesting similar initial exchange transfer rates. Additionally, the acetone molecules are dynamically disordered which partially averages the $^1H-^1H$ couplings between the framework and the methyl group of the acetone molecules. For this reason contacts between the CH_3-groups and the aromatic protons are at least as close as the protons of the framework themselves.

For the same mixing time (τ_{mix} = 2 ms) the $^1H-^1H$ spin-diffusion exchange measurements of MIL-53-NHCHO/ethanol (Figure S21) and MIL-53-NHCHO/H_2O (Figure S22) do not show any correlations between the guest molecules and framework. The most likely explanation is that the dynamics of the water and ethanol guest molecules is isotropic and so all dipolar couplings between the framework and the guest molecules are averaged out. This is also indicated by the lack of spinning side bands for these guest molecules (see Figure S23). Our results imply that the acetone molecules are selectively bound to the functional group while the ethanol and water molecules are not. As a consequence when water and acetone molecules are coadsorbed (see above) the acetone will outcompete water for selective binding sites.

CONCLUSIONS

We were able to successfully assign all the proton resonances of three samples MIL-53, MIL-53-NH_2, and MIL-53-NHCHO loaded with acetone guest molecules and for comparison also MIL-53-NHCO with adsorbed ethanol and water molecules. The assignment was accomplished by means of $^1H-^{27}Al$ *D*-HMQC, $^1H-^{14}N$ *D*-HMQC, and $^1H-^{13}C$ HETCOR spectra based on a dipolar RN transfer sequence (PRESTO-II). The $^1H-^{13}C$ and $^1H-^{14}N$ HETCOR spectra for MIL-53-NHCHO reveal, mostly independent of the adsorbed guest molecules, two different sites for the formamido group. This indicates that, for all formamido functionalized samples, either two different oriented functional groups exist in the asymmetric unit or only a part of the anchor groups is involved in host guest interactions.

The chemical shift of the μ-OH-group does not depend on the intercalated guest molecules, suggesting that no bonding at this site of the framework occurs. The general downfield shift of the proton resonances of all guest molecules reflects their confinement in the pore structure.[31,35] For example, water depicts a similar, medium chemical shift for all samples, which is typical for confined molecules but too low for specific hydrogen bonding.[85] In contrast, the ^{13}C carbonyl chemical shift of the acetone guest molecules in the functionalized samples is downfield shifted compared to MIL-53/acetone where only van der Waals interactions occur, indicating that the acetone molecules in MIL-53-NH_2 and MIL-53-NHCHO form NH···OC hydrogen bonds. In the case of MIL-53-NHCHO this shift is even higher, implying that acetone is bound more strongly to the formamido groups than to the amino groups.

No cross peaks for the methyl and methylene groups of ethanol in the $^1H-^{13}C$ HETCOR spectra were observed. Additionally, narrow lines for the methylene group in the proton one-pulse spectra are found due to the absence of spinning sidebands. Finally, the $^1H-^1H$ spin-diffusion spectra exhibit no cross peaks between host and guest resonances in the case of ethanol and water. All these findings suggest a fast isotropic reorientational motion for the ethanol and water guest molecules. Thus, for both adsorbates, no specific interactions are established in the MIL-53-NHCHO framework at room temperature. In the case of adsorbed acetone, the dynamics seems to be less isotropic since a cross peak for the proton and carbon atoms of the methyl group of the acetone was observed in the $^1H-^{13}C$ HETCOR spectrum for MIL-53-NH_2/acetone. Additionally, also cross peaks between host and guest arise in the $^1H-^1H$ spin-diffusion spectra for MIL-53-NH_2/acetone and MIL-53-NHCHO/acetone at short mixing times. On the same time scale, the correlations (see Figure 9) of the strongest intraframework connectivities emerge which allows to derive a close spatial proximity between the guest molecules and the aromatic protons of the amino/formamido-bdc linker molecules. As a consequence, a structure model is proposed (Figure 10), which preferably aligns the acetone molecules within the pores. It includes the carbonyl group of the acetone forming a

dx.doi.org/10.1021/jp4063252 | J. Phys. Chem. C 2013, 117, 19991−20001

NH···OC hydrogen bond with the functional groups of the bdc linker molecules and the methyl groups of the guest extending into the pores in close vicinity to the aromatic ring of the bdc linker molecules.

■ ASSOCIATED CONTENT

Supporting Information

Additional experimental details as described in the text. This material is available free of charge via the Internet at http://pubs.acs.org/.

■ AUTHOR INFORMATION

Corresponding Author

*E-mail: lmafra@ua.pt; juergen.senker@uni-bayreuth.de. Phone: +351 234 370 620, +49 921 55 2532. Fax: +49 921 55 2788.

Notes

The authors declare no competing financial interest.

■ ACKNOWLEDGMENTS

We gratefully thank the ENB Graduate School "*Structure, Reactivity and Properties of Oxide Materials*" and the DFG (SPP1362, Se 1417/3-1, 1417/3-2, and STO 643/5-1, 643/5-2) for funding. The authors also thank FEDER, via "*Programa Operacional Factores de Competitividade - COMPETE*", CICECO, the University of Aveiro, PEst-C/CTM/LA0011/2011. The FCT Project PTDC/QUIQUI/100998/2008 and the Portuguese National NMR Network (RNRMN), which hosts the highfield 18.8 T NMR spectrometer, is also greatly acknowledged.

■ REFERENCES

(1) Miller, S. R.; Heurtaux, D.; Baati, T.; Horcajada, P.; Greneche, J. M.; Serre, C. Biodegradable Therapeutic MOFs for the Delivery of Bioactive Molecules. *Chem. Commun.* **2010**, *46*, 4526−4528.

(2) Horcajada, P.; Chalati, T.; Serre, C.; Gillet, B.; Sebrie, C.; Baati, T.; Eubank, J. F.; Heurtaux, D.; Clayette, P.; Kreuz, C.; et al. Porous Metal-Organic-framework Nanoscale Carriers as a Potential Platform for Drug Delivery and Imaging. *Nat. Mater.* **2010**, *9*, 172−178.

(3) Chalati, T.; Horcajada, P.; Couvreur, P.; Serre, C.; Ben Yahia, M.; Maurin, G.; Gref, R. Porous Metal Organic Framework Nanoparticles to Address the Challenges Related to Busulfan Encapsulation. *Nanomedicine (London, U.K.)* **2011**, *6*, 1683−1695.

(4) Della Rocca, J.; Liu, D. M.; Lin, W. B. Nanoscale Metal-Organic Frameworks for Biomedical Imaging and Drug Delivery. *Acc. Chem. Res.* **2011**, *44*, 957−968.

(5) Banerjee, R.; Phan, A.; Wang, B.; Knobler, C.; Furukawa, H.; O'Keeffe, M.; Yaghi, O. M. High-Throughput Synthesis of Zeolitic Imidazolate Frameworks and Application to CO_2 Capture. *Science* **2008**, *319*, 939−943.

(6) Li, J. R.; Kuppler, R. J.; Zhou, H. C. Selective Gas Adsorption and Separation in Metal-Organic Frameworks. *Chem. Soc. Rev.* **2009**, *38*, 1477−1504.

(7) Liu, X.; Oh, M.; Lah, M. S. Adsorbate Selectivity of Isoreticular Microporous Metal-Organic Frameworks with Similar Static Pore Dimensions. *Cryst. Growth Des.* **2011**, *11*, 5064−5071.

(8) Xie, S. M.; Zhang, Z. J.; Wang, Z. Y.; Yuan, L. M. Chiral Metal-Organic Frameworks for High-Resolution Gas Chromatographic Separations. *J. Am. Chem. Soc.* **2011**, *133*, 11892−11895.

(9) Dinca, M.; Long, J. R. Hydrogen Storage in Microporous Metal-Organic Frameworks with Exposed Metal Sites. *Angew. Chem., Int. Ed.* **2008**, *47*, 6766−6779.

(10) Rowsell, J. L. C.; Yaghi, O. M. Strategies for Hydrogen Storage in Metal-Organic Frameworks. *Angew. Chem., Int. Ed.* **2005**, *44*, 4670−4679.

(11) Lee, J.; Farha, O. K.; Roberts, J.; Scheidt, K. A.; Nguyen, S. T.; Hupp, J. T. Metal-Organic Framework Materials as Catalysts. *Chem. Soc. Rev.* **2009**, *38*, 1450−1459.

(12) Ma, L. Q.; Falkowski, J. M.; Abney, C.; Lin, W. B. A Series of Isoreticular Chiral Metal-Organic Frameworks as a Tunable Platform for Asymmetric Catalysis. *Nat. Chem.* **2010**, *2*, 838−846.

(13) Wang, C.; Xie, Z. G.; deKrafft, K. E.; Lin, W. L. Doping Metal-Organic Frameworks for Water Oxidation, Carbon Dioxide Reduction, and Organic Photocatalysis. *J. Am. Chem. Soc.* **2011**, *133*, 13445−13454.

(14) Xie, Z. G.; Ma, L. Q.; deKrafft, K. E.; Jin, A.; Lin, W. B. Porous Phosphorescent Coordination Polymers for Oxygen Sensing. *J. Am. Chem. Soc.* **2010**, *132*, 922−923.

(15) Chen, B. L.; Xiang, S. C.; Qian, G. D. Metal-Organic Frameworks with Functional Pores for Recognition of Small Molecules. *Acc. Chem. Res.* **2010**, *43*, 1115−1124.

(16) Lu, G.; Farha, O. K.; Kreno, L. E.; Schoenecker, P. M.; Walton, K. S.; Van Duyne, R. P.; Hupp, J. T. Fabrication of Metal-Organic Framework-Containing Silica-Colloidal Crystals for Vapor Sensing. *Adv. Mater.* **2011**, *23*, 4449−4452.

(17) Farha, O. K.; Mulfort, K. L.; Hupp, J. T. An Example of Node-Based Postassembly Elaboration of a Hydrogen-Sorbing, Metal-Organic Framework Material. *Inorg. Chem.* **2008**, *47*, 10223−10225.

(18) Yee, K.-K.; Reimer, N.; Liu, J.; Cheng, S.-Y.; Yiu, S.-M.; Weber, J.; Stock, N.; Xu, Z. Effective Mercury Sorption by Thiol-Laced Metal-Organic Frameworks: in Strong Acid and the Vapor Phase. *J. Am. Chem. Soc.* **2013**, *135*, 7795−7798.

(19) Reinsch, H.; van der Veen, M. A.; Gil, B.; Marszalek, B.; Verbiest, T.; de Vos, D.; Stock, N. Structures, Sorption Characteristics, and Nonlinear Optical Properties of a New Series of Highly Stable Aluminum MOFs. *Chem. Mater.* **2013**, *25*, 17−26.

(20) Biswas, S.; Ahnfeldt, T.; Stock, N. New Functionalized Flexible Al-MIL-53-X (X = −Cl, −Br, $-CH_3$, $-NO_2$, $-(OH)_2$) Solids: Syntheses, Characterization, Sorption, and Breathing Behavior. *Inorg. Chem.* **2011**, *50*, 9518−9526.

(21) Bae, Y. S.; Farha, O. K.; Hupp, J. T.; Snurr, R. Q. Enhancement of CO_2/N-2 Selectivity in a Metal-organic Framework by Cavity Modification. *J. Mater. Chem.* **2009**, *19*, 2131−2134.

(22) Ahnfeldt, T.; Gunzelmann, D.; Loiseau, T.; Hirsemann, D.; Senker, J.; Ferey, G.; Stock, N. Synthesis and Modification of a Functionalized 3D Open-Framework Structure with MIL-53 Topology. *Inorg. Chem.* **2009**, *48*, 3057−3064.

(23) Ahnfeldt, T.; Gunzelmann, D.; Wack, J.; Senker, J.; Stock, N. Controlled Modification of the Inorganic and Organic Bricks in an Al-Based MOF by Direct and Post-synthetic Synthesis Routes. *CrystEngComm* **2012**, *14*, 4126−4136.

(24) Allen, C. A.; Cohen, S. M. Near-UV Photo-induced Modification in Isoreticular Metal-Organic Frameworks. *J. Mater. Chem.* **2012**, *22*, 10188−10194.

(25) Tanabe, K. K.; Cohen, S. M. Postsynthetic Modification of Metal-Organic Frameworks-a Progress Report. *Chem. Soc. Rev.* **2011**, *40*, 498−519.

(26) Bernt, S.; Guillerm, V.; Serre, C.; Stock, N. Direct Covalent Post-Synthetic Chemical Modification of Cr-MIL-101 Using Nitrating Acid. *Chem. Commun.* **2011**, *47*, 2838−2840.

(27) Wang, Z. Q.; Tanabe, K. K.; Cohen, S. M. Tuning Hydrogen Sorption Properties of Metal-Organic Frameworks by Postsynthetic Covalent Modification. *Chem.—Eur. J.* **2010**, *16*, 212−217.

(28) Spencer, E. C.; Howard, J. A. K.; McIntyre, G. J.; Rowsell, J. L. C.; Yaghi, O. M. Determination of the Hydrogen Absorption Sites in Zn4O(1,4-benzenedicarboxylate) by Single Crystal Neutron Diffraction. *Chem. Commun.* **2006**, *0*, 278−280.

(29) Sutrisno, A.; Huang, Y. N. Solid-State NMR: A Powerful Tool for Characterization of Metal-Organic Frameworks. *Solid State Nucl. Magn. Reson.* **2013**, *49*−*50*, 1−11.

(30) Hoffmann, H. C.; Debowski, M.; Muller, P.; Paasch, S.; Senkovska, I.; Kaskel, S.; Brunner, E. Solid-State NMR Spectroscopy of Metal-Organic Framework Compounds (MOFs). *Materials* **2012**, *5*, 2537−2572.

(31) Buntkowsky, G.; Breitzke, H.; Adamezyk, A.; Roelofs, F.; Emmler, T.; Gedat, E.; Grunberg, B.; Xu, Y.; Limbach, H. H.; Shenderovich, J.; Vyalikh, A.; Findenegg, G. Structural and Dynamical Properties of Guest Molecules Confined in Mesoporous Silica Materials Revealed by NMR. *Phys. Chem. Chem. Phys.* **2007**, *9*, 4843−4853.
(32) Huang, J.; Jiang, Y.; Marthala, V. R. R.; Hunger, M. Insight into the Mechanisms of the Ethylbenzene Disproportionation: Transition State Shape Selectivity on Zeolites. *J. Am. Chem. Soc.* **2008**, *130*, 12642−12644.
(33) Brunner, E. Solid-state NMR - A Powerful Tool for the Investigation of Surface Hydroxyl-Groups in Zeolites and Their Interactions with Adsorbed Probe Molecules. *J. Mol. Struct.* **1995**, *355*, 61−85.
(34) Fyfe, C. A.; Brouwer, D. H. Optimization, Standardization, and Testing of a New NMR Method for the Determination of Zeolite Host-Organic Guest Crystal Structures. *J. Am. Chem. Soc.* **2006**, *128*, 11860−11871.
(35) Vogel, M. NMR Studies on Simple Liquids in Confinement. *Eur. Phys. J.: Spec. Top.* **2010**, *189*, 47−64.
(36) Cadiau, A.; Auguste, S.; Taulelle, F.; Martineau, C.; Adil, K. Hydrothermal Synthesis, Ab-initio Structure Determination and NMR Study of the First Mixed Cu-Al Fluorinated MOF. *CrystEngComm* **2013**, *15*, 3430−3435.
(37) Devautour-Vinot, S.; Maurin, G.; Serre, C.; Horcajada, P.; da Cunha, D. P.; Guillerm, V.; Costa, E. D.; Taulelle, F.; Martineau, C. Structure and Dynamics of the Functionalized MOF Type UiO-66(Zr): NMR and Dielectric Relaxation Spectroscopies Coupled with DFT Calculations. *Chem. Mater.* **2012**, *24*, 2168−2177.
(38) Hertel, S.; Wehring, M.; Amirjalayer, S.; Gratz, M.; Lincke, J.; Krautscheid, H.; Schmid, R.; Stallmach, F. NMR Studies of Benzene Mobility in Metal-organic Framework MOF-5. *Eur. Phys. J.: Appl. Phys.* **2011**, *55*, 20702.
(39) Gassensmith, J. J.; Furukawa, H.; Smaldone, R. A.; Forgan, R. S.; Botros, Y. Y.; Yaghi, O. M.; Stoddart, J. F. Strong and Reversible Binding of Carbon Dioxide in a Green Metal-Organic Framework. *J. Am. Chem. Soc.* **2011**, *133*, 15312−15315.
(40) Hoffmann, H. C.; Assfour, B.; Epperlein, F.; Klein, N.; Paasch, S.; Senkovska, I.; Kaskel, S.; Seifert, G.; Brunner, E. High-Pressure in Situ Xe-129 NMR Spectroscopy and Computer Simulations of Breathing Transitions in the Metal-Organic Framework Ni-2(2,6-ndc)(2)(dabco) (DUT-8(Ni)). *J. Am. Chem. Soc.* **2011**, *133*, 8681−8690.
(41) Kolodziejski, W.; Klinowski, J. Kinetics of Cross-Polarization in Solid-State NMR: A Guide for Chemists. *Chem. Rev.* **2002**, *102*, 613−628.
(42) van Rossum, B.-J.; de Groot, C. P.; Ladizhansky, V.; Vega, S.; de Groot, H. J. M. A Method for Measuring Heteronuclear (^{1}H−^{13}C) Distances in High Speed MAS NMR. *J. Am. Chem. Soc.* **2000**, *122*, 3465−3472.
(43) Seyfarth, L.; Senker, J. An NMR Crystallographic Approach for the Determination of the Hydrogen Substructure of Nitrogen Bonded Protons. *Phys. Chem. Chem. Phys.* **2009**, *11*, 3522−31.
(44) Seyfarth, L.; Seyfarth, J.; Lotsch, B. V.; Schnick, W.; Senker, J. Tackling the Stacking Disorder of Melon-structure Elucidation in a Semicrystalline Material. *Phys. Chem. Chem. Phys.* **2010**, *12*, 2227−2237.
(45) Brown, S. P. Probing Proton-proton Proximities in the Solid State. *Prog. Nucl. Magn. Reson. Spectrosc.* **2007**, *50*, 199−251.
(46) Mafra, L.; Siegel, R.; Fernandez, C.; Schneider, D.; Aussenac, F.; Rocha, J. High-resolution (1)H Homonuclear Dipolar Recoupling NMR Spectra of Biological Solids at MAS Rates up to 67 kHz. *J. Magn. Reson.* **2009**, *199*, 111−114.
(47) Mafra, L.; Gomes, J. R. B.; Trebosc, J.; Rocha, J.; Amoureux, J. P. (1)H-(1)H Double-Quantum CRAMPS NMR at Very-Fast MAS (nu(R)=35 kHz): A Resolution Enhancement Method to Probe (1)H-(1)H Proximities in Solids. *J. Magn. Reson.* **2009**, *196*, 88−91.
(48) Schmidt, M.; Wittmann, J. J.; Kress, R.; Schneider, D.; Steuernagel, S.; Schmidt, H.-W.; Senker, J. Crystal Structure of a Highly Efficient Clarifying Agent for Isotactic Polypropylene. *Cryst. Growth Des.* **2012**, *12*, 2543−2551.
(49) Schmedt auf der Gunne, J. Distance Measurements in Spin-1/2 Systems by ^{13}C and ^{31}P Solid-state {NMR} in Dense Dipolar Detworks. *J. Magn. Reson.* **2003**, *165*, 18−32.
(50) Carravetta, M.; Eden, M.; Johannessen, O.; Luthman, H.; Verdegem, P.; Lugtenburg, J.; Sebald, A.; Levitt, M. Estimation of Carbon-Carbon Bond Lengths and Medium-Range Internuclear Distances by Solid-State Nuclear Magnetic Resonance. *J. Am. Chem. Soc.* **2001**, *123*, 10628−10638.
(51) Brown, S. P. Applications of High-Resolution H-1 Solid-state NMR. *Solid State Nucl. Magn. Reson.* **2012**, *41*, 1−27.
(52) Elena, B.; Pintacuda, G.; Mifsud, N.; Emsley, L. Molecular Structure Determination in Powders by NMR Crystallography from Proton Spin Diffusion. *J. Am. Chem. Soc.* **2006**, *128*, 9555−9560.
(53) Salager, E.; Stein, R. S.; Steuernagel, S.; Lesage, A.; Elena, B.; Emsley, L. Enhanced Sensitivity in High-resolution 1H Solid-State NMR Spectroscopy with DUMBO Dipolar Decoupling under Ultra-fast MAS. *Chem. Phys. Lett.* **2009**, *469*, 336−341.
(54) Sehnert, J.; Senker, J. A Concerted Approach for the Determination of Molecular Conformation in Ordered and Disordered Materials. *Chem.—Eur. J.* **2007**, *13*, 6339−6350.
(55) Senker, J.; Sehnert, J.; Correll, S. Microscopic Description of the Polyamorphic Phases of Triphenyl Phosphite by Means of Multi-dimensional Solid-state NMR Spectroscopy. *J. Am. Chem. Soc.* **2005**, *127*, 337−349.
(56) Bronnimann, C. E.; Hawkins, B. L.; Zhang, M.; Maciel, G. E. Combined Rotation And Multiple Pulse Spectroscopy As An Analytical Proton Nuclear Magnetic-Resonance Technique For Solids. *Anal. Chem.* **1988**, *60*, 1743−1750.
(57) Vinogradov, E.; Madhu, P. K.; Vega, S. Strategies for High-resolution Proton Spectroscopy in Solid-State NMR. *New Tech. Solid-State NMR* **2005**, *246*, 33−90.
(58) Siegel, R.; Mafra, L.; Rocha, J. Improving the (1)H Indirect Dimension Resolution of 2D CRAMPS NMR Spectra: A Simulation and Experimental Investigation. *Solid State Nucl. Magn. Reson.* **2011**, *39*, 81−87.
(59) Madhu, P. K. High-resolution Solid-state NMR Spectroscopy of Srotons with Homonuclear Dipolar Decoupling Schemes under Magic-Angle Spinning. *Solid State Nucl. Magn. Reson.* **2009**, *35*, 2−11.
(60) Vinogradov, E.; Madhu, P. K.; Vega, S. Phase Modulated Lee-Goldburg Magic Angle Spinning Proton Nuclear Magnetic Resonance Experiments in the Solid State: A Bimodal Floquet Theoretical Treatment. *J. Chem. Phys.* **2001**, *115*, 8983−9000.
(61) Vinogradov, E.; Madhu, P. K.; Vega, S. High-resolution Proton Solid-state NMR Spectroscopy by Phase-Modulated Lee-Goldburg Experiment. *Chem. Phys. Lett.* **1999**, *314*, 443−450.
(62) Vinogradov, E.; Madhu, P. K.; Vega, S. Proton Spectroscopy in Solid State Nuclear Magnetic Resonance with Windowed Phase Modulated Lee-Goldburg Decoupling Sequences. *Chem. Phys. Lett.* **2002**, *354*, 193−202.
(63) Sakellariou, D.; Lesage, A.; Hodgkinson, P.; Emsley, L. Homonuclear Dipolar Decoupling in Solid-State NMR Using Continuous Phase Modulation. *Chem. Phys. Lett.* **2000**, *319*, 253−260.
(64) Loiseau, T.; Serre, C.; Huguenard, C.; Fink, G.; Taulelle, F.; Henry, M.; Bataille, T.; Ferey, G. A Rationale for the Large Breathing of the Porous Aluminum Terephthalate (MIL-53) upon Hydration. *Chem.—Eur. J.* **2004**, *10*, 1373−1382.
(65) Maciel, G. E.; Natterst, J. J. Carbon-13 Chemical Shifts of Carbonyl Group 0.3. Solvent Effects. *J. Chem. Phys.* **1965**, *42*, 2752−2759.
(66) Hawkes, G. E.; Herwig, K.; Roberts, J. D. Nuclear Magnetic-resonance Spectroscopy - Use of C-13 Spectra To Establish Configurations of Oximes. *J. Org. Chem.* **1974**, *39*, 1017−1028.
(67) Zhao, X.; Hoffbauer, W.; Guenne, J. S. A. D.; Levitt, M. H. Heteronuclear Polarization Transfer by Symmetry-Based Recoupling Sequences in Solid-state NMR. *Solid State Nucl. Magn. Reson.* **2004**, *26*, 57−64.

(68) Cavadini, S.; Antonijevic, S.; Lupulescu, A.; Bodenhausen, G. Indirect Detection of Nitrogen-14 in Solids Via Protons by Nuclear Magnetic Resonance Spectroscopy. *J. Magn. Reson.* **2006**, *182*, 168−172.
(69) Cavadini, S.; Abraham, A.; Bodenhausen, G. Coherence Transfer Between Spy Nuclei and Nitrogen-14 in Solids. *J. Magn. Reson.* **2008**, *190*, 160−164.
(70) Tricot, G.; Lafon, O.; Trebosc, J.; Delevoye, L.; Mear, F.; Montagne, L.; Amoureux, J. P. Structural Characterisation of Phosphate Materials: New Insights Into the Spatial Proximities Between Phosphorus and Quadrupolar Nuclei Using the D-HMQC MAS NMR Technique. *Phys. Chem. Chem. Phys.* **2011**, *13*, 16786−16794.
(71) Lesage, A.; Sakellariou, D.; Hediger, S.; Elena, B.; Charmont, P.; Steuernagel, S.; Emsley, L. Experimental Aspects of Proton NMR Spectroscopy in Solids Using Phase-modulated Homonuclear Dipolar Decoupling. *J. Magn. Reson.* **2003**, *163*, 105−113.
(72) Bosman, L.; Madhu, P. K.; Vega, S.; Vinogradov, E. Improvement of Homonuclear Dipolar Decoupling Sequences in Solid-state Nuclear Magnetic Resonance Utilising Radiofrequency Imperfections. *J. Magn. Reson.* **2004**, *169*, 39−48.
(73) Leskes, M.; Madhu, P. K.; Vega, S. A Broad-Banded Z-rotation Windowed Phase-modulated Lee-Goldburg Pulse Sequence for H-1 Spectroscopy in Solid-state NMR. *Chem. Phys. Lett.* **2007**, *447*, 370−374.
(74) Pines, A.; Gibby, M. G.; Waugh, J. S. Proton-Enhanced NMR of Dilute Spins In Solids. *J. Chem. Phys.* **1973**, *59*, 569−590.
(75) Fung, B. M.; Khitrin, A. K.; Ermolaev, K. Improved Broadband Decoupling Sequence for Liquid Crystals and Solids. *J. Magn. Reson.* **2000**, *142*, 97−101.
(76) De Paepe, G.; Hodgkinson, P.; Emsley, L. Improved Heteronuclear Decoupling Schemes for Solid-State Magic Angle Spinning NMR by Direct Spectral Optimization. *Chem. Phys. Lett.* **2003**, *376*, 259−267.
(77) Elena, B.; de Paepe, G.; Emsley, L. Direct Spectral Optimisation of Proton-proton Homonuclear Dipolar Decoupling in Solid-State NMR. *Chem. Phys. Lett.* **2004**, *398*, 532−538.
(78) Brinkmann, A.; Levitt, M. H. Symmetry Principles in the Nuclear Magnetic Resonance of Spinning Solids: Heteronuclear Recoupling by Generalized Hartmann-Hahn Sequences. *J. Chem. Phys.* **2001**, *115*, 357−384.
(79) Brinkmann, A.; Kentgens, A. P. M. Proton-selective O-17-H-1 Distance Measurements in Fast Magic-Angle-Spinning Solid-state NMR Spectroscopy for the Determination of Hydrogen Bond Lengths. *J. Am. Chem. Soc.* **2006**, *128*, 14758−14759.
(80) Brinkmann, A.; Kentgens, A. P. M. Sensitivity Enhancement and Heteronuclear Distance Measurements in Biological O-17 Solid-State NMR. *J. Phys. Chem. B* **2006**, *110*, 16089−16101.
(81) Lafon, O.; Wang, Q.; Hu, B. W.; Vasconcelos, F.; Trebosc, J.; Cristol, S.; Deng, F.; Amoureux, J. P. Indirect Detection via Spin-1/2 Nuclei in Solid State NMR Spectroscopy: Application to the Observation of Proximities between Protons and Quadrupolar Nuclei. *J. Phys. Chem. A* **2009**, *113*, 12864−12878.
(82) Mao, K. M.; Pruski, M. Directly and Indirectly Detected Through-bond Heteronuclear Correlation Solid-state NMR Spectroscopy Under Fast MAS. *J. Magn. Reson.* **2009**, *201*, 165−174.
(83) Paulson, E. K.; Morcombe, C. R.; Gaponenko, V.; Dancheck, B.; Byrd, R. A.; Zilm, K. W. Sensitive High Resolution Inverse Detection NMR Spectroscopy of Proteins in the Solid State. *J. Am. Chem. Soc.* **2003**, *125*, 15831−15836.
(84) Ishii, Y.; Yesinowski, J. P.; Tycko, R. Sensitivity Enhancement in Solid-state C-13 NMR of Synthetic Polymers and Biopolymers by H-1 NMR Detection with High-speed Magic Angle Spinning. *J. Am. Chem. Soc.* **2001**, *123*, 2921−2922.
(85) Fulmer, G. R.; Miller, A. J. M.; Sherden, N. H.; Gottlieb, H. E.; Nudelman, A.; Stoltz, B. M.; Bercaw, J. E.; Goldberg, K. I. NMR Chemical Shifts of Trace Impurities: Common Laboratory Solvents, Organics, and Gases in Deuterated Solvents Relevant to the Organometallic Chemist. *Organometallics* **2010**, *29*, 2176−2179.
(86) Cavadini, S. Indirect Detection of Nitrogen-14 in Solid-State NMR Spectroscopy. *Prog. Nucl. Magn. Reson. Spectrosc.* **2010**, *56*, 46−77.
(87) Olah, G. A.; White, A. M. Carbon-13 Nuclear Magnetic Resonance Spectrum of Stable Nonclassical Norbornyl Cation . Incompatibility With Equilibrating Classical Ion Conception and Further Proof for Protonated Nortricyclene Structure. *J. Am. Chem. Soc.* **1969**, *91*, 3954−3956.
(88) Steiner, T. The Hydrogen Bond in the Solid State. *Angew. Chem., Int. Ed.* **2002**, *41*, 48−76.
(89) Serra-Crespo, P.; Gobechiya, E.; Ramos-Fernandez, E. V.; Juan-Alcaniz, J.; Martinez-Joaristi, A.; Stavitski, E.; Kirschhock, C. E. A.; Martens, J. A.; Kapteijn, F.; Gascon, J. Interplay of Metal Node and Amine Functionality in NH2-MIL-53: Modulating Breathing Behavior through Intra-Framework Interactions. *Langmuir* **2012**, *28*, 12916−12922.

Identifying Selective Host-guest Interactions Based on Hydrogen Bond Donor Acceptor Pattern in Functionalized Al-MIL-53 Metal-Organic Frameworks

Julia Wack,[†] Renée Siegel,[†,‡] Tim Ahnfeldt,[†,¶] Norbert Stock,[¶] Luís Mafra,[*,‡] and Juergen Senker[*,†]

Department of Inorganic Chemistry III, University of Bayreuth, 95440 Bayreuth, Germany, Department of Chemistry, CICECO, 3810-193 Aveiro, Portugal, and Department of Chemistry, Christian Albrechts University Kiel, 24118 Kiel, Germany

E-mail: lmafra@ua.pt; juergen.senker@uni-bayreuth.de

Phone: +351 234 370 620; +49 921 55 2532. Fax: +49 921 55 2788

Section: Implementation of the experiments on MIL-53/acetone

[*]To whom correspondence should be addressed
[†]University of Bayreuth
[‡]University of Aveiro
[¶]Christian Albrechts University Kiel

Section: Comparison of all the proton spectra for all systems

Figure S4: Comparison of 1D proton spectra of MIL-53/acetone, MIL-53-NH_2/acetone, MIL-53-NHCHO/acetone, MIL-53-NHCHO/ethanol and MIL-53-NHCHO/water.

Section:Assignment of MIL-53-NHCHO with different guest molecules

Figure S5: ^{1}H-^{13}C-HETCOR spectrum with selective PRESTO transfer and eDUMBO during t_1-evolution for MIL-53-NHCHO with ethanol in the pores.

Figure S6: ^{1}H-^{27}Al *D*-HMQC MAS spectrum for MIL-53-NHCHO with ethanol in the pores.

Figure S7: ^{1}H-^{14}N *D*-HMQC MAS spectrum for MIL-53-NHCHO with ethanol in the pores.

Figure S8: ^{1}H-^{13}C-HETCOR spectrum with selective PRESTO transfer and eDUMBO during t_1-evolution for MIL-53-NHCHO with water in the pores.

Figure S9: ^{1}H-^{27}Al *D*-HMQC MAS spectrum for MIL-53-NHCHO with water in the pores.

Figure S10: ^{1}H-^{14}N *D*-HMQC MAS spectrum for MIL-53-NHCHO with water in the pores.

Section: 1D ^{27}Al MAS spectra

Figure S11: 1D ^{27}Al MAS spectrum for MIL-53/acetone and SIMPSON simulation.

Figure S12: 1D ^{27}Al MAS spectrum for MIL-53-NH_2/acetone and SIMPSON simulation.

Figure S13: 1D ^{27}Al MAS spectrum for MIL-53-NHCHO/acetone and SIMPSON simulation.

Figure S14: 1D ^{27}Al MAS spectrum for MIL-53-NHCHO/ethanol and SIMPSON simulation.

Figure S15: 1D ^{27}Al MAS spectrum for MIL-53-NHCHO/water and SIMPSON simulation.

Section: 1D ^{13}C CP spectra of MIL-53/acetone, MIL-53-NH_2/acetone and MIL-53-NHCHO/acetone

Section: Host-guest interactions in MIL-53-NHCHO with ethanol and water molecules

Section: Dynamics of the guest molecules

Calibration on MIL-53/acetone

Due to the space symmetry of MIL-53 only few individual resonances for proton and carbon atoms are expected.[1] In figure S1 the 1D ^{1}H MAS NMR spectra of MIL-53/acetone recorded at different magnetic fields and with or without homonuclear decoupling are shown. The line width of the aromatic protons at 7.9 ppm is 2.6 ppm for the single pulse spectrum at the 400 MHz spectrometer and it is reduced to 1.0 ppm with the homonuclear decoupling. The resolution enhancement at the

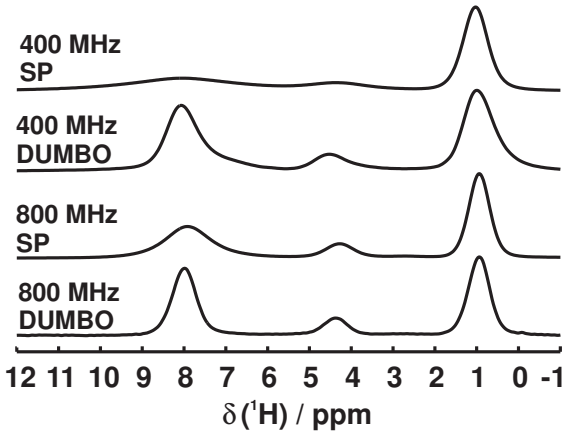

Figure S1: Comparison of the single pulse (SP) 1D proton spectra for MIL-53 with acetone in the pores at magnetic fields of B_0 = 9.4 and 18.8 T with 1D proton spectra measured with homonuclear decoupling (DUMBO).

800 MHz spectrometer is from 1.1 ppm line-width to 0.6 ppm. We chose the aromatic protons for this analysis since they exhibit the strongest dipolar couplings within the framework and, therefore, DUMBO is expected to have the largest effect on the resolution of this resonance.

The ^{1}H-^{13}C HETCOR spectrum of MIL-53/acetone is shown in figure S2. Figure S2 displays one correlation peak at 129.3 ppm/7.9 ppm, which is common for aromatic systems and can be assigned to C1, C2, C4 and C5, all the aromatic carbon atoms which have a proton covalently bound. The resonances at 137.2 ppm and 171.3 ppm assigned to the quaternary atoms C_3 C_6 C_7 C_8 in the ^{13}C CP spectrum show no correlations with protons. This demonstrates that we have chosen a sufficiently short mixing time for the ^{1}H-^{13}C HETCOR spectra.

The ^{1}H-^{27}Al *D*-HMQC spectrum is shown in figure S3. It depicts a correlation peak between the ^{27}Al and the proton signal at 4.2 ppm. The shape of the cross peak in the F1-dimension equates to the shape of a 1D ^{27}Al spectrum measured with a Hahn echo sequence (see figure S11) and is reflected by the refinement parameters of $\delta_{iso} = 2.7$ ppm, $C_Q = 9.2$ MHz and $\eta = 0.08$. These values correspond to a distorted octahedral surrounding and are in the range of the parameters published for this material.[1,2] The noise seen at the left border of the spectrum is caused by t_1-noise as described in the experimental section.

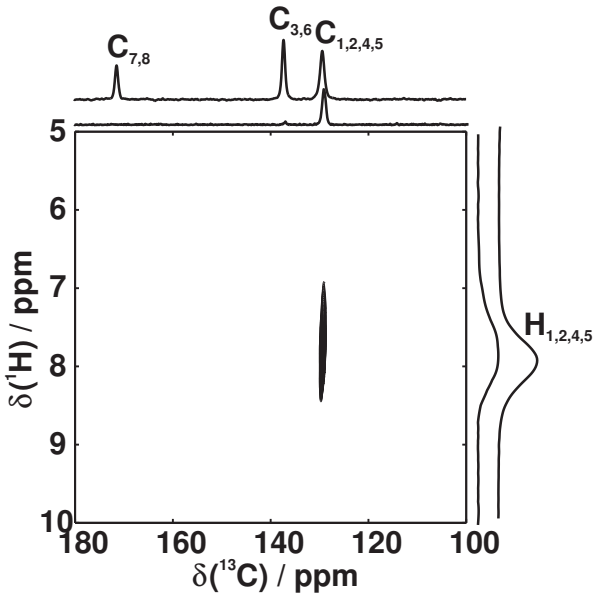

Figure S2: ^{1}H-^{13}C 2D HETCOR MAS spectrum with the respective projections using a selective PRESTO transfer ($\tau_{rec} = 62.5\mu s$) for MIL-53/acetone, identifying the strongest carbon proton couplings. On the top of each projection the corresponding 1D experiment is displayed.

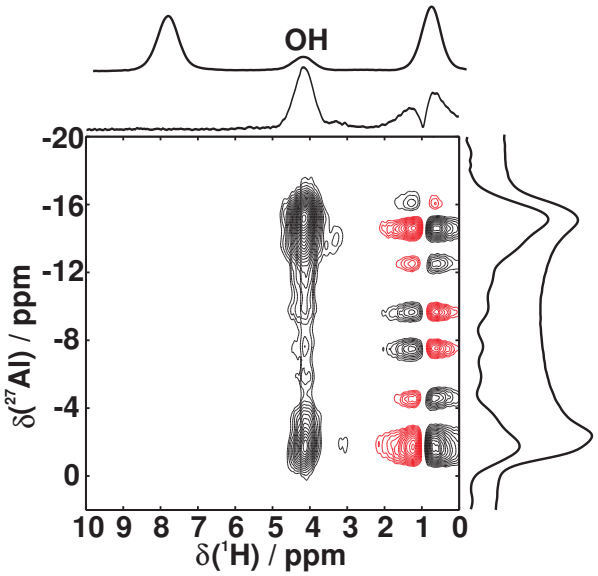

Figure S3: ^{1}H-^{27}Al 2D HETCOR MAS spectrum with the respective projections for MIL-53 with acetone in the pores. On top of each projection the corresponding 1D experiment is displayed. Positive and negative intensities are color coded in black and red, respectively.

Comparison of all the proton spectra for all systems

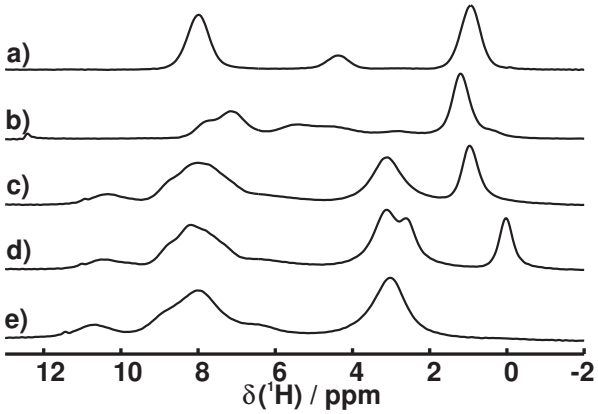

Figure S4: Comparison of 1D proton spectra of MIL-53/acetone (a), MIL-53-NH_2/acetone (b), MIL-53-NHCHO/acetone (c), MIL-53-NHCHO/ethanol (d) and MIL-53-NHCHO/water (e) all measured at a magnetic field of B_0 = 18.8 T with ^{1}H homonuclear decoupling.

Assignment of MIL-53-NHCHO with adsorbed ethanol

The assignment of the proton spectra for MIL-53-NHCHO with ethanol and water in the pores was performed with the same combination of HETCOR spectra presented for MIL-53-NHCHO/acetone and MIL53-NH_2/acetone. The ^{1}H-^{13}C HETCOR of MIL-53-NHCHO with ethanol molecules adsorbed (see figure S5) depicts correlation peaks for the aromatic carbon atoms and proton atoms at 8.7 ppm/125.0 ppm (H1/C1), at 7.8 ppm/125 ppm (H2/C2) and at 8.3 ppm/ 132.2 ppm (H4/C4). The proton in the formamido-group of the functionalization (H10) is represented in the PRESTO spectrum as a cross peak at 7.3 ppm/159.1 ppm and 8.1 ppm/162.8 ppm. From the fact that two different cross peaks are observed for the formamido-group we again conclude that different sites for the functional group exist.

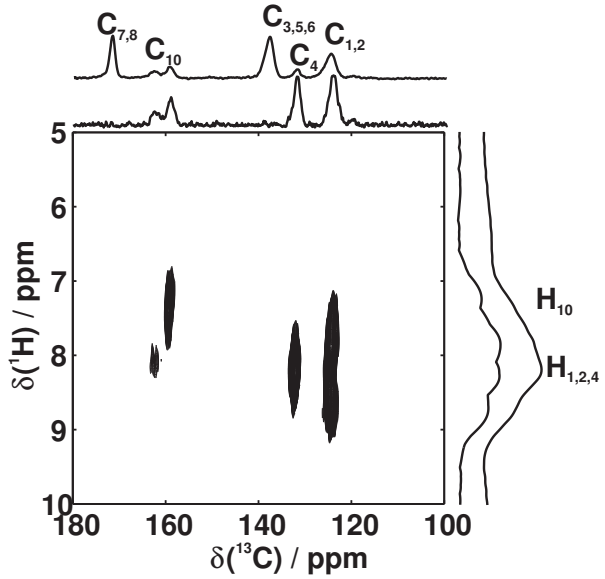

Figure S5: ^{1}H-^{13}C 2D HETCOR MAS spectrum with the respective projections using a selective PRESTO transfer ($\tau_{rec} = 62.5\mu s$) for MIL-53-NHCHO/ethanol, identifying the strongest carbon proton couplings. On the top of each projection the corresponding 1D experiment is displayed. The inset exhibits the region of the correlation peaks for the methyl group of the acetone molecules.

The ^{1}H-^{27}Al *D*-HMQC spectrum is shown in figure S6. The proton closest to the aluminum nuclei resonates at 6.1 ppm. The line shape of the aluminum spectrum corresponds to refinement parameters of $\delta_{iso} = 3.6$ ppm, $C_Q = 10.4$ MHz and $\eta = 0.04$. These are in the same range as the ones for MIL-53-NHCHO/acetone, which means that the influence of the guest molecule has no

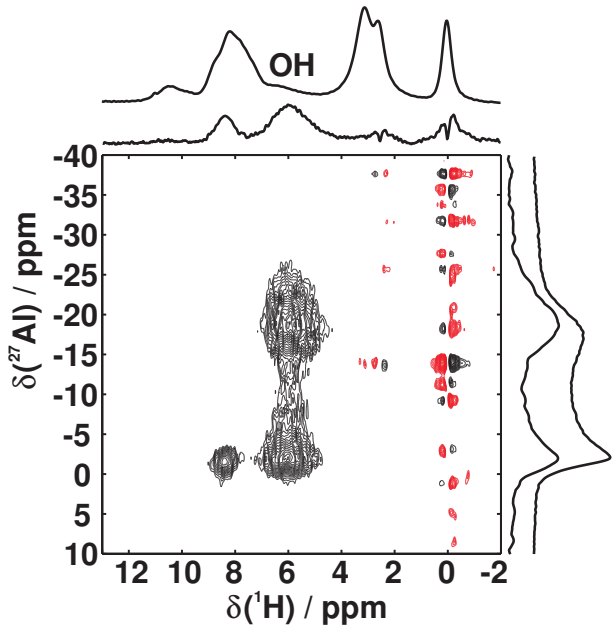

Figure S6: ^{1}H-^{27}Al 2D HETCOR MAS spectrum with the respective projections for MIL-53-NHCHO with ethanol in the pores. On top of each projection the corresponding 1D experiment is displayed. Positive and negative intensities are color coded in black and red, respectively..

influence on the quadrupolar parameters. As for MIL-53-NHCHO/acetone a very sharp and small signal at 8.0 ppm (^{1}H)/0.0 ppm (^{27}Al) is a small impurity of aluminum hydroxide ($Al(OH)_3$), which forms during the PSM of MIL-53-NH_2, in the projection it seams to be large but this is resulting from the very sharp peak compared to the very broad one for the framework.

In figure S7 the ^{1}H-^{14}N *D*-HMQC spectrum for MIL-53-NHCHO/ethanol is shown. The exchange peaks between ^{14}N and ^{1}H occur at 10.3 ppm, 9.4 ppm and a small onee at 8.5 ppm. In the case of ethanol molecules in the pores two main and one small site of NH-groups (H9) are distinguishable.

Assignment of MIL-53-NHCHO with adsorbed water

The ^{1}H-^{13}C HETCOR of MIL-53-NHCHO with water molecules in the pore (see figure S8) depicts correlation peaks for the aromatic carbon atoms and proton atoms at 8.6 ppm/125.0 ppm (H1/C1), at 7.6 ppm/125 ppm (H2/C2) and at 8.0 ppm/ 132.2 ppm (H4/C4). The CH proton in the

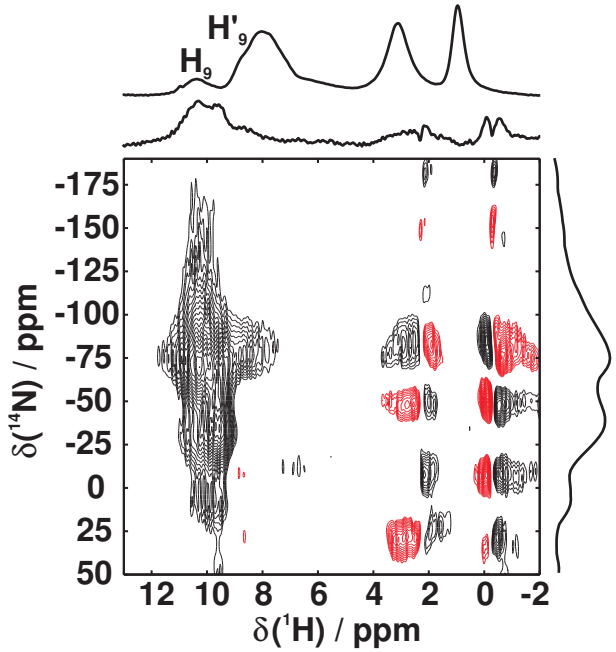

Figure S7: ^{1}H-^{14}N 2D *D*-HMQC with the corresponding projections for MIL-53-NHCHO with ethanol in the pores. On top of the F2 projection the 1D homonuclear decoupled proton spectrum is displayed. Positive and negative intensities are color coded in black and red, respectively.

formamido-group of the functionalization (H10) is represented in the PRESTO spectrum as a cross peak at 6.8 ppm/160.4 ppm and 7.4 ppm/162.5 ppm. As in all other MIL-53-NHCHO samples two different cross peaks are observed for the formamido-group revealing that the two sites for the functional groups are independent from the adsorbed guest molecule.

The ^{1}H-^{27}Al *D*-HMQC spectrum is shown in figure S9. The proton closest to the aluminum nuclei resonates at 6.12 ppm. The line shape of the aluminum spectrum corresponds to refinement parameters of $\delta_{iso} = 3.3$ ppm, $C_Q = 10.2$ MHz and $\eta = 0.06$. Since all the MIL-53-NHCHO samples were prepared with the same MOF all exhibit very sharp and small signal at 8.0 ppm (^{1}H)/0.0 ppm (^{27}Al) which is a small impurity of aluminum hydroxide ($Al(OH)_3$) forming during the PSM of MIL-53-NH_2, is observed in all MIL-53-NHCHO samples.

The ^{1}H-^{14}N *D*-HMQC spectrum in figure S10 reveals two exchange peak for proton nuclei with nitrogen nuclei at 10.5 ppm (H9) and 8.9 ppmm (H'9). From this it follows that in all the samples of MIL-53-NCHO at least two different formamido groups occur.

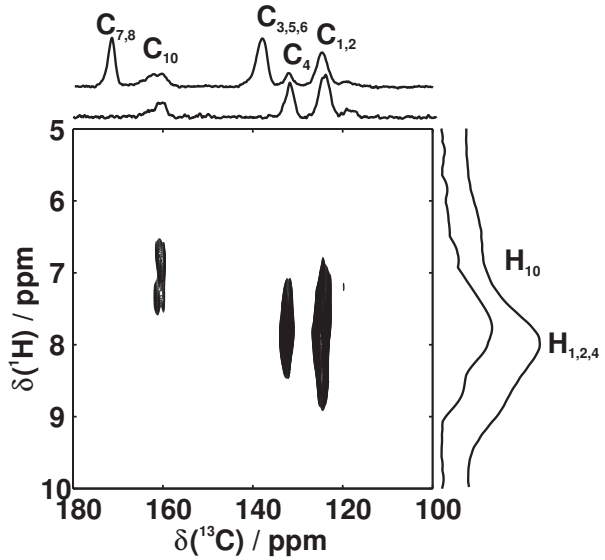

Figure S8: ^{1}H-^{13}C 2D HETCOR MAS spectrum with the respective projections using a selective PRESTO transfer ($\tau_{rec} = 62.5\mu s$) for MIL-53-NHCHO/water, identifying the strongest carbon proton couplings. On the top of each projection the corresponding 1D experiment is displayed.

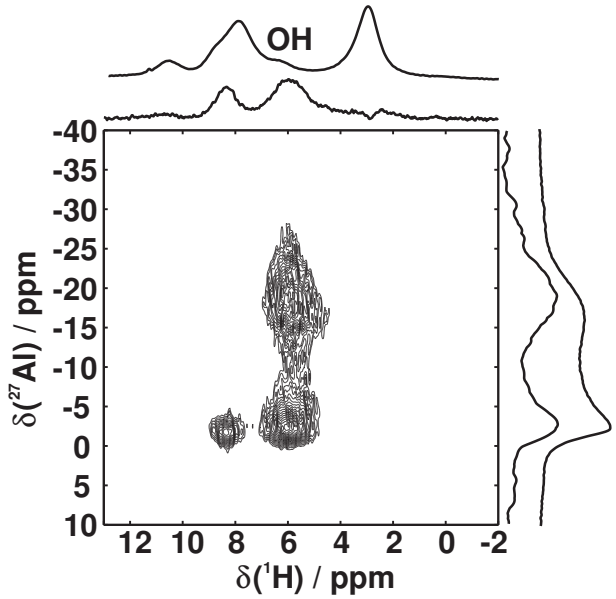

Figure S9: ^{1}H-^{27}Al 2D HETCOR MAS spectrum with the respective projections for MIL-53-NHCHO with water in the pores. On top of each projection the corresponding 1D experiment is displayed.

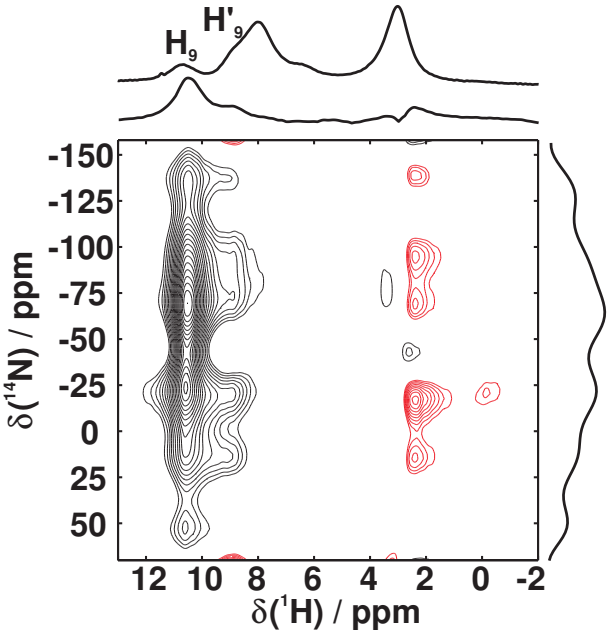

Figure S10: ^{1}H-^{14}N 2D *D*-HMQC with the corresponding projections for MIL-53-NHCHO with water in the pores. On top of the F2 projection the 1D homonuclear decoupled proton spectrum is displayed. Positive and negative intensities are color coded in black and red, respectively.

1D ^{27}Al MAS spectra

The simulations of the 1D ^{27}Al MAS spectra were performed with the SIMPSON simulation package.[3] The simulations included a single ^{27}Al spin with second order quadrupolar coupling. For powder averaging a repulsion file with 8000 crystal orientations was used. A Gaussian line broadening with 750 Hz was used for all simulations of the functionalized samples and of 500 Hz for MIL-53/acetone. The resulting parameters of the simulation of the 1D ^{27}Al MAS spectra for all the samples are summarized in Table S1.

Table S1: Quadrupolar paramters of ^{27}Al for all the samples

parameter	MIL-53/ acetone	NH_2/ acetone	NHCHO/ acetone	NHCHO/ ethanol	NHCHO/ water
δ_{iso} / ppm	2.7	1.9	3.6	3.6	3.3
η	0.08	0.12	0.05	0.04	0.06
C_Q / MHz	9.2	8.6	10.3	10.4	10.2

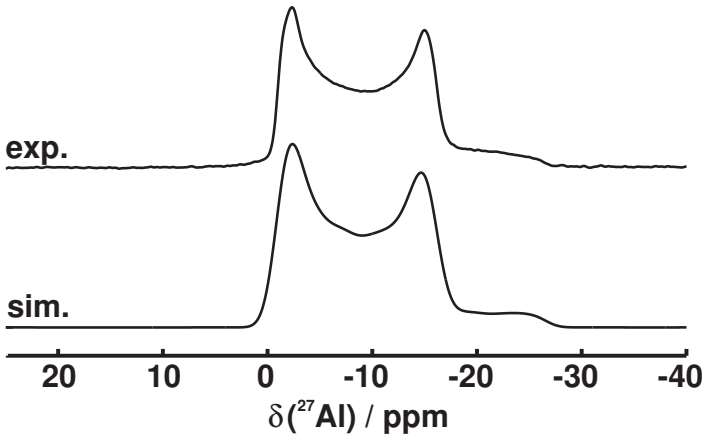

Figure S11: 1D ^{27}Al MAS spectra measured with the Hahn echo sequence for MIL-53/acetone with the SIMPSON simulation.

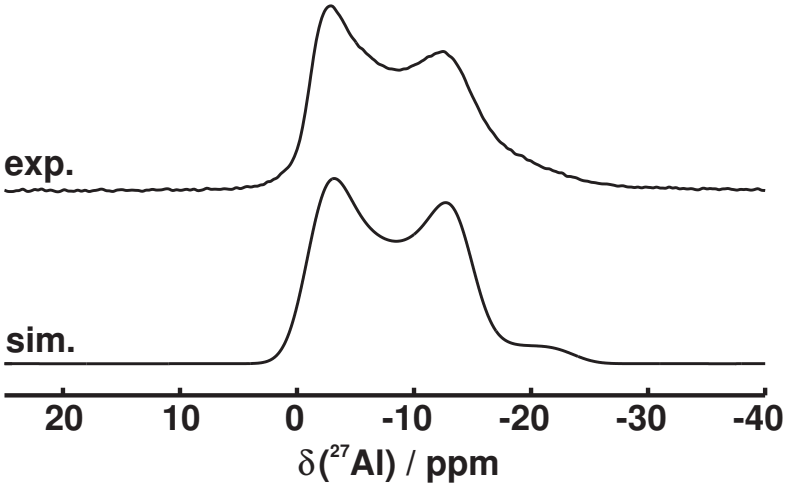

Figure S12: 1D ^{27}Al MAS spectra measured with the Hahn echo sequence for MIL-53NH_2/acetone with the SIMPSON simulation.

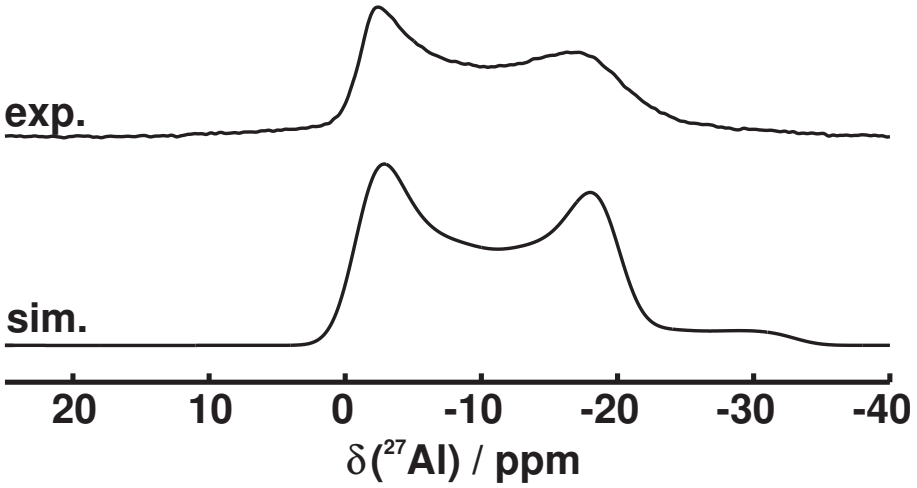

Figure S13: 1D ^{27}Al MAS spectra measured with the Hahn echo sequence for MIL-53NHCHO/acetone with the SIMPSON simulation.

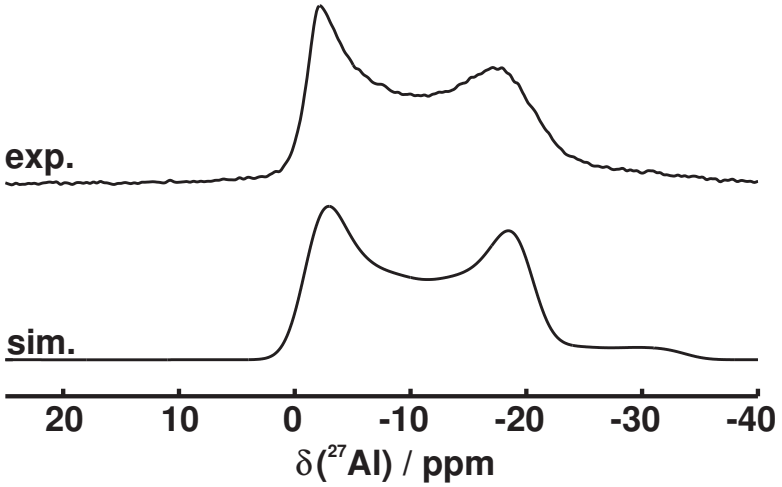

Figure S14: 1D ^{27}Al MAS spectra measured with the Hahn echo sequence for MIL-53NHCHO/ethanol with the SIMPSON simulation.

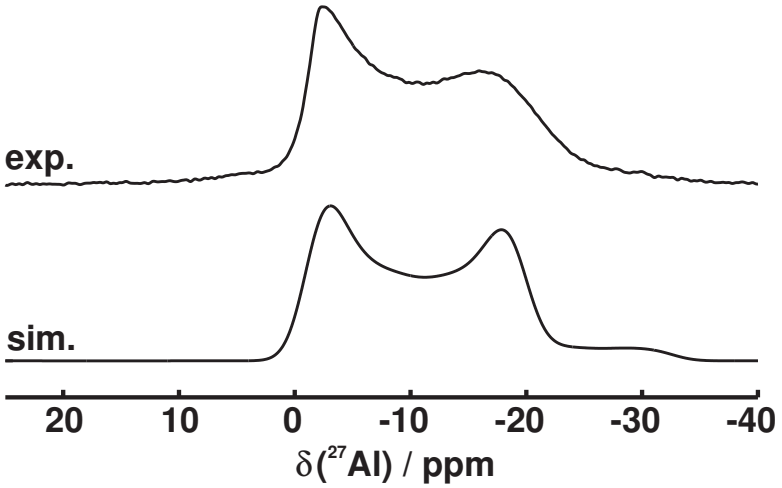

Figure S15: 1D ^{27}Al MAS spectra measured with the Hahn echo sequence for MIL-53NHCHO/water with the SIMPSON simulation.

1D ^{13}C CP spectra of MIL-53/acetone, MIL-53-NH_2/acetone and MIL-53-NHCHO/acetone

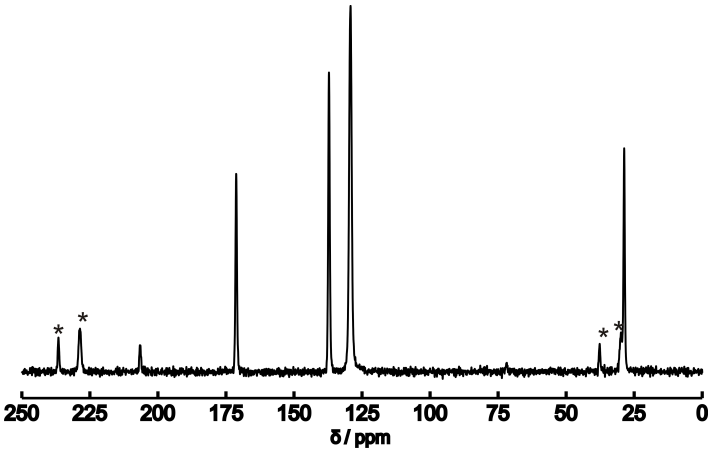

Figure S16: ^{13}C CP spectrum for MIL-53 with acetone in the pores.

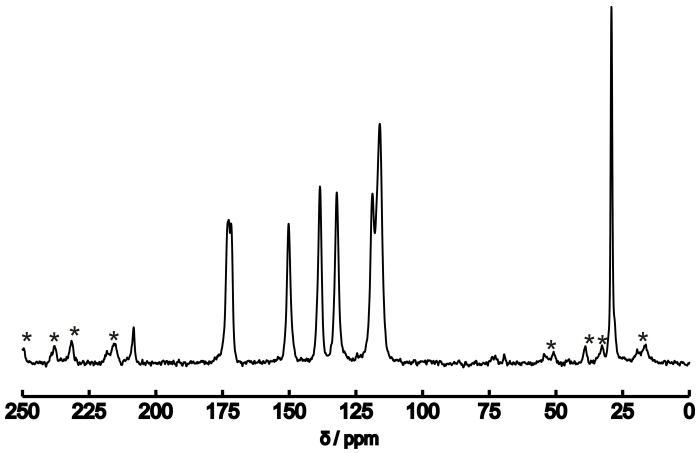

Figure S17: ^{13}C CP spectrum for MIL-53-NH_2 with acetone in the pores.

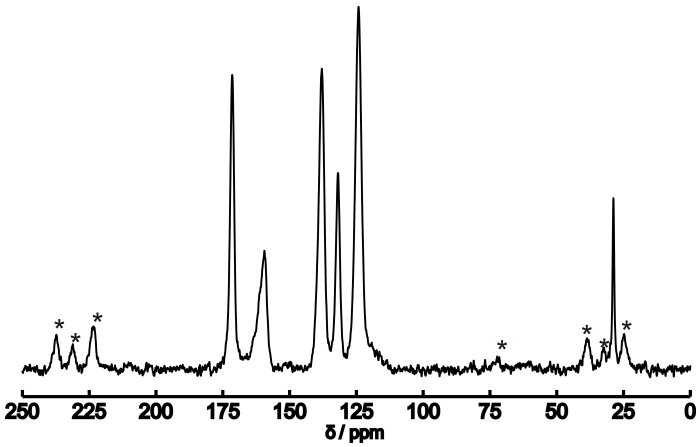

Figure S18: ^{13}C CP spectrum for MIL-53-NHCHO with acetone in the pores.

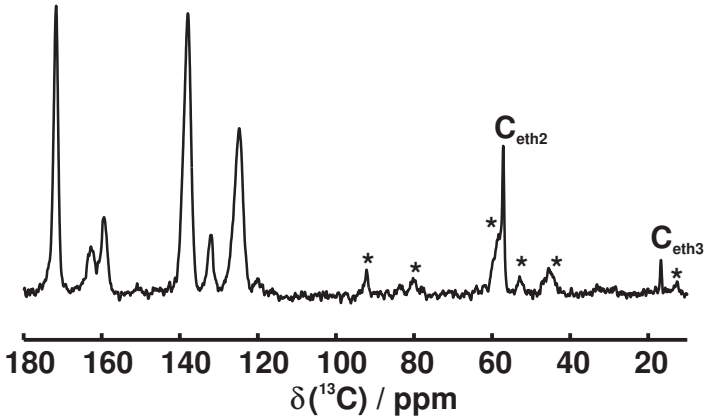

Figure S19: ^{13}C CP spectrum for MIL-53-NHCHO with ethanol in the pores.

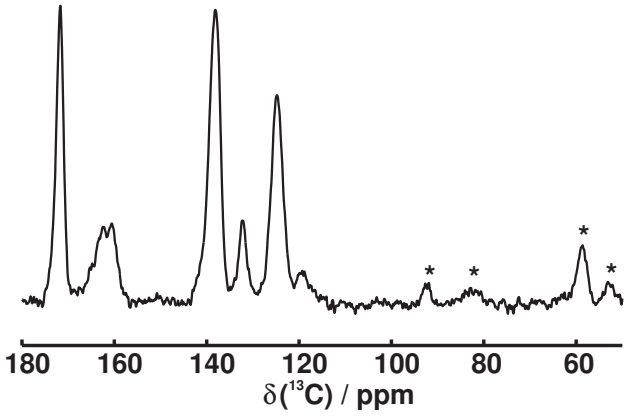

Figure S20: ^{13}C CP spectrum for MIL-53-NHCHO with water in the pores.

Host-guest interaction in MIL-53-NHCHO with ethanol and water

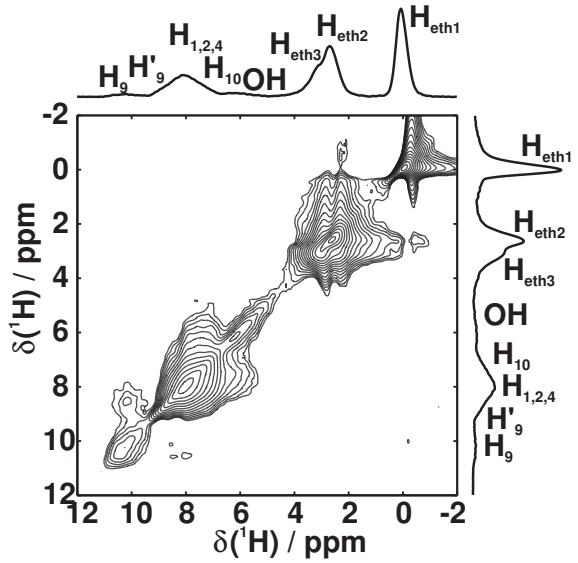

Figure S21: ^{1}H-^{1}H spin-diffusion spectra for MIL-53-NHCHO/ethanol at τ_{mix} = 2ms. On top and on the right sides of the 2D spectra the F2 and F1 projections including the preceding full assignment of the proton resonances are shown.

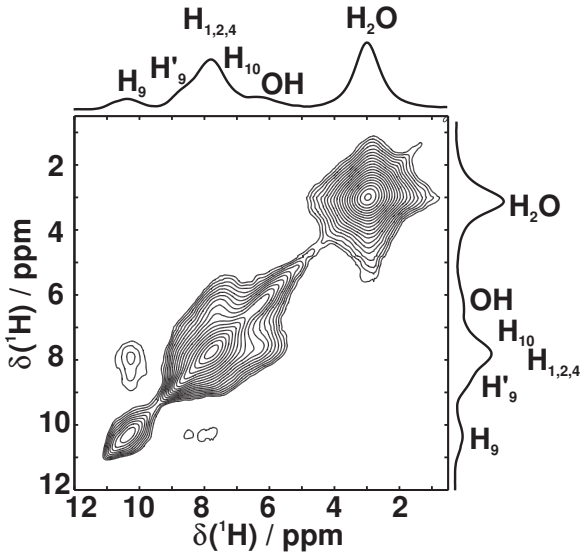

Figure S22: ^{1}H-^{1}H spin-diffusion spectra for MIL-53-NHCHO/water at τ_{mix} = 2ms. On top and on the right sides of the 2D spectra the F2 and F1 projections including the preceding full assignment of the proton resonances are shown.

Dynamics of the guest molecules

As already observed by the lack of exchange peaks for the guest molecules in the ^{1}H-^{13}C HETCOR spectra and in the ^{1}H-^{1}H spin-diffusion exchange experiments the guest molecules exhibit as pronounced mobility. This is additionally illustrated by the lack of spinning side bands in the proton one-pulse spectra, as shown exemplary for MIL-53-NHCHO and the three guest molecules – acetone, ethanol and water – in Figure S23. In particular, for CH_2 groups and for water molecules - with their large ^{1}H-^{1}H dipolar couplings ($D_{dip} \approx 35$ kHz) and short proton-proton distances of $\approx$ 1.5 Å - very broad lineshapes ($\approx$ 60 kHz) are observed e.g. in the wide-line spectra. This should give rise to pronounced spinning sidebands in the ^{1}H MAS spectra. In contrast, the spectra depicted in Figure S23 show almost no spinning side bands for the resonance of water and CH_2 resonance of the ethanol. This effect is not as pronounced for the CH_3 groups of the ethanol and acetone molecules since the well known methyl rotation preaverages the ^{1}H-^{1}H dipolar couplings by a factor of $\approx$ three. Thus even non-isotropic reorientational jump processes might cancel the spinning sidebands in the case of the CH_3 groups of the ethanol and acetone. A more detailed analysis, however, would require temperature dependent measurements for protonated and deuterated guest molecules.

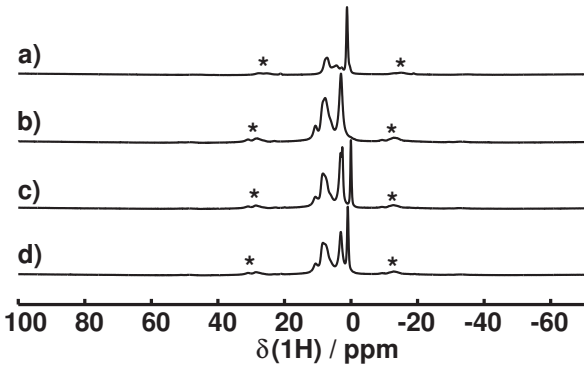

Figure S23: ^{1}H 1D proton spectra of MIL-53-NH_2/acetone (a), MIL-53-NHCHO/water (b), MIL-53-NHCHO/ethanol (c) and MIL-53-NHCHO/acetone (d) all measured at a magnetic field of B_0 = 18.8 T and a spinning speed of 16 kHz with a one-pulse excitation.

References

(1) Loiseau, T.; Serre, C.; Huguenard, C.; Fink, G.; Taulelle, F.; Henry, M.; Bataille, T.; Ferey, G. *Chem. Eur. J.* **2004**, *10*, 1373–1382.

(2) Lieder, C.; Opelt, S.; Dyballa, M.; Henning, H.; Klemm, E.; Hunger, M. *J. Phys. Chem. C* **2010**, *114*, 16596–16602.

(3) Bak, M.; Rasmussen, J. T.; Nielsen, N. C. *J. Magn. Reson.* **2000**, *147*, 296–330.

Publikationsliste

1. Dunja Hirsemann, Thomas K.-J Köster, Julia Wack, Leo van Wüllen, Josef Breu, Jürgen Senker, *Covalent Grafting to μ-Hydroxy-Capped Surfaces? A Kaolinite Case Study*, Chem. Mater. **23**, 3152–3158 (2011).

2. Thomas Rödl, Richard Weihrich, Julia Wack, Jürgen Senker, Arno Pfitzner, *Rational Syntheses and Structural Characterization of Sulfur-Rich Phosphorus Polysulfides: α-P_2S_7 and β-P_2S_7*, Angew. Chem. Int. Ed. **50**, 10996–11000 (2011).

3. Stephan Bernt, Mark Feyand, Antje Modrow, Julia Wack, Jürgen Senker, Norbert Stock, *[Zn($C_3H_3N_2$($C_3H_2N_2$-N=N-C_6H_5)], a Mixed-Linker ZIF Containing a Photoswitchable Phenylazo Group*, Eur. J. Inorg. Chem., 5378–5383 (2011).

4. Helge Reinsch, Martin Krüger, Julia Wack, Jürgen Senker, Fabrice Salles, Guillaume Maurin, Norbert Stock, *A new aluminium-based microporous metal-organic framework: Al(BTB) (BTB = 1,3,5-benzenetrisbenzoate)*, Microporous Mesoporous Mater. **157**, 50 – 55 (2012).

5. Helge Reinsch, Bartosz Marszałek, Julia Wack, Jürgen Senker, Barbara Gil, Norbert Stock, *A new Al-MOF based on a unique column-shaped inorganic building unit exhibiting strongly hydrophilic sorption behaviour*, Chem. Commun. **48**, 9 486–9488 (2012).

6. Tim Ahnfeldt, Daniel Gunzelmann, Julia Wack, Jürgen Senker, Norbert Stock, *Controlled modification of the inorganic and organic bricks in an Al-based MOF by direct and post-synthetic synthesis routes*, CrystEngComm **14**, 4126–4136 (2012).

7. Julia Wack, Renée Siegel, Tim Ahnfeldt, Norbert Stock, Luís Mafra, Jürgen Senker *Identifying Selective Host-guest Interactions Based on Hydrogen Bond Donor Acceptor Pattern in Functionalized Al-MIL-53 Metal-Organic Frameworks*, J. Phys. Chem. C **117**, 19991–20001 (2013).

8. Julia Wack, Tim Ahnfeldt, Carsten B. L. Tschense, Norbert Stock, Jürgen Senker *Preferred orientation of the formamido hydrogen bond anchor in MIL-53-NHCHO*, **to be submitted**.

Liste der Tagungsbeiträge

1. *Investigation of the hindered nucleation in the system triphenylphosphite via spin diffusion 13C solid-state NMR and computational methods*, The 6th Alpine Conference on Solid-State NMR, Chamonix (Frankreich), **2009** (Poster).

2. *Investigation of the hindered nucleation in the system triphenylphosphite via spin diffusion 13C solid-state NMR and computational methods*, 31^{st} Discussion Meeting Magnetic Resonance in Chemistry and Materials Research, Dresden (Deutschland), **2009** (Poster).

3. *Investigation of host-guest interactions in Metal-Organic Frameworks – Measuring chemical shift tensor orientations under slow MAS*, 15^{th} AK meeting, Halle (Deutschland), **2010** (Vortrag).

4. *Solid-state NMR study on structure and host-guest interactions in MIL53-NH*^{13}*CHO*, 2^{nd} International Conference on Metal-Organic Frameworks and Open Framework Compounds, Marseille (Frankreich), **2010** (Poster).

5. *Relative chemical shift tensor orientations in solid-state NMR under slow magic angle spinning*, 32^{nd} Discussion Meeting and Joint Benelux/German Magnetic Resonance Conference, Münster (Deutschland), **2010** (Poster).

6. *High-resolution solid-state NMR study of guest molecules in functionalized Al-MIL53 MOFs*, Seminario de RMN do CICECO/Universidade de Aveiro e da FCT/UNL, Aveiro (Portugal), **2011** (Vortrag).

7. *High-resolution solid-state NMR study of guest molecules in functionalized Al-MIL53 MOFs*, 2^{nd} SMARTER Crystallography Workshop, Aveiro (Portugal), **2011** (Poster).

8. *Elucidation of Host-Guest Interactions in Functionalized MIL-53 MOFs by High-Resolution Solid-State NMR Spectroscopy*, EUROMAR 2011 – Magnetic Resonance Conference, Frankfurt (Deutschland), **2011** (Poster).

9. *Elucidation of Host-Guest Interactions in Functionalized MIL-53 MOFs by High-Resolution Solid-State NMR Spectroscopy*, The 7th Alpine Conference on Solid-State NMR, Chamonix (Frankreich), **2011** (Poster).

10. *Elucidation of Host-Guest Interactions in Functionalized MIL-53 MOFs by High-Resolution Solid-State NMR Spectroscopy*, International Symposium on Metal-Organic Frameworks, Dresden (Deutschland), **2011** (Poster).

11. *Elucidation of Host-Guest Interactions in Functionalized MIL-53 MOFs by High-Resolution Solid-State NMR Spectroscopy*, 17^{th} AK meeting, Łagow (Polen), **2012** (Vortrag).

12. *Solid-State NMR Study on the Binding Sites of Acetone Molecules in Functionalized MIL-53 MOFs*, EUROMAR 2012 – Magnetic Resonance Conference, Dublin (Irland), **2012** (Poster).

13. *Solid-State NMR Study on the Binding Sites of Acetone Molecules in Functionalized MIL-53 MOFs*, 3^{nd} International Conference on Metal-Organic Frameworks and Open Framework Compounds, Edinburgh (UK), **2012** (Poster).

14. *Targeting selective host-guest interactions inf functionalized MOFs – synthesis and solid-state NMR studies*, Status Report Meeting 2012, Dresden (Deutschland), **2012** (Vortrag).

Danksagung

Danke – Thank You – Obrigada –Merci

An dieser Stelle möchte ich Allen danken, die durch ihre Unterstützung zum Gelingen dieser Arbeit beigetragen haben.

Besonderer Dank gilt vor allem meinem Doktorvater Prof. Dr. Jürgen Senker für die Bereitstellung des sehr vielseitigen und interessanten Themas, dass er mir bei der Bearbeitung jegliche Freiheit gelassen hat und jederzeit ein offenes Ohr für Fragen und bei Problemen hatte. Ich bedanke mich für die Zeit, die er sich genommen hat, für die langen wertvollen Diskussionen und für die daraus entstandenen neuen Denkanstöße.

Des weiteren möchte ich Dr. Luís Mafra für die freundliche Aufnahme in seiner Arbeitsgruppe in Aveiro danken. Ebenso dass er mir die Möglichkeit geboten hat, nicht nur seine NMR Geräte zu nutzen, sondern auch Messzeit am 800 MHz NMR zur Verfügung gestellt hat, sowie für die vielen fruchtbaren Diskussionen. Besonderer Dank gilt auch Dr. Renée Siegel bei der Unterstützung der NMR Messungen in Portugal.

Allen Kollaborationspartnern in Kiel, Prof. Dr. Norbert Stock, Dr. Tim Ahnfeldt, Dr. Stephan Bernt und Dr. Helge Reinsch, danke ich für die sehr gute und erfolgreiche Zusammenarbeit.

Ein großer Dank geht an alle meine Praktikanten, Hiwis und Bachelorstudenten, Johannes Wittmann, Maria Mesch, Christoph Zehe, Sandra Haupt, Carsten Tschense und Adrian Schmutzler. Danke für euer Interesse und eure unermüdliche Motivation.

Allen Mitgliedern der Lehrstühle AC I und AC III danke ich für die wunderbare Atmosphäre, für die Hilfsbereitschaft, für die vielen gemütlichen Stunden im Kaffeezimmer, für

viele wissenschaftliche und nicht wissenschaftliche Diskussionen zu allen Tages- und Nachtzeiten und für viele unvergessliche Abende auf der AC Terrasse. Ich habe mich in der Zeit an diesem Lehrstuhl sehr zu Hause gefühlt!

Außerdem möchte ich besonders Dr. Dunja Hirsemann, Ramona Deinlein, Maria Mesch und Dr. Caroline Keenan für die sehr schöne und lustige Zeit in unserem kleinen "Labor" danken. Danke, dass ihr mich auch trotz des vielen Singens ertragen habt.

Des weiteren danke ich dem Elitenetzwerk Bayern (ENB), für das Stipendium im internationalen Graduiertenkolleg *Struktur, Reaktivität und Eigenschaften oxidischer Materialien*. Dies hat mir nicht nur den Auslandsaufenthalt und die Teilnahmen an zahlreichen Tagungen und Soft Skill Seminaren ermöglicht, ich konnte hierdurch auch mal fachlich über den Tellerrand in die Welt der Geologie schauen.

Der größte Dank geht an meine Familie und ganz besonders an meine Mutter, die mir immer zur Seite gestanden hat und ohne die weder Studium, noch die Promotion möglich gewesen wäre. Vielen, vielen Dank für Alles!!

(Eidesstattliche) Versicherungen und Erklärungen

(§5 2 Nr. 4 PromO)

Hiermit erkläre ich, dass keine Tatsachen vorliegen, die mich nach den gesetzlichen Bestimmungen über die Führung akademischer Grade zur Führung eines Doktorgrades unwürdig erscheinen lasse

(§8 S. 2 Nr. 5 PromO)

Hiermit erkläre ich mich damit einverstanden, dass die elektronische Fassung meiner Dissertation unter Wahrung meiner Urheberrechte und des Datenschutzes einer gesonderten Überprüfung hinsichtlich der eigenständigen Anfertigung der Dissertation unterzogen werden kann.

(§8 S. 2 Nr. 7 PromO)

Hiermit erkläre ich eidesstattlich, dass ich die Dissertation selbständig verfasst und keine anderen als die von mir angegebenen Quellen und Hilfsmittel benutzt habe.

(§8 S. 2 Nr. 8 PromO)

Ich habe die Dissertation nicht bereits zur Erlangung eines akademischen Grades anderweitig eingereicht und habe auch nicht bereits diese oder eine gleichartige Doktorprüfung endgültig nicht bestanden.

(§8 S. 2 Nr. 9 PromO)

Hiermit erkläre ich, dass ich keine Hilfe von gewerblichen Promotionsberatern bzw. - vermittlern in Anspruch genommen habe und auch künftig nicht nehmen werde.

Bayreuth, den

.....
Julia Wack